SST Review, February 2013

Authors:

T. Greenshaw (Liverpool University) ;

for the 1M-SST -

D. della Volpe DPNC - Universitè de Genéve, Switzerland

R. Moderski Nicolaus Copernicus Astronomical Center- Krakow - Poland

T. Montaruli DPNC - Universitè de Genéve, Switzerland

J. Niemiec IFJP - Institute of Nuclear Physics, Krakow, Poland

K. Seweryn Space Research Centre, Polish Academy of Sciences, Warsaw, Poland ;

for ASTRI -

A. Antonelli INAF-Osservatorio Astronomico di Roma

S. Billotta INAF-Osservatorio Astrofisico di Catania

G. Bonanno INAF-Osservatorio Astrofisico di Catania

G. Bonnoli INAF-Osservatorio Astronomico di Brera

R. Canestrari INAF-Osservatorio Astronomico di Brera

O. Catalano INAF-IASF Palermo

V. de Caprio INAF-Osservatorio Astronomico di Capodimonte

M. Fiorini INAF-IASF Milano

E. Giro INAF-Osservatorio Astronomico di Padova

A. Grillo INAF-Osservatorio Astrofisico di Catania

N. La Palombara INAF-IASF Milano

G. La Rosa INAF-IASF Palermo

G. Pareschi INAF-Osservatorio Astronomico di Brera,

G. Rodeghiero INAF-Osservatorio Astronomico di Padova

J. Schwarz INAF-Osservatorio Astronomico di Brera

G. Sironi INAF-Osservatorio Astronomico di Brera

L. Stringhetti INAF-IASF Milano

G. Tosti Universita' di Perugia

M. Trifoglio INAF-IASF Bologna

S. Vercellone INAF-IASF Palermo;

for GATE -

D. Dumas Observatoire de Paris

P. Laporte Observatoire de Paris

J-L. Dournaux Observatoire de Paris

J. M. Huet Observatoire de Paris

H. Sol Observatoire de Paris

A. Zech Observatoire de Paris

G. Fasola Observatoire de Paris

F. De Frondat Observatoire de Paris

J-P. Amans Observatoire de Paris

C. Costille Observatoire de Paris

F. Sayède Observatoire de Paris

I. Jégouzo-Giroux Observatoire de Paris

C. Rulten Observatoire de Paris ;

for CHEC -

R. White (University of Leicester)

J. Hinton (University of Leicester)

D. Ross (University of Leicester)

J. Sykes (University of Leicester)

S. Ohm (University of Leicester)

J. Schmoll (University of Durham)

P. Chadwick (University of Durham)

M. K. Daniel (Liverpool University)

G. Cotter (University of Oxford)

G. S. Varner (University of Hawaii)

S. Funk (SLAC)

J. Vandenbroucke (SLAC)

L. Sapozhnikov (SLAC)

J. Buckley (Wash U.)

P. Moore (Wash U.)

D. Williams (UCSC)

S. Markoff (Amsterdam University)

J. Vink (Amsterdam University)

D. Berge (Amsterdam University)

N. Hidaka (Solar-Terrestrial Environment Laboratory, Nagoya University)

A. Okumura (Solar-Terrestrial Environment Laboratory, Nagoya University)

H. Tajima (Solar-Terrestrial Environment Laboratory, Nagoya University) ;

SST engineer -

S. Blake University of Leicester

Approved By: (institutes)

- Liverpool
- INAF
- Leicester
- Paris
- DPNC - Universitè de Genéve, Switzerland
- IFJ PAN - Institute of Nuclear Physics, Krakow, Poland
- Space Research Centre, Polish Academy of Sciences, Warsaw, Poland
- Jagiellonian University - Krakow, Poland
- AGH University of Science and Technology - Krakow - Poland
- Universität Zürich, Switzerland
- Universität Tübingen, Germany
- Max Planck Institute for Nuclear Physics, Heidelberg, Germany

List of Abbreviations:

ACS ALMA Common Software

AIV Assembly, Integration and Verification

AMCU Active Mirror Control Unit

ASTRI Astrofisica con Specchi a Tecnologia Replicante Italiana

AoI Angle of Incidence

BEE Back–End Electronics

CACS Calibration/Auxiliary Control System

CADC Camera Ancillary Devices Control

CAS Camera Ancillary Subsystems

CCS Camera Control System

CDS Camera Detection Subsystem

CFRP Carbon Fiber Reinforced Plastic

CoG Centre of Gravity

COTS Commercial Off-The-Shelf

CTA Cherenkov Telescope Array

CTE Coefficient of Thermal Expansion

DACOS Data Collection System

DAQ Data Acquisition System

DCS Detector Control Software

DDS DAQ Software

DHS Data Handling System

DOF Degree Of Freedom

ECAP Erlangen Centre for Astrophysics

EMC Electromagnetic Compatibility

FE Finite Element

FEA Finite Element Analysis

FEM Finite Element Model

FoV Field of View

GPS Global Positioning System

GPU Graphical Processing Unit

GUI Graphical User Interfaces

ICS Instrument Control System

INAF Istituto Nazionale di Astrofisica

KIP Key Integration Point

LST Large Size Telescope

M1 Primary Mirror

M2 Secondary Mirror

MASS Mini–Array Software System

MLE Maximum Likely Earthquake

MPPC Multi–Pixel Photon Counter

MST Medium Size Telescope

MTBF Mean Time Before Failure

NCR Non–Conformity Report

NIST National Institute of Standards and Technology

NI National Instruments

NSB Night Sky Background

NTP Network Time Protocol

OBE Operating Basis Earthquake

OS Operating System

OCS Observatory Control System

OMC Operations Monitoring and Control

OPC–UA OLE for Process Control – Unified Architecture

PDE Photon Detection Efficiency

PDM Photon Detection Module

PLC Programmable Logic Controller

PMMA Poly-methyl methacrylate

PSF Point Spread Function

RAMS Reliability, Availability, Maintainability and Safety

RT Real Time

S-C Schwarzschild-Couder

SiPM Silicon Photo-Multiplier

SLS Serviceability Limit State

SQM Sky Quality Meter

SRD System Requirement Document

SST Small Size Telescope

TAC Time Allocation Committee

TCS Telescope Control System

TCU Telescope Control Unit

TMCDB Telescope Monitoring and Configuration Database

TMD Tuned Mass Damped

TP Test Point

TBD To Be Determined

ULS Ultimate Limit State

VCD Verification Control Document

VI Virtual Instrument (Labview's programs and sub-programs)

History:		
1.0	2013-01-31	Initial Version
1.1	2013-02-12	Added GATE & ASTRI
1.2	2013-02-15	Added CHEC
1.3	2013-02-17	Added SST-1M
1.4	2013-02-18	First completed draft

Distribution: SST Group

Contents

1 Overall Introduction

The Cherenkov Telescope Array (CTA) represents a major step forward in sensitivity and precision for astronomy across 4 decades in energy at the high-energy end of the electromagnetic spectrum. It will provide data of unprecedented precision and scope that will address key questions in astroparticle and fundamental physics. CTA will achieve this sensitivity to gamma rays of energies from below ~ 20 GeV up to ~ 300 TeV by using Cherenkov telescopes of three sizes, covering the low, intermediate, and high energy regimes. These will be located at two sites, one in the northern and one in the southern hemisphere. Here, we concentrate on the instrumentation for the southern site, which will study both galactic and extra-galactic sources. The lowest energy photons ($\sim 20 - 200$ GeV) from these sources will be detected with a few, ~ 23 m diameter Large Size Telescopes (LSTs), collecting as many Cherenkov photons from low-energy air showers as possible, with a moderate Field of View (FoV) of 4.4°. At intermediate energies, from around 200 GeV to a few TeV, the sensitivity will be dominated by about 25 Medium Size Telescope (MSTs) of 12 m diameter with a FoV of over 7°. These single-mirror telescopes will later be supplemented with a further 36 dual mirror telescopes of similar size, increasing the sensitivity of CTA in the intermediate energy range. Gamma rays at the highest energies (from ~ 1 TeV to ~ 300 TeV) produce enough Cherenkov photons to be detectable with ~ 4 m diameter Small Size Telescopes (SSTs). However, gamma rays above 1 TeV become increasingly rare due to the steeply falling energy spectra of typical sources. Therefore, a large area on the ground (about 5 to 10 km^2) must be covered, requiring many (~ 70) SSTs. A large FoV of above 8° is needed to image showers whose axis falls far from a given telescope, thereby increasing the number of telescopes that see a given shower and improving the angular resolution of the array.

The exploration of the extreme high-energy end of the electromagnetic spectrum with the SST array will enable the investigation of a range of topics in both fundamental physics and astrophysics. For example, observing over a large spectral range up to a few hundred TeV with good energy and spatial resolution will make it possible to analyze extreme acceleration processes and the nature and maximum energies of the particles responsible for very high energy (VHE) photon emission, especially for galactic sources. In extragalactic space, it should become possible to find out whether the observed cut-offs in blazar spectra at various redshifts are mostly intrinsic to the sources, are induced by the effect of the Extragalactic Background Light (EBL) absorption, or indeed whether they indicate the presence of axion-like particles that can travel long distances without suffering absorption.

This document presents progress in the prototyping of the three SST designs that are being investigated within CTA. In contrast to the first SST review, the progress with the design and prototyping of cameras that can be used on these telescopes is also presented. Two of the telescopes that are being developed are dual mirror (2M) instruments, the SST-GATE and ASTRI designs under development in France and Italy, respectively. These have a focal length of about 2 m, allowing the use of a compact camera of diameter about 35 cm with a pixel size of about $6\times$ 6 mm^2. The third telescope uses single mirror (1M) Davies-Cotton (D-C) optics and has a focal length of 5.6 m. The pixels of the camera required for this telescope are of size about 23×23 mm^2. This 1M-SST is being developed by groups in Switzerland and Poland. The reason for the development of these novel telescopes is the need to reduce the SST cost. In the case of the 2M telescopes, the camera can use multi-pixel detectors, such as multi-anode photomultiplers (MAPMs) or multi-pixel Geiger-mode avalanche photodiodes (GAPDs, also referred to as silicon photomultipliers, SiPMs). The two camera designs that use these sensors and are matched to the 2M telescopes promise significant cost savings with respect to the conventional photomultiplier (PM) based camera that would typically be

used on a D-C telescope. In the case of the 1M telescope, a large hexagonal GAPD has been developed for its camera, with a flat-to-flat dimension of about 10 mm. The difference between the GAPD and pixel size is bridged by using Winston cones to concentrate the light onto the sensor. Again, the camera, and hence telescope, cost promises to be lower than that of a PM-based device because of the use of the SiPMs.

Early versions of the SST-GATE and ASTRI telescope structures were presented at the previous SST review and useful feedback was obtained on their designs. Significant progress has been made since that review, and first elements of these telescopes are now production ready. It is planned that prototypes of the 2M telescopes and cameras will be produced and tested in 2014, the SST-GATE telescope in Paris and the ASTRI design at the Serra La Nave observing station on Mount Etna. If these telescopes demonstrate that 2M systems can provide the required performance, the groups involved have agreed that they will then work to produce a single 2M design, which they will construct in the first instance for a "mini-array" on the CTA site. A similar agreement has been reached by the groups designing the 2M cameras. The "mini-array" will form the first section of CTA and will consist of a handful of SSTs and probably also an MST. It will form a test-bed for the operation of a multi-telescope array, aiding, for example, the development and testing of the triggering, control and data acquisition software for CTA.

The progress with the 1M-SST and its camera will be reviewed on a similar timescale to the above tests. If this is also able to meet the specifications for the SST, CTA will then have to decide how to proceed with the construction of the high energy section of the array, given the costs of the 1M and 2M telescopes, the performance they achieve and the resources available to the groups pursuing their construction.

A further telescope was presented at the first SST review. This was a 7 m diameter D-C device, designed to use a PM-based camera similar to that needed for the MST. Useful feedback on this design was obtained at the last review, and it was modified according to the panel's recommendations. The design of the structure of this telescope is now complete, and it is no longer being actively pursued. If, however, none of the above telescopes were to prove satisfactory, a 7 m D-C SST could be produced on a timescale concomitant with CTA plans.

The remainder of this document is divided into sections which consider: the status of the 1M-SST telescope with its camera; the status of the ASTRI 2M design and its camera; the progress with the development of the structure and mirrors of the SST-GATE telescope; and the design of a Compact High-Energy Camera (CHEC) suitable for either the ASTRI or SST-GATE telescopes. Additional information is provided in appendices. These describe: the requirements for the SST derived by CTA from the scientific and technical requirements for the array; the ASTRI data analysis chain being developed for both the prototype tests and for the "mini-array"; details on some aspects of the SST-GATE design; general considerations regarding the study of the response of the SST to seismic activity; and first studies of peak power reduction strategies for the SST array.

2 The Single Mirror Davies Cotton SST (1M-SST)

2.1 Introduction

Here and in the following we will present a single mirror Davies-Cotton design for the CTA Small Size Telescope. Davies-Cotton telescopes are currently used successfully in many astrophysics experiments (H.E.S.S., MAGIC, VERITAS, HEGRA) for Cherenkov gamma-ray observation. The requirements for the Small Size Telescope of the CTA array are defined in [7] and [20].

The proposed telescope has a 4 m-diameter mirror dish with f/D ratio of 1.4 which implies the camera is mounted at 5.6 m from the dish. The proposed camera is a new design in which the photo detection plane (PDP) is completely separated from the readout electronics which will sit on the rear of the mirror support. The photo detector plane will use GAPD photosensors. This technology has been proven to work in gamma astronomy by the FACT experiment.

The reason for this choice has two main motivations:

1. The physics goals of SSTs are in the energy range between 1-300 TeV (e.g. large scale surveys, high precision measurement of high energy tail of spectra, search for cosmic ray sources). It is then fundamental to achieve the longest possible exposure times to collect the poor photon statistics above 10 TeV. GAPDs (as demonstrated by FACT on the Canary islands) can be operated in this energy region with moonlight, hence gaining about 30% exposure time.
2. The choice of GAPD sensors it is not only convenient as their size naturally fits the size of 4 m dish, but it also represents in the long term a more promising technology than photomultipliers (PMs). Such a development for SST Davies-Cotton telescopes, can be easily adapted for a second generation of MST and LST cameras. Even if GAPDs still have a limited market in this field of application, a number of companies (such as Hamamatsu, Ketek, SenSL and Excelitas) are already competing, esulting in rapid improvements and decreasing costs. A similar number of Ultra-bialkali small PMTs used by FlashCam-MST is about a factor two more expensive than GAPDs and the photo-detection efficiency is comparable. [1]

2.2 Telescope Structure

The telescope structure consists of several sub-systems, as shown in Fig. 2.1. The mast (1) is directly connected to the dish support structure (2) to which the counterweight (3) is also attached. The rigidity of the mast is increased by the use of thin pre-tensioned steel rods. The mast positions the camera (4) with respect to the mirrors (5) mounted on the dish (6) that is attached to the dish support structure (2). The basic material used is steel. All steel profiles and tubes can be obtained as off-shelf products from industry.

[1] The photo-detection efficiency for GAPDs convolves quantum efficiency, fill factor and avalanche probability and should be convolved with the Cherenkov spectrum at ground. This is the quantity that should be compared to photomultiplier quantum efficiency, convolved with the first dynode collection efficiency and spectral response.

The dish support structure is mounted on the telescope support (7). The dock station (8) locks the telescope in a parking position.

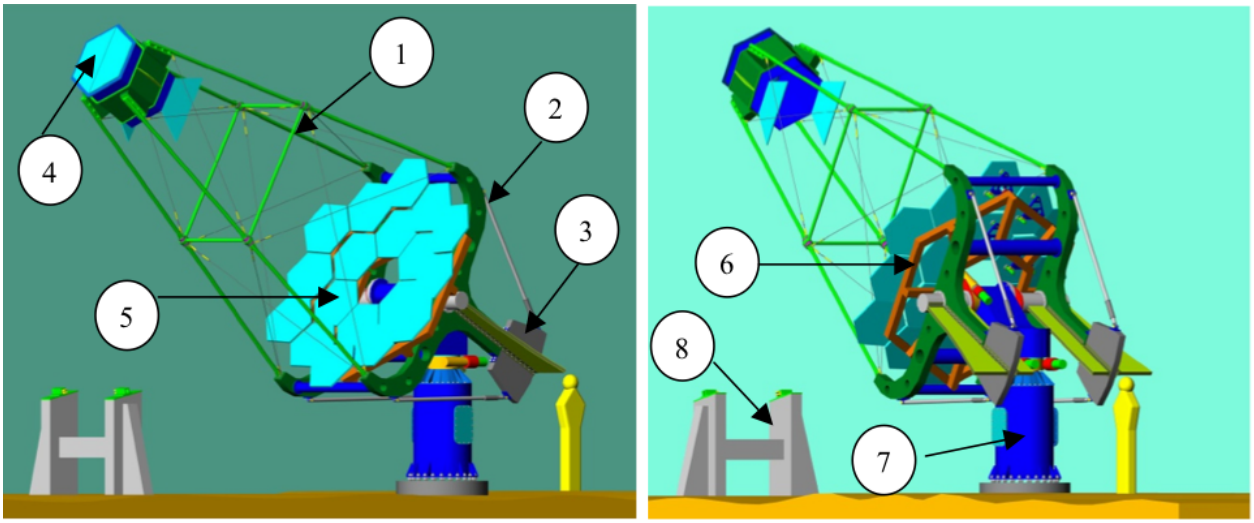

Figure 2.1: 1M-SST telescope sub-systems.

The main dimensions of the telescope structure are shown in Fig. 2.2. The design has been optimized in such a way that the telescope structure can be divided into smaller units that fit the standard size of a top-loading container of standard size ($2.3\ m \times 2.6\ m \times 12\ m$ in order to cut transportation costs. When the telescope is in its parking position, the distance between the camera and the ground is 1 m. This ensures easy and quick access to the camera for maintenance. The camera is locked in the dock station (8) in fig 2.1 and the locking system enables an axial displacement of the camera.

The total weight of the current design is about 9 tons. The weight of the telescope sub-systems is depicted in Table 1.

2.3 Mirror Dish

The layout of 18 mirror tiles on the dish is shown in Fig. 2.3 (with the empty space in the center due to obscuration by the camera). The 1M-SST sub-consortium has decided to use hexagonal facets of size 0.78 m flat-to-flat that make up the reflecting dish of about 4 m diameter (with space between the tiles of 2 cm). Both the number and size of the facets are chosen to satisfy the requirement on the PSF (B-SST-0130 in [20] as will be discussed in Sec. 2.4.1). The radius of curvature of a single mirror is 11.2 m and the thickness of a glass mirror tile is about 2 cm. The maximum weight of the single mirror is assumed to be 25 kg for glass mirrors, similar to those used by H.E.S.S.. Other technical solutions for the mirror tiles are under evaluation (see sec. 2.4.3), and for these cases the weight can go as low as 6-7 kgs. In Tab. 2 are summarized the requirements that are satisfied by the main general characteristics of the telescope.

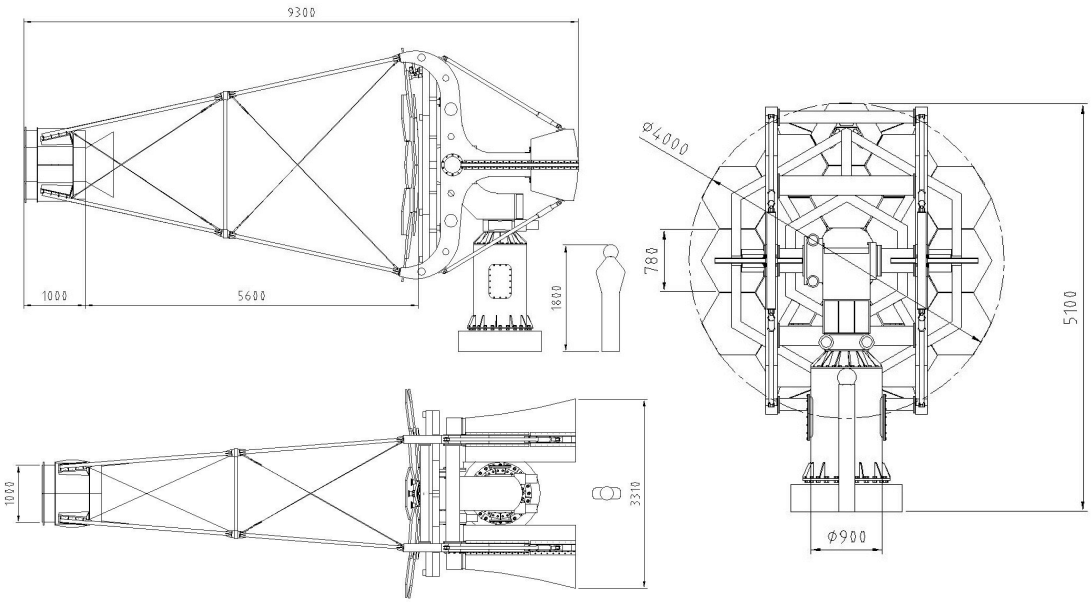

Figure 2.2: Main dimensions of the 1M-SST telescope structure (side, rear, and top view).

telescope support	tower & head slew drives & bearings (2 x 500 kg)	1.9 t 1.0 t
dish support structure + mast	dish support structure counterweight mast	2.7 t 1.6 t 0.2 t
dish + mirrors	dish mirrors + mounts (18 mirrors x 35 kg)	0.5 t 0.6 t
camera	camera total weight	0.3 t 8.8 t

Table 1: Weight of 1M-SST subsystems.

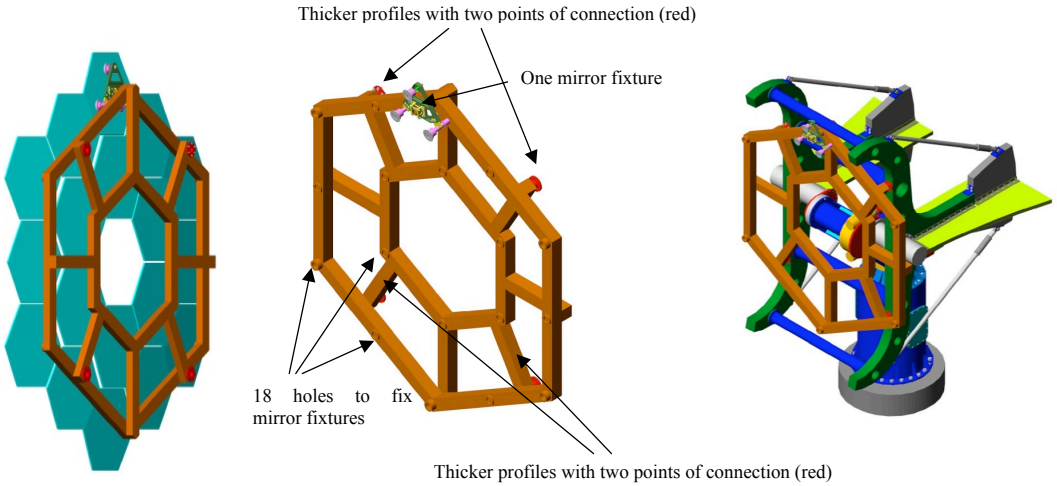

Figure 2.3: Design of the dish with mirrors(left); the dish connected (middle) to the dish support structure (right).

The SST should satisfy CTA requirements summarized in Tab. 2.

The dish, Fig. 2.3, is built of square steel profiles of 0.12 m × 0.12 m with wall thickness of 4 mm, except for the thicker profiles of 6 mm used in areas where the dish is connected to the dish support structure. The dish is a welded structure connected to the dish support structure at four points. The required spherical shape of the dish is obtained with two hexagonal welded sections. Each hexagonal section is welded to eight straight star-forming profiles. The design uses as many as possible identical components to reduce the cost of manufacturing. There are 18 holes in the dish enabling the mounting of the mirror fixtures.

Mirror fixtures The use of the mirror fixtures enables regulation of the mirror facet position with respect to the camera. The relative orientation of the mirror facets has to be stable at the arcminute level. The design of the fixtures allows for a simple and easy mounting/removel from the dish. Each fixture consists of the following main components, Fig. 2.4-left:

- triangular frame (1) with 3 fixing points (2) made of aluminum,
- threaded rod (3) with a sphere at one end and a threaded flange at the other end made of steel.

Eighteen threaded flanges are bolted to the dish in the defined positions (holes) (see Fig 2.4)-right. The threaded rod with the sphere at its end enables the pre-adjustment of a mirror position in the direction

[1] without shadowing;
[2] for Al+SiO_2 coating;
[3] for Al+SiO_2+HfO_2 coating;
[4] for H.E.S.S. coating;
[5] geometrical factor.

	CTA Req.	1M-SST	Note
Mirror Effective area	$> 5\ m^2$	9.4 m^2 [1]	B-SST-0110
Dish outer diameter	3.98 m		
Focal length	5600 ± 5 mm		
Radius of curvature	11.2 m (2f)		
Hex Facet		$780^{+0}_{-3}\ mm$	face-to-face
Mirror Reflectivity	$> 83\%$	90% [2] 94% [3] 83% [4]	B-SST-0120 Averaged over 300-550 nm wavelength range
Angular pixel pitch	$< 0.25°$	0.24°@3.6°	B-SST-0130 over 80% of camera FoV
Camera FoV	$> 7°$	9°	B-SST-1130
Optical time spread (rms)	$< 1.5\ ns$	1.2 ns [5]	B-SST-0140 - Over 80% of camera FoV

Table 2: Telescope Optical properties: CTA requirements and 1M-SST parameters.

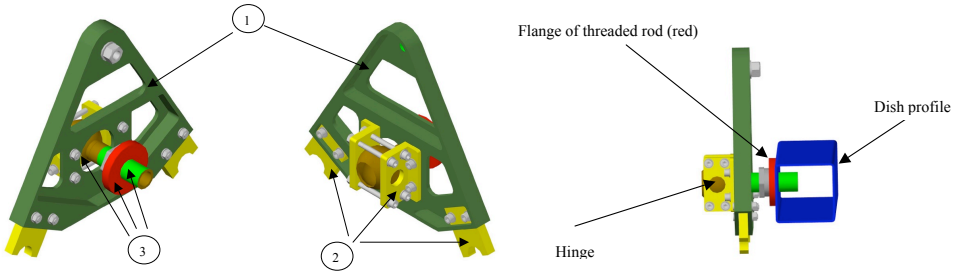

Figure 2.4: Left: Mirror fixture. Right: Mirror fixture bolted to dish.

perpendicular to the surface of the dish tubes. The sphere of the threaded rod is tightened in the central fixing point of the triangular frame to create a hinge that allows for additional degrees of freedom during the pre-adjustment of the mirror position.

The mirror fixture houses three interfaces providing 3-point support of the mirror facets and enables the final adjustment of the mirror orientation with respect to the camera plane (see Fig. 2.5) (on the left). One interface is a so-called fixed point of the mirror (1), while two other actuators or AMCs (2) allow for movement in one or two directions. Each mirror is fixed to the interfaces via steel pads (3) glued on its rear surface. The pads are uniformly distributed on a circle having its center in the center of the mirror. The final orientation of the mirrors with respect to the camera is realized by means of the AMCs. The orientation of each mirror can also be later modified during observations using the actuators, if necessary.

Mast and dish support structure

The design of the mast guarantees a proper setup of the camera with respect to the reflecting mirror surface at the focal distance of 5.6 m. The main components of the mast, Fig. 2.5 (on the right), are eight circular steel tubes (1) OD= 0.06 m and 5 mm thick, bolted together into four longer beams (2) to provide the required focal length. At one end, the four tubes are connected with the camera interface (3) that is made of aluminium sheet. At the second end, the tubes are bolted to the dish support structure (4). This solution practically disconnects deformations of the mast from the deformations of the dish.

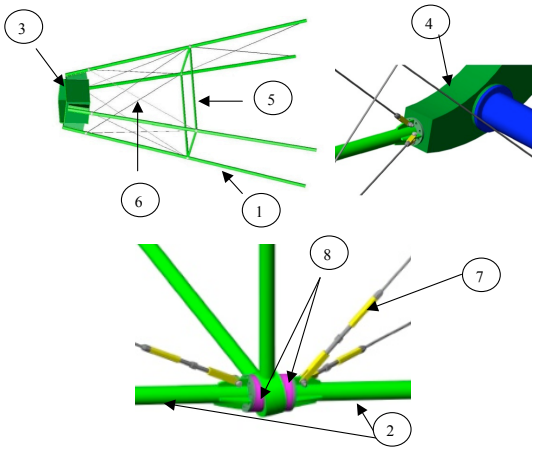

Figure 2.5: Details of Mast Design.

There is a rectangular frame (5) in the plane at half roughly the mast height. The frame is made of circular steel tubes of diameter OD=0.05m and thickness 4 mm. It bonds the long tubes roughly in the middle of their length, increasing the stiffness of the mast. There are also sixteen steel rods (6) of 8 mm diameter that are fixed to the long tubes. The rods are pre-stressed with a force of 500 N by means of turnbuckles (7) and increase significantly the rigidity of the mast structure. The design requires eight interfaces (8) between the rectangular frame and the circular tubes to ensure the proper geometry of the mast. The geometry of the interfaces is identical but requires CNC machining. Such interfaces are not needed at the points at

which the circular tubes are bolted to the dish support structure. The dish support structure is shown in Fig. 2.3-right. The structure is welded out of various components. Two Y-shaped fork pieces (1) are box (hollow) structures welded out of steel sheets and tubes.

The Y-shaped fork pieces are spaced by four steel tubes (2). As mentioned above, the long tubes of the mast are bolted to the four ends of the forks. Counter-weights (3) made of cast-iron are fixed at two remaining ends. Four struts (4) and steel sheets (wings) (5) provide the necessary stiffness of the structure, the latter also improve the resistance to wind. There are also two circular tubes with pads (6) incorporated in the forks. The pads represent the interfaces to which the elevation drive system components (slew drive and the ball bearing mounted on the sides of the head of the telescope support) are bolted.

Telescope support

The 1M-SST telescope support comprises two main components: the tower (1) and the head (2), Fig. 6(a). The elements of the azimuth drive system (3) are incorporated into the tower and those of the elevation drive system (4) into the head. The tower (1) is bolted to a concrete-reinforced foundation (2) specially prepared (see Fig. 6(b)). The diameter of the part of the foundation that is above ground level is 1.4 m and its height is 0.4 m. The part below ground level is assumed to have a hexagonal shape of size about 2 m and depth of 1.2 m. There is a steel anchor grid structure with two reinforcement rings (3) made in industry inside the foundation, enabling an easy and precise mounting/removal of the support from the foundation. The slew drive (4) realizing the azimuth rotation of the telescope is fixed to the conical part of the tower (the tower cap). Inside the tower, there is a radial ball bearing (5) connected to the azimuth slew drive with the tube that stabilizes the whole structure. The housing of the azimuth ball bearing (6) is built into the tower. It can be accessed via two openings (7) for installation and maintenance.

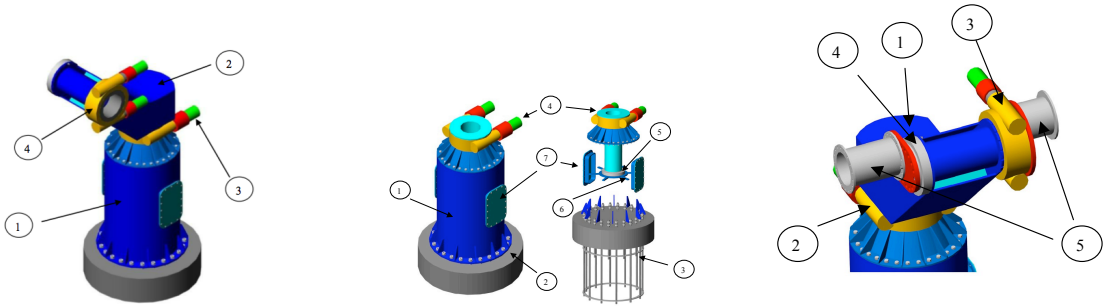

(a) (b) (c)

Figure 2.6: Design of the telescope support (a), tower and foundation (b), and its Head (c).

The head (1) is rotated by the azimuth slew drive (2), Fig. 6(b). The elevation drive system, including the slew drive (3) and the ball bearing (4), are bolted to the pads (red) of the circular tubes (5) incorporated in the forks of the dish support structure. The slew drives and the bearings of both the azimuth and elevation drive systems are identical.

2.4 Telescope Optical Layout

The telescope optical and focal plane requirements are described in [20] and we reported in Sec. 2.3 the 1M-SST parameters that satisfy these requirements. Here we discuss the mirror system composed of 18 hexagonal facets, of size 78 cm flat-to-flat (the central one will not be installed due to the obscuration of the camera). Both the number and size of the facets are chosen to satisfy the PSF requirement (B-SST-0130 in [20]).

2.4.1 Optical point spread function

The point spread function represents the intrinsic limit of optical quality of the imaging capability of the telescope. The optical point spread function (PSF), usually denoted by $D_{80\%}$ or Θ_{80} is defined as the angular diameter of a circle in the focal plane of the telescope containing 80 % of the photons intercepting the focal plane. The center of the circle is chosen to be the center of gravity of the resulting photon distribution.

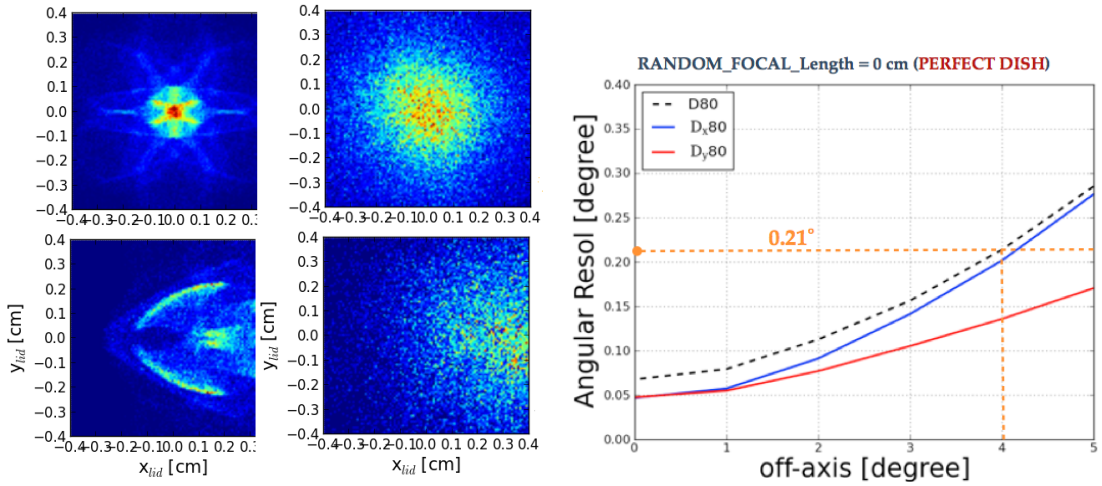

Figure 2.7: Left: Photon Distribution vs off-axis position in case of perfectly aligned mirror (left column) and with misalignment a la H.E.S.S. (right column) for 0° and 4° off-axis. Right: Telescope optical point spread function for perfect mirror alignment vs (left) off-axis angle (the projection x and y of $D_{80\%}$ and the sum in quadrature).

Given the fact that the spot profile at the focal plane is not a double-Gaussian (see Fig. 2.7)(left), we define the $D_{80\%}$ by starting from the centre of gravity of the photon distribution, and integrate the signal in larger and larger circles until 80% of the total emission is reached. Hence, $D_{80\%}$ is the diameter of the region of the plane of the camera containing 80% of the photons. Fig. 2.7(right) shows the angular resolution (the projection x and y of $D_{80\%}$ and the sum in quadrature) for a perfect mirror with no misalignments and perfect Davies-Cotton design obtained with `sim_telarray`, the ray tracing simulation used in CTA [14].

Through this simulation, we selected the 78 cm facet size satisfying the requirement: The telescope must focus light over 80% of the required camera FoV with $\Theta_{80} < 0.25°$ (cfr. B-SST-0130 in [20]). For the camera field of view of 9° the PSF needs to be determined for the light rays coming from a source located at $\sqrt{0.8}\,4.5° \simeq 4°$ off-axis (the sqrt is because of the 80% requirement on the FoV area above). **The PSF for that angle is 0.21°.** The effect of a wrong focal length by 5 cm for all facets is an about 7% increase of the PSF and a 10% effect is expected for misalignments of facets, implemented in `sim_telarray` as HESS misalignments.

2.4.2 Optical time spread

Depending on the incident angle, the arrival time of the Cherenkov wave front on the SST array can be spread over a few nanoseconds. **It is then fundamental that the telescope must focus light (over 80 % of the required camera field of view) with an rms optical time spread of < 1.5 ns.(B-SST-0140)**.

The results of the simulations presented in subsection 2.4.1 have been used to determine the distribution of the photon arrival time to the focal plane. The results for different off-axis angles are presented in Figure 2.8 (left).

For the 80 % of the camera field of view of 9° – within 4° off-axis – the worst time spread is 0.244 ns for on-axis rays.

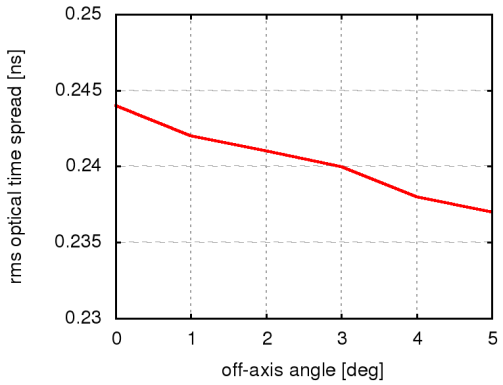

Figure 2.8: RMS of the telescope optical time spread as a function of off-axis angle.

2.4.3 The Mirror technology

Definitions and terminology concerning facets

The terminology and definitions are provided below and refer to the mirror facet structure shown in the oval insert in Fig. 2.9(right), taken from reference [11]:

- **Substrate**: The substrate is the chassis of the facet, its structural component.
- **Intermediate layer**: The optional layer between the reflective layer and the substrate. It does not carry loads, but it is intended to improve the quality of the surface of the substrate.
- **Reflective layer**: Typically, substrates are not reflective by themselves (except some cases like the all-aluminum mirrors). For these, a reflective layer is added.
- **Passivation layer**: Typically, the reflective layer can be passivated by protective layers.
- **Rear pads**: All facets need to be supported and connected to the telescope structure possibly through actuators. On the rear of the substrate three supporting pads should be designed by the mirror developers.

The mirror design proposed aims at addressing the SST requirements but also the CTA Mirror requirements as specified in the Mirror Specification Document [11].

There are different technologies considered for the SST telescope mirror facets: glass mirrors, SMC composite mirrors and honeycomb mirrors.

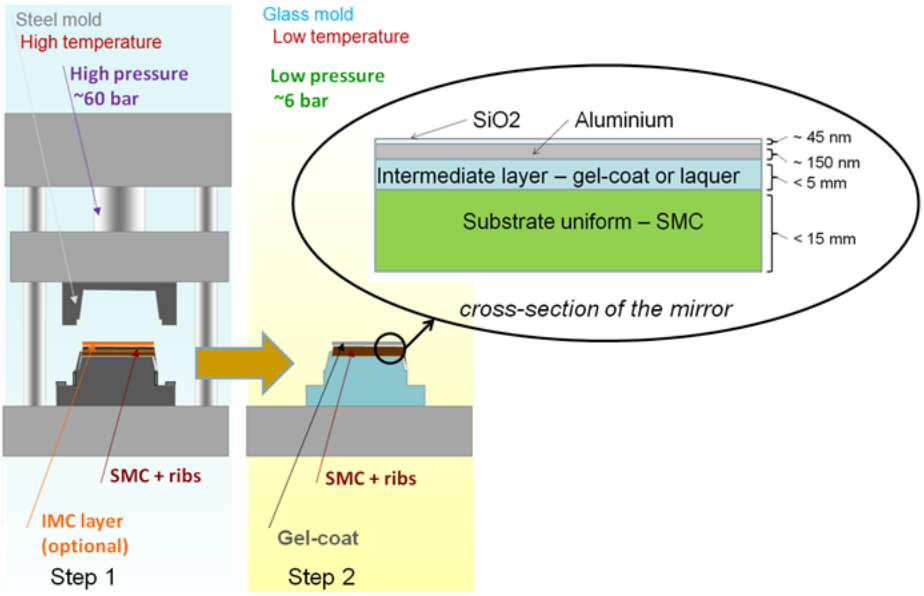

Figure 2.9: Forming of composite mirrors - SMC technology with steel mould (step 1 - left) and application of an intermediate layer (step 2 - right) with indicated cross-subsection of layers (in the ellipse). The structure of the mirror facet is shown in the oval insert.

All of them are applicable for the SST short focal length. The current baseline solution is glass mirrors, since this technology is well proven in the frame of previous projects (eg. H.E.S.S.). The mechanical interface drawing is provided on Fig. 2.10. The glass is at the moment the technology that can be used, but also the composite mirror technique is under evaluation. A detailed list of the mirror's specification and verification

procedure to assess the mirror quality have been defined and sent to 4 potential providers: Galaktika, EuroComposite, Olomuc, Flabegg and SRC PAS.

Below the technology for all considered solutions is described in details.

- **Glass Mirrors:** The pros of the glass mirror technology are that it is well knows and that glass (with proper coatings) may achieve 95% reflectivity. The con is that the technology is very time consuming, so the mass production schedule should be considered very carefully according to the manufacturer's capacity. The Galactika company has just provided an offer for a glass mirror which meet most of the requirements.
- **Sheet Moulding Compound (SMC) composite Mirrors**: Currently, in the SRC PAS institute, the SMC composite mirror technique is being developed; this technique has two major features: the structure is composed of one isotropic, thermally conductive material; there is no glass in the structure. The substrate of the mirror is formed during a compression of SMC material in a mould on a press. The idea behind SMC material forming is shown in the Fig. 2.9. SMC is a low-cost, widespread and semi-fabricated product used for compression moulding.

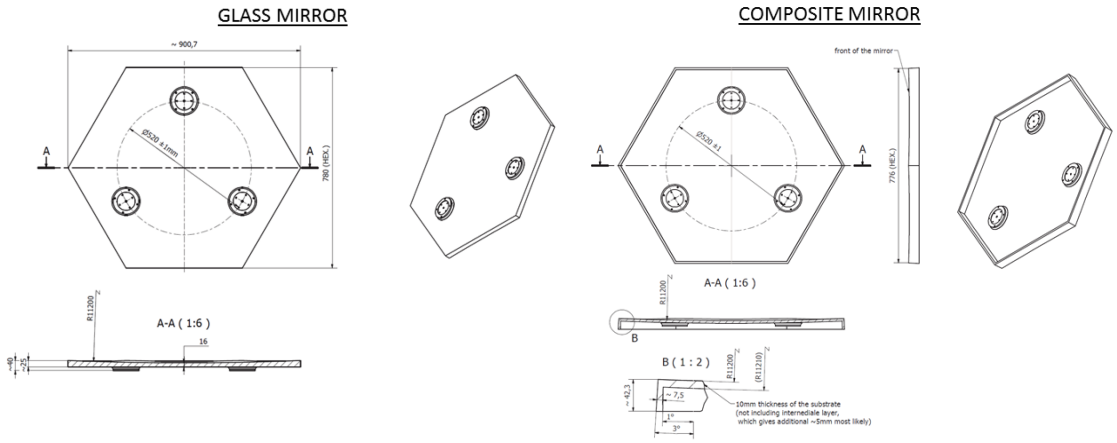

Figure 2.10: The mechanical interface drawing for glass (left) and SMC composite (right)mirror facet for SST telescope

The idea is to form mirrors for CTA telescopes during such a SMC compression moulding process. It is a proven technology in the automotive industry and some of its many advantages include: possible one-step process to obtain the structure, quick forming process which takes only 3 min and possibility to obtain 0 % shrinkage.

The top surface of the composite mirror does not require polishing, as its smooth surface is obtained through high gloss mould. Therefore, the most difficult task in this technology is to get an optical surface directly on the SMC composite. Preliminarily, it was intended to achieve a proper surface quality directly from the steel

mould during compression forming (by using an IMC In-Mold Counting process) but due to the insufficient (from the optical properties point of view) accuracy of the SMC composite surface micro-geometry, it was necessary to use an additional, intermediate layer to smooth out the SMC surface. This layer has to meet CTA requirements but also to allow the coating of the surface with Aluminum, to have a temperature stability from -20°C to 40°C and stability in high vacuum (about 5×10^{-5} mbar) during aluminum sputtering,as well as mechanical, atmospheric and UV resistance.

Three types of technology for the intermediate layer were tested:

- Thin (a few μm) layers, designed to smooth out the roughness. The thin film example are lacquers.
- Thick (several hundred μm to about a mm) layer, used in order to smooth out the surface roughness, waviness and to reduce the small shape errors. An example of such a thick layer is gelcoat.
- A combination of the two above technologies: thin lacquer film on the gelcoat layer.

Figure 2.11: The SMC mirror prototype developed by Space Research Centre

Recently a scaled version of the SMC mirror prototype was developed (see Fig. 2.11) and it is currently being tested in environmental conditions.

Technology description of mirrors by other companies

Mirrors from Galaktika - the glass technology is well known from the H.E.S.S experience. The company seems to be able to deliver mirrors which will meet CTA mirrors requirements. The timeline of the mass production should be carefully defined with the company since glass mirror technology is time consuming. Olomouc and Flabeg use a technology very similar to Galaktika's.

Mirrors from Euro-Composites - the company collaborates with the WP-MIR team on the LST honeycomb mirror structure. The technology seems to meet the CTA mirror requirements in the case of the LST mirrors. Hence, the 1M-SST group started to collaborate to adapt this technology to the SSTs. The main difference between SST and LST facets is the radius of curvature and the size of the panel. The bending of the glass is critical for this technology.

Mirrors from Weule - The company offer three different technologies: 1) to use the special glass blocks made by Schott and grind and polish the mirror out of these. The general shape is plano-concave. 2) to use laminated float glass of appropriate thickness. The mirrors will be ground and polished from these. The

general shape is plano-concave. 3) third option is to mould float glasses according to the radius of curvature. The concave part will be exactly ground and polished, the convex backside will come matt ground. The general shape is therefore concave-convex. This would give rise to the lowest weight design. They have worked very closely with BTE in Elsoff, Germany for many years, who make the coating for mirrors of 2 mm thickness which are going to be laminated to form composite mirrors. They have also coated the mirrors for the H.E.S.S. telescopes. Their intention is to cooperate with BTE for the CTA SST-DC mirrors which means that Weule would manufacture the mirror substrates and BTE will produce the appropriate coating. As we want to deliver appropriate quality for our telescopes, BTE is certainly the partner of choice.

2.4.4 Active Mirror control

The Active Mirror Control (AMC) is a set of mechanical and electronics units to control the position of each mirror in the CTA telescope. The fig. 2.12 presents concept of the AMC set.

The parts of AMC are:

- Fix-point (1).
- Actuators (5).
- Electronic driver (3).
- Mechanical interface (triangle) (4).
- Mounting sphere with telescope fixation (6).

Actuators are the main part of the AMC, whose main function is to keep the mirrors in the desired position. The mirror should be mounted in three points in an iso-static way. The mounting points should have an adequate number of degrees of freedom. Actuators should provide precision movement during mirror alignment and adequate stiffness during telescope observations.

In the AMC for one miroor panel there are two types of actuators with different mounting joints (4 DoF and 5 DoF). The stepper motor is connected with the screw lead unit through an Oldham clutch. The position of the actuator is controlled by a magnetic encoder which consists of a magnetic strip and integrated Hall sensor.

The mounting joint is located at the end of the linear movement unit of the actuator. The main parts of the mounting joint are as follows: ball transfer unit, element connected to the ball (depends on the type of actuator: plane or prism) and springs. The ball transfer unit can withstand axis loads up to 1200 N. The springs are designed to resist double the maximum force caused by wind.

2.4.5 The Mirror alignment system

The idea of the telescope's automatic alignment process is to position the mirror's focus on the detector using optical feedback.

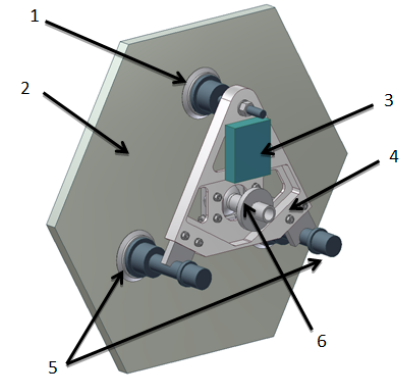

SST Mirror, 3 – electronic driver, 4 – mechanical interface, 5 – actuators, 6
Mounting sphere with telescope fixation

Figure 2.12: AMC Mirror set

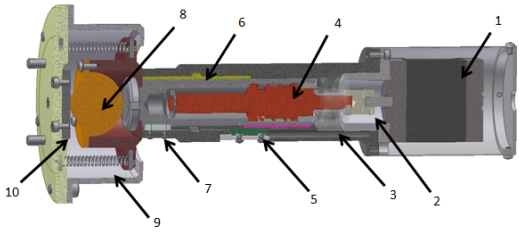

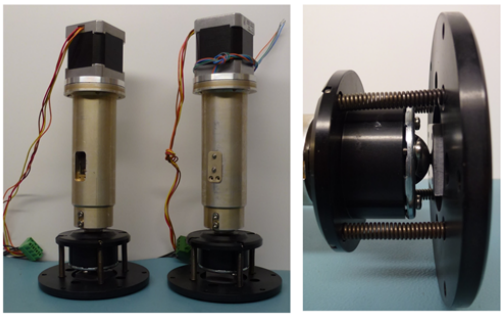

1 – stepper motor, 2 – Oldhama clutch, 3 – balls bearing, 4 – lead screw unit, 5 – magnetic encoder, 6 – linear bearing, 7 – sliding key, 8 – ball transfer unit, 9 – springs (×4), 10 – plane

Figure 2.13: (a): Actuator with 2 translational DoF; (b): and picture of Actuators prototype (on the left), mounting joint (on the right)

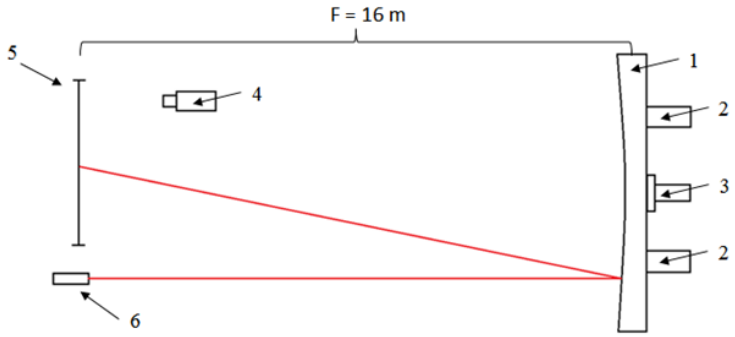

1—mirror, 2—actuators, 3—fix-point, 4—camera included in the central part of the dish, 5—screen on focal plane, 6—point like source¶

Figure 2.14: Sketch of alignment system test set-up

The mirror focuses the light from a distant source at its focal plane, creating a spot on the screen. The coordinates of the position of the spot $p = [x, y]^T$ are related to the actuators' positions by one-to-one map

$$f : D_q \rightarrow D_p, q = f(p), (1)$$

where $D_q \subset R^2, D_p \subset R^2$ are the ranges of the actuator and spot positions, respectively. It can be demonstrated that the mapping is approximately linear in the operation range of the actuators, therefore the Jacobian matrix $J = \frac{\delta f(q)}{\delta q}$ is constant.
The actuators' control system allows for operation in a sequence of displacements defined as differences of positions in discrete time n , i.e. $\Delta p_n = p_n - p_{n-1}$. Hence, the displacement of the spot is related to these displacements by $\Delta p_n = J\Delta q_n, (2)$. Once the reference position of the spot p_{ref} and the position tolerance ϵ are defined, then the alignment control can be obtained as the sequence of desired actuator displacements $\Delta q_n = kJ^{-1}(p_{n-1} - p_{ref}), (3)$ iterated from position p_0 until the spot reaches the desired position p_0 with the specified tolerance, i.e. $|p_i - P_{ref}| \leqslant \epsilon$. The constant k is the control gain which allows for the adjustment of the strength of the control from gentle ($k \approx 0$) to aggressive ($k \approx 1$). In the case of $k = 1$, the control target is achieved in one step. The main difficulty in adjusting the parameters in (3) is the necessity of computation of the Jacobian matrix, which needs the precise measurement of the geometric properties of the system, for each mirror separately.

2.4.6 Verification plan for the Mirror Actuators and Alignment system

Final qualification and acceptance of the mirror facets, actuators and alignment system will be done according to CTA standards and will be divided into the following stages:

- Verification of the documentation provided by subsystems supplier.
- Verification of the subsystem quality in laboratory conditions.
- Verification of the subsystem performance in on-site conditions.

Stage 1 This stage is an ongoing activity in the 1M-SST consortium. A dedicated document with requirements definition has been delivered to all suppliers interested in delivering subsystems for the 1M-SST. The suppliers were asked to prepare the preliminary technical description of the subsystems and based on that we started to prepare a compliance matrix in which the technical data of all subsystems are compared with requirements. In these documents, the status (assumed, designed, tested) of the technical parameters is provided. These matrices are the basis for the preparation of interface control documents, RAMS documents and manuals.

Stage 2 All subsystems will be verified by tests on test-bed systems available in the SRC. Currently there two test-bed systems available, a 2-f setup and 1-f setup. The 2-f setup allows for the measurement of the Point Spread Function (PSF) shape and dimensions, radius of curvature and reflectance of the mirror into the focal spot. A point-like light source is placed at the distance which is equal to the mirror radius of curvature. The detector is placed at the same distance to register the image (spot) obtained after laser beam reflection from the examined mirror. The system is presented in fig. 2.15. If required, the detailed analysis of the 1-f system available in SRC will be used.

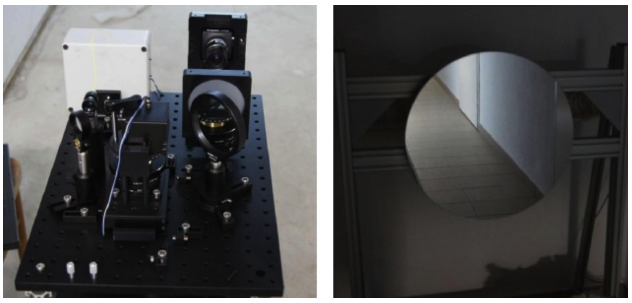

Figure 2.15: 2-f system implemented in the SRC. Measurement unit and mirror stand (with HESS mirror mounted).

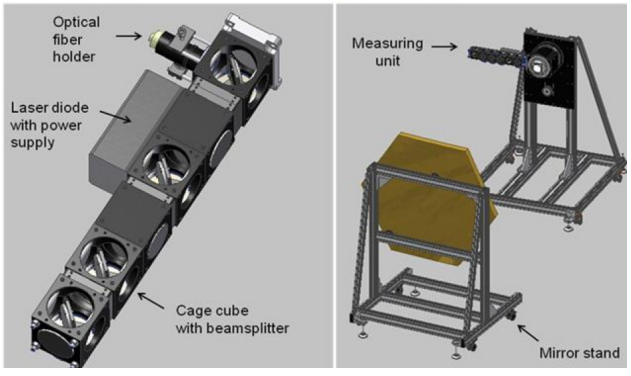

Figure 2.16: 1-f system.

This system allows to measure the PSF shape and dimensions and also local deformation of the mirror. Parallel light sources are located on the rotating arm in the focal plane of the tested mirror. Every laser diode beam is collimated and after reflection from the mirror it is focused on the focusing screen and registered by the CCD camera which is located on the optical axis.

During arm rotation, different parts of the mirror are illuminated and local surface deformation can be measured. The system is presented in fig. 2.16.

In addition it is possible to take advantage of the tests set-up's available in the different institutiona working in the WP-MIR group.

Stage 3 In this stage the mirror facets, actuators and alignment system will be tested on prototypes which are currently under development by the SST DC consortium. It is planned to perform the tests in June 2014.

2.4.7 Cost, Milestones, Timeline

		Mirror Qty			
Producer		1	18	1000	Notes
Galaktica	Cost	5000	2075	1750-2050	
	Prod	4	4-12	52-104	
SRC PAS	Cost	in-kind	in-kind	1000	
	Prod	1	4	24-52	
Euro-composite S.A.	Cost	6346[1] 3860[2]	3576 2572	2720 1954	[1] dieletric coating [2] metal coated
	Prod	6-8	6-10	52-72	
Weule	Cost	12'000	3924[3]	2000[4]	[3] includes coating [4] depend on coating
	Prod	12-16	24	104	
Olomouc	Cost	1800-2600[5]	1600-2600[6]	no estimation	[5] rough estimation [6] part can be in-kind
	Prod[7]	2	8	200	[7] not available before 12/2013
Flabeg	Cost	∼40'000	no info	no info	
	Prod	no info	no info	no info	

Table 3: Mirror brut cost (in €) and production rate (in weeks) for prototype and mass production

2.5 Verification of performance requirements

The following simulation studies aim to demonstrate that the requirements in [20] are fulfilled by the single mirror telescope and by an array of such telescopes, also called the SST sub-system.

For the evaluation of the performance, the simulation needs to model some of the system components and their response. Most important for these studies are:

- The Winston Cone transmission efficiency as a function of the off-axis angle as shown in Fig. 2.17-left.
- The Photon Detection Efficiency (PDE) as a function of the incident light wavelength (Fig. 2.17-right).
- The Mirror reflectance as a function of incident light wavelength. In Fig. 18(a), the reflectance is shown for the different types of coating which can be applied to the mirror and which are under evaluation.

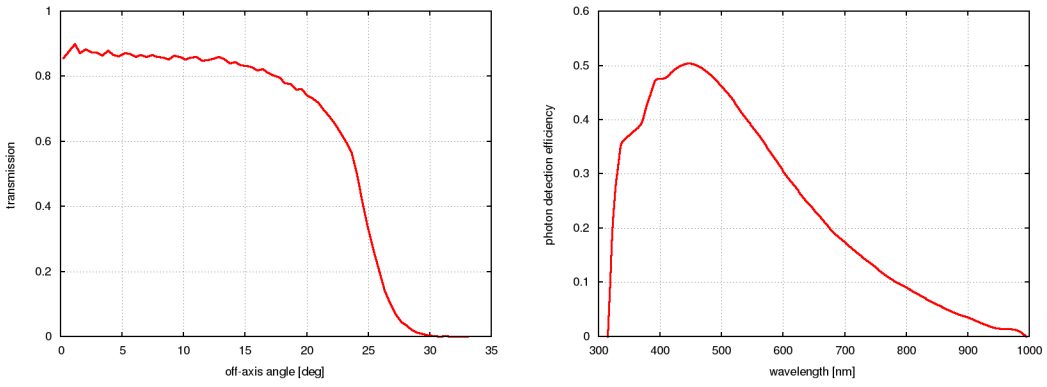

(a)

Figure 2.17: Left: Winston cone transmission as a function of off-axis angle.; Right: The Hamamatsu S10985-050C PDE is used in the simulation (including after pulses and cross-talk as required by sim_telarray), which is similar to first measurements of the PDE of the hexagonal Hamamatsu G-APD.

- **Site geography**
  All simulations presented in this section have been performed for an altitude of the site of **2000 m** which lies in the altitude range of **1500 - 3800 m** defined in the requirements (cfr. **A-ENV-0130** in [20]). The performance for other altitudes within the required specification hasn't yet been determined.
- **Night Sky Background**
  The NSB level for the telescope has been calculated according to the formula:

$$R_{\mathrm{NSB}} = F_{\mathrm{NSB}} \times A_{\mathrm{eff}} \times d \times M_{\mathrm{ref}} \times W \times QE \ , \tag{1}$$

[1] according to the CTA naming convention, a single telescope is a product, while the array of telescopes of a particular size represents a sub-system.

$F_{\rm NSB}$ is the wavelength integrated NSB flux that can be calculated using the spectra given in Figure 18(b), in the wavelength range $300 - 950\,$nm. The value has been calculated to be $F_{\rm NSB} = 12.65 \times 10^{12}\,{\rm ph\,s^{-1}\,m^{-2}\,sr^{-1}}$.

$A_{\rm eff}$ $= 9.4\,{\rm m}^2$ is the effective collection area of the telescope (see Table 2) including the effects of mirror inclination and shadowing)

d is the angular pixel size. For a linear pixel size of 2.323 cm and 5.6 m focal length, $d = 1.5 \times 10^{-5}\,$sr.

$M_{\rm ref}$ represents the mirror reflectances, weighted with the NSB spectrum shown in Fig. 18(b), in the wavelength range $300 - 950\,$nm for the mirror coatings presented in Fig. 18(a). It is found that $M_{\rm ref} = 0.748$, 0.645, and 0.089 for Al+SiO_2, Al+SiO_2+HfO_2, and dielectric coatings, respectively.

W is the Winston cone's transmission efficiency weighted with the NSB spectrum.

QE is the photodetector efficiency weighted with the NSB spectrum For the Hamamatsu S10931-050P photodetector and has been calculated to be $QE = 0.134$ in the wavelength range $300 - 950\,$nm.

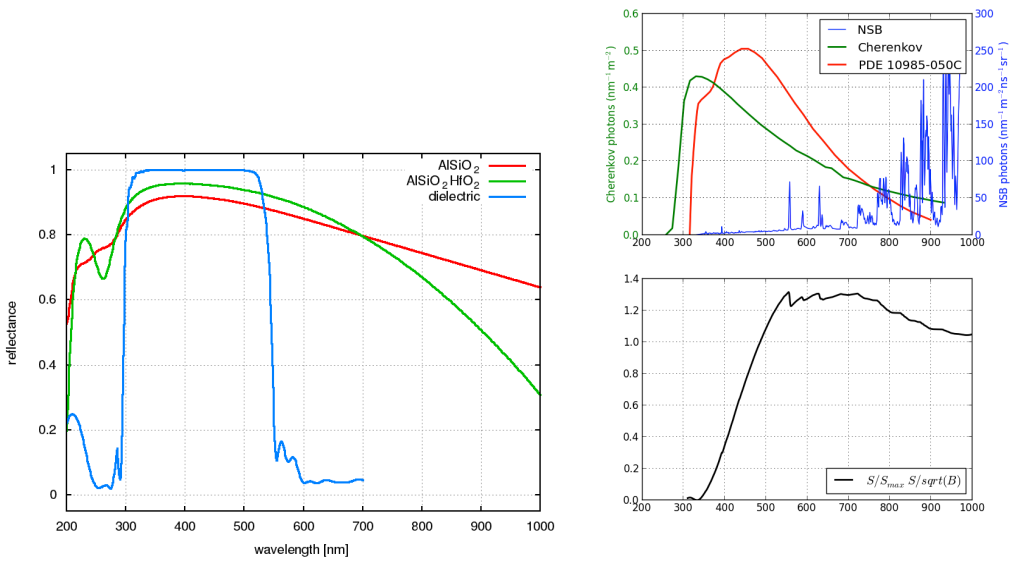

(a) (b)

Figure 2.18: **(a)** Mirror reflectance as a function of incident light wavelength for various coatings considered for the 1M-SST telescope. Note that the curves for Al+SiO_2 and Al+SiO_2+HfO_2 coatings have been extrapolated in the wavelength range $700 - 1000\,$nm; **(b)** Spectrum of the NSB and of the Cherenkov light from showers on the ground. The Cherenkov light spectrum is shown for showers at 20° zenith angles and detected at 2000 m above sea level. Also the PDE (arbitrary scale) is shown. In the bottom panel, the S/B ratio between Cherenkov emission and NSB is shown.

Thus, the nominal NSB level for the 1M-SST has been determined to be **110**, **95**, and **13 MHz** for Al+SiO_2, Al+SiO_2+HfO_2, and dielectric coatings, respectively.

The numerical simulations of the telescope performance have been performed for NSB levels of 121, 242, 484, and 968 MHz to allow for comparison with Prod-1 results.

2.5.1 Single 1M-SST telescope performance

Optical efficiency **The overall optical efficiency of the telescope for signal photons, ε_{sig}, is required to be $> 9.3\,\%$ (A-PERF-2020)**. It is defined in eq. 2, where $F(\lambda)$ is the nominal Cherenkov spectrum shown in Figure 18(b) and ε is the probability that a photon of a given wavelength, incident on the primary mirror and parallel with the optical axis, results in the generation of a detectable photoelectron.

The optical efficiency for signal photons has been calculated with dedicated software for mirror reflectances (see Fig. 18(a)). The Winston cone characteristic is presented in Fig. 2.17-left, and results in an average optical efficiency of 0.835. No entrance window has yet been taken into account in the calculation. The Hamamatsu S10985-050C GAPD has been used as a photodetector in the simulation (see fig. 2.17). The average and Cherenkov spectrum weighted PDE in the wavelength range $200 - 1000\,\mathrm{nm}$ has been calculated to be 0.30.

$$\varepsilon_{\mathrm{sig}} = \frac{\int_0^{\infty} F(\lambda)\varepsilon(\lambda)\mathrm{d}\lambda}{\int_{300\,\mathrm{nm}}^{550\,\mathrm{nm}} F(\lambda)\mathrm{d}\lambda}, \qquad (2)$$

The Hamamatsu S10985-050C GAPD has been used as a photodetector in the simulation (see fig. 2.17). The average and Cherenkov spectrum weighted PDE in the wavelength range $200 - 1000\,\mathrm{nm}$ has been calculated to be 0.30.

The final optical efficiency of the telescope for signal photons has been calculated to be $\varepsilon_{\mathrm{sig}} = \mathbf{0.216}$, $\mathbf{0.225}$, and $\mathbf{0.185}$ for Al+SiO_2, Al+SiO_2+HfO_2, and dielectric coatings, respectively.

The overall optical efficiency of the system for background photons $\varepsilon_{\mathrm{bg}}$ is defined similarly to Equation (2), but the $F(\lambda)$ is the nominal NSB spectrum shown in Figure 18(b).

The optical efficiency of the telescope to background light has been calculated to be $\varepsilon_{\mathrm{bg}} = 0.582$, 0.573, and 0.22 for for Al+SiO_2, Al+SiO_2+HfO_2, and dielectric coatings, respectively. Thus calculated ratios of the signal photons to background light are: $\varepsilon_{\mathrm{sig}}/\sqrt{\varepsilon_{\mathrm{bg}}} = \mathbf{0.284}$, $\mathbf{0.297}$, and $\mathbf{0.395}$ for Al+SiO_2, Al+SiO_2+HfO_2, and dielectric coatings, respectively. As specified in the requirement A-PERF-2050, **the overall optical efficiency of the telescope to background light, ε_{bg}, must be such that $\varepsilon_{sig}/\sqrt{\varepsilon_{bg}} > 0.3$.**

Signal reconstruction **The required value of the systematic error on the absolute intensity of the Cherenkov light at the position of each telescope must be $< 10\,\%$ (A-PERF-2050) and the goal is $5\,\%$ (A-PERF-2060).** The systematic error has been derived under the following assumptions: 1) Hamamatsu S10985 photodetector; 2) electronics parameters as described in the FlashCam report [12]; 3) sampling rate: 250 MS/s; 4) electronic noise amplitude (sigma) corresponds to 15% of 1 p.e. signal; 5) thermal noise: 6 MHz; 6) Cherenkov photons arrival time: random within (-5,+5) ns; 7) random phase between photon arrival time and ADC sampling time.

The results presented in table 4 have been obtained for a sample consisting of 2000 simulated events. The pixel signal amplitude has been computed from the maximum of the so-called deconvolved and shaped pulses of a simulated FlasCam camera. To the pulses measured by the ADCs, a pole-zero cancellation (deconvolved) and then several moving averages (shaped) are applied. From the maximal amplitude a base signal level (pedestal) is subtracted to obtain the net amplitude that is converted from ADC counts into p.e. number using a calibration factor. The photon arrival time is associated with the time of the pulse maximum minus some delay time characterizing the detector and electronics. Simulations are done for single pixels. Typically, several pixels are needed to trigger as well as more than about 50 p.e. summed over all pixels. If camera pixels are uniform (e.g. similar PDE), the systematic error can be applied to the sum. Therefore both SST requirements (10% and 5% systematic error) are fulfilled.

Signal amplitude (p.e)	5	10	20	50	100
Amplitude systematic error (deconvolved) (%)	19.5	13.4	9.3	6.0	4.3
Amplitude systematic error (shaped) (%)	18.5	12.4	8.4	5.5	3.9
Time resolution (deconvolved) (ns)	0.93	0.71	0.52	0.36	0.27
Time resolution (shaped) (ns)	0.59	0.41	0.30	0.19	0.14

Table 4: Estimate of systematic errors.

2.5.2 1M-SST sub-system performance

The SST array can be arranged in several configurations. What matters for the scientific case is the area covered and the inter-telescope spacing. Simulations have been performed for four telescopes located on a rectangle with different side lengths (grid "cell"). The results have been extrapolated to an array of telescopes located on a rectangular grid, following the procedure described in [13]. Other configurations are under investigation.

Effective area **The goal SST sub-system collection area at $100\,\mathbf{TeV}$ is $> 7\,\mathbf{km}^2$ (A-PERF-1230).** In the case of a large array, the total effective area can be well approximated using "cells" (see [13]). The array effective area is defined as $n \times d^2$, where n is the number of grid cells and d is the telescope separation. Therefore, the required number of cells can be derived for a given telescope separation and a given effective area.

The number of cells, N_{cells}, is defined as:

$$N_{cells} = \frac{\text{Required Effective Area}}{d^2} \tag{3}$$

The number of telescopez, N_{tel}, in the grid built using square cells is:

$$N_{tel} = (\sqrt{N_{cells}} + 1)^2 \tag{4}$$

d [m]	N_{cells}	N_{tel}
200	175	202
300	78	96
400	44	58

Table 5: Number of telescopes and cells of a given separation to reach 7 km^2 effective area.

Equations 3 and 4 can be used to derive the number of cells and telescopes for a given telescope separation and a required effective area of 7 km^2. The numbers are presented in table 5.

Sensitivity The array sensitivity for 58 and 96 telescopes separated by 400 m and 300 m, respectively, is presented in Fig. 2.19, together with the required sensitivity. Requirements are: The SST sub-system sensitivity must be within a factor of 2 (1.5) of that required for the system as a whole at all energies above 10 (100) TeV (A-PERF-1210/1220).

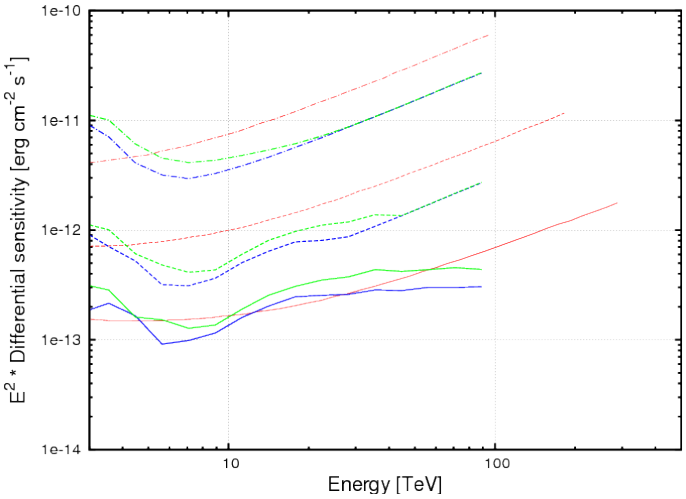

Figure 2.19: Array differential sensitivity. The solid lines show sensitivity for 50 h, dotted lines are sensitivity curves for 5 h and dashed-dotted lines show sensitivity for 0.5 h. The required sensitivity is represented by red curves (see: SST Requirements Document). The green lines are for 58 telescopes (44 cells) with $d = 400$ m and the blue lines are for 96 telescopes (78 cells) and $d = 300$ m. Unfortunately, some of these curves are still limited by the statistics of the simulation we obtained until now.

2.6 The Camera

The 1M-SST camera uses a novel approach: the photodetector plane (PDP) based on Geiger-Avalanche Silicon Photodetectors (GAPD s, in the following) and the electronics are two physically separated entities. The electronics that will be used is based on the FlashCam design (see [12]), which is proposed for the Medium Size Telescopes of the CTA observatory based on photomultipliers. It will be adapted to the new PDP which has different characteristics. The design and prototyping of the camera electronics is done in cooperation with the FlashCam sub-consortium.

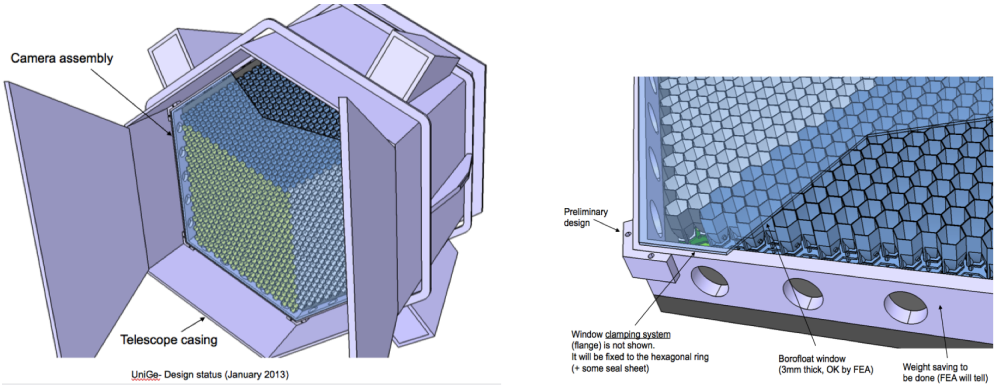

Figure 2.20: CAD design of the camera.

2.6.1 The Photodetector Plane

The 1M-SST camera uses a novel technique in gamma-astronomy, Geiger-APD photosensors. A GAPD-based camera has been proven by FACT to have the capability to observe the sky with moonlight, thus increasing the observational time by $\sim 30\%$. The area of the camera is constrained by the reflector diameter, the focal length and the desired FoV. On the other hand the Point Spread Function constrains the camera pixel angular size. As explained in Sec. 2.4.1, the goal PSF is achieved with a pixel angular size of 0.25°.

The required pixel size is too small for a conventional PMT, but also too large for available GAPDs. A light funnel can be used to enlarge the effective pixel area. The FACT camera, with a pixel angle of 0.1°, adopted a 3×3 mm^2 square MPPC with a small solid cone that adapts the square entrance window to the hexagonal exit window with linear dimensions of about 1 cm. In our case, the pixel angle is larger which implies a larger sensor. To avoid the larger absorption of a thicker solid cone, the increase in weight and complicated manufacturing processes, we adopted an hexagonal larger sensor (10.4 mm side-to-side, area of 94 mm^2 divided in 4 channels) with an open hexagonal light funnel. The cone efficiency has to be carefully taken into account. Simulation studies at the the university of Geneva have compared different solutions and designs and showed that a dichroic coating helps to increase the transmission efficiency and to reduce the NSB at large wavelengths. The result is an improvment over the efficiency of solid cones.

The PDP design The camera PDP is a hexagon of 98 cm flat-to-flat composed of 1296 hexagonal pixels. By pixel, we here mean the optical unit composed of a Winston cone mounted on the hexagonal GAPD as shown in Fig. 2.21(left).

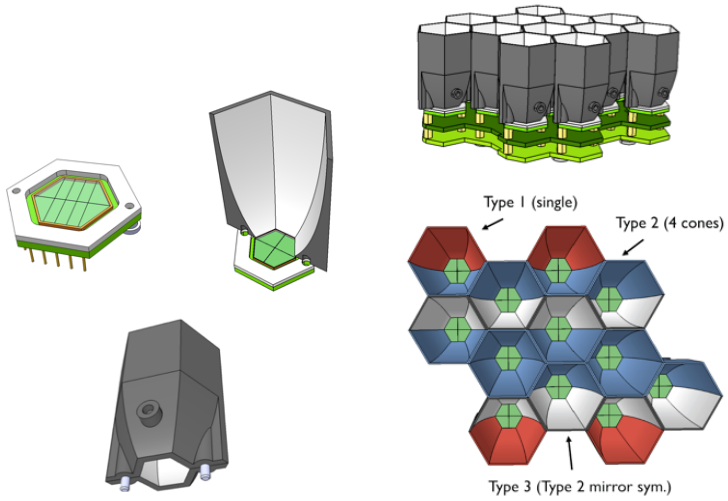

Figure 2.21: Left: Assembly of a pixel: the Winston cone is fixed to the hexagonal pixel via 2 pins. Right: Assembled 12 pixel Module: the pixel is fixed to the PCB that includes also the preamplifier and bias-voltage distribution. Three types of Winston cones are used for the assembly (in 3 colors: red, blue and white)

In Fig.s 2.21(right) and 2.22(left) the PDP concept is illustrated. The modular plane is composed of 108 modules, each housing 12 pixels. The pixels, once assembled, are mounted on the PCB front-end board. This board will host the pre-amplifier for the GAPDs, the services (such as bias-voltage distribution and power supplies) the related slow control electronics and will also provide the mechanical stiffness. The possibility of using more than one PCB allowing a more relaxed design by distributing the components is under evaluation. The ground planes in this PCB stacks could also help to distribute and remove the heat and they couldbe connected with the PDP cooling system.

The 12-pixel modules are fixed to a backplate which will provide further stiffness to the whole structure. The PDP will be closed by a transparent window to provide the needed weatherproofing of the system. It should be recalled that the camera has to work in a harsh environment and that it should be water-tight according to the IP5-IP6 Standard. At the moment, the preferred solution is a Borofloat window. FEA studies are on-going. In fig. 2.22(right) the effect of the weight in observation conditions (wind < 36 km/h, no other load) on the entrance window of 3 mm of Borofloat is shown. Borofloat experiences only 0.5 mm displacement in the middle of the window without any anchor point other than the clamps on the border. It is important to have the smallest thickness ensuring mechanical safety for optical efficiency. The window thickness has an impact on the transmitted UV-light which is a substantial amount of the Cherenkov light. Borofloat has good optical characteristics, but using a filter coating, the performance of the system can be enhanced in the UV region and the large wavelengths above 700 nm where NSB dominates can be eliminated. A study of the S/B-ratio resulted in a suitable region to cut at about 720 nm (see Fig. 18(b)).

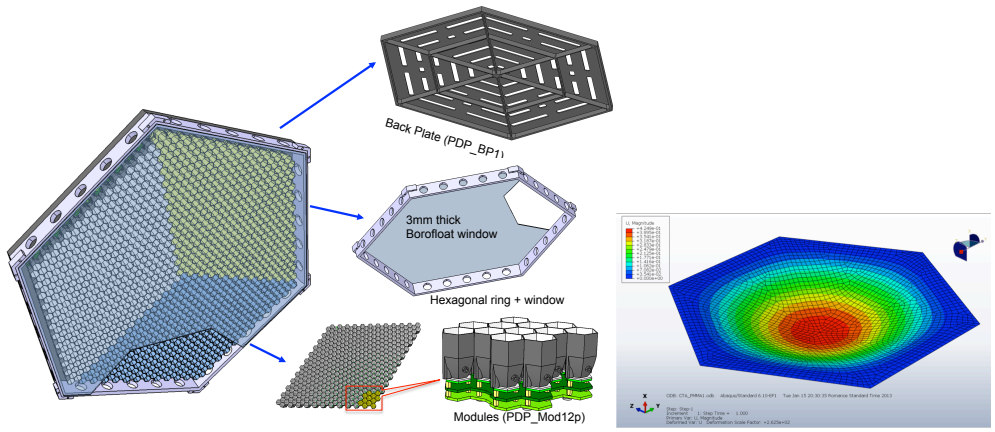

Figure 2.22: Left: The PDP camera concepts. Right: Preliminary FEA study of the entrance window of 3 mm BoroFloat in observational conditions.

The PDP will be connected to the camera electronics via cables. The cables will run on the telescope mast and connect to the Flashcam-based electronics housed in mini-crates sitting on the telescope support structure. There will be 2 different types of cables: 324 analogue cables, 10 m long, which will send the analogue output of the pre-amplifier boards to the FastADCs in the mini crate; 192 digital cables will send the trigger information. There are 2 possible solutions for the cables under consideration: standard Cat6 cables with are reliable but, given the high number of cables, will be heavy (180 kg); slim STP (Shielded Twisted Pair) cables which are much lighter (52 kg) but also less reliable. A description of the Trigger and Readout electronics will be given later in sec 2.6.2.

The Winston Cones The Winston cone dimensions are constrained by the telescope design. The PSF will dictate the angular size of the pixel, which in our case is 0.25°; given the focal length of 5.6 m, the pixel can be a hexagon with 23.2 mm flat-to-flat size. The focal length and dish size (and the camera diameter) limits the cut-off angle, i.e. the maximum angle at which the light collection efficiency is more the 60%. For our case, this is about 24°, as can be seen in Fig. 2.23. From the figure it can be seen that an empty cone is about equivalent to a full one, but if a dichroic coating is used on the empty cone a larger transmittance can be achieved. We are collaborating with Thin Films of Zurich to select and test various coatings. The cut-off angle then constrains the Winston cone length [15] and determines the compression factor. Solid cones have a larger compression factor (ratio of exit and entrance window linear dimensions) for the same cut-off angle. The figure includes the losses due to the presence of a PMMA entrance window of 3 mm thickness.

In addition to the problems of light absorption, the production technique (mould injection) of solid cones has to achieve consistent quality of the cone transmission efficiency. Also, the coupling of the cones with the sensor by gluing is a time consuming approach which for a single camera like FACT can work, but does not scale easily for 70 cameras as in the SST case. For these reasons, the baseline solution for the 1M-SST camera is empty Winston cones, which can be easily and cheaply mass-produced and afterwards also coated. These studies have been performed using various simulation codes (Zeemax, Fluka, Robast) to cross-check the results. The optimal choice is a cone whose length is 36.7 mm and bottom area is a hexagon of 9.4

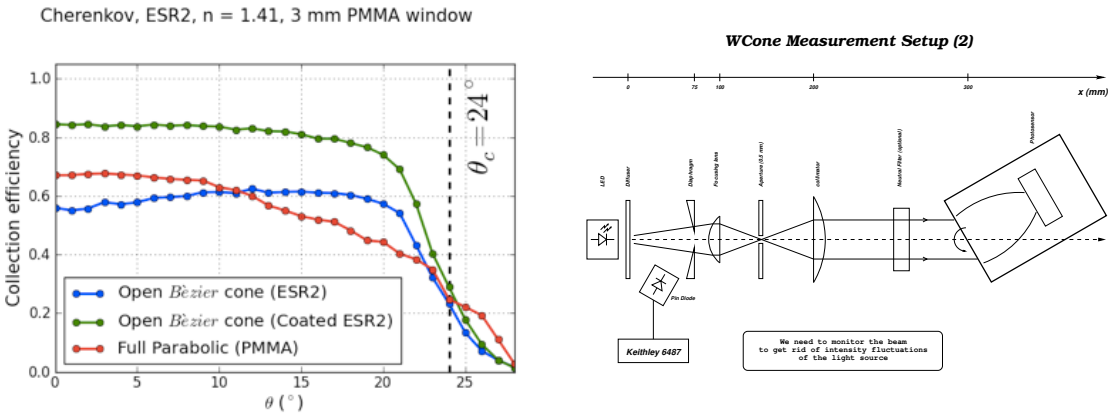

Figure 2.23: Left: Light collection efficiency convoluted with the Cherenkov spectrum for Winston cones of parabolic and Bézier shapes: blue curves are for open cones covered with Vikuiti ESR2, green are for the same configuration with a dichroic coating on the Vikuiti, red are full PMMA cones attached to the PMMA window. Right: Scheme of the optical set-up for the measurement of the Winston cone transmission efficiency.

mm flat-to-flat size matching the sensor developed with Hamamatsu by UniGE. The best lateral shape is a Bézier shape [16]. This has an interesting feature: the pure quadratic shape is in truth approximated with Bezier curve in numerically-controlled machine processes used in industrial production and so the real cone will correspond perfectly to the model.

In order to measure the optical transmission of cones we set-up the test bench in Fig. 2.23 (right). The measurement is done by comparing the light measured first directly on a calibrated photodiode and then with the same device mounted on the back of the cone. A first set of cones has been produced to study the performance, evaluate the production and construction approach and also to start evaluating optical transmission with different coatings.

Cone Mass Production Given the high number of pixels involved (1300 pixel/camera $\times$70 cameras $\sim$ 100000 pixels) the production of the Winston cones has to be industrial. In order to reduce the complexity of the assembly of the cones and also of the coupling to the GAPDs, a solutoin has been proposed in which parts of cones are produced as preformed modules which can be mounted together to form a cluster of cones. In Fig. 2.21(right) is shown the proposed solution: by using three different type of modules, a cluster of 12 cone can be assembled. This kind of technique will allow mass-production at low cost.

The hexagonal GAPD Since there was no commercially available GAPD matching the shape and size of our design, the University of Geneva group has worked out with Hamamatsu a new custom hexagonal device shown in Fig. 2.24. The first 2 prototypes arrived in Geneva on Dec. 22 and are being tested.

The device micro-cells are the same as standard Hamamatsu devices (and so share the same characteristics),

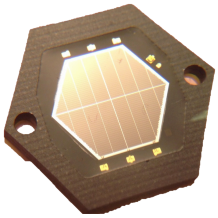

(a)

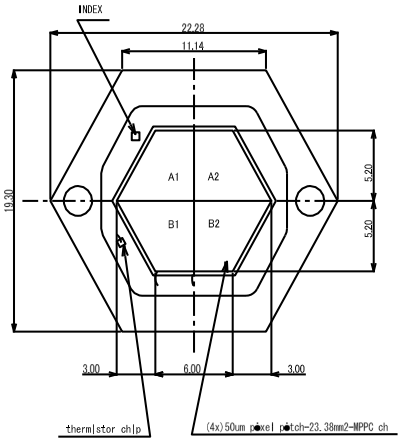

(b)

Figure 2.24: Photo (left) and scheme (right) of the new Hamamatsu hexagonal device (dimensions in mm).

and they are combined to form the hexagonal shape. At the moment, two square micro-cell sizes are under test: 50 μm and 100 μm. The cell size has an impact on the overall detector performance: the signal rise time decreases with cell size (about 4.13/2.35 ns for 50/100 μm) while the decay time increases with cell size (about 55.77/92.80 ns for 50/100 μm). The fill factor (ratio between active and dead zone) should be better with bigger cells. The cell size plays a relevant role also in the cross-talk and the dark current rates, even if recent studies show that these effects are strictly related to the quality of the substrate on which the junction is implanted and on the implantation technique itself. Recent developments by Hamamatsu have shown that they can keep under control these two factors for the next generation of devices.

The University of Geneva is characterizing these devices and the first results, even if preliminary, are available. It is important to note that to cross-check the result, all the measurements are performed not only for these new devices but also for other standard Hamamatsu GAPDs, as well as Ketek and SensL sensors. The qualification of these sensors goes through a set of measurements, here briefly summarized:

C-V and I-V measurement The measurement of the I-V curve is done directly with a Keithley 6487 picoammeter/voltage source controlled via software. The measurement of the C-V GAPD characteristic curve requires an additional LCR meter. As the biasing voltage of the LCR meter is limited to only 2 V, a Keithley 6487 pico-ammeter/voltage source is added in series to the AC source in order to provide sufficient bias for our purposes.

Measurement of the PDE The detector PDE measurement relies on the absolute measurement of the light which reaches the GAPD compared to the light reaching a (NIST) calibrated Hamamatsu photodiode (S1337-1010BQ), working as reference. To remove biases coming from the light direction of incidence, an integrating sphere is used to obtain a diffuse light source. The light is generated using pulsed LEDs (390, 470, 525, 572, 595, 637 nm). The GAPD signal is amplified and then read-out using a VME charge sensitive ADC gated by the light pulser to avoid the effect of after pulses and dark counts (thermal noise). The effect of crosstalk is measured and removed off-line. The absolute light which reaches the GAPD is determined using the calibrated photodiode. The first results are shown in the figure below 2.26. It is worth mentioning that this PDE measurement is an absolute PDE measurement and depends only on the NIST calibrated photodiode which is more reliable than measuring the photocurrent at different wavelength and then normalizing the whole distribution to a single point.

The first thing to notice is the difference between the PDE from the Hamamatsu Datasheet (black solid line in Fig. 2.26 and our result (blue points). This is due to the fact that Hamamatsu measurement are not corrected for afterpulsing and cross-talk. What is particularly important, is that the for different devices, including the hexagonal one, with the same micro-cell size, the PDE is consistent (all devices with 050C in their name which stands for 50 μm cell). This is not trivial at all as the sensitive area of the hexagonal device is much greater then that of the rest. An important remark is the fact that the 100 μm device seems to have a higher PDE. This can be explained by the higher fill factor, but has to be cross checked by looking at the detail design of the device.

Cross-talk and Uniformity measurement For an ideal detector the probability of two or more simultaneous photon thermal excitations should be negligible. The crosstalk will be measured by comparing the rate at 1 p.e. with the rate above 1 p.e.. The light pulse rate as a function of the signal pulse height will be measured by counting with a scaler the discriminated signals for different thresholds.

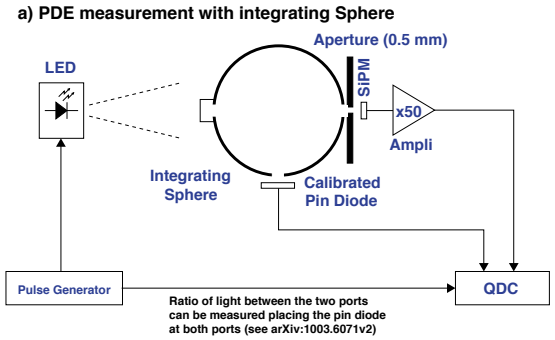

Figure 2.25: **Left:** PDE measuring setup with the integrating sphere. **Right:** PDE setup without the deployment of the integrating sphere.

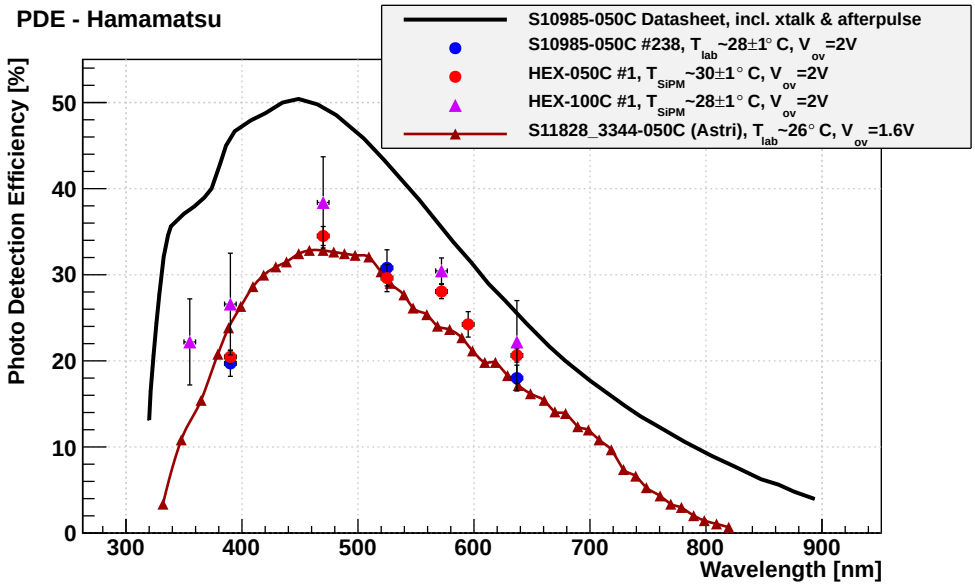

Figure 2.26: Comparison of PDE measurement for different devices. The data points with errors are the measurements done by the Geneva group, shoe the curve are result by other reported for comparison.

The crosstalk probability is:

$$P_{\text{crosstalk}} = \frac{f_{1\ pe}}{f_{>1\ pe}} \approx \frac{f_{>0.5\ pe}}{f_{>1.5\ pe}} \tag{5}$$

The measurement will be performed inside a light-tight black box which will prevent contamination from ambient light, for different GAPD bias voltages (gains). The crosstalk probability can also be measured independently for each cell by determining the $f_{>0.5\ pe}/f_{>1.5\ pe}$ ratio from the *uniformity scans* where single cells are pulsed directly, one by one. The uniformity of the gain and response of the single GAPD cells will be measured by performing a 2D scan of the GAPD with a point-like light source (LED coupled to a single mode optical fibre and focussing optic) with a resolution of about 1 μm.

After-pulse measurement The afterpulse measurement can be done using the dark count rate. Adding a multi hit TDC (time to digital converter) will allow the measurement of the afterpulse probability at the same time as the cross-talk.

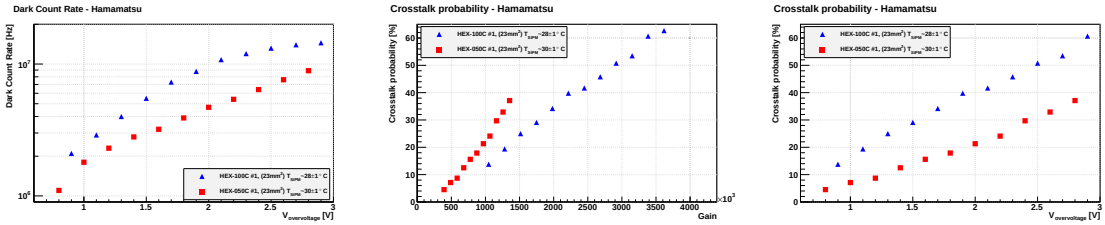

Figure 2.27: Dark count rate vs over-voltage (Left), cross-talk vs gain (middle) and vs over-voltage (right) for the new Hexagonal devices

2.6.2 Trigger and DAQ Electronics: the FlashCam

The FlashCam data processing inside the camera is fully digital in order to provide accurate triggering and an easily scalable architecture in a cost-effective way. Signal digitization and trigger processing are performed in a single readout chain per detector pixel. For a group of pixels, such a chain consists of Flash ADCs and a Field-Programmable Gate Array (FPGA) module, both commercially available and reasonably priced. A camera-wide event trigger is subsequently computed in separate trigger units. The camera data is transferred from the cameras over Ethernet to a central computer farm using a custom network protocol. The architecture of FlashCam is based on the concept of a "horizontal" integration of its components: the photon detector plane is a self-contained unit, consisting of photon detectors, high voltage supplies, preamplifiers, and control logic, which are supported by a monolithic mechanical carrier. The signal digitization and triggering electronics are organized in boards and crates, which are kept at the rear side of the camera body. Such an approach allows different photon detectors to be adopted. A detailed description of the FlashCam Architecture and performance can be found in the review document [12].

Integration and readout window To achieve the currently anticipated dynamic range of up to 3000 photoelectrons (p.e.) per pixel, the FlashCam concept foresees the use of preamplifiers with non-linear gain characteristics, instead of splitting the signal into two separate digitization channels with different (low and high) gain. Figure 2.28 (left) shows the resulting output of the amplifier for different input signals. High amplitude signals (¿ 200 p.e.) will saturate the amplifier, but the input signal can be restored since the output signal broadens with a defined recovery time

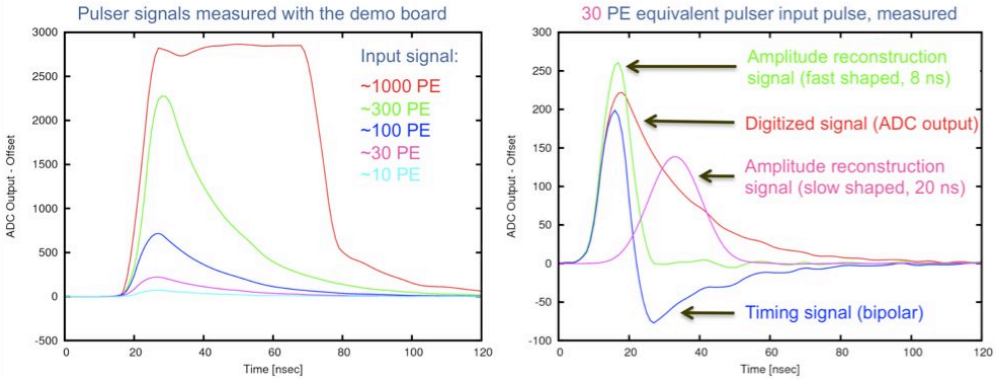

Figure 2.28: Output of the preamplifier for different input pulses (left), and processed output for a typical 30 pe pulse (right). All signals were measured with the FlashCam parallel demo board.

The analysis of the digitized signal will therefore run in two regimes. Below 200 p.e., the full time-resolved signal can be stored (with a window of 60-80 ns), and digital filtering performed at server computer level allows the signal amplitude to be directly computed. Above 200 p.e., the signal is reconstructed directly in the FPGA through an integration of up to 200 ns. The available bandwidth is sufficient to transmit the information from both regimes for all pixels simultaneously, allowing e.g. for cross-calibration in the

transition regime. The relatively long tail of the unclipped signals (< 200 p.e.) can be cancelled by the FPGA firmware as well as offline in the analysis software. Figure 2.28 (right) shows the analysis output for a typical 30 p.e. input signal and shows that effective integration times of less than 20 ns can be achieved. FlashCam can then work with the goal readout window as specified in the SST requirements (B-SST-1210 and B-SST-1220).

Amplitude Resolution The requirements and the goal amplitude resolution are shown in fig. 2.29-left (cfr. B-SST-1010 and B-SST-1020 in [20]). As can be seen, the amplitude resolution will fulfill the requirements if it does not exceed $dQ/Q = 1.44/\sqrt{N}$ for five to several hundreds p.e., corresponding to the blue line in fig.2.29-left).

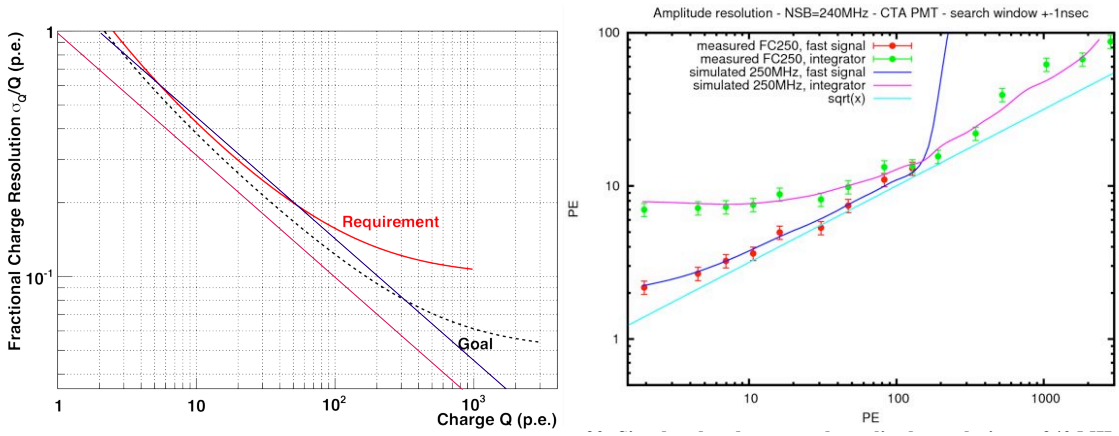

Figure 2.29: Left: Fractional rms charge resolution σ_Q/Q per pixel for different Cherenkov light signal amplitudes, expressed in units of photoelectrons (p.e.). The red line describes the required performance and the dashed black line the goal performance for a specified background level of 0.125 photoelectrons/ns. Right: Simulated and measured FlashCam amplitude resolution at 240 MHz NSB.

dQ is essentially the resolution shown on the y-axis, Q the input amplitude on the x-axis and N the number of incoming p.e.. The charge Q and the amplitude N are essentially the same. From Fig. 2.29 for 5 p.e., the amplitude (charge) resolution is 2 p.e., which would yield a ratio 0.4 which is below the goal. In the same way at 100 p.e. the amplitude is 9 p.e. and then the ratio is below 0.1. In Fig. 2.29(right), the cyan line corresponds to $dQ/Q = 1/\sqrt{N}$ (magenta line in Fig. 2.29).

Time Resolution The goal rms time resolution for signal amplitudes of more than 5 photoelectrons is 2 ns. As can be seen from Fig. 2.30, both the simulation (line) and the measurements (point) show a resolution for 5 photoelectrons of less than 1 ns.

Camera dead-time and readout rate The MST-FlashCam can transfer, at 10 kHz trigger rate, 20 samples (corresponding to 80 ns) for each of the 1764 pixels without dead time. This is enough to cope with

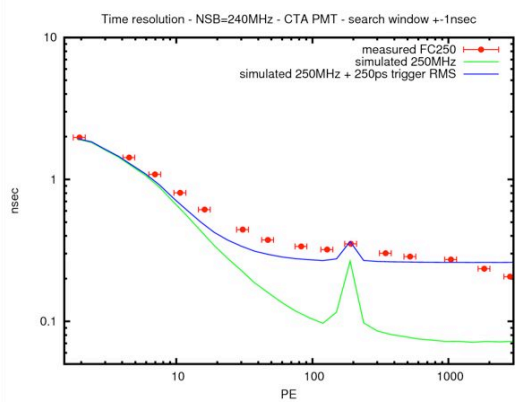

Figure 2.30: Simulated and measured time resolution at 240 MHz NSB. The peaks in the simulation are due to 200 p.e. signals, where FlashCam starts to work in saturated mode (see Fig. 2.29).

the 1296 pixels of the SST camera and address the following requirements. Under this condition, FlashCam is essentially dead-time free. The requirements for the read-time and readout rate for the SST are then fulfilled (see B-SST-1250, B-SST-1260, B-SST-1270, B-SST-1280, B-SST-1290 in [20]). More details are in [12], where simulation studies are shown for a PMT-based PDP and PMT analogue signals processed by the FlashCam electronics. The assumption that what is reported in [12] can be directly translated to the GAPD case will be verified with simulation studies of the full chain of the camera using the analogue signals of the GAPDs.

2.6.3 DAQ and control software

The SST Requirements document does not include any specific performance requirements on the 1M-SST interface to the ACTL system. The 1M-SST telescope is part of CTA and will be interfaced to the ACTL system in compliance with the standards being defined by the ACTL working group.

The 1M-SST camera interface to ACTL will be directly inherited from FlashCam. Commands will be received from the ACTL system and slow control, monitoring and alert streams will be sent to it. The raw data and trigger information will be interfaced with the ACTL DAQ software. This interface is under definition.

The 1M-SST drive system is a copy of that used on the MST and implemented in a PLC; the interface to ACTL will also be inherited from the MST. Specific internal tables and parameters will be defined for the 1M-SST. The active mirror control (if needed) and the bias control will be encapsulated in ACTL (ACS) components. Both systems will be launched, monitored and controlled via the main CTA control and logging systems. We expect that the 1M-SST will reuse as much as possible the definitions and software of the MST.

2.7 The Telescope Positioning and Tracking system

2.7.1 Finite Element Method Analysis

In order to perform FEM analysis, a simplified CAD model of the telescope structure was built. The model assumes the telescope is fixed to the foundation and to the azimuth ball bearing inside the tower. No motion is allowed in the elevation slew drive, whereas the telescope can revolve around the elevation ball bearing. In order to obtain more exact results, a CFX model was created within the ANSYS® software. The details of the model and results will be provided in a separate report.

The FEM analysis assumes dead and wind loads with the average wind velocity of 36 km/h and a wind gust coefficient of 1.67 (see Table 6) for the observation mode, and a wind velocity of 200 km/h for the survival conditions. The observation mode parameters represent the extreme conditions at which the observations can still be performed and thus the optical specifications need to be fulfilled. The survival conditions assume the telescope to be in the parking position with the mast locked in the camera docking station. The emergency mode condition, that allows the wind speed increase to the velocity of 100 km/h while the telescope is not parked, was also analyzed. The results were used for the selection of the drive system components. They proved the telescope structure does not suffer any plastic deformations. The structural calculations show the structure deformations and stresses for five different wind direction cases which are illustrated in Fig. 31(b).

Wind speed [km/h]	V_w	36	200
Wind speed [m/s]	V_m	10.0	55.6
Drag coefficient (Flat Plate)	c_d	1.2	1.2
Wind gusts coefficient	α	1.67	1
Air density [kg/m^3]	ρ	1.23	1.23
Air pressure [Pa]	P_a	62	1898
Wind Velocity Pressure [Pa]	P_{vel}	123	2278

Table 6: Wind velocity pressure input data. The air pressure $P_a = 0.5 \times \rho \times V_m^2$ and $P_{vel} = 0.5 \times \rho \times V_m^2 \times c_d \times \alpha$

Figure 31(a) illustrates the frame of reference used for the FEM analysis. The displacements of the camera along the telescope optical axis (x-axis; red arrow) define a defocus, whereas the y-z surface (green and blue arrows) defines the decentre in the camera plane. Table 7 presents the results of the analysis for the observation conditions and five elevation angles for the wind direction cases considered. The maximum camera defocus along the optical axis is 0.61 mm for the 45°-back-wind W_{45B36}. The maximum decentre is 8.2 mm for the same case of W_{45B36} at elevation angles of 30° and 45°. **Therefore, the maximum contributions to the PSF from the telescope structure deformations are kept well within 1/3 of the pixel angle.**

Similar FEM analysis for five wind-direction cases was conducted for the survival mode conditions, during which the telescope is locked in its parking position at -13°. The results of these calculations provide information about the localization of the specific weak points in the mechanical structure that was taken

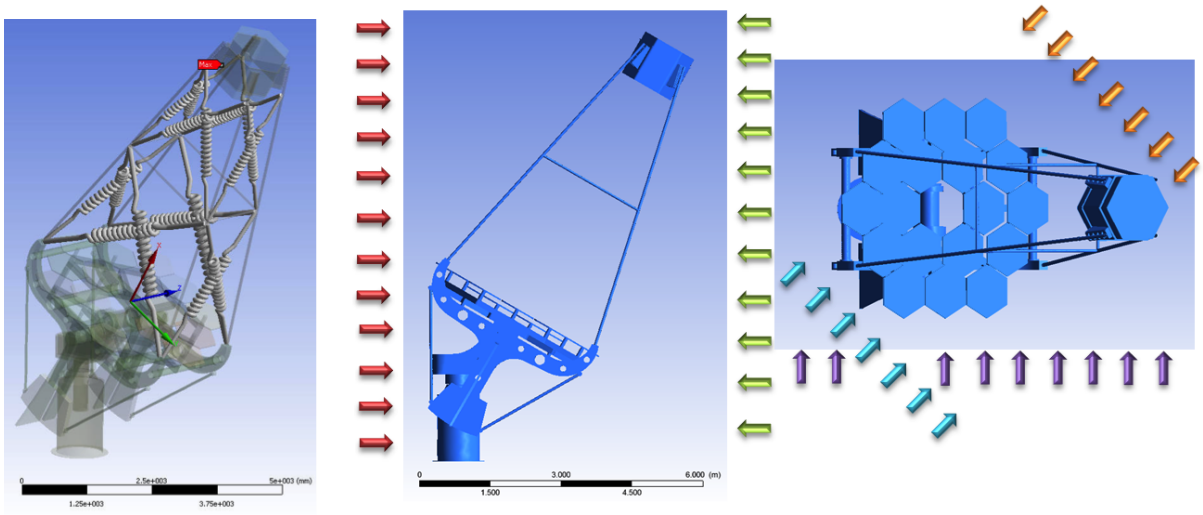

(a) (b)

Figure 2.31: Coordinate system used for the FEM analysis (**a**). Wind direction cases considered for the FEM calculations (**b**). The telescope at 60° elevation angle is viewed from the side and from above. The arrows illustrate the wind direction cases: back-wind W_{B36} (red), front-wind W_{F36} (green), side-wind W_{S36} (purple), 45°-front-wind W_{45F36} (orange), and 45°-back-wind W_{45B36} (blue).

into account during the re-design of the detailed solutions and the structure optimization process. The largest stresses of 63 MPa occurred for the back-wind conditions. **Thus all stresses are well below the plasticity of the materials used for the mechanical construction.**

elevation angle [deg]	30		45		60		75		90	
wind dir.	YZ	X	YZ	X	YZ	X	YZ	X	YZ	X
W_{F36}	6.7	0.38	5.9	0.12	5.0	-0.14	4.0	-0.39	2.4	-0.-57
W_{B36}	7.8	0.59	7.6	0.31	7.8	0.07	7.6	-0.21	6.2	-0.52
W_{S36}	7.5	0.46	7.0	0.17	6.3	-0.09	5.8	-0.33	4.9	-0.57
W_{45F36}	6.6	0.34	5.9	0.11	5.1	-0.14	3.9	-0.41	2.7	-0.6
W_{45B36}	8.2	0.61	8.2	0.33	8.0	0.07	7.6	-0.21	6.6	-0.5

Table 7: FEM analysis results for the observation conditions for different wind directions and elevation angles. YZ is the decentre in mm, while X represent the defocus in mm.

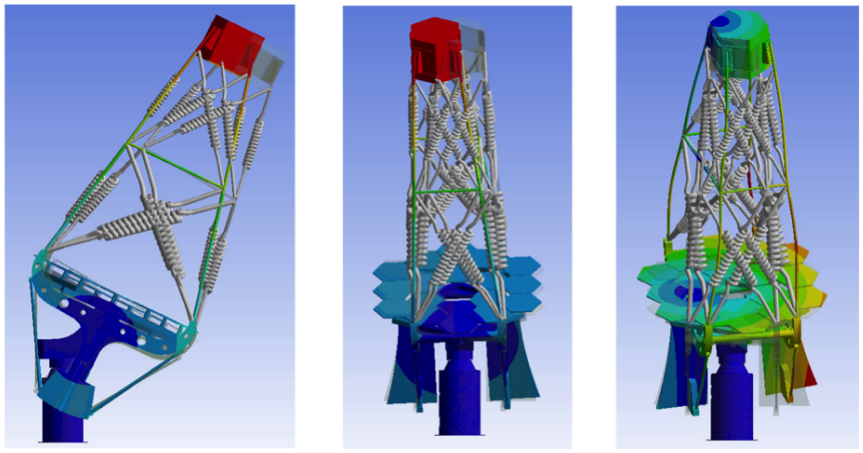

Figure 2.32: Results of the modal analysis showing three lowest frequencies and their corresponding modes.

We have also performed FEM analysis of the deformations and stresses under ice loads. As defined by the CTA specifications, the telescope structure should survive a load of ice with thickness of 20 mm and density of 900 kg/m^3 on all telescope surfaces in parking position.

Such a load corresponds to a pressure force of about 200 Pa. The maximum obtained displacement is about 0.3 mm, whereas the maximum stress is less than 32 MPa. Thus the ice load has very little effect on the structure.

Table 8 below shows the results of the modal analysis and Fig. 2.32 illustrates the modes at the elevation

	Elevation angle				
Modes	30	45	60	75	90
I [Hz]	3.8	3.9	3.8	3.8	3.8
II [Hz]	4.9	4.9	4.7	4.6	4.5
III [Hz]	11.4	12.8	13.2	12.5	11.8

Table 8: Modal analysis results for the observation conditions and different elevation angles.

angle of 60°. **The lowest eigenfrequency is 3.8 Hz and is well above the minimum value of 2.5 Hz specified for CTA telescopes.**

2.8 Drive System

The movement of the telescope about the elevation and the azimuth axes is realized by means of IMO slew drives and radial ball bearings. The IMO slew drive is a compact system that combines a worm gear with a motor and also a roller bearing, thus enabling transmission of both radial and axial forces. It has a fully enclosed and self-supporting housing. Rotating components are fixed to the housing with bolts. Each IMO slew drive contains a twin worm gear with two motors that help increase the torque capacity and reduce backlash, Fig. 33(a). The MST drive systems are also based on IMO slew drives and the choice of this type of drive for the 1M-SST has been partially done for the sake of uniformity among the various CTA telescope array sub-components. The general features of an IMO slew drive of the WD-H type, adopted in the 1M-SST design, are illustrated in Fig. 33(a). The telescope positioning and tracking system is realized with two independent drive axes: the azimuth axis and the elevation axis. The system uses one IMO slew transmission with twin worm gears and one ball bearing for each axis. Both axes are driven by two servo-motors. Such a solution has a number of advantages. It eliminates backlash ensuring a higher pointing accuracy, increases the reliability of the system (in the case of a failure of one drive or its controller the other drive can move the telescope to the safe position) and provides for higher flexibility that can be used if high acceleration is needed, e.g., for fast slewing. In the latter case, both servo-motors deliver torque in the same direction. As a consequence, smaller drives can be selected and the costs reduced.

The elevation and the azimuth drive systems realize rotations of the telescope around the horizontal and vertical axes, respectively (Fig. 33(b)). The elevation drive system ensures a movement of the telescope in a range between -13° (parking position) and 95°, whereas the rotation range for the azimuth drive system is $\pm 270^\circ$. In this way, the system meets the requirements for the positioning range during observations, technical tests, and stowing.

Drive System requirements

The drive system parameters have been determined according to the initial CTA requirements for the 1M-SST available at the time the calculations were made. The assumed environmental conditions specify the telescope site altitude as 2500 m above sea level and the operation temperature range between -20°C and $+30^\circ$C. The observation mode assumed has a 10 min-average maximum wind velocity of 50 km/h and the emergency mode allows for safe parking of the telescope in conditions with the maximum wind velocity reaching 100 km/h, including gusts. Presently, the observational condition has been relaxed to 36 km/h. The emergency mode also includes the possibility of reaching the parking position at decreased angular acceleration in the case of a failure of one of the drives. It is assumed that in the operation mode the telescope can fast slew to any defined point in the sky within 1 minute, including 6 seconds for both the acceleration at a constant rate from the start position and the deceleration. Resulting maximum angular velocities are $\omega_{max,a} = 6^\circ/s$ and $\omega_{max,e} = 2^\circ/s$ with respect to the azimuth and the elevation axes, respectively. The pointing accuracy is to be within 7 arcsec and the tracking accuracy is assumed not to exceed 5 arcmin.

Drive mechanical torque calculations

For the specified conditions, mechanical torques and power requirements have been calculated that allow for the selection of the drive system components. The calculations follow the guidelines of the Drive Power Estimates for CTA Telescopes document, provided by the Project Office. The method uses a simplified approach that assumes the mechanical shaft power (the power required to move the telescope at the elevation

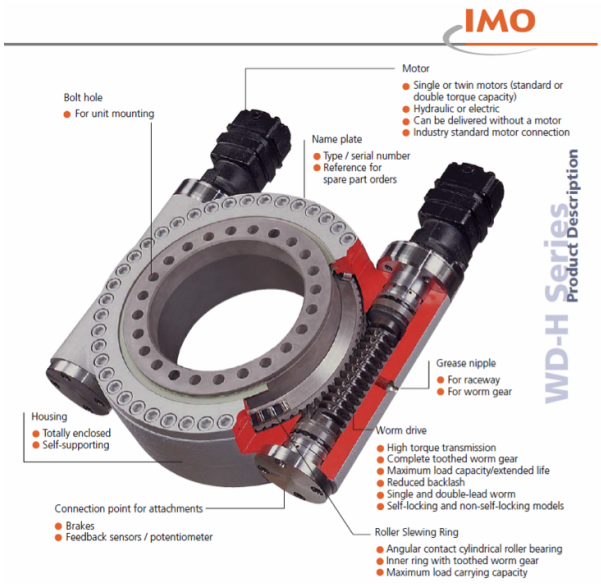

(a) General features of the IMO slew drive chosen for 1M-SST.

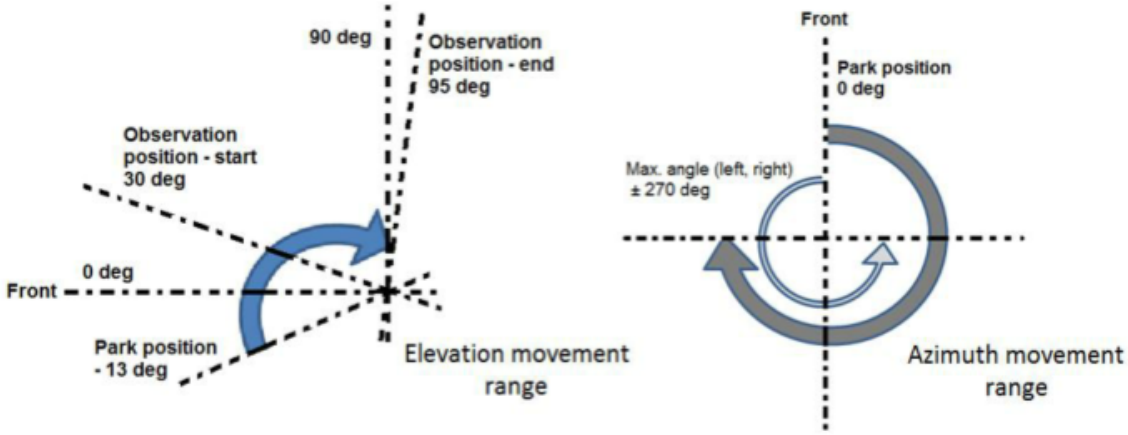

(b) The drive system movement range in elevation and azimuth.

Figure 2.33: The Slew drive System

and azimuth axes) is comprised of three components: friction, wind power, and the power required to accelerate the telescope. The total mechanical power is calculated as the product of the required total mechanical torque and the telescope angular velocity. The maximum values of the latter are given above. The maximum total torques about the elevation and the azimuth axes are 3426 Nm and 6828 Nm, respectively, for the 50 km/h wind, and 6064 Nm and 11842 Nm for the wind velocity of 100 km/h. Details of the calculations are provided in a separate document.

The friction torque represents the smallest component of the total moment. The total mass load on the elevation axis is 5.93 t, resulting in a radial load of 58.2 kN. The mass load on the azimuth axis is 8.83 t and the total radial load of this axis is 86.6 kN. The calculation of the acceleration torques assumes the drive velocity profile described below. The torque is estimated to be the product of the resulting angular acceleration and the moments of inertia about each axis. The latter are taken from the CAD calculations in Catia v5 and are 34118 kg m^2 and 23692 kg m^2 about the azimuth and the elevation axes, respectively. The total torque is dominated by the wind torque. The moments exerted on each axis result from the wind velocity pressure, the effective area of the telescope exposed to the wind, and the moment arm of the centre of pressure from the axis. The velocity pressure P_{vel} is calculated in accordance with Eurocode 1 Part 4 as $P_{vel} = 0.5\rho \times V_m^2 \times c_d \times \alpha$, where ρ is the air density in units of (kg/m^3) and V_m is the mean wind velocity in (m/s). The coefficients c_d and α represent the corrections for the wind drag and wind gusts, respectively. Tab. 9 lists the parameters used for the wind velocity pressure calculations.

Wind speed [km/h]	V_w	50	100
Wind speed [m/s]	V_m	13.9	27.8
Drag coefficient (Flat Plate)	c_d	1.2	1.2
Wind gust coefficient	α	2.2	1
Air density [kg/m^3]	ρ	1.23	1.23
Air pressure [Pa]	P_a	119	4.75
Wind velocity pressure [Pa]	P_{vel}	313	569

Table 9: Wind velocity pressure input data. The air pressure is $P_a = 0.5\rho V_m^2$.

Note that the wind gust coefficient is assumed to take the value of 2.2, this is unrealistic under normal operating conditions. Also, the assumed average wind speed for the observation mode (when servo-motors have to work with its nominal speed) is $V_w = 50$ km/h, while this was recently changed to $V_w = 36$ km/h in the current CTA specifications. Thus, the parameters of the drive system components selected on the basis of these calculations include a fair amount of safe margin that leaves a wide field for optimization during the telescope structure prototyping process. The wind torques have been calculated for a number of the load cases that include side wind and front wind scenarios at elevation angles in the range between 30^o and 90^o for which the torques acting on both axes were derived, and the side wind case with the telescope pointing towards the horizon, in which position the torques on the azimuth axis were calculated. The latter load case represents the maximum torque exerted on the azimuth axis for both wind velocity pressure values examined. The maximum torques on the elevation axis are exerted for the front wind case at the elevation angle of 60^o. In the process of the selection of the drive system, the data obtained for the 100 km/h wind velocity case were used to define the parameters of the gearboxes (gear-boxes have to withstand the loads

during telescope parking).

Drive System components

The final selection of the drive system components was based on the above calculations to which additional corrections have been made. The latter take into account a decrease in the motor efficiency at high altitudes, an increased resistance in the gears at negative temperatures, and the increased resistance in case of operation in the emergency mode, as described above. For both the azimuth and the elevation axis, the worm drive WD-H 0373/3-00028 produced by IMO has been selected. The gear ratio of the worm drive is 1:56. The servo-motors chosen for both axes are synchronic units Bosch-Rexroth MKS70C-0450-NN, together with the gear reducer GTM 140-NN2-050, that is mechanically compatible with the motor. With the moto-reducer gear ratio of 50, the total gear ratio is 2800. The motor speed limit is 6000 rpm. The Bosch-Rexroth motor can run at a speed of less than 1 rpm. Movement with minimal speed may not be smooth, but it should not affect the movement of the telescope due to its high moment of inertia. The choice of the same components for both drives was dictated by the preference to simplify the system. The detailed characteristics of the drive system components are provided in a separate document.

2.8.1 Power Requirements

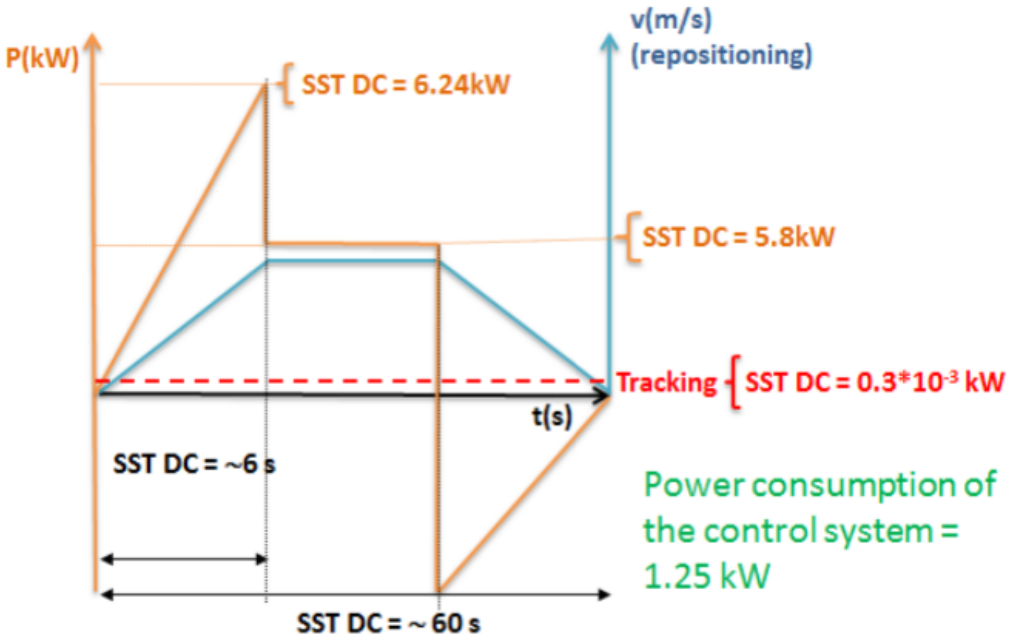

Figure 2.34: Electrical power consumption diagram for the 1M-SST in the operation mode.

Fig. 2.34 shows the power consumption diagram for the 1M-SST for different cases in the observation mode

at wind conditions with the average velocity of 50 km/h. The average power consumption by both the azimuth and the elevation drives during the telescope positioning is 5.8 kW. The peak consumption of 6.24 kW occurs during the start-up time of 6 s. The power needed for tracking should not exceed 300 mW. It has been estimated assuming the maximum motor speed of 2 rpm and taking into account motor resistance losses that are important for this range of speed. The power consumed by the control system and the air conditioning amounts to 1.25 kW.

Control and safety

The control software concept and structure and the safety concept will be based on the solutions applied to the MST prototype. The details applicable specifically to the 1M-SST are not yet worked out in detail. Collaboration with the MST team on this topic is foreseen.

2.9 Telescope Assembly and Installation

The telescope prototype structure is designed so as to fit into one standard-size (length: 5758 mm, width: 2352 mm, height: 2385 mm) open-top transportation container. The total weight of the container and the telescope structure will not exceed 10 t. The elements of the telescope will be unloaded from the container with the use of a 15-ton truck-crane. The same truck-crane can be used to set-up the telescope. The telescope assembly process requires a space of about 30×30 m^2. Additional workshop space is not needed. The assembly process is illustrated in Fig. 2.35 and described below.

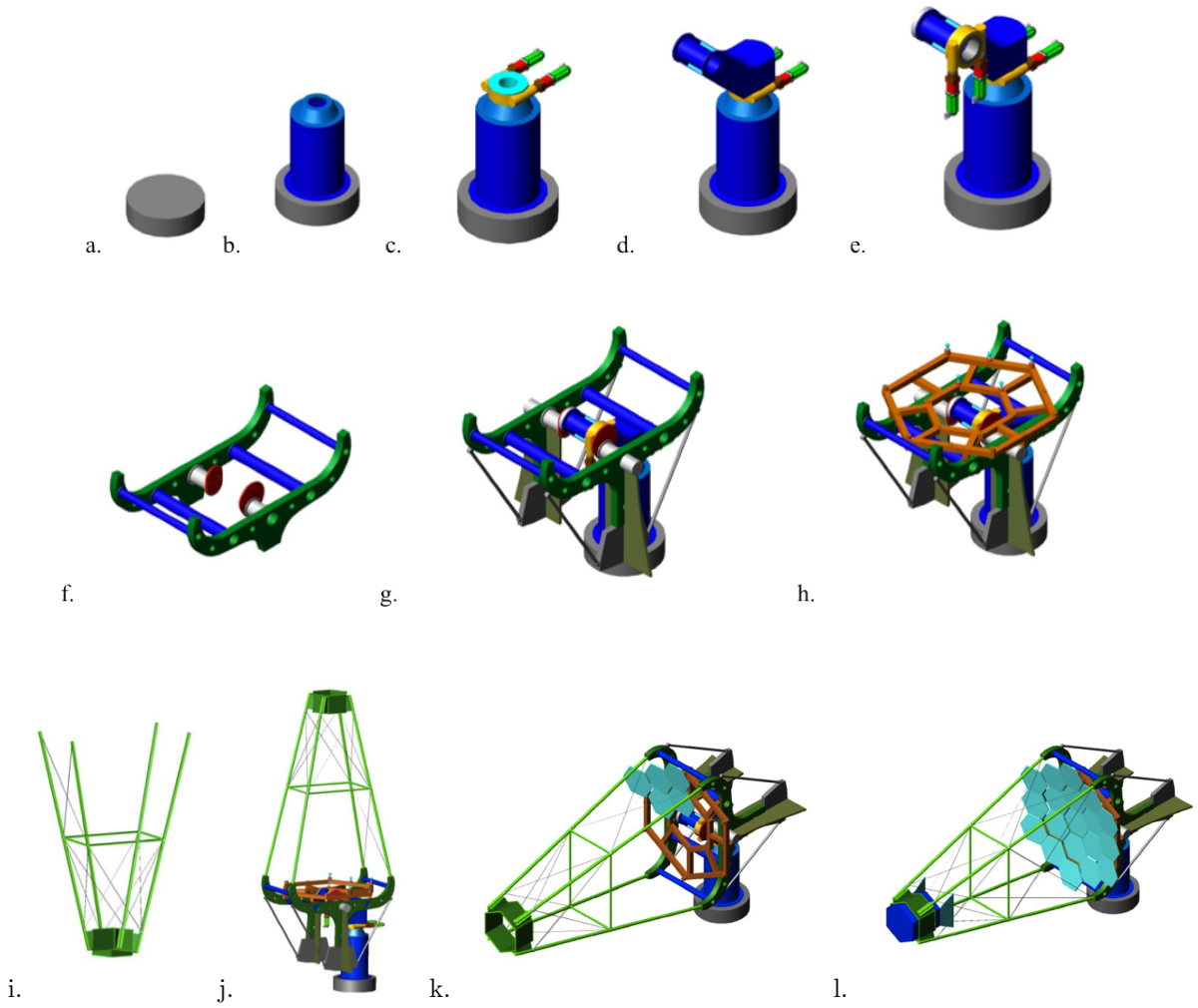

Figure 2.35: Telescope assembly process through steps a. to l.

In the first step, the telescope foundation is to built (Fig. 2.35 a). The foundation is made of reinforced

concrete with the anchors and bolts to fix and level the telescope tower. The diameter of the part of the foundation that is above the ground level (height of 0.4 m) is Ø=1.4 m. 50 pins of M32 type are required to mount the tower with the use of the crane (Fig. 2.35 b). After the tower cylinder is screwed to the foundations, the azimuth ball bearing with the inner cylinder is placed inside the tower. The side windows in the tower cylinder give access to the bolt that attach the bearing to the tower (see Fig. 6(b) above). The tower cap is then screwed on the tower cylinder. In the next step, the azimuth slew drive is mounted on top of the tower (Fig. 2.35 c) and the head with yoke is attached to the azimuth slew drive (Fig. 2.35 d) to which the elevation slew drive and ball bearing are connected next (Fig. 2.35 e). The slew drive is mounted with the motor side downwards to enable the installation of the dish support structure from above. At this stage, the installation of the remaining components of the azimuth and elevation drive systems (motors, gear boxes, controllers, and encoders) is possible and the power can be connected to the telescope.

The dish support structure is assembled prior to transportation during the production process (Fig. 2.35 f). This is to ensure that the structure has the appropriate shape. The dish support structure is attached to the head and then the counterweights, stabilization beams, wings, and axis sites are fixed (Fig. 2.35 g). In the next step the telescope dish is lowered from above (Fig. 2.35 h). The dish is also assembled at a producers site and only the special balls, a subcomponent of the mirror attachment system, are mounted on the dish at the construction site prior to its fixation to the dish support structure. The dish is screwed to the support at four points (see Fig. 2.3 in section 2.2).

The mast of the telescope with the camera fixation is set-up on its side (Fig. 2.35 i). Selected tension rods (these which do not interfere with the mirror attachment step, see Fig. 2.35 k) are also installed, but are not pre-loaded at this stage. The mast structure is then mounted from above on the dish support structure (Fig. 2.35 j) so that the camera side points upwards. In the next step the telescope is rotated into the park-out position (0°) and the mirrors are mounted (Fig. 2.35 k). Then the camera is installed at the parking position (-13°) and the telescope moved back into the park-out position, in which the remaining tension rods are mounted (Fig. 2.35 l). In the last step, the telescope is rotated into the zenith position (90°) and the load of 500 N is applied to the tension rods. The telescope set-up is thus completed.

2.10 Organization, Timeline and Cost

The project is structured as show in the organigram below.

The present design and prototyping phase of the project of is being carried out by a large consortium, which also includes the FlashCam Camera team. The consortium is composed of the following institutions:

- DPNC - Universitè de Genéve, Switzerland
- IFJ PAN - Institute of Nuclear Physics, Krakow, Poland
- Jagiellonian University - Krakow, Poland
- AGH University of Science and Technology - Krakow - Poland
- Space Research Centre, Polish Academy of Sciences, Warsaw, Poland
- Universität Zürich, Switzerland
- Universität Tübingen, Germany
- Max Planck Institute for Nuclear Physics, Heidelberg, Germany
- Nicolaus Copernicus Astronomical Center- Warsaw - Poland

The milestones of the project are presented in the table 10 below. It is worth noting that the timeline and chart shown here assume that funds will be available on time. The fund spending profile can change the schedule and affect the corresponding milestones.

The project is in an advanced prototyping phase. The PDP is still in an R&D phase, as finding for this has only recently been received. In order to determine the milestones, a careful and detailed plan of the whole project has been made. The project progress and achievements are continuously monitored and mapped into the plan. In the Gantt chart below, the project plan for this phase is shown.

2.10.1 Prototype Costs

The cost of the telescope assumed in tab. 11 is the cost of the prototype, based on the quotes available at the moment and without any assumption on cost savings which will result from the mass production in industry. This cost represent then an upper limit, which for the mass production can go lower by at least 10-15%.

2.10.2 Transition to mass production: model and timeline

The effort for the production of telescopes can be split into six sub-tasks.

1. **Production of the telescope frame.**
   This subtask includes the telescope mechanical structure with the drive system components such as

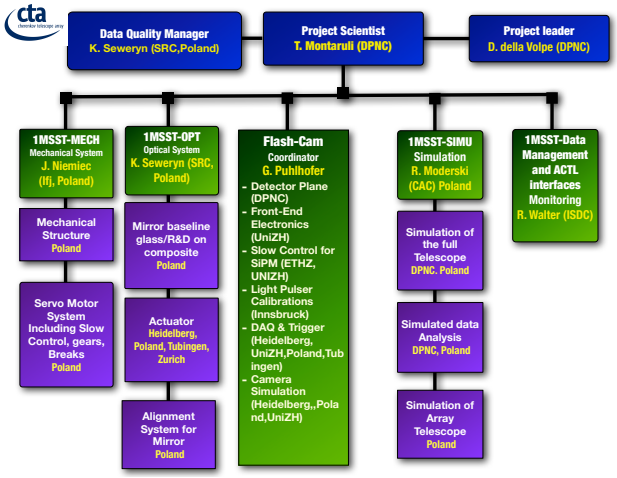

Figure 2.36: Organigram of the 1M-SST project.

Table 10: Relevant milestones for the design and prototyping of the 1M-SST project. The milestone can move according to funding availability.

Telescope Structure	
Final design	March 2013
Drive Final Selection	April 2013
Prototype Assembled at IFJ PAN	December 2013
Mirror & Actuator	
Order of 18 Mirror for prototype	End of 2013
Actuator Final Selection	April 2013
Integration and installation on prototype	May 2014
Readout electronics	
Full scale prototype	End 2014
Photodetector plane	
144-Pixel PDP ready	End 2013
144-Pixel Camera (PDP+electronics)	June 2014
Full camera prototipe	2^{nd} Quarter 2015
Full Scale Prototype	3^{rd} Quarter 2015

Title	Effort	Start	End
1) Telescope Structure and Drive	157w 0.5d	**8/2/12**	12/31/13
1.1) Telescope Structure Design	71w	**8/2/12**	3/29/13
1.1.1) Mechanical Design	34w 2d	8/2/12	3/29/13
1.1.2) FEA Analysis	21w 3d	8/2/12	12/31/12
1.1.3) Design Consultation with Industrial Partner	12w 4d	1/1/13	3/29/13
1.1.4) Cost Calculation	2w 1d	3/15/13	3/29/13
1.1.5) Final Design		3/29/13	3/29/13
1.2) Drive System	32w 2d	**9/25/12**	7/19/13
1.2.1) Drive Selection	14w 4d	9/25/12	1/4/13
1.2.2) Drive System Delivery		2/19/13	2/19/13
1.2.3) Testing of Drive System at IFJ PAN	17w 3d	3/20/13	7/19/13
1.3) Telescope Construnction	53w 3.5d	**4/1/13**	12/31/13
1.3.1) Call For Tender	3w 1d	4/1/13	4/22/13
1.3.2) Structure Construction	46w 0.5d	**4/23/13**	12/31/13
1.3.2.1) Foundation at IFJ PAN	10w	4/23/13	7/1/13
1.3.2.2) Structure Contruction at Producer Site	26w 1d	4/23/13	10/22/13
1.3.2.3) Transport of Structure to IFJ PAN	1w 2d	10/23/13	10/31/13
1.3.2.4) Assembly of the Structure and Drive System At IFJ PAN	8w 2.5d	11/1/13	12/31/13
1.3.3) Preliminary Commissioning and Functional Tests at IFJ PAN	4w 2d	12/2/13	12/31/13
2) Mirrors & Actuators	122w 1d	**8/1/12**	5/9/14
2.1) Mirror R&D and qualification	65w 3d	8/1/12	11/1/13
2.2) Mirror Order	4w	11/4/13	11/29/13
2.3) Mirror shipment		1/31/14	1/31/14
2.4) Mirror QC	4w 1d	2/3/14	3/3/14
2.5) Actuator and alignment Qualification	25w 4d	1/1/13	6/28/13
2.6) Actuator Solution Decision		4/2/13	4/2/13
2.7) Actuator Order	4w 4d	7/1/13	8/1/13
2.8) Actuator Shipnent		1/6/14	1/6/14
2.9) Actuator QC	13w 4d	1/7/14	4/11/14
2.10) Integration of Mirror, Actuatori & Alignment System	4w	4/14/14	5/9/14
3) Camera	270w	**8/1/13**	4/17/15
3.1) PDP - Design and Prototyping	146w	**8/26/13**	4/17/15
3.1.1) 144 Pixel Prototype	58w	**8/26/13**	4/9/14
3.1.1.1) 144 sensor verification	12w	8/26/13	11/15/13
3.1.1.2) 1300 Cone Qualification and Test	8w	10/17/13	12/11/13
3.1.1.3) Front-end Assembly	4w	10/10/13	11/6/13
3.1.1.4) Cone Mass production	8w	9/16/13	11/8/13
3.1.1.5) PDP prototype Assembly	2w	10/10/13	10/23/13
3.1.1.6) PDP Prototype Qualification	8w	10/24/13	12/18/13
3.1.1.7) PDP Prototype Test	16w	12/19/13	4/9/14
3.1.2) Full Camera Prototype	88w	**11/11/13**	4/17/15
3.1.2.1) PDP Modules Assembly	30w	11/11/13	6/6/14
3.1.2.2) PDP Modules Qualification	24w	3/10/14	8/22/14
3.1.2.3) PDP Mechanical Integration	4w	8/25/14	9/19/14
3.1.2.4) PDP Qualification	8w	9/22/14	11/14/14
3.1.2.5) PDP and camera integration	2w	11/17/14	11/28/14
3.1.2.6) Full Camera deployment & Test	20w	12/1/14	4/17/15
3.1.2.7) Full prototype Camera		4/17/15	4/17/15
3.2) Flash Cam - Design and Prototyping	124w	**8/1/13**	9/26/14
3.2.1) Mechanics and cooling	56w	8/1/13	8/28/14
3.2.2) Electronics	32w	8/1/13	3/13/14
3.2.3) Assembly and test	36w	1/20/14	9/26/14

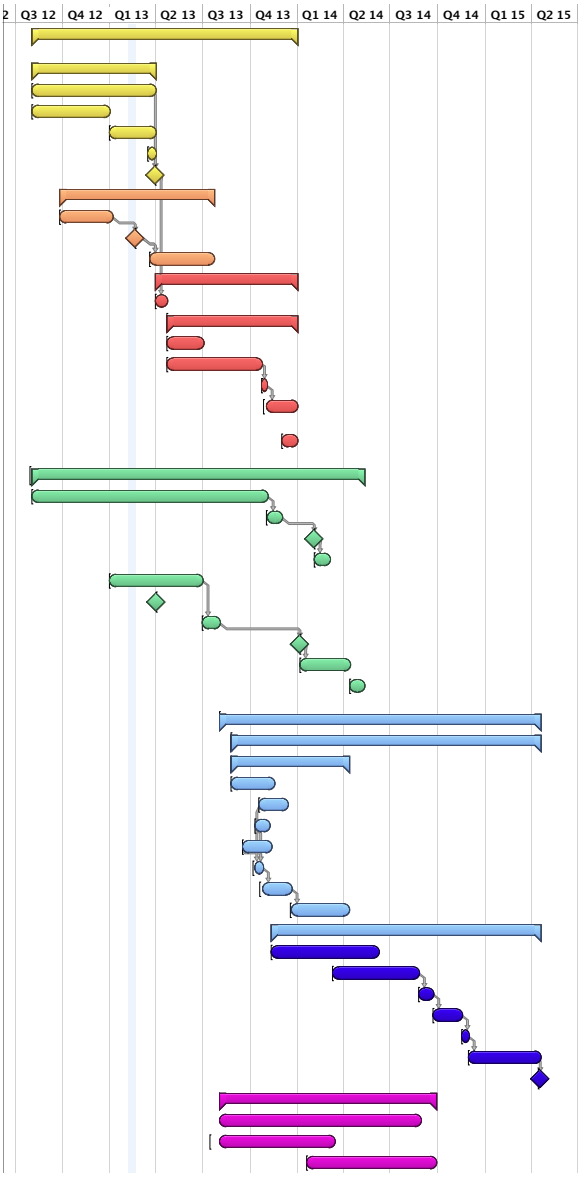

Figure 2.37: Design & Prototyping Global Schedule

Component	Quantity	Unit cost [€]	Total cost [€]
Photo Detector Plane			
Hexagonal SiPM	1300	74	96'200
Light Funnel	1300	20	26'000
Detector plane electronics	108	350	37'800
PDP Mechanical Structure Calib. system, entrance window PDP container, cooling	1	60'000	60'000
		Subtotal	**220'000**
Readout Electronics			
backplane	9	300	2'700
FADC Cards	63	1'100	69'300
Trigger	9	700	6'300
Master Card	1	700	700
DAQ Crates	9	200	1'800
Power Supply	2	1'200	2'400
Analog+Network cables			2'500
Network server	1	5'000	5'000
Switch	3	1'500	4'500
Slow Control	1	10'000	10'000
		Subtotal	**105'200**
Telescope Structure			
Telescope structure	1	60'000	60'000
Telescope foundation	1	2'000	2'000
Drives & power system	1	62'000	62'000
		Subtotal	**124'000**
Mirrors			
Mirror actuators	18	960	13'680
Alignment system	1	8'000	8'000
Mirrors	18	2'000	32'000
		Subtotal	**53'680**
		Gran Total	**502'880**

Table 11: Estimated cost of the complete telescope for large mass quantity

slew drives, ball bearings, gearboxes, and servo-motors. The frame will be produced in industry. The telescopes will be pre-assembled at the producer site where also basic tests of their functionality will be performed. The telescopes will then be packed for shipping. To cut the transportation costs, a division of the telescope structure into smaller units that fit the standard size of a shipping container is made. In fact, three telescopes structures should fit into one container of standard size (2.3m x 2.6m x 12m). There is no need to completely disassemble the telescope after the pre-installation and tests because the telescope can be shipped as a few sub-components. These subcomponents are: the telescope mount with the azimuth slew drive and ball bearing, the telescope head with the elevation slew drive and ball bearing, the telescope dish support structure, the dish, the mast (in two pieces), the camera mounting interface, and the docking station. This approach facilitates an easy and cheap integration at the observatory site and in addition does not require further extensive quality control checks.

The pre-assembly and testing at the producer site, together with the quality control, will be supervised by an engineer from IFJ PAN. The producer will be selected in the call for tender process. One of the prospective industrial partners is Ponar Zywiec sp. z o. o. (www.ponarzywiec.com.pl).

The mechanical elements of the drive system will be delivered by industry: the chosen servo- motors and gear reducers are Bosch-Rexroth units, and the slew drives (of the WD-H type) will be delivered by IMO.

The elements of the telescope will be unloaded from the container with the use of a 15-ton truck-crane. The same truck-crane can be used to set-up the telescope.

2. **Production of the telescope power system.**
This subtask assumes the integration of the telescope power components (power supply, slow-control, micro-processor, etc.) into power-supply cabinets. They will be integrated and tested in industry and shipped to the observatory site. Tests of functionality at the telescope frame production site are also foreseen beforehand. The tests will be supervised by an engineer from IFJ PAN.

3. **Production of the mirror and alignment system.**
The 18 mirror panels for the SST-DC mirror prototype will be tested as a task, "2.4 Mirror QC" in the schedule (Feb-Mar 2014). Mirror Quality Control will be realized using SRC PAS 2-f testing system, SRC PAS 1-f testing system and any other which will be required.

   The qualification process will be realized in collaboration with CTA WP-MIR.

   The actuators and alignment system will be produced in Poland. There are identified manufacturers which have gained experience producing actuators for H.E.S.S. telescopes as well as for space applications.

4. **Production of the lightning protection.**
Produced in industry and shipped to the observatory site.

5. **Production of the Photodetector plane**
The PDP component production will be done by companies. The main work in the production phase is then the assembly and test. The light funnels will be produced with standard techniques and coated by a company (Thin Film in Zürich) in such a way as to be ready for their assembly with the hexagonal GAPD s. The same will apply to the preamplifier board which will be produced and qualified in a company.

We plan a complete automation of the assembly of the light funnel over the hexagonal GAPD s (termed "sensor" in the following). Here we assume we can assemble 70 cones per day (either in an automatic way or by 2 technicians).

The plane is composed of 108 modules each hosting 12 sensors. It is safe to assume that 6 modules can be assembled per day and that one complete sensor plane can be assembled in 3 weeks by 2 full-time technicians supervised by a physicist. For the integration in the mechanical chassis and tests we can assume that we need 1 full-time physicist and 1 technician at 30% of his/her time for 3 weeks of testing.

6. **Production of the readout electronics**
   The readout electronics boards will be tested by the company which produces them. For the assembling and the test of the mini-crate, some test set-up will be put in place in the responsible institute.

Planning of the mass production has been based on the best understanding of the system we have at the moment. There are still many open questions and possibilities, but in the project planning and in the technical decisions, we always keep in mind the impact these will have on mass production. This is in order to guarantee that the telescope we are planning to deploy can be built, installed and commissioned in the desired quantity on the timescale imposed by the CTA schedule.

Title	Effort	Start	End
1) Camera	398w	**8/4/14**	11/22/16
1.1) PDP Mass Production	164w	**8/4/14**	7/21/15
1.1.1) SiPM Ordering	4w	8/4/14	8/29/14
1.1.2) SiPM delivery	40w	9/29/14	7/3/15
1.1.3) Cone Mass Production	24w	9/29/14	3/13/15
1.1.4) Plane mechanics mass production	24w	9/29/14	3/13/15
1.1.5) Front-end board production	32w	10/3/14	5/14/15
1.1.6) front-end board qualification	40w	10/15/14	7/21/15
1.2) PDP assembly	60w	11/17/14	1/8/16
1.3) PDP Test and Mechanical integration	60w	1/15/15	3/9/16
1.4) Readout Electronics	114w	**6/1/15**	11/22/16
1.4.1) Board Mass production	14w	6/1/15	9/4/15
1.4.2) Boards Assembly & Test	40w	9/7/15	6/10/16
1.4.3) Mini Crate Assembly and test	60w	9/30/15	11/22/16
2) Telescope Structure	143w	**1/5/15**	9/30/16
2.1) Telescope Structure mass Production	82w	1/5/15	7/29/16
2.2) Telescope packaging for shipment	61w	8/3/15	9/30/16
3) Mirror and actuator	220w	**11/3/14**	3/25/16
3.1) Mirror Mass Production	60w	11/3/14	12/25/15
3.2) Mirrors qualification	60w	1/1/15	2/24/16
3.3) Actuator mass production	40w	11/3/14	8/7/15
3.4) Mirror & Actuator integration	60w	2/2/15	3/25/16
4) CTA Site ready for installation		1/1/16	1/1/16
5) Delivery to CTA site	40w	3/28/16	12/30/16
6) Commissioning	72w	**2/15/16**	6/29/17
6.1) First 5 Telescope installation and training of local crew	20w	2/15/16	7/1/16
6.2) Installation and commissioning	52w	7/1/16	6/29/17

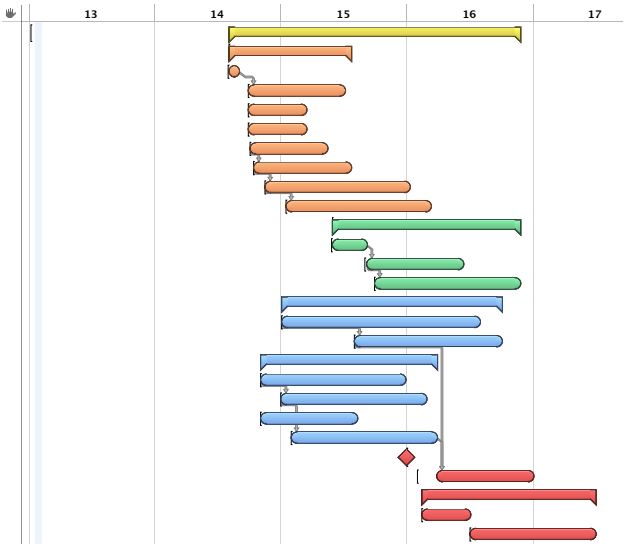

Figure 2.38: Mass production tentative schedule. This schedule refer to the production of 20 telescope. The remaining 50 can be produced on a similar timescale with parallel effort of other group.

3 ASTRI

3.1 Introduction

ASTRI ("Astrofisica con Specchi a Tecnologia Replicante Italiana") is a flagship project of the Italian Ministry of Education, Universities and Research strictly linked to the development of the ambitious Cherenkov Telescope Array (CTA). CTA plans the construction of many tens of telescopes divided in three kinds of configurations, in order to cover the energy range from a tens of GeV (Large Size Telescope, LST), to a tens of TeV (Medium Size Telescope, MST), and up to 100 TeV (Small Size Telescope, SST).

Within this framework, the Italian Istituto Nazionale di Astrofisica (INAF) is currently developing an end-to-end prototype of the CTA small-size telescope in a dual-mirror configuration (SST-2M) to be tested under field conditions, and scheduled to start data acquisition in 2014. INAF is in charge of the design of the mirrors and the focal plane, development of the Monte-Carlo, control, acquisition, data-handling and archiving software and end-to-end operations, while the telescope structure is designed by external firms. Moreover, INAF supports all activities related to CTA, such as the participation in the CTA management and Project Office activities, the Monte-Carlo simulations, and the data handling.

For the first time, a wide field of view (FoV = 9.6 degrees in diameter) dual-mirror Schwarzschild-Couder (SC) optical design will be adopted on a Cherenkov telescope, in order to obtain a compact ($F_{\#} = 0.5$) optical configuration and equipped with a light ($\sim$ 50 kg) and compact ($\sim$ 50cm $\times$ 50 cm $\times$ 50 cm) camera based on Hamamatsu S11828-3344M Silicon photo-multipliers which offer high photon detection sensitivity in the 300–700 nm band, a fast temporal response and a suitable logical pixel size of 6.2 mm $\times$ 6.2 mm. The proposed telescope layout (whose mount exploits the classical alt-azimuthal configuration) is fully compliant with the CTA requirements for the SST array. The telescope design is compact having a 4.3 m-diameter segmented primary mirror, a 1.8 m-diameter monolithic secondary mirror, and a primary-to-secondary distance of 3 m. The SC optical design has a focal ratio $F_{\#} = 0.5$, a plate scale of 37.5 mm/degree, a logical pixel size of approximately 0.17° and an equivalent focal length of 2150 mm. Considering 1984 pixels, this setup delivers the above mentioned FoV and a mean value of the active area of about 6.5 square meters, taking into account all the possible attenuation and occultation factors.

The ASTRI Prototype will be placed at Serra La Nave, 1735 m a.s.l. on the Etna Mountain near Catania, at the INAF "M.G. Fracastoro" observing station. Although the ASTRI SST-2M prototype is mainly a technological demonstrator, it will perform scientific observations on the Crab Nebula, Mrk 421 and Mrk 501. Preliminary calculations show that in the maximum sensitivity range (E > 1 TeV) we can detect a flux level of 1 Crab at 5-sigma in a few hours, while in the energy range E > 10 TeV the same flux at 5-sigma can be reached in a few tens of hours.

A remarkable improvement in terms of performance could come from the operation, in 2016, of a SST–2M mini-array, composed by a few SST–2M telescopes and to be placed at final CTA Southern Site. The SST mini-array will be able to study in great detail relatively bright sources (a few $\times 10^{-12}$ erg cm^{-2} s^{-1} at 10 TeV) with an angular resolution of a few arcmin and an energy resolution of about 10–15 %. Moreover, thanks to the array approach, it will be possible to verify the wide FoV performance to detect very high energy showers with the core located at a distance up to 500 m, to compare the mini-array performance with the Monte Carlo expectations by means of deep observations of few selected targets, and to perform the first CTA

science, with its first solid detections during the first year of operation. Prominent sources such as extreme blazars (eg 1ES 0229+200), well-known BL Lac objects (eg PKS 2155-304, Mrk 421) and radio-galaxies, galactic pulsar wind nebulae (Crab Nebula, Vela-X), supernovae remnants (Vela-junior, RX J1713.7−3946) and microquasars (LS 5039), as well as the Galactic Center can be observed in a previously unexplored energy range, in order to investigate the electron acceleration and cooling, relativistic and non relativistic shocks, the search for cosmic-ray (CR) Pevatrons, the study of the CR propagation, and the impact of the extragalactic background light on the spectra of the sources.

3.1.1 High level architectural description

The prototype under realization with ASTRI design will be a fully functioning telescope. It will be also possible to perform an End to End test in order to verify all the performance requirements and to validate the ASTRI optical and structural design and the ASTRI camera. To achieve that, the ASTRI prototype will be installed in Serra La Nave, as already specified, and beside the telescope all the facilities necessary to perform the End to End tests will be installed. In order to give a more precise picture of the ASTRI project, an extract of the ASTRI Product Tree is herafter presented (Figure 3.1).

The product tree is related whenever possible to the Official CTA PBS and for those items for which a direct correspondence exists double coding is shown. The presented table is limited only to the higher levels of the product tree. The complete product tree is available in the ASTRI documentation.

The telescope will be integrated following as much as possible the architecture that will be used in CTA. The actual architecture definition with which ASTRI engineers and scientists are working to develop the SW and to prepare the site is presented in Figure 3.2. The telescope architecture is shown in Figure 3.3, and the baseline architecture design for the control cabinet which will be installed on the telescope is presented in Figure 3.4.

ASTRI CODE			CTA CODE		
Lv1	Lv2	Lv3	Code	Acronym	Product Description (Lv0)
			2	ARRAY	Array control
			2.1	ARRAY-MON	Instrument monitoring software
3700			2.2	ARRAY-SLOW	Instrument slow control software
	3710		2.2.1	ARRAY-SLOW	Telescope drive control
	3720		2.2.2	ARRAY-SLOW	Camera control
	3730		2.2.3	ARRAY-SLOW	Mirror control
	3740		2.2.4	ARRAY-SLOW	Aux. instruments
3900			2.3	ARRAY-OPS	Instrument operation software
	3910		2.3.1	ARRAY-OPS	Telescope operation
	3920		2.3.2	ARRAY-OPS	Aux instruments operation
3800			2.4	ARRAY-DAQ	Monitoring System
	3810		2.4.1	ARRAY-DAQ	Quick Look (HW/SW)
	3820				Data Archive and ICT
	3830		2.6	ARRAY-ONLINE	Online IT infrastructure
6000			3	DATA	Data management
			3.1	DATA-MODEL	Data model
			3.2	DATA-PIPE	Data pipelines
			3.3	DATA-ARCH	Data archives
			3.4	DATA-ACCESS	Observer data access
	6500		3.5	DATA-ICT	ICT-infrastructures
			4	SST	Small Size Telescope
3100			4.1	SST-MECH	Mechanical System
	3110		4.1.1	SST-MECH	MOUNT (assembly)
		3111			Base Structure
		3112			Azimuth Column
		3113			Azimuth Fork
	3120		4.1.2	SST-MECH	OPTICAL SUPPORT STRUCTURE
		3121			M1 Dish
		3122			Counterweights
		3123			Mast
		3124			M2 Backup Structure
		3125			Central Tube
		3126			M1 Segment Support Triangle
		3127			M1 Segment Support Spacer
		3128			M2 Load Spreader Assembly
3200			4.3	SST-CAM	Camera
	3210		4.3.2	SST-CAM	Focal plane optics (MPPC)
	3220		4.3.3	SST-CAM	Camera Electronic
		3221			FEE PCB
		3222			FPGA PCB
		3223			Back end Electronic
	3230		4.3.5	SST-CAM	CAMERA MECHANICS
		3231			Ass. Camera Backbone Structure
		3232			Ass. Pdms Support Structure
		3233			Ass. Back-End Electronic & Distribution Thensions Board
		3234			Ass. Thermal Enclosure
		3235			Ass. Pmma Window
		3236			LID System
		3237			Light Collector
		3236			Electronic Basket
	3240		4.3.6	SST-CAM	Fiber Optic Calibration (FOC) systems
		3241			Fiber Optic (FO)
		3242			FOC- Electronic Box
	3250		4.3.7	SST-CAM	Camera auxiliary systems
		3251			Temperature control
		3252			Thermoelectric Assembly (Peltier)
	3260				Voltage Distribution Box (VDB)
3400			4.4	SST-FOUND	Foundation
	3410		4.4.1	SST-FOUND	Telescope base
	3420		4.4.2	SST-FOUND	Camera access
3600			4.5	SST-AUX	Auxiliary Systems
	3610		4.5.1	SST-AUX	Power system
	3620		4.5.2	SST-AUX	Lightning protection
	3630		4.5.3	SST-AUX	Calibration and pointing control
		3631			UVScope
		3632			UVSiPM
	3640		4.5.4	SST-AUX	Environment and sky monitoring
		3641			Weather Station
		3642			All-sky Camera
		3643			Sky Quality Meter

Figure 3.1: General view and nomenclature of the ASTRI telescope structure.

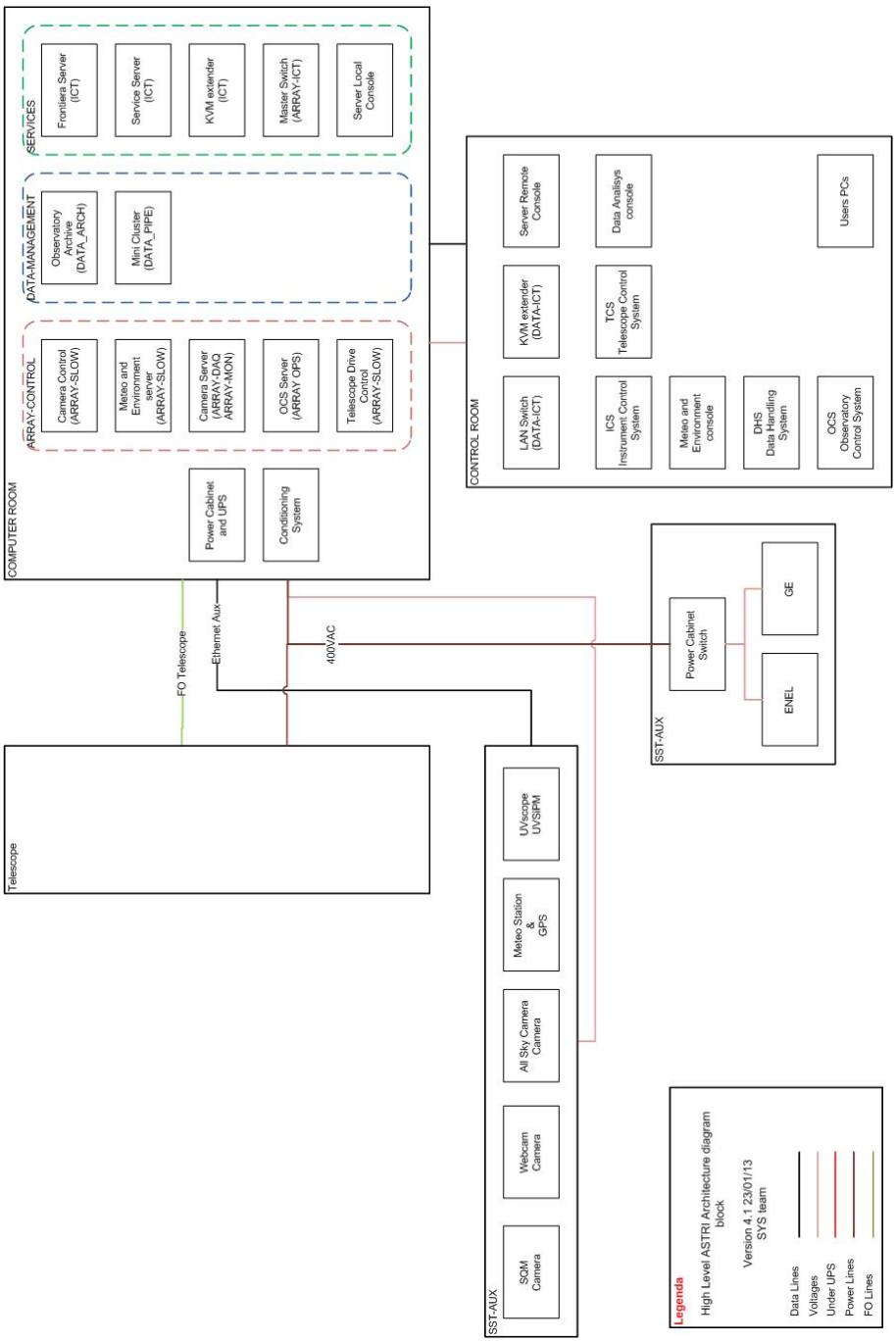

Figure 3.2: Block diagram of the ASTRI SST–2M Architecture.

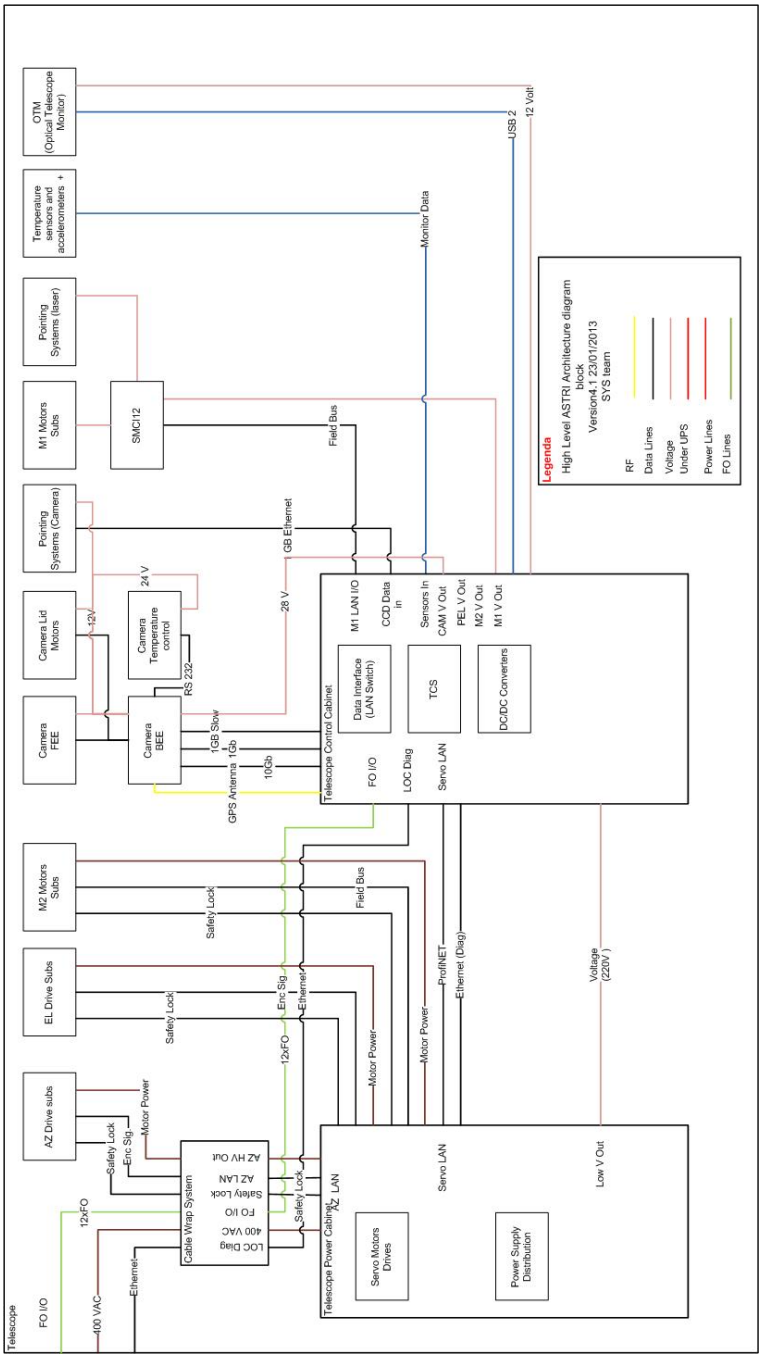

Figure 3.3: Block diagram of the ASTRI SST–2M Telescope Architecture.

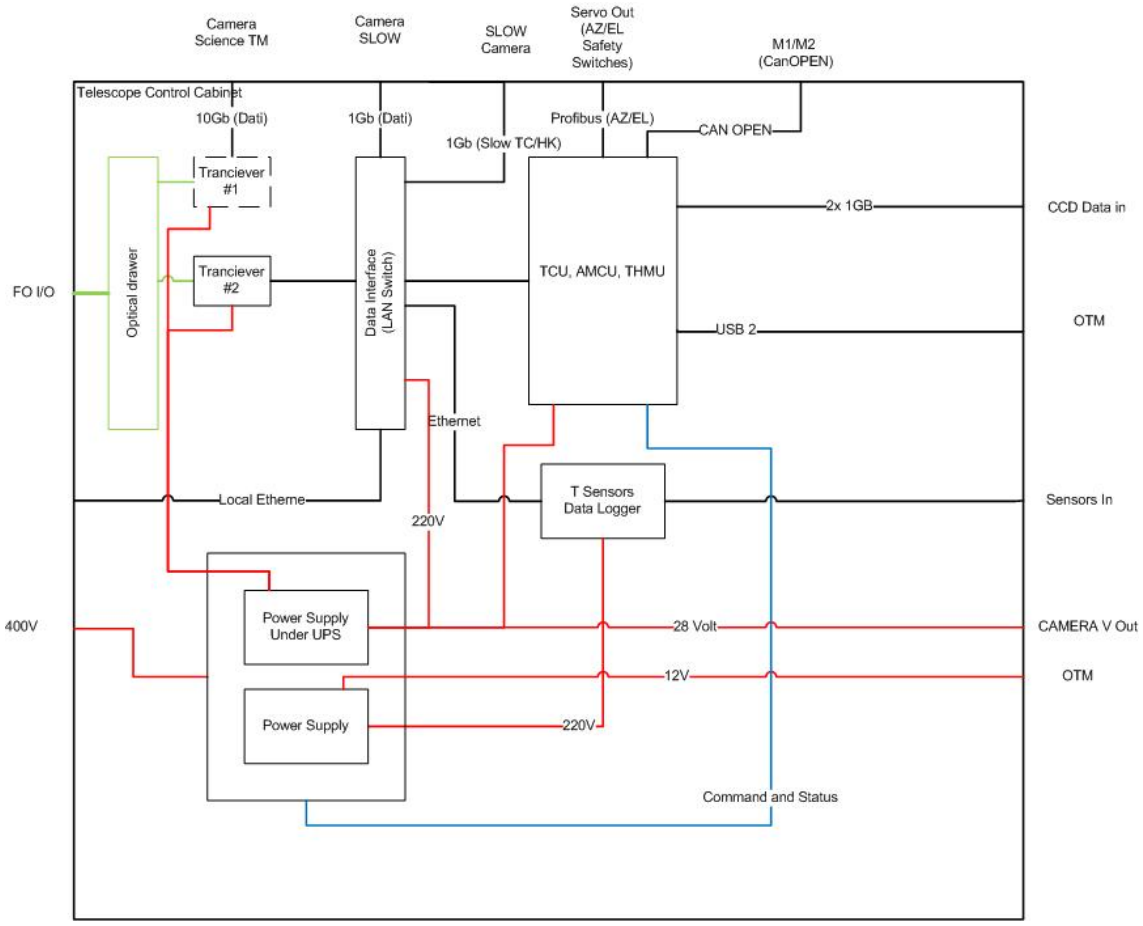

Figure 3.4: Block diagram of the ASTRI SST–2M Control Cabinet.

3.2 Structure

The telescope is presented in Figure 3.5. The major parts are:

- the mount, that is composed of the base, the tower and the fork;
- the optical support structure, composed of the primary mirror dish (with the mirrors and their supports), the mast with the central tube, the secondary mirror back-up structure (with the mirror and its supports) and the counterweights.

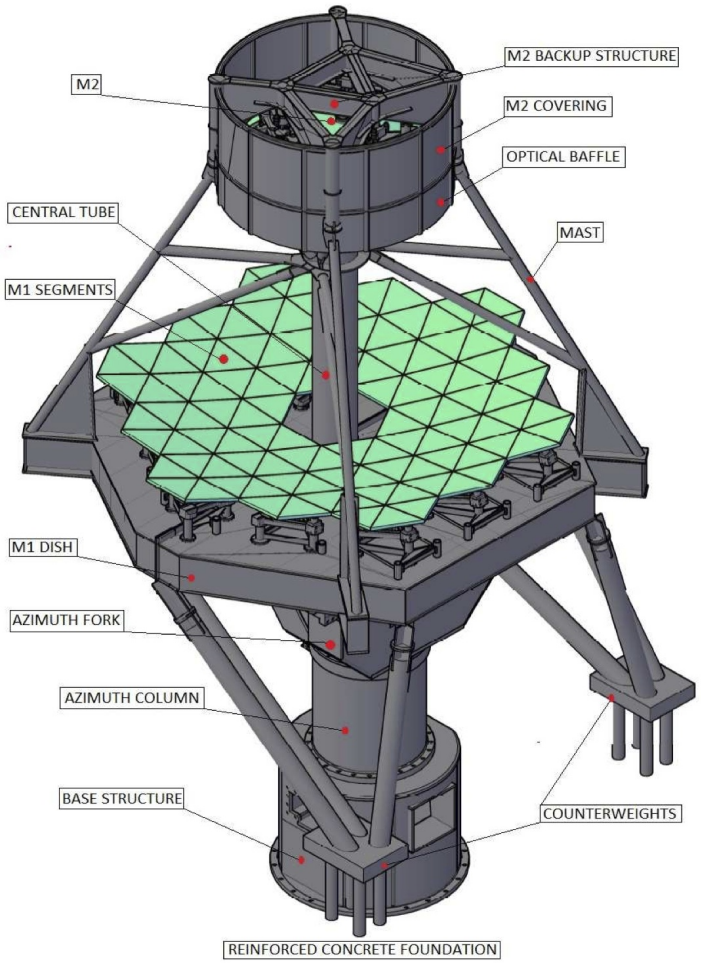

Figure 3.5: General view and nomenclature of the ASTRI telescope structure.

The telescope mount is of the alt-azimuthal type. The fork supports the telescope, hosts the elevation subsystems and connects the telescope with the column. This hosts the azimuth drive and bearing systems. The azimuth axis will admit a useful rotation range between -270° and +270° over a total run of 550°. In a similar way, the elevation axis admits a useful movement range between -5° and +95° over a total run of 110°.
The optical support structure has a thick ribbed plate to support the 18 primary mirror segments. This plate (the M1 dish) is connected with the mast and, to balance the torque due to the overhang of the telescope structure, with two long arms supporting the counterweights. The mast is a slim quadrupod with an eccentric symmetry and some radial bracings to improve the bending stiffness. A central tube links the bracings with the main legs; it improves the torsional stiffness and provides the support for the detector. Finally, on top of the mast a lattice structure forms the back-up for the secondary mirror. This also provides the connections with the alignment devices of the secondary mirrors and to the shield against stray light.
The telescope will be made in steel (different grades will be used for the different structural elements) because of a number of advantages compared to other structural materials such as aluminum or carbon fiber reinforced plastic (CFRP). They are mainly: cost with respect to CFRP, thermo-mechanical performance (stiffness vs specific weight and coefficient of thermal expansion (CTE)) with respect to aluminum. Also, manufacturing processes for steel are simpler than for aluminum ones (i.e. welding).
The dimensions of the telescope are driven by the optical design already described in the report of the past review, and in particular the relative distances between the different optical elements (primary and secondary mirrors and the focal surface). Additional parameters used for the dimensioning take into account the safety of operations around the telescope (e.g. risk of collisions with the counterweights). Meanwhile, the dimensioning of the structural components is imposed both by the tolerances required to maintain the optical performance and by the design loads.

3.2.1 The structural design

In this chapter we present the structural design of the telescope. At the time of writing, the design here presented and all the relevant documentation is at the level of an *Executive Design*. Extensive documentation has been issued, including more than 30 technical drawings and technical specifications for construction. The aim, here, is to give a global view of the telescope structure for an easy understanding of its main parts. Detailed descriptions of the work performed, parameters investigated and performance are not reported here, however they can be found in a variety of documents on the ASTRI internal repository.
The approach used in designing the telescope structures has followed the path hereafter reported. For each main part of the telescope (i.e. the mast and the M1 dish) a variety of configurations have been individually proposed, sketched and evaluated. Through a trade-off activity (typically between performance, mass, ease of production and assembling) one option is selected for advancing the design. At this stage, each part has been considered as constrained to infinitely stiff points. Once the main parts are selected a simplified global model of the entire telescope is modeled and evaluated. In order to access the integrated performance of the selected solutions, only a limited subset of loading conditions are considered. The outcomes of this phase are used to highlight the weak points of the actual design and to allow its refinement to improve the performance and meet the project requirements. Moreover, the forces acting on the mechanical components such as the bearings, the drives, the gears and other devices are evaluated to ensure the proper sizing of these components. Finally, the very detailed integrated model of the telescope is generated. This model takes into account also the performance specifications of the mechanical components, the mirrors and other

devices possibly on board the telescope (shields, scientific detector, etc.). The full set of loading cases is applied and the comprehensive behavior of the telescope is studied.
All the telescope structural components are modeled and evaluated by means of the finite element numerical approach (Finite Element Model (FEM) and Finite Element Analysis (FEA)).

The mast The configuration emerging from the trade-off study is presented in Figure 3.6. The mast is composed of an eccentric quadrupod with a radial bracing system connecting the M2 backing structure, the central tube and the quadrupod legs. This solution shows increased performance in comparison with simpler configurations. In particular, the quadrupod confers the adequate rigidity against later deformations and, being eccentric, gives enhanced performance along the elevation axis. Finally, the central tube increases the torsional stiffness. It also achieves a certain amount of saving in obstruction of off-axis rays. Moreover, the construction and assembly of the complete system seems quite simplified, for instance with respect to the use of pre-tensioned ropes. As a last but not least point, this configuration allows some freedom in adjusting the relative distances between the optical components (namely M1, M2 and the detector) in case of slight modifications of the optical design emerging from in-field tests. The thermo-elastic behavior has also been investigated in order to check the impact on the optical performance and pointing errors of the telescope. Thermal gradients have been imposed along the optical axis, the elevation and cross-elevation axes. Negligible effects are observed in the optical performance, while modest contributions to the pointing errors are seen.

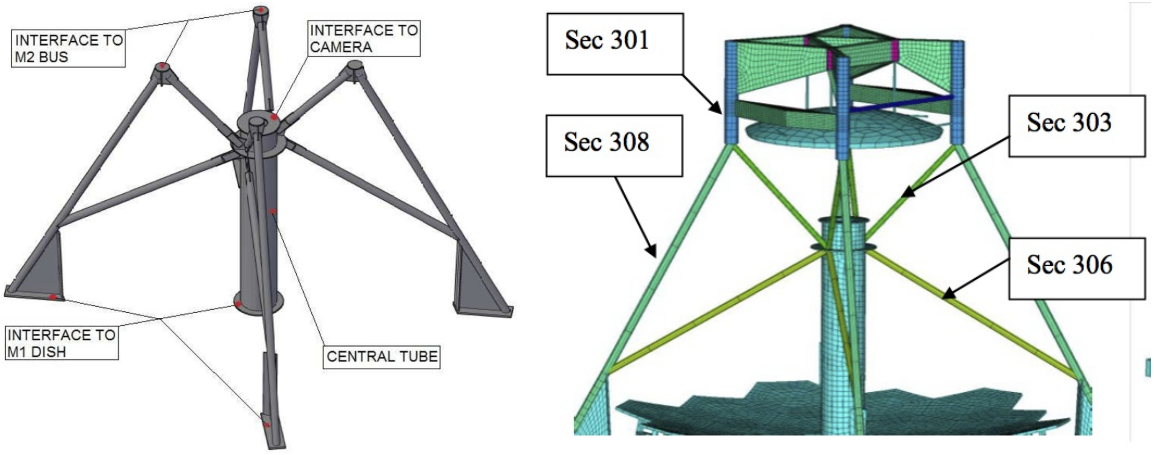

Figure 3.6: (left) Simplified 3D view of the mast. (right) FEM with indications of the different beams.

The M1 dish The dish has a T-ribbed plate structure with a box section at the elevation axis in order to increase the torsional stiffness. It is composed of two asymmetric halves (the dish exceeds the dimensions of common freight containers) connected along the middle plane by means of plugs. The connection line is orthogonal to the elevation plane. As regards the rear side of the dish, the upper half hosts the connection with the linear actuator of the elevation drive system, while the lower half has the interfaces with the two arms of the fork where the elevation axis lies. The connections with each mirror segment are made on the front

side of the dish. Given the flat geometry of the dish, mirror segment spacers provide the gross position to the mirrors. On top of these, triangular frames, each one having three separated contact points, individually support the mirrors through actuators. This solution seems to be considerably stiffer with respect to a solution with a single leg connection. Also connected to the dish are the counterweight supporting arms. The mast quadrupod subsystem is connected with the dish thorough cantilevered beams; this solution has been adopted in order to save mass while keeping the necessary rigidity. Figure 3.7 shows the 3D views of the dish and mirror support systems (left and right panels) and the FEM (right panel).

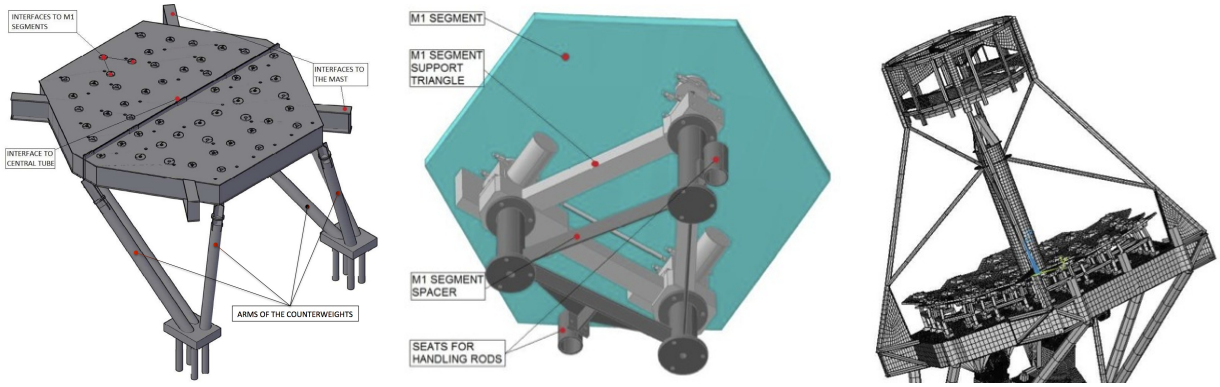

Figure 3.7: Simplified 3D view of the (left) M1 dish and (center) mirror segments support. (right) Combined FEM of the M1 dish, the mast and the M2 Back-Up structures.

The M2 Backing Structure The M2 Backing Structure consists of an arrangement of tapered welded I-Beams and a central torsionally-stiff triangular prism. The tapered beams connect the four flanged tubes bolted to the mast, while the triangular prism supports the M2 axial load-spreaders. Moreover, two box sections provide the connection between the lateral support systems of the secondary mirror and the mast. These box sections also help to increase mast stiffness in the plane of gravity loads. The proposed layout allows a complete decoupling of the lateral and axial M2 behaviors enhancing telescope pointing performance and reducing the mass of these structures. Figure 3.8 shows this element.

The global model of the telescope The selected solutions presented above have been assembled together to form the global model of the telescope. The FEM of the entire telescope system has been generated, see Figure 3.9. Some engineering solutions under design are also visible. It comprises all the telescope structural parts and components such as the base, the column, the fork, the primary mirror ensemble (dish, mirror segment support assemblies), the mast, the secondary mirror ensemble (backing structure, monolithic mirror, M2 load-spreader assembly and shields) and the counterweights. The model considers also the bearings and drive system's mechanical properties. The computational dimension of the model is about 700 kDOFs (Degrees Of Freedom). A variety of load cases (i.e. gravity, winds, temperature bulks and gradients, snow, ice and OBE/MLE earthquakes) have been applied together with load combinations in accordance with the relevant norms (Eurocodes EN1990 and EN1991). These have been adopted to perform the Ultimate Limit State (ULS) checks.

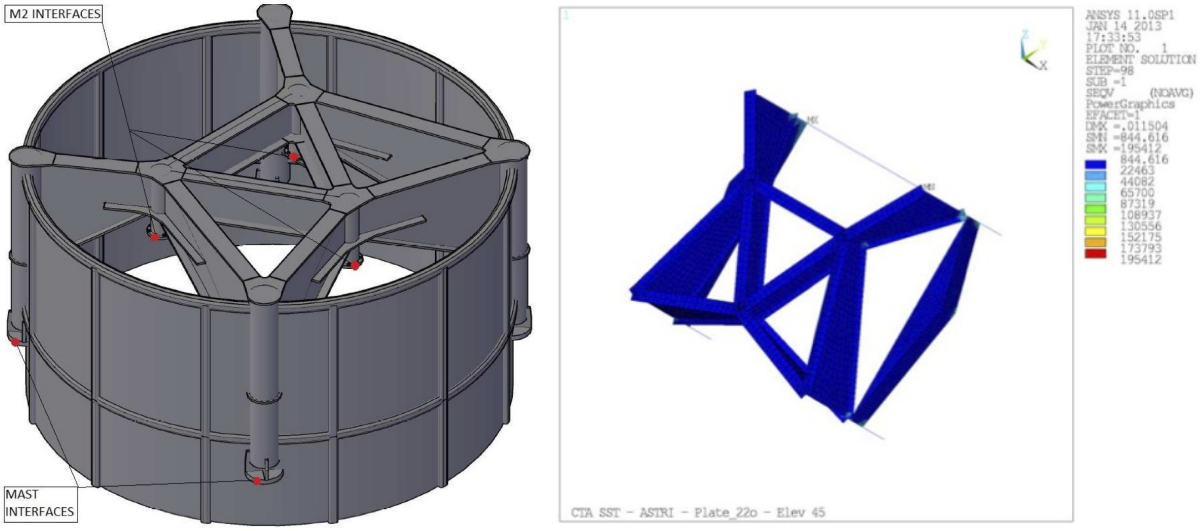

Figure 3.8: (left) Simplified 3D view of the M2 Back-Up Structure and (right) Equivalent Von Mises Stress retrieved by FEA. Large scale maximum does not exceed 90 MPa.

Serviceability Limit State (SLS) checks are not derived from the norms (i.e. the telescope is not a building in terms of performance) but the evaluation of the telescope performance has been also accessed (by means of a joint effort of FEA and ray-tracing). Results concerning vignetting and optical Point Spread Function (PSF) degradation are provided in Figure 3.10. Pointing performance have been related to flexures of the telescope structures and mis-alignments/mis-orientations of the optical devices. Results are reported in a dedicated paragraph.

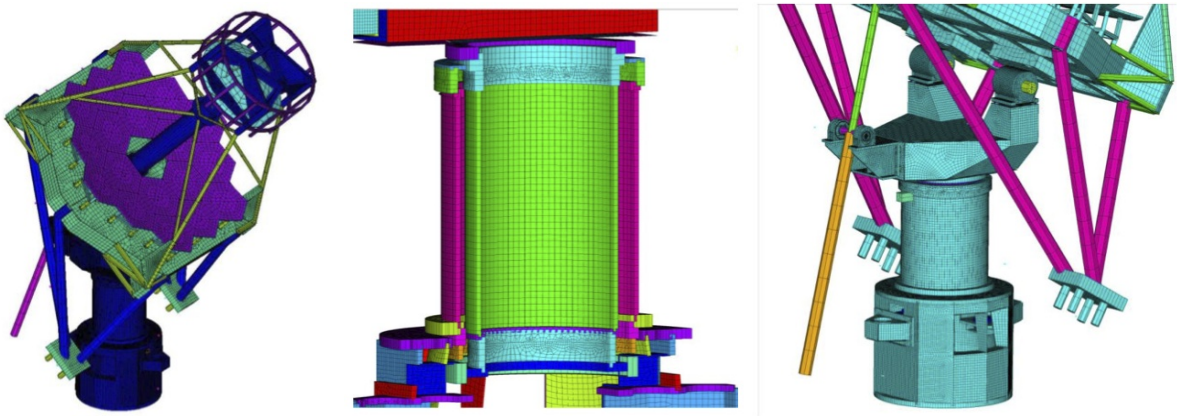

Figure 3.9: FEM of the entire telescope system and details.

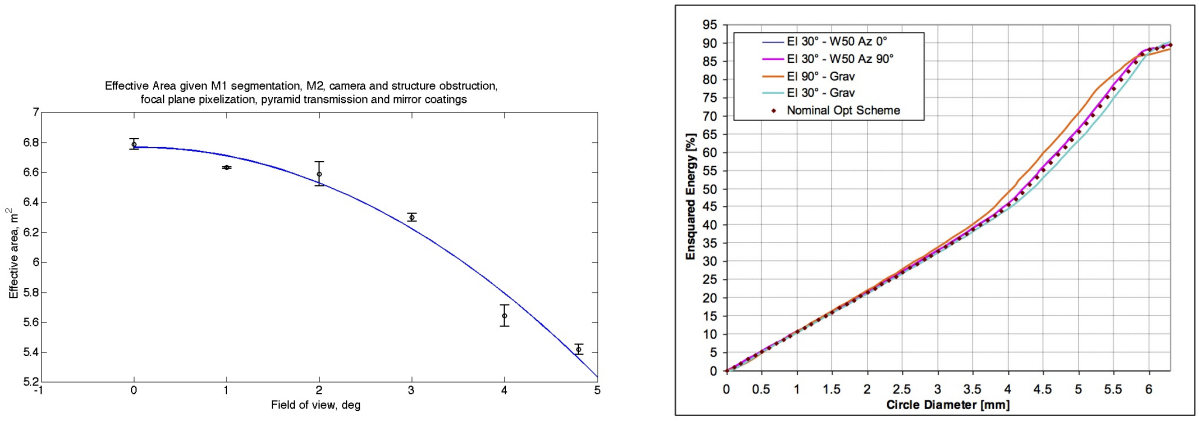

Figure 3.10: (left) Evaluation of the effective area of the ASTRI telescope. The obstruction of the structures accounts to about 14 %. (right) Evaluation of the PSF degradation.

The evaluation of the eigenfrequencies of the telescope gives a nearly constant behavior with respect to the azimuthal position and shows values well above the project specifications. In the worst case scenario (i.e. horizon pointing), the first two modes are higher than 4 Hz and are respectively the oscillations around the azimuth and elevation axes. As a reference, we report in Figure 3.11 some modes at different pointings.

3D CAD views have been generated, while only detailed 2D CAD technical drawings have been released for construction. Some drawings of the telescope are presented for reference in Figure 3.12.

The mass budget The mass budget has been computed from the FEM implemented to evaluate the telescope, some contingency is also provided to take into account for additional unmodelled masses (e.g. bolts, small interfaces etc.). This is reported in Table 12. A detailed mass budget of the electro-mechanical items is also provided.

3.2.2 The electro-mechanical components

Three major parts form the pillar: the base, the tower and the fork. This has the main purpose of supporting and moving the telescope main structure (i.e. the M1 dish, the mast and the M2 dish) with the required velocity, acceleration and position accuracy, under the defined loads and environmental conditions.
Initially, an innovative solution for the mounting system of the telescope was been proposed and studied: the cardanic mount. This concept was based on the use of a common drive and bearing system to achieve the full-sky orientation of the telescope structure. Unfortunately, a major limitation was found in the minimum eigenfrequency of the telescope. It dropped to a very low value in when the telscope was horizontal, making the safety of the structure a crucial point.
Therefore, the classical alt-azimuth mounting has been preferred. The sketch in Figure 3.13 shows the solution implemented, it is described in the following.

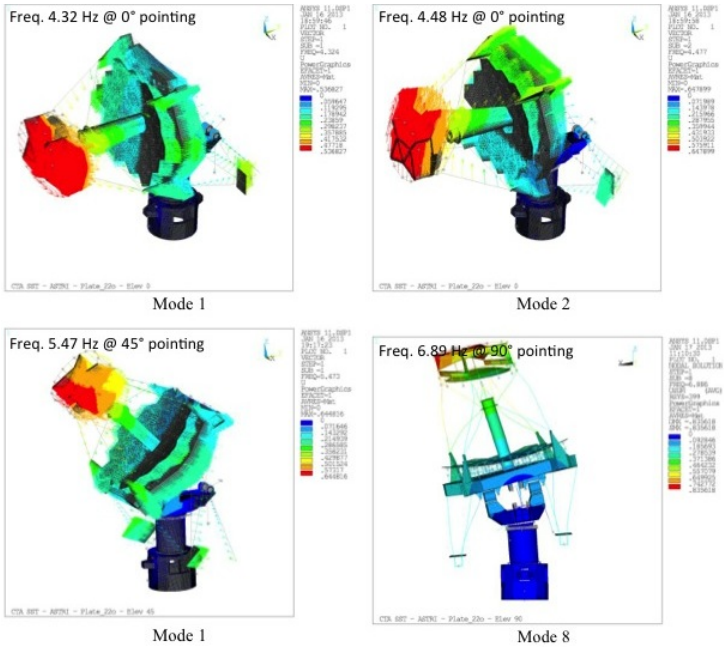

Figure 3.11: Evaluation of the eigenfrequencies of the ASTRI telescope.

The Azimuth components The subsystem for the azimuth movement is hosted by the base and the tower where, respectively, are located the drive and the bearing systems. The base is a large box fixed on its lower part to the foundation; it hosts the complete drive system for the azimuth axis as shown in Figure 3.14. It comproses the following devices. There are two drive chains in a master-slave configuration. Each one is composed of one commercial epicycloid gearbox and one suitable designed gearbox. The pinions link the gearboxes to brushless servomotors. In this solution, the two motors can work with a preloaded differential torque that gives a number of advantages. Among them are: higher torque and stiffness capability due to the sum of the two gears chains; less preloading torque between the two pinions; minimized backlash between the pinions and rim gear in all the positioning operations. Moreover, their maintenance is very simple because thay are easily accessible. For safety reasons, both motors are endowed with a braking system that locks the axis without power supply. In addition, one of the two drive chains is equipped with a couple of emergency driving systems: a toothed clutch which can be engaged by powering a 24 V DC motor and an irreversible gearbox; and a shaft for the manual drive, accessible by demounting a safety cover endowed with an electro-mechanical switch. Both the emergency systems are decoupled in operational conditions.

The tower is composed of two concentric large tubes at the ends of which two ball bearings are located (see Figure 3.15). An adjustable spacer axially preloads them; this has the purpose of avoiding axial backlash and increasing the axial stiffness. The lower bearing and the external tube support the weight of the entire telescope. Meanwhile the inner tube (acting as the azimuth shaft) and the upper bearing transfer the azimuth movement to the telescope. The positioning is retrieved by means of an absolute angular transducer placed at the lower end of the azimuth shaft, close to the drive system. The full rotation stroke of the azimuth

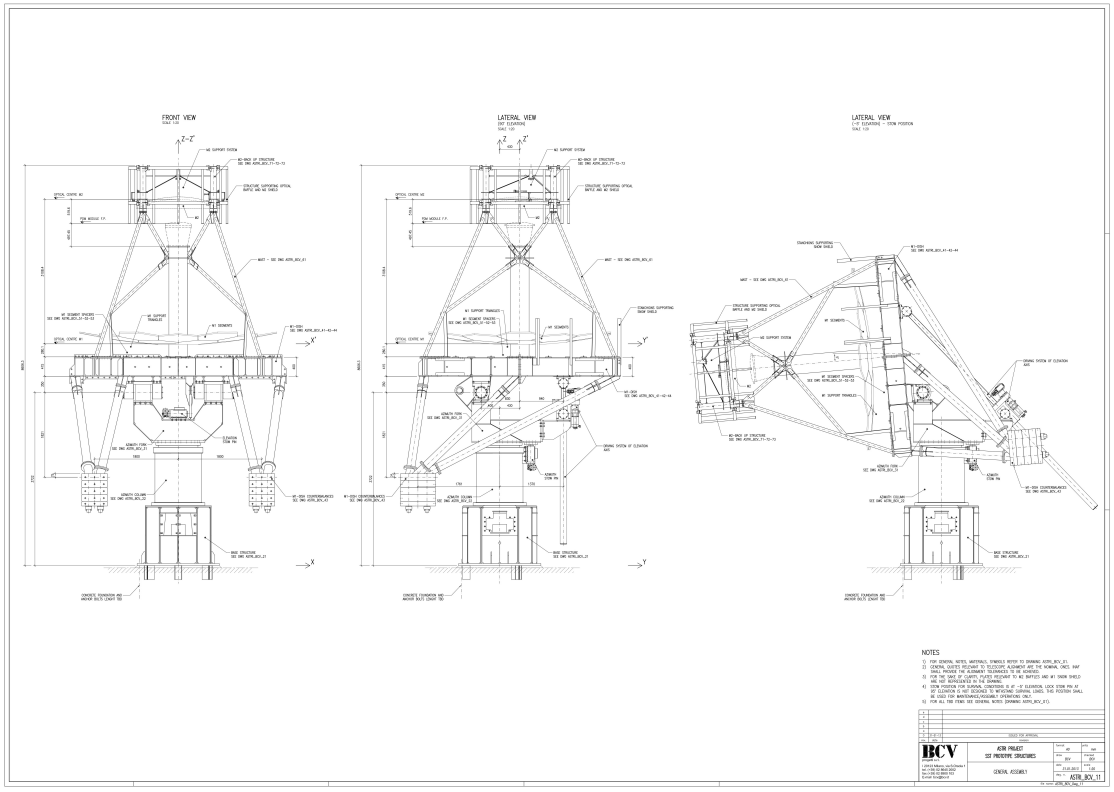

Figure 3.12: Executive technical drawing of the complete ASTRI telescope assembly.

axis reaches 540°. This range is software limited by reading the azimuth encoder. However, since the stroke allows more than one rotation, a special system is designed to recover the information about the direction of the motion. There is a roller lever yoke that constantly maintains the contact with the flange of the bottom bearing. The flange is equipped with special references that allow the main rotation to e distinguished from the second one, and therefore to commutate the two electromechanical limit switches of the main direction with the two of the opposite direction.

Finally, an electromechanical stow pin is foreseen at the parking position. This device mainly consists of a pin axially guided into a cylindrical bush; it is moved by a motor-driven screw with an irreversible gearbox. Two electro switches detect the stroke of the pin. It is designed by taking into account the maximum loads and torques on the axis acting during the survival conditions. In this way, it will allow the locking of the telescope in position up to the worst load conditions.

Description	**Mass** [kg]	**Cont.** [%]
Base	2.630	2
Column	2.390	2
Fork	1.524	2
Counterweights	4.500	–
Struct. for counterw.	565	20
M1 dish	4.331	10
M2 Back-Up Structure	195	5
Optical devices	488	–
Mirrors supports	1.450	5
Mast and central tube	617	20
Bearing supports	416	2
Electro-mech. devices	2.027	–
Baffle and shields	376	–
Total	21.509	–

Description	**Nr.**	**Unit mass** [kg]
Upper azimuth bearings	1	130
Lower azimuth bearings	1	110
Azimuth Motors and gears	2	101
Emergency Azimuth Motors and gears	1	145
Elevation Bearings	8	5,25
Axial actuator gearbox	1	49
Axial actuator emergency motor	1	25
Axial actuator bearings	8	3,65
M1 Segment Fixed point	18	5,5
M2 Axial Actuators	3	34
M2 Load spreader structure	3	25
M2 Lateral Restrains	6	2
Elevation Stow-Pin	1	170
Azimuth Stow-Pin	1	140
Power cabinets	2	250
Supporting structure	2	100
Total	–	2030

Table 12: Mass budget of the telescope structures and details on the electro-mechanical devices.

The Elevation components The subsystem for the elevation movement is mounted on the fork. The main components are the bearings, the drive and the locking systems. The motion is accomplished by means of a linear actuator. It is composed of a fixed preloaded ball screw (the shaft), a rotating preloaded nut, the gearboxes and the motor. The ball screw is moved up and down by the rotating nut, which is driven by the motorized gearbox. There are also a couple of joints: one is screwed to the M1 dish and the other to the fork. This last one also supports the body of the actuator, the gearbox and the motor. Both joints are realized by means of preloaded tapered roller bearings and have their axes parallel to the elevation axis. In the same way in which the azimuth axis is designed, for safety reasons, the motor is endowed with a braking system that locks the axis without power supply. In addition, a couple of emergency drive systems are also available: a toothed clutch which be engaged by powering a 24 V DC motor and an irreversible gearbox; and a shaft for the manual drive, which is accessible by demounting a safety cover endowed with an electro switch. Both the emergency systems are decoupled in operational conditions. The left panel of Figure 3.16 shows the drive system described above.

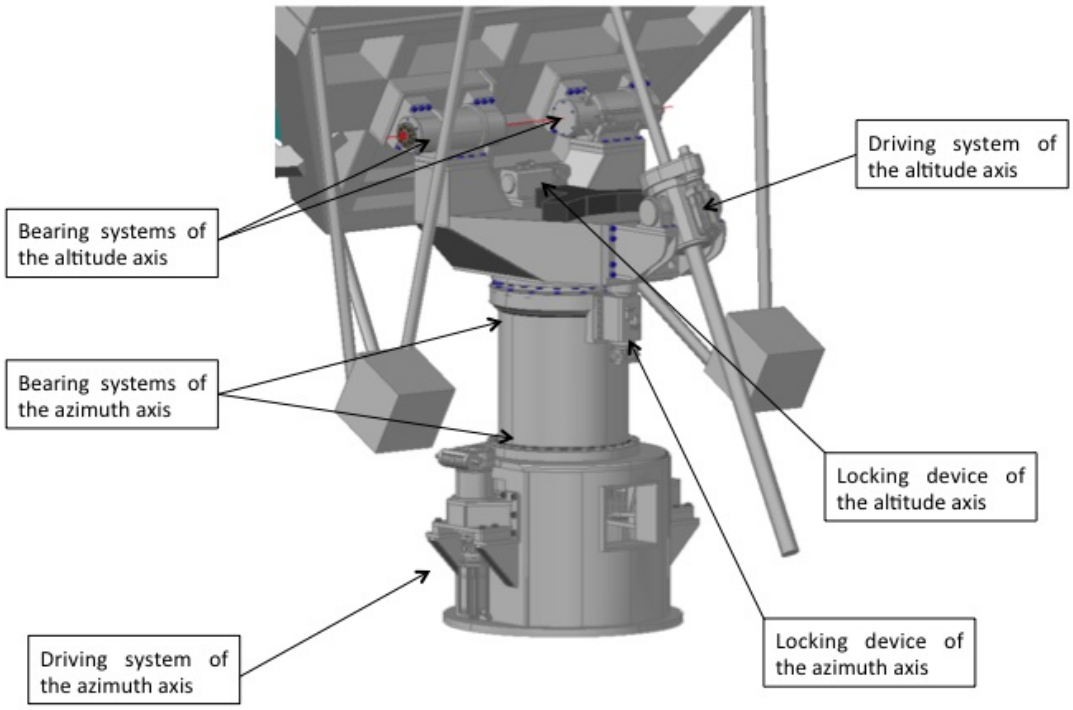

Figure 3.13: General description of the ASTRI telescope's electro-mechanical components.

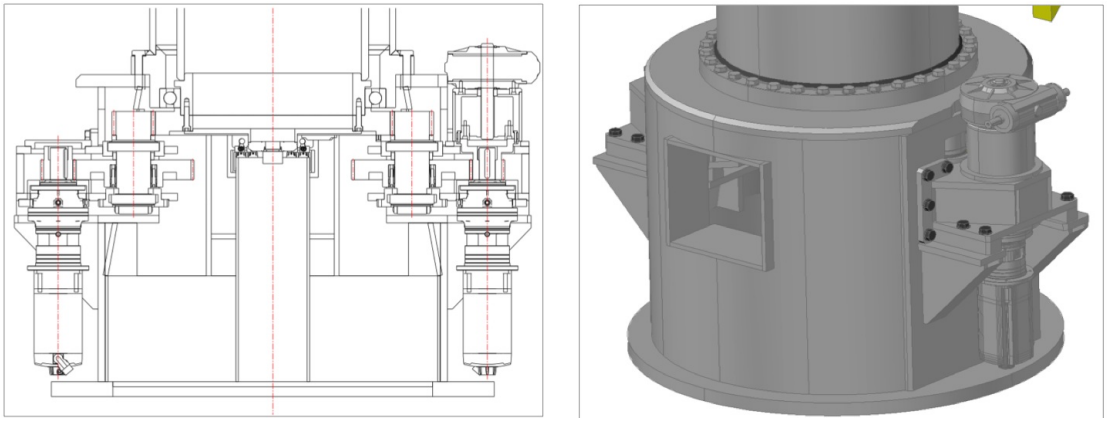

Figure 3.14: 2 (left) Cross-section view of the driving system of the azimuth axis. (right) 3D CAD view of the telescope's base.

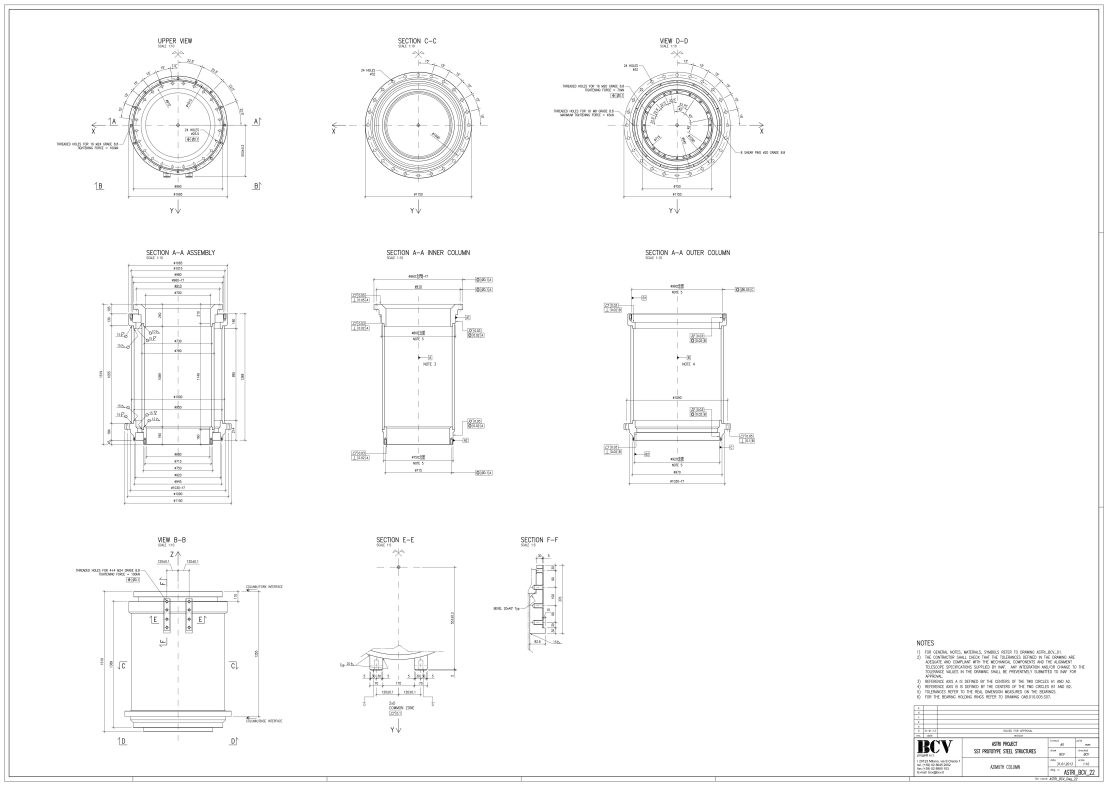

Figure 3.15: Executive technical drawing of the azimuth column.

The elevation axis lies on the arms of the fork. The shaft is divided into two parts at the end of the arms where two identical bearing systems are located. Each one connects and supports the telescope through the M1 dish. Each bearing unit (see Figure 3.17) is composed of eight tapered roller bearings; they are axially preloaded by means of suitable threaded bushes in order to minimize the backlash. A rotating support is screwed to the back of the M1 dish. One of the two bearing units hosts the absolute angular encoder to retrieve the positioning. The elevation axis admits a total stroke between -5° up to +95°; this range is software limited by reading the elevation encoder. Additional angular motion is permitted for safety reasons with two electromechanical switches that limit the run in case of software failure. This solution is sketched in the right panel of Figure 3.16. Bumpers are also envisaged. In a manner similar to the azimuth axis, an electromechanical stow pin is foreseen. This device will allow the locking of the telescope in two positions: horizontal (the parking position) and zenith pointing.

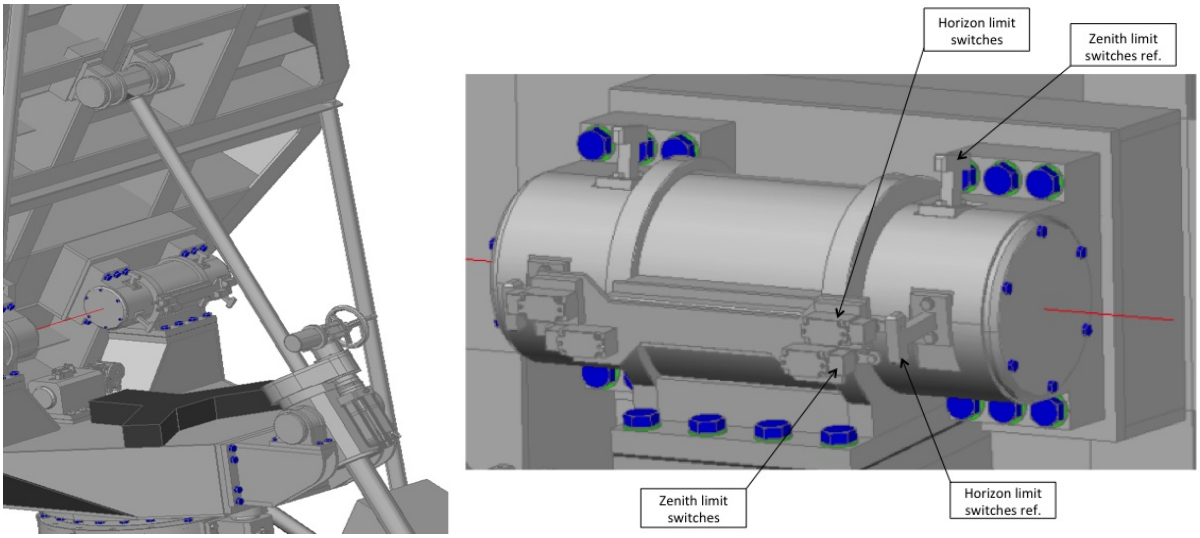

Figure 3.16: (left) 3D CAD view of the elevation components: bearings, drive and locking devices. (right) close-up view of the limit switches for the elevation axis.

3.3 Mirrors

3.3.1 The Primary mirror: M1

The M1 mirror is composed of 18 panels distributed on three concentric rings (see Figure 3.18 left panel). Since the optical profile follows an aspherical function and each ring has a different radial distance from the telescope vertex, the design of the panels is different for each of the three cases and consequently three different mirror types are required to produce the primary. Moreover, each ring has a distinct encircled energy function (see Figure 3.18 right panel). Hence the optical quality of each panel has to be verified using the encircled energy function appropriate to the ring to which it belongs.

Technology The mirror segments are manufactured by means of a modified version of the cold slumping process where a thin sheet of glass is formed at room temperature over a mould. This has been developed by Media Lario Technologies company under the scientific supervision of INAF–OAB, starting from the developments for the ALMA panels. Subsequently, it has been successfully applied in the MAGIC–II experiment. In the present case, a further modification of the technology is under development; in particular by preforming the glass trough a thermal process. This step is mandatory to allow the realization of very curved mirrors such as those for ASTRI (or the SST dual-mirror in general). The technique proposed is time and cost saving when tessellated collectors have to be manufactured because it is based on the replica concept and the mould can be reused to produce many mirror's without suffering evident surface deterioration.
In the following, a brief description of the technology is presented with corresponding images collected during

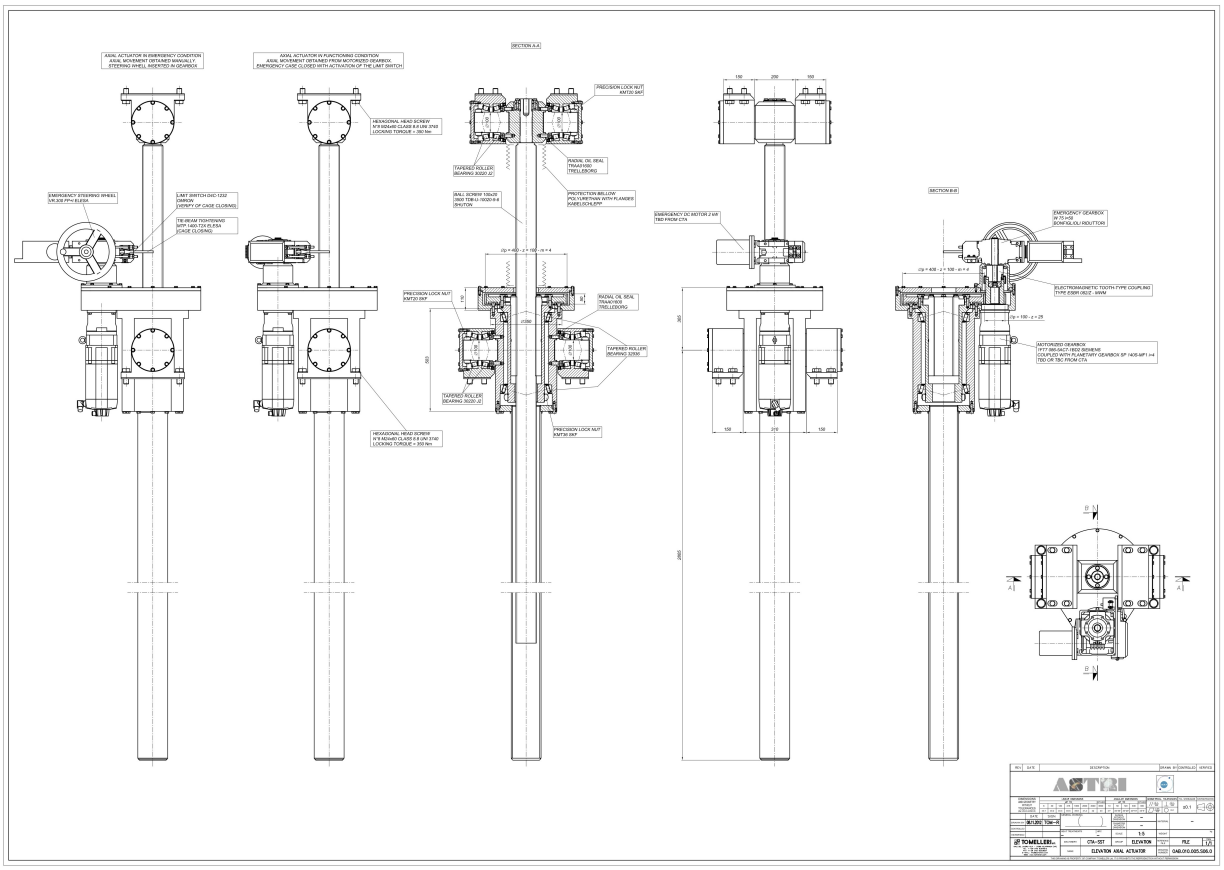

Figure 3.17: Executive technical drawing of the linear actuator and its bearings.

the assembly of a prototype panel (see Figure 3.19):

- An Aluminum mould is machined until its shape reproduces the negative of the theoretical mirror design within the tolerances. For ASTRI, three different moulds were produced, one for each ring.
- A pair of thin glass foils, typically 2 mm thick, and one sheet of aluminum honeycomb (the mirror segment will have a sandwich-like structure) are prepared by cutting them out from larger blanks. The cutting can easily be done by using shape templates and cutters. Glass tiles are then carefully cleaned.
- The first glass foil is positioned, bent and fixed over the mould; then it is made to adhere by vacuum suction (see Figure 3.19). In this way the shape of the mould is replicated; afterwards the sandwich is assembled. The connection between the honeycomb sheet and the glass foils is achieved by bonding the three parts together with epoxy resin. Photographic images of the sandwich preparation are shown in Figure 3.19.

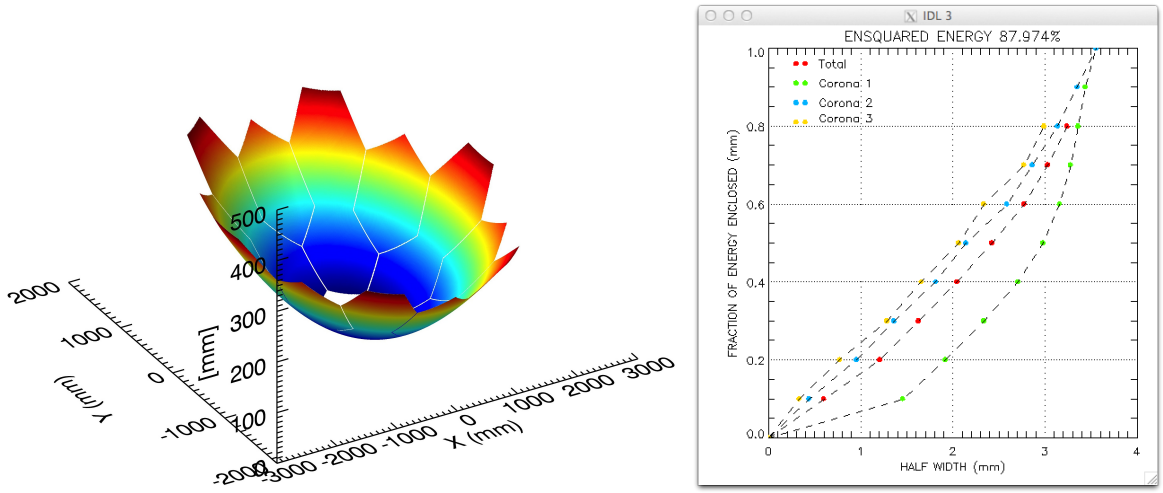

Figure 3.18: (left) Sketch of the whole ASTRI primary mirror. M1 is composed of 18 panels distributed on three concentric rings. (right) Encircled energy functions of the whole M1 (red) and of the single rings (C1: green; C2: Blue; C3: yellow).

- The resin is made to polymerize with the proper curing cycle. Temperatures and timing play a role in the resulting shape of the mirror, as well as the amount of glue (see Figure 3.19).
- Once the polymerization has taken place, the vacuum suction is stopped and the sandwich is carefully released from the mould (see Figure 3.19).
- After a deep cleaning of the front glass, the reflecting coating is deposited. Methods and layers are chosen in accordance with the final use of the mirror. It is also worth mentioning that, since the sandwich is kept together by the glue, attention must be paid to the heating caused by the coating process. Details of the specific coating are presented below.
- Finally, the interfaces with the supporting structure are fixed and the edges of the mirror are sealed. This solution also ensures high rigidity and mechanical protection of the mirror edges/corners.

Results from prototypes Some prototype panels of the third ring were already assembled and tested at INAF–OAB, the moulds necessary for the other two rings are now under construction. Moreover, to guarantee the final panel's optical quality, step by step verification has been implemented. The contribution to the optical quality degradation introduced by each different production phase is evaluated with respect to the optical performance of the theoretical design and taken into account. In particular we will go through the following steps:
– Mold Shape Error Evaluation.
– Glass Sheet Shape Error Evaluation.
– Mirror Segment Shape Error Evaluation.
– Coating.

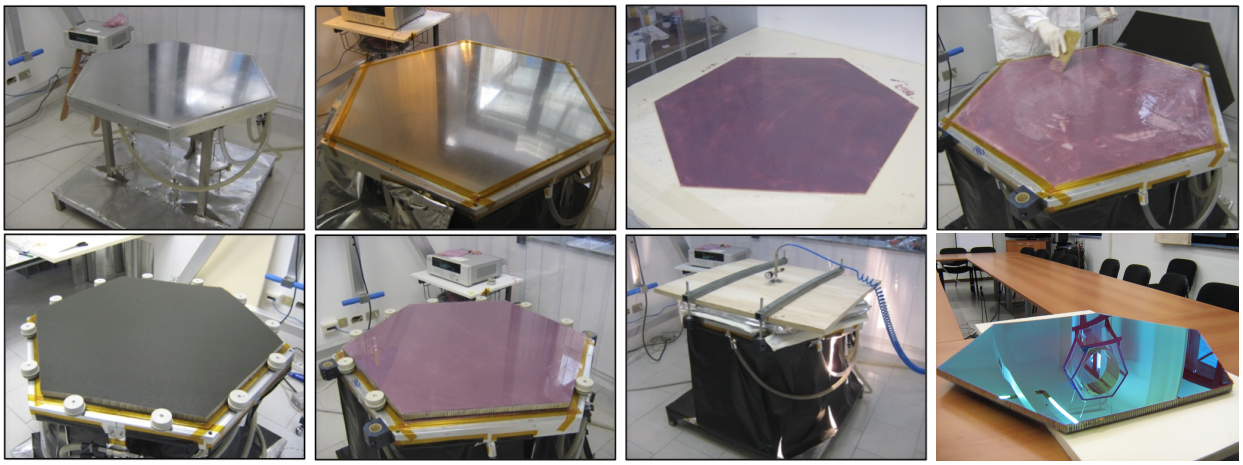

Figure 3.19: Main steps of the panels manufacturing. From top-left, clockwise: mold realization; front glass is made to adhere by vacuum suction to the mold; the epoxy resin structural adhesive is spread on the glass; the Aluminum honeycomb is positioned and the back glass foil is added on the top. The resin is made polymerize with the proper curing cycle and sandwich is finally released and coated.

Mould Shape Error Evaluation The mould mechanical drawing was obtained from the mirror segment optical design. After machining, the mould shape quality was evaluated using a 3D coordinate measuring machine (Zeiss UPMC 1200) and analyzed to find the shape error. It is characterized, with respect to the nominal profile ($r_{fix} = r_{des} = 8223$ mm), by a standard deviation of 27 μm (see Figure 3.20 left panel). Fitting also the best radius of curvature, we got a standard deviation of 21 μm with $r_{var} = 8272$ mm. It is useful to take into account both these shape error evaluations because minor errors in the radius of curvature can be corrected through adaptation of the distances between the primary and secondary mirrors. The obtained shape errors were used to simulate the optical path of the incoming photons by means of ray tracing able to take into account the measured mesh. The resulting focal spots are visible in Figure 3.20 (central panel) and the corresponding ensquared energy functions are reported in the right panel.

Glass Sheet Shape Error Evaluation About ten glass tiles were produced by a thermal forming process; they are 2 mm thick glass sheets shaped to the profile required by the third ring. The sheets were measured my means of the metrological equipment available at Erlangen Centre for Astrophysics (ECAP). With these measurements, we can verify the presence of local shape errors at medium/high frequencies that can be only partially corrected by the cold slumping process (see Figure 3.21). Moreover, a statistics on the glass shape errors can be used to improve the manufacturing process, and to mitigate the observed errors in the radius of curvature. The values are reported in Table 13 .

Mirror Segment Shape Error Evaluation The evaluation of the mirror segments optical quality should be verified before the panels are mouted on the telescope. The testing procedure adopted to verify the mirrors conformity is organized in two steps:
– A first step is an *optical test* used to discriminate the panels with macroscopic shape errors.
– The second step is a *quantitative analysis* obtained by measuring the panel's shape and ray-tracing the optical system using the acquired data.

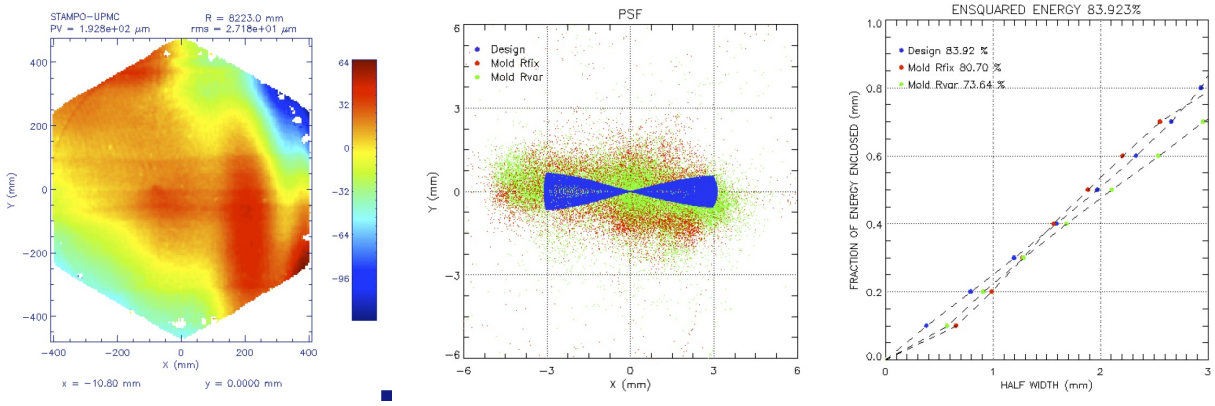

Figure 3.20: (left) Shape error of the mold for the third corona at the nominal radius of curvature. (center) Focal spots obtained simulating the reflection on a mirror with the same shape error measured on the mold. (right) Corresponding encircled energy function.

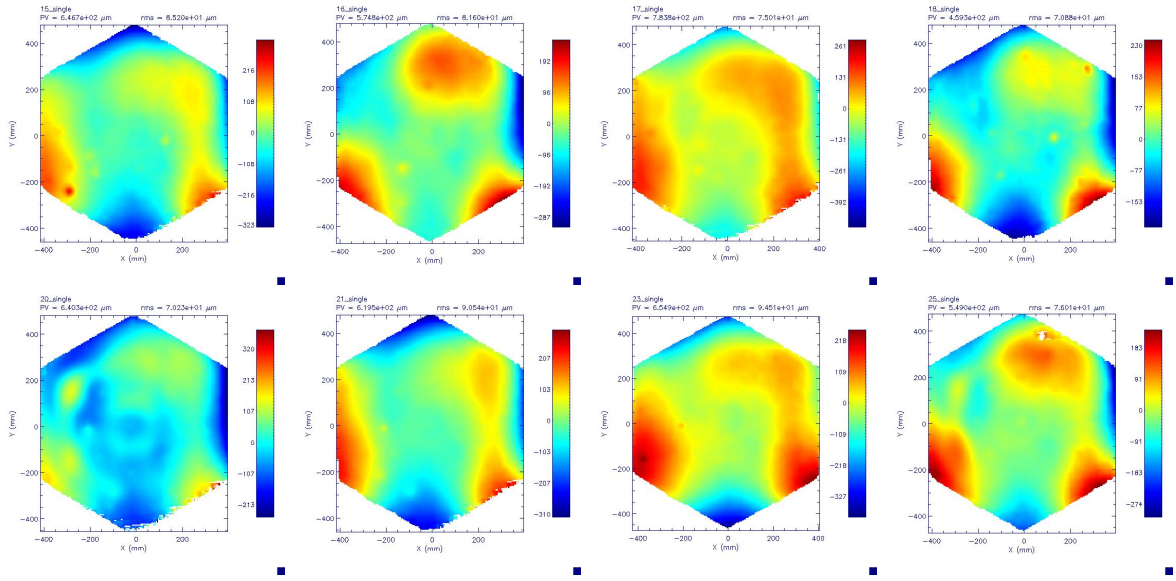

Figure 3.21: Local shape error measured at ECAP on the thermally formed glass. The displayed residuals are obtained after the correction for the gravity effect and considering a variable radius of curvature.

Optical test: the optical test is performed by illuminating the panel and comparing the focal spot produced at the panel focal length after a single reflection with the focal spot that a perfect panel is expected to produce in the same configuration. Since the total M1 diameter is comparable to its radius of curvature, the spherical aberrations are strong. The focal distance considered for the optical test and the focal spot morphology is different for each ring. As an example, we report the case of the third ring. Mirror segments were tested

	#1	#2	#3	#4	#5	#6	#7	#8	#9	#10
rms @ r_{fix} **[μm]**	283	265	290	265	278	302	315	198	250	145
rms @ r_{var} **[μm]**	85	81	75	71	70	90	89	94	76	89
best r r_{var} **[mm]**	8854	8813	8884	8823	8853	8908	8949	8618	8780	8479

Table 13: Values of the total shape error standard deviation, shape error obtained for variable radius of curvature and of the relative radius of curvature.

in this configuration (see Figure 3.22 top-left panel). The image is then compared to that generated by the theoretical optical design: the focal spot has a noticeable vertex that can be easily searched for by moving along the optical axis (top-right panel). The result obtained for the qualitative optical test is visible in the bottom panels, where it is evident how this simple qualitative test is efficient in the discrimination of mirrors that are within specification from those that are not (bottom).

Quantitative analysis: the mirror segment shape is measured using a 3D coordinate measuring machine and the mesh analyzed to find the shape error. The mirror segment shows the shape error characterized, with respect to the nominal profile ($r_{fix} = r_{des} = 8223$ mm), by a standard deviation of 23 μm. Comparing to a fit of the best radius of curvature gives a standard deviation of 20 μm with $r_{var} = 8255$ mm. Using ray-tracing, we have simulated the optical path of the incoming photons; the focal spot and the corresponding ensquared energy are reported in Figure 3.23. To validate the qualitative optical test method and the ray-tracing algorithm we compared the images acquired with the optical test and the focal spots predicted by the code at different focal positions. The correspondence is good (see Figure 3.23).

Coating Two different solutions are under study. In particular, as a baseline a coating following the well established and tested recipe in operation on MAGIC–II since summer 2008. This is based on Al + SiO_2; this has been deposited on test samples and onto a prototype full–size panel. The test panel is now undergoing environmental and performance testing. As an alternative, and more innovative solution, a fully dielectric multi–layer coating embodying an interference wavelength filter is being developed and tested. Early deposition attempts involving dioxide layers (SiO_2 + TiO_2) have provided reflectivity profiles cutting sharply wavelengths above $650 - 700$ nm (depending on the specific recipe, see Figure 3.24). This property reduces considerably (~ 5 times) the Night Sky Background (NSB) contamination produced by the intense molecular bands emitting in the $600 - 900$ nm waveband where Silicon Photo-Multipliers (SiPMs) maintain a small but non-negligible sensitivity. In spite of the technical difficulty of depositing homogeneous layers onto large (~ 1 m) surfaces, the segments of the primary mirror are the most suitable optical part for implementing a filter due to the small range of angle of incidence (AoI) involved ($0° - 10°$). Further tests involving TiO_2/Ta_2O_5 admixtures as high–index material are ongoing, with the aim of enhancing the performance below 400 nm where TiO_2 introduces significant absorption. In Figure 3.24 the reflectivity curve of the first dielectric coating prototypes measured on test glass samples is displayed. The performance is already close to the CTA requirement ($R > 83$ % in the $300 - 500$ nm band). Also, durability tests (thermal cycling, salt mist) on samples have been performed, while outdoor testing on full-scale prototype panels has started recently.

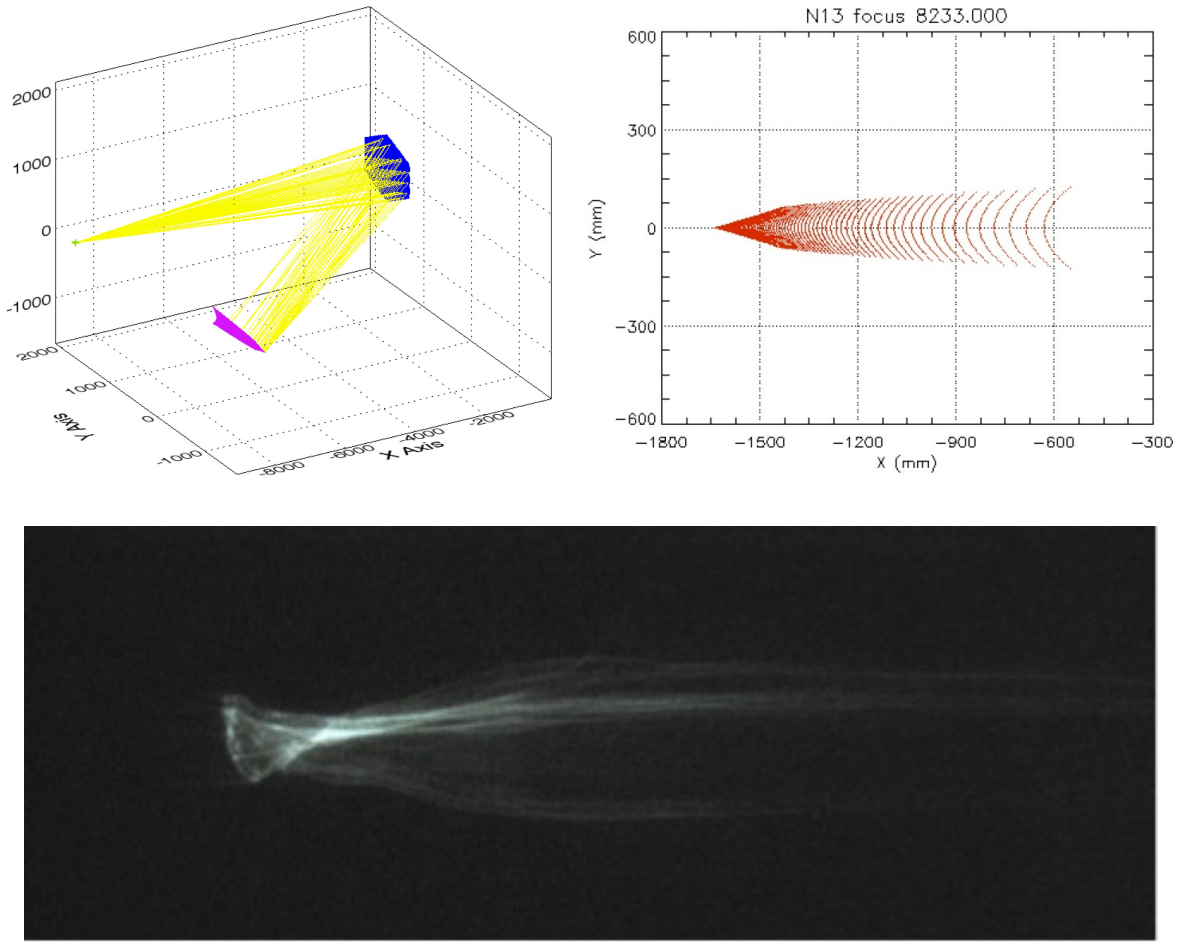

Figure 3.22: (Top-left) Optical test configuration adopted. The point-like source (green point) is at about 11 m from the panel (blue) and the focal spot (magenta) is acquired at about 8 m. (Top-right) Focal spot expected for a panel with theoretical optical design mounted in the nominal position. (Bottom) Focal spot obtained for a not compliant mirror.

Support and alignment system The M1 segment support triangles have been designed to support and actively align (tilts around x and y axes) the primary mirror segments in order to maintain the PSF specification of the telescope. During pointing and tracking operations, flexures and misalignments due to gravity, wind and temperature are well inside PSF requirements and they can in principle only affect pointing tolerances. For this reason, the actuation of mirrors is performed in open loop mode during scientific acquisition. Each segment of the primary mirror is supported in an isostatic way by one fixed support (axial fixed point), two active supports (axial actuators) placed at suitable distances, and a tangential rod, giving the required six constraints to the segment. In this way, it is possible to tune the two direction tilts of the panel, moving the optical axis in the desired direction. The left panel in Figure 3.25 shows this system.

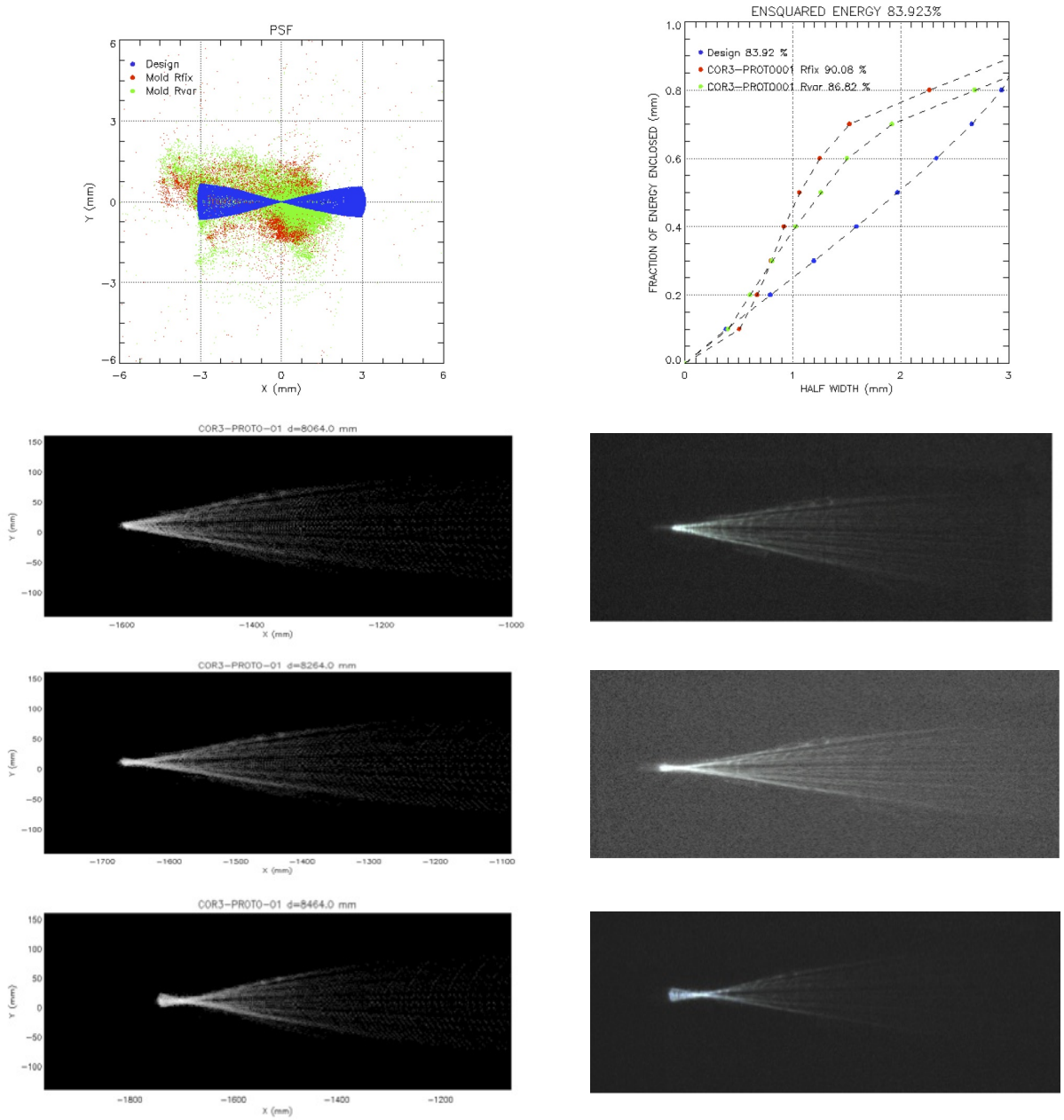

Figure 3.23: (Top-left) Focal spot obtained simulating the reflection on a prototype mirror. (Top-right) Corresponding encircled energy function. (Bottom panels - left column) PSF obtained by means of the ray-tracing code taking into account the measured shape of the mirror. (Bottom panels - right column) Images acquired during the optical tests. Images and ray-tracing were done for different focal distances.

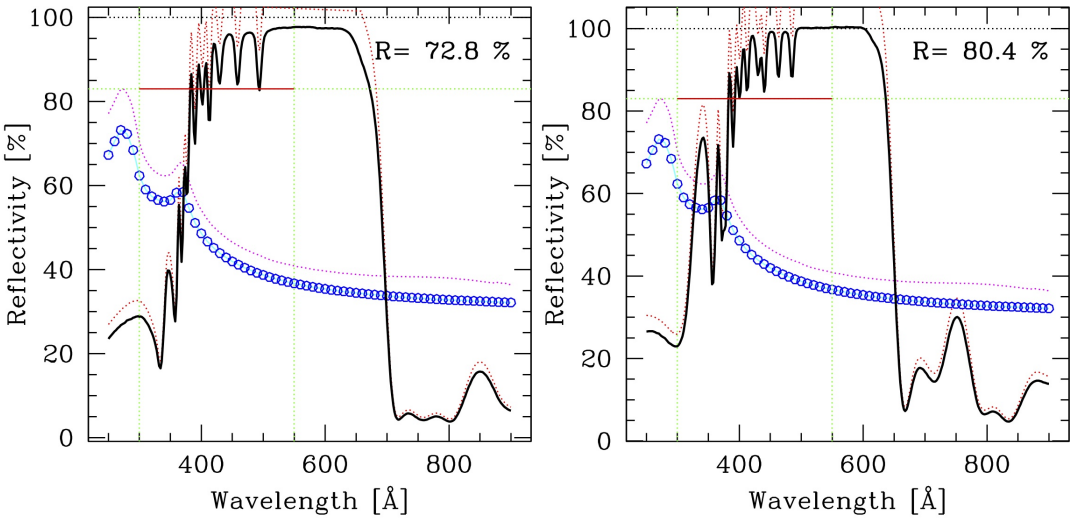

Figure 3.24: (Left) Reflectivity profile of the first recipe tested, cutting at $\lambda \sim 700$ nm. (Right) Reflectivity profile of another test sample, cutting at $\lambda \sim 650$ nm. The dashed red line plots the raw reflectivity measurement, while the thick solid black line is the calibrated measurement. In both cases, a Silicon wafer has been used as calibrator; the magenta dotted line represents the measured reflectivity, while the cyan solid line plots an interpolation of the expected reflectivity found in literature (plotted in open blue circles). The red horizontal line marks wave band of interest for the CTA requirement (300–550 nm) and the reflectivity threshold that has to be met in average on that band ($R \geq 83$ %). The required performance is already within reach of the second recipe.

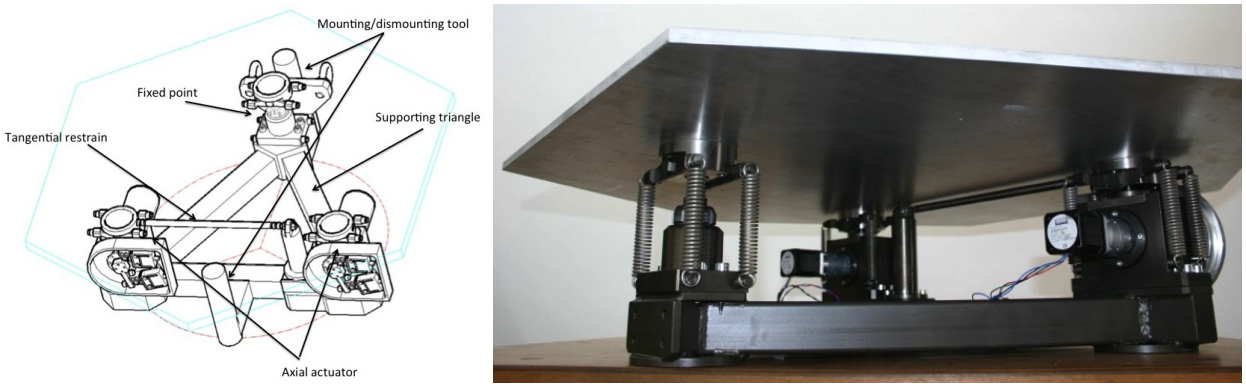

Figure 3.25: (Left) 3D CAD view of the support and alignment system of the M1 segments. (Right) The complete prototype.

The actuators used are designed with an eccentric shaft coupled with a stepper motor. A short piston rod is mounted to avoid lateral loads on the actuators. The correct positioning of the actuators is assured by

a zeroing procedure to be performed at start-up that calibrates the incremental encoders applied to the actuators. The complete prototype has been realized and tested (see the right panel in Figure 3.25). The total stroke of each actuator is more than 10 mm, they show an axial resolution better than 5 μm with an accuracy of about 3 μm.
The system is designed to allow mounting and removal, in a fast but safe way, of each segment together with its support assembly without involving the others. To this end, a tool with suitable pins has been designed.

3.3.2 The Secondary mirror: M2

Technology A suitable technology based on the same approach developed for the M1 mirror segments is under development.

Results from prototypes Industrial programmes are ongoing with specialized firms; these contracts are devoted to the development of the glass shells and of the honeycomb structure, both will be bent to the proper shape. Concerning the glass shells, the contract foresees the production of several shells of different thicknesses ranging from 6 mm, for the sandwich option, to 19 mm for the solid glass option. At the time of writing, the bending tool with its supports and all the handling tools have been manufactured, the glass has been procured and some tests on smaller samples are ongoing. Concerning the honeycomb, it will be custom made in carbon-fiber following the prescriptions given by the structural analysis performed (i.e. the cell size, wall thickness, core thickness and other mechanical properties). The contract also foresees an extensive characterization campaign (based on ISO/ASTM standards) of the mechanical properties. At the time of writing, the raw materials (i.e. carbon-fibre and glue) have been procured and the production of the samples is started. A scaled-down prototype has been also realized (see Figure 3.26)

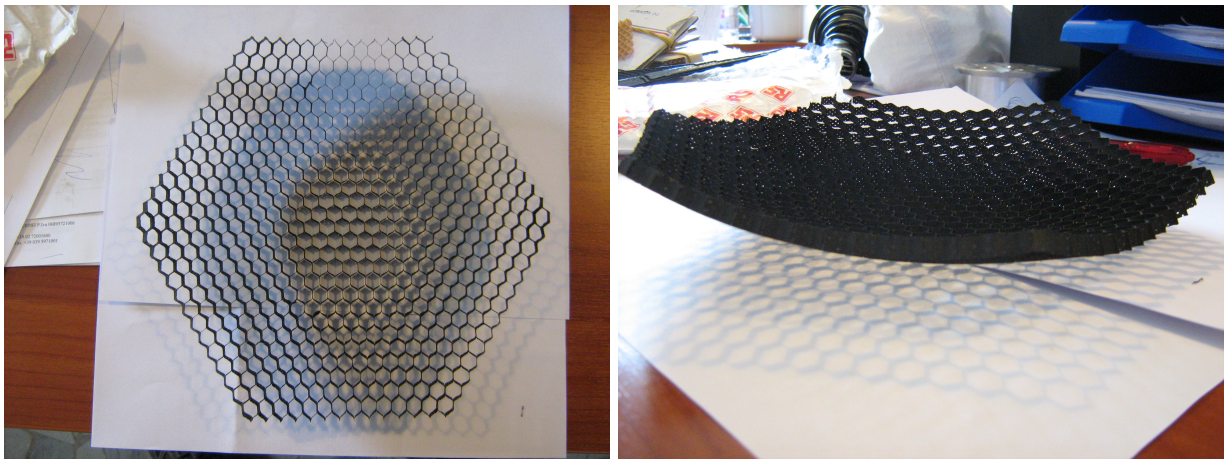

Figure 3.26: Scaled-down prototype of the honeycomb core structure of the monolithic secondary mirror

Coating The large dimensions ($D = 1.8$ m) and small curvature radius ($r = 2.2$ m) envisaged for M2 cause some critical issues regarding deposition homogeneity of the coating. The main aim of this coating is to

achieve a high reflectivity in the whole passband, as any kind of wavelength filter will be installed elsewhere in the optical chain. Moreover, the lowest possible dependence of reflectivity on incidence angle is needed, because the angles of incidence on the secondary mirror span a rather large range ($20° \leq \theta \leq 60°$). As a result of all these considerations and constraints, the baseline solution is deposition of the well established Al+SiO_2 dual layer. The only difference with respect to the classical applications is that the coating will not be operating at normal incidence; this leads to a different tuning for the thickness of the SiO_2 layer, in order to achieve maximum reflectivity at $\lambda \sim 400$ nm for AoI $\sim 40°$ which is the barycenter of the AoI distribution. SiO_2 thicknesses in the $130-150$ nm range have been simulated and should provide the required performance. For the secondary mirror, at present only simulations are available; no deposition has been attempted yet. However, given the relative ease of this kind of deposition and the experience in the field gained with previous applications (e.g. MAGIC–II and CTA–MST) we are confident that this deposition will not be critical. The large dimensions and the strong curvature of the dish are properly taken into account in the design of the coating chamber, which is being built specifically for this application with a dedicated industrial contract.

Support and alignment system The secondary mirror support is designed around three actuators permitting tilts and the piston necessary to align the mirror inside the optical system. This system is also used to correct the focus position. To better share loads and weight the actuators are connected to the mirror by means of three whiffletrees as shown in the left panel in Figure 3.27. Three lateral constraints with high axial stiffness are also present. They support the lateral loads, locking the three remaining degrees of freedom and supporting the mirror in an isostatic way. Concerning the actuators, a rotating nut driven by a stepper motor composes the single actuator permitting the actuation. Three absolute encoders track the position of the actuators. The system is design to have a total stroke of 15 mm with an axial resolution of 10 μm and accuracy of $\pm$ 20 μm. A cross-sectional view of one of the three M2 supports (actuator and loadspreader) is shown in Figure 3.27 (right panel).

3.4 Flexures and performance

The Schwarzschild–Couder telescope, in contrast to the Davis–Cotton design, has a dual mirror configuration. For this reason the effects of flexures in such a mechanical structure due to environmental factors (gravity, wind, etc.) can affect the performance in a different way with respect to PSF or pointing. In the next section 3.4, we discuss the foreseen flexures analyzed in the case of ASTRI SST–2M telescope. Moreover, on the basis of this estimation we evaluate the effects on the alignment (3.5) and pointing (3.6).

We analyze the effects of misalignments induced on the telescope structure (see Figure 3.28) by the following factors:

- Gravity.
- Thermal conditions.
- Wind.

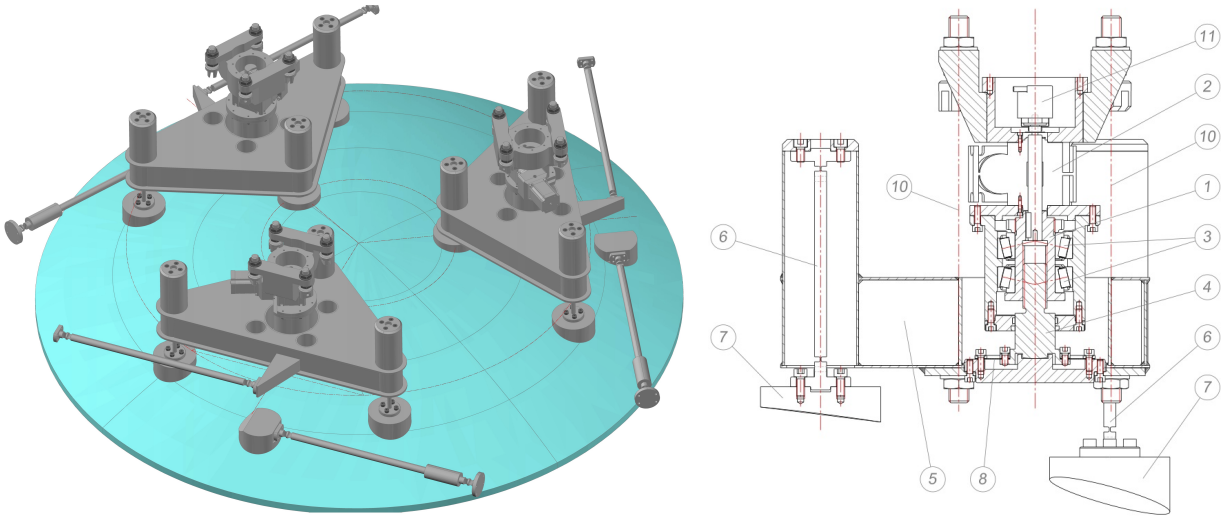

Figure 3.27: (Left) 3D CAD view of the support and alignment system of M2. (Right) Executive design cross-section view of the actuator.

Gravity represents a reproducible contribution to the error budget of the telescope as a function of the telescope elevation. The flexures induced by gravity can create an opto–mechanical mismatch between the different segments of M1, between M1 and M2 and between the camera and the mirrors.

The thermal effects can be assumed to be deterministic if a reliable model of the temperature and gradients affecting the telescope is applied. Thermal effects act in different ways during the night and they are stronger during twilight.

Wind effects are both systematic and random. In our analysis only the former are effective, because the random contributions can easily be removed by mapping the centroid of the target in photon counting mode acquisition.

The flexure errors due to gravity, wind and thermal effects are independent, and the total distortion around a certain axis (consider x elevation axis) is computed by adding these in quadrature:

$$\Delta X_{tot} = \sqrt{\delta^2_{gravity} + \delta^2_{thermal} + \delta^2_{wind}} \tag{6}$$

In Figure 3.29 a distribution of the typical flexure effects is reported. As one can see, gravity is the most important factor in the telescope error budget. The values indicated in the histogram are fully deterministic and of the order of ~ 1 arcmin. After removing gravity effects (see section 3.6) and thermal factors with a proper look-up table, a suitable strategy for removing the effects if wind has to be considered. In principle, these flexure effects can be corrected for during observations with the *Active Mirror Control Unit* (AMCU) from the PSF point of view, and by an ad hoc model for pointing estimation. In the next two sections, we

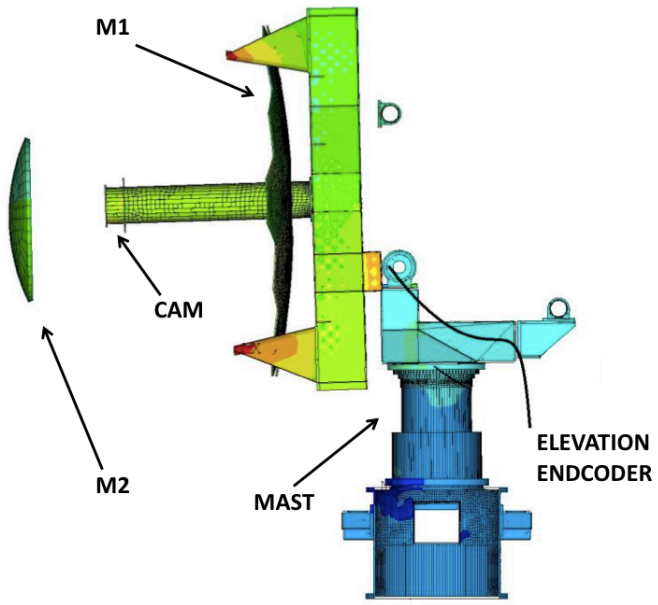

Figure 3.28: Schematic view of the telescope components subjected to flexures.

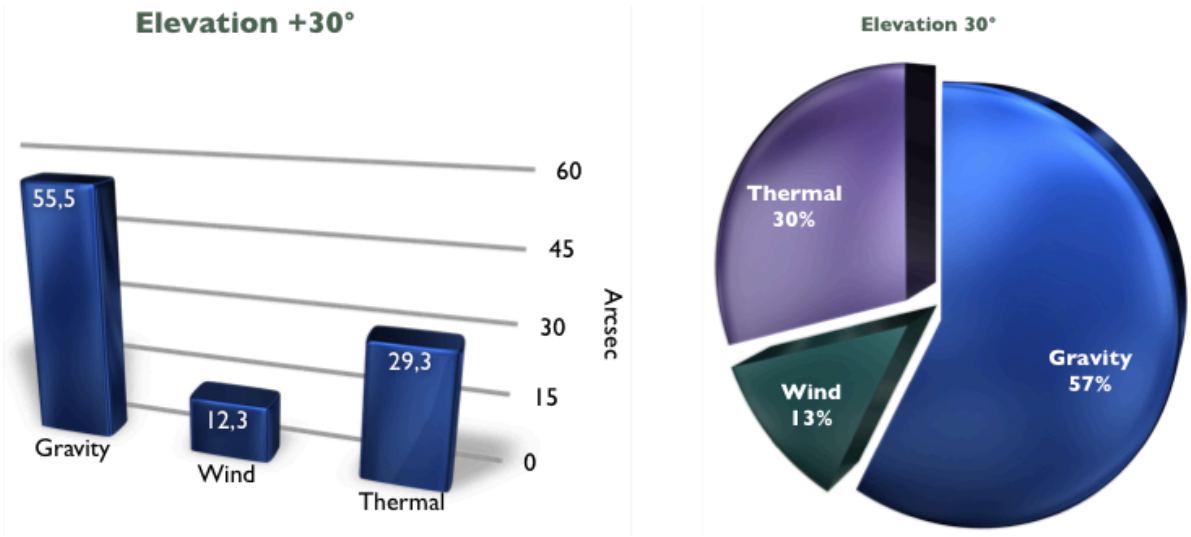

Figure 3.29: *Left*: histogram of the flexure contributions in arcsec due to gravity, wind and thermal effects. *Right*: pie chart of the percentage contributions of the same environmental factors.

will illustrate the strategies for removal of flexure effects used for the ASTRI telescope in the case of optics and pointing.

3.5 Calibration and Alignment

The AMCU system is used for superimposing the PSF created by each M1 segment. The largest flexures (gravity) do not affect significantly the PSF if a good alignment is obtained before pointing (for example using a look up table). In fact, the maximum degradation of the PSF is between 9.6 arcmin (design performance and facets aligned) to 9.65 arcmin (maximum gravity flexure effect). For this reason, the *AMCU* is foreseen to be used in open loop mode (see 3.9 for details). In this context, the alignment calibration is a process that assures the design performance is obtained. In the dual mirror configuration, a strategy has to be implemented to ensure that shifts and tilts of the single optical elements (M1 facets and M2 mirror) are inside the optical tolerances. In the case of the ASTRI telescope, the following procedure is proposed and it will be carefully analyzed in the AIT plan.

Pre–requirements:

- M2 and dummy camera mounted on the telescope structure and aligned with mechanical tolerances (see Figure 3.30).
- A first M1 segment is mounted with the mechanical tolerances (actuators positioned at half axial stroke).
- Point at a bright star and tilt the mirror until the PSF full width is minimized.
- The centroid is considered the reference point for alignment.

The following procedure has to be iterated for each segment:

- Acquire a PSF of the bright star obtained with all the M1 facets mounted and aligned, image 1a in Figure 3.31.
- Mount the segment on its mechanical support and point the telescope at a bright star.
- Acquire an image with the ccd camera with the star in the centre of the FoV, image 1b in Figure 3.31.
- Obtain the difference map of the two frames (1a - 1b), the distance of the residuals will represent the direction and shift to be applied to align the facet, image 1c in Figure 3.31.

3.6 Pointing

The ASTRI telescope will be modeled by TPOINT, which is state of the art software for astronomical telescope/antenna modeling[2]. The accuracy of a TPOINT model is related to the quantity of pointing data,

[2]http://www.tpsoft.demon.co.uk/

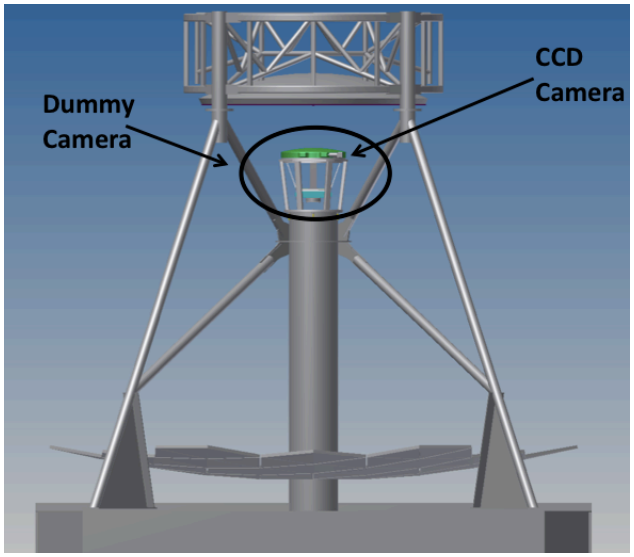

Figure 3.30: Snapshot of the ASTRI telescope with the dummy camera hosting the ccd camera for the mirror alignment operations.

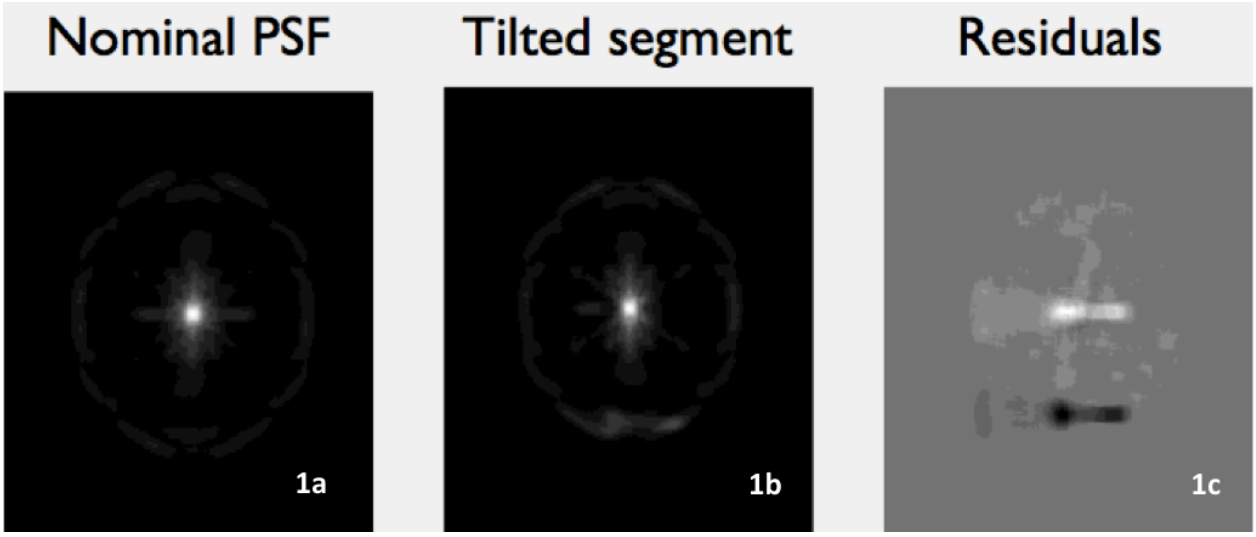

Figure 3.31: Zemax simulations of the ASTRI PSFs. *Left*: nominal PSF with all the mirror facets aligned; *middle*: PSF when a mirror facet is tilted; *right*: the difference between the two frames points out the contribution of the tilted mirror facet.

the sky coverage and data noise. As a rule of thumb, we can consider that it is easy to reduce by a factor of 1/10 the systematic errors in the uncertainties in the pointing. In our case, with a total estimated flexure due to gravity of about 1 arcmin, a pointing accuracy below 7 arcsecs is assured. The ASTRI prototype is designed to demonstrate that performance of the telescope is inside CTA specifications. For this reason, particular attention will be devoted to a system that will track pointing behaviour in dynamic conditions (such as wind and thermal gradients). Using a typical design of Cherenkov telescope, each M1 segment will be equipped with a laser that will track the tilt on small ccd cameras housed inside the Cherenkov main camera (see Figure 3.32). The mirror coatings have a red leak at 850 nm (outside the Cherenkov region of interest) that can be used for lasers to avoid interference with observations (as shown in Figure 3.24).

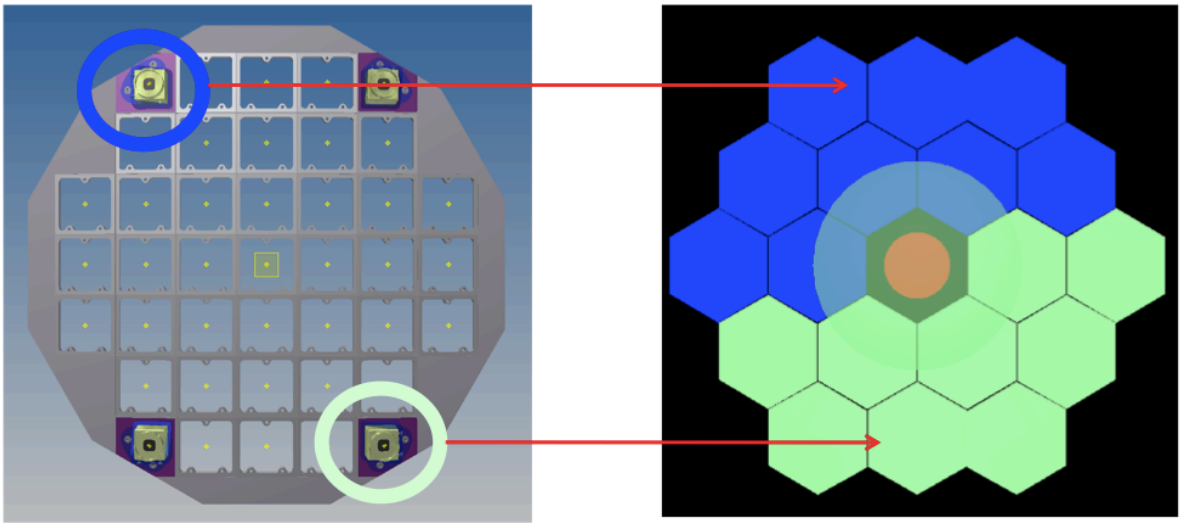

Figure 3.32: *Left*: the two ccd cameras are positioned at the corner of the focal plane, each of them collects the laser image spots from half of the primary mirror (*right*).

The best position for the ccd would be the centre of the focal plane, in place of a unit of the Photon Detection Modules (PDMs). Unfortunately this position is unsuitable from the sensitivity point of view[3]. The actual ASTRI solution under consideration is to mount two small ccd cameras on the edge of the focal plane, each one imaging the spots of half of the M1 facets (see Figure 3.32). In this way, every low frequency flexure ($\nu < 3$ Hz) can be measured and tracked for each segment, for M2 and the camera. In Figure 3.33 is shown how the laser spots will be imaged by one camera with the telescope close to zenith (*left*) and at an elevation of 30°. In principle, with these cameras the pointing position of the telescope can also be obtained using stars in the field of view during Cherenkov acquisition. The major limitation is due to the PSF of the star images, which is comparable with the field of view of the ccd cameras. In addition, the ccd cameras can be used for TPOINT calibrations with bright stars.

Taking into account flexures (gravity, wind, thermal), the TPOINT calibration and laser tracking system we

[3]From the analysis of about 175000 Crab events, simulated on–axis with CORSIKA and with core position randomly ranging within a distance of 300 m from the telescope axis, the central PDM plays its main role in 92 % of cases, being hit as essential part of a Region of Interest (RoI) equal to 3x3 PDMs

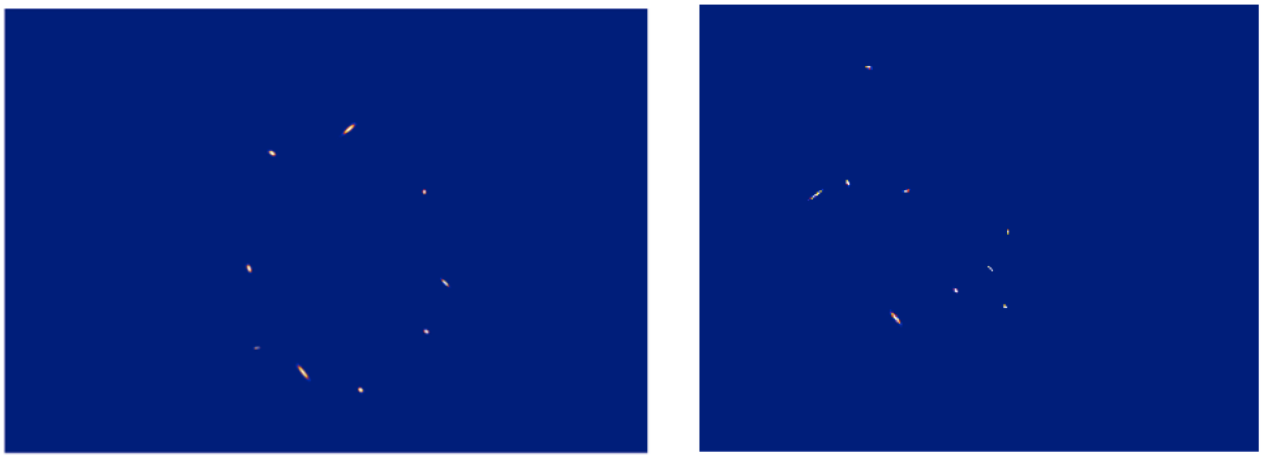

Figure 3.33: Zemax simulations of the laser image spots as seen by the camera. *Left*: the spots are arranged along an ellipse for a telescope at zenith. *Right*: for a telescope elevation of 30°, the spot pattern loses its regularity due to the flexures induced by gravity.

estimate we can reach a pointing error of 12 arcsec for a single telescope, corresponding to 7 arcsec rms on Cherenkov images with 3 telescopes.

The last pointing issue is due to the parallactic angle close to zenith. In fact, alt-azimuthal telescope models assure an error of ~ 1 arcmin at HA $= 0$ for a zenithal angle $\sim 1°$ that will be propagated in the array pointing error. To characterize the pointing accuracy of ASTRI prototype, an auxiliary wide field camera ($\sim 8°$) will be mounted on the telescope structure with the aim of obtaining an astrometric solution independent of TPOINT for targets close to the zenith.

3.7 Camera options and interface

3.7.1 Introduction

The camera of the ASTRI prototype telescope is designed to record Cherenkov light pulses in the wavelength interval from 300–700 nm, produced by charged particles in the Air Shower (AS) cascade initiated by primary particles entering the earth's atmosphere. The Cherenkov photons are detected by means of fast light–sensors and converted to appropriate digital signals which represent the Air Shower Cherenkov image. This image will appear almost instantaneously on the Focal Surface (FS), exhibiting a local maximum intensity surrounded by less intense signals fading gradually away. The shower images on the camera last from a few ns to tens of ns and must be separated from the unavoidable NSB light and detector dark noise. The Cherenkov image is buried in the background (NSB + detector dark noise) and its identification depends strongly on several telescope and camera parameters that must be taken into account and optimized in order to obtain the required performance. Figure 3.34 shows a simulated γ–ray event together with NSB light and detector dark

noise on the camera.

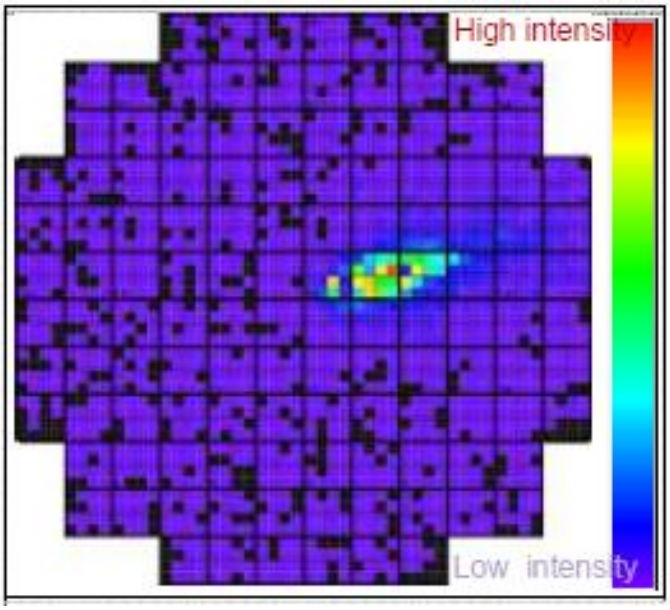

Figure 3.34: Simulated γ–ray event. A characteristic Cherenkov image formed on the camera focal surface.

This chapter comprises the design guidelines and general principles used in the design of the ASTRI prototype Camera. Starting from the definition of the scientific objectives (iterative process with science team), analysis of the technical solutions (mechanics, electronics, thermal) has been carried out to satisfy system and scientific requirements. Identification of critical elements and analysis of expected performance are currently in progress in order to finalize the trade–off processes and consolidate the design. The design criteria, when applicable, are in compliance with the SST–CTA requirements and aim to achieve maximum quality and reliability.

3.7.2 Sensors

Laboratory To obtain the best performance from our characterization system, before starting the characterization campaign of the detectors for the ASTRI project, we tested and improved all the characterization apparatus. New software to manage the entire optical apparatus was implemented (Figure 3.35); the new software allows the management of some new devices and means that several measurements can be made automatically. We also re–calibrated our reference sensors using a NIST (National Institute of Standards and Technology) calibrated photodiode.

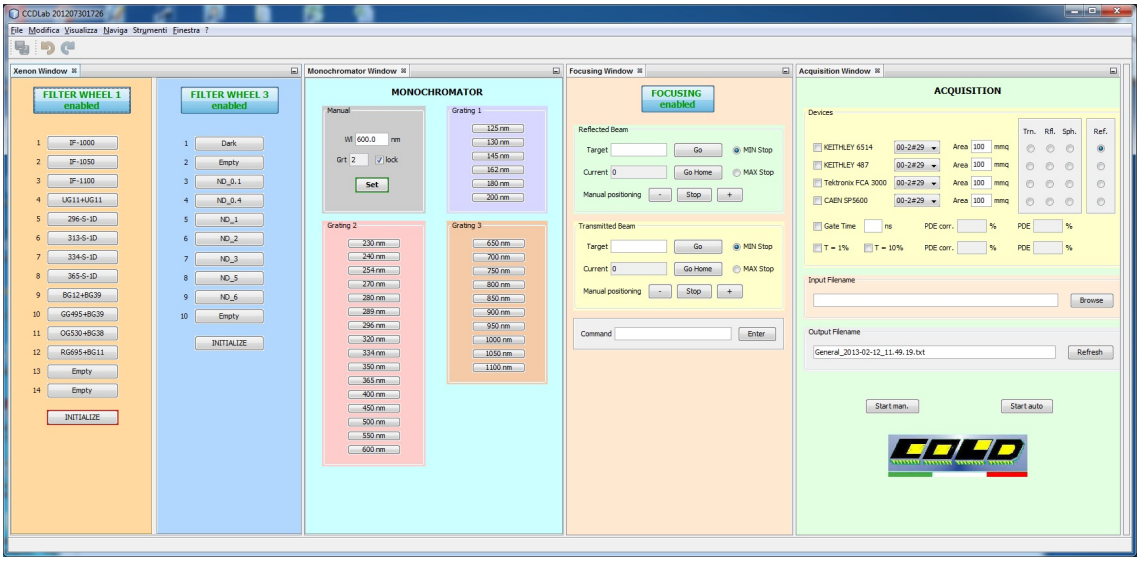

Figure 3.35: Laboratory Software: The Main Panel/Acquisition Window

Current–Voltage Characterization – I–V plots We have performed I-V measurements on several ASTRI detectors (> 20 % of the 550 detectors), obtaining the same results reported by Hamamatsu on the datasheet of each Multi–Pixel Photon Counter (MPPC). An example of the I–V plots obtained is shown in Figure 3.36. The I–V measurements are also used to evaluate the breakdown voltage and establish the best operating conditions of the sensors.

Test Board For the following measurements (PDE, Gain, Dark current, Cross–Talk) we realized a test board onto which the Hamamatsu MPPC is soldered (Figure 3.37).

Gain In order to evaluate non–uniformity problems due to the different operation voltage of each MPPC in a 4x4 array, we measured the gain of a pixel of an MPPC array as a function of the operating voltage (Figure 3.38). For this measurement we used a pulsed laser with a picosecond pulse (Picoquant PDL 200-B + LDH-P-C-405), an amplifier (CAEN SP5600) and a digitizer (CAEN DT5720) to obtain the charge distribution.

Cross–talk and Dark Versus Vov To evaluate the noise of the detector, we measured the dark current and cross–talk as a function of the operating voltage. The Crosstalk is evaluated from the ratio of the primary and secondary event count rates. This can be done by measuring the dark count rate as a function of the threshold of the comparator of the counter. In this way we obtained a "stair" plot (Figure 3.39),

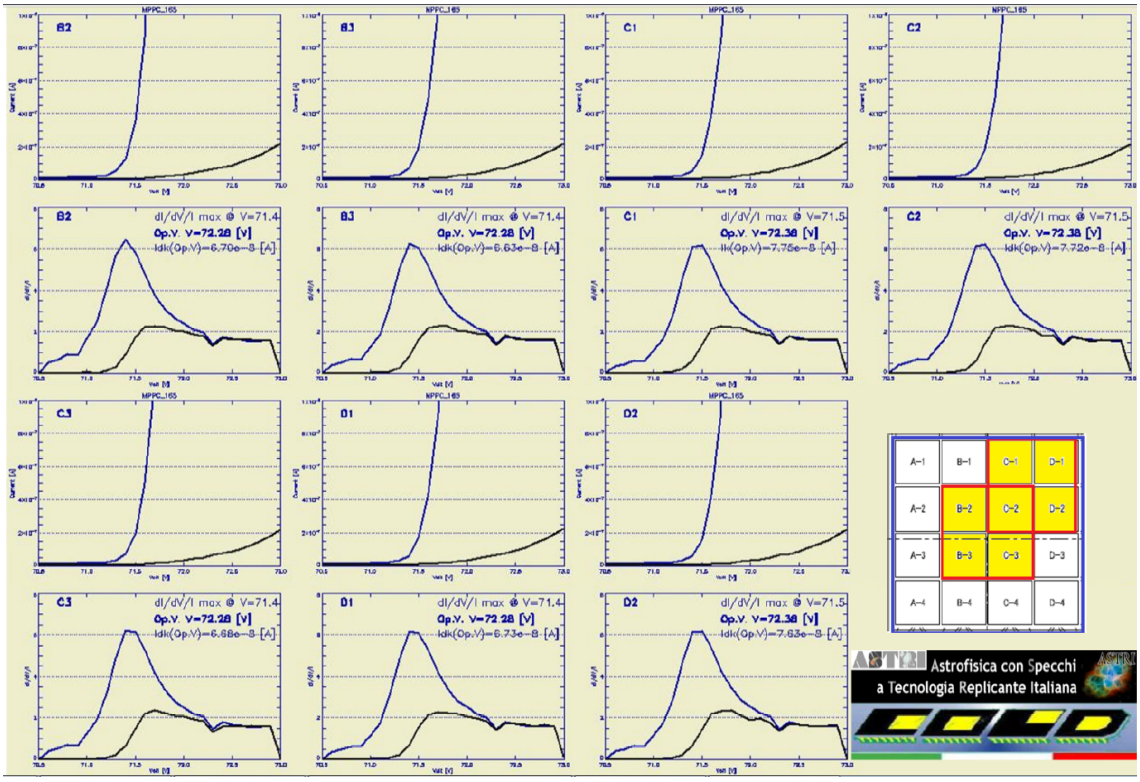

Figure 3.36: Example of the graphics in a test report realized in our laboratory.

where the first step is due to a one photo–electron pulse, the second is due to pulses of two pixels and so on. From the stair, we evaluate the cross–talk (Figure 3.40) and the dark count rate (Figure 3.41).

Dark count rates at different Gate Time from 20 ns to 100 ns We measured the dark count rate as a function of a gate time (Figure 3.42) in order to evaluate the presence of after-pulsing. In the following measurements, to remove after-pulse contributions in the first nanoseconds, we decided to set a gate time of 70 ns and statistically correct the count from the MPPC.

Linearity measurements In order to prevent the SiPM from saturating during PDE measurements, preliminary linearity measurements have to be carried out. Measurements were performed by illuminating an integrating sphere and selecting the wavelength of 440 nm. The SiPM is operated by selecting the Hamamatsu operating voltage and a gate time of 70 ns. The plots (Figure 3.43) report the linearity at 440 nm with and without Dead Time correction. From this plot we deduce that the device saturates at about 2.7 MHz uncorrected, that means at about 4 MHz corrected for dead time. Hence, the PDE measurements

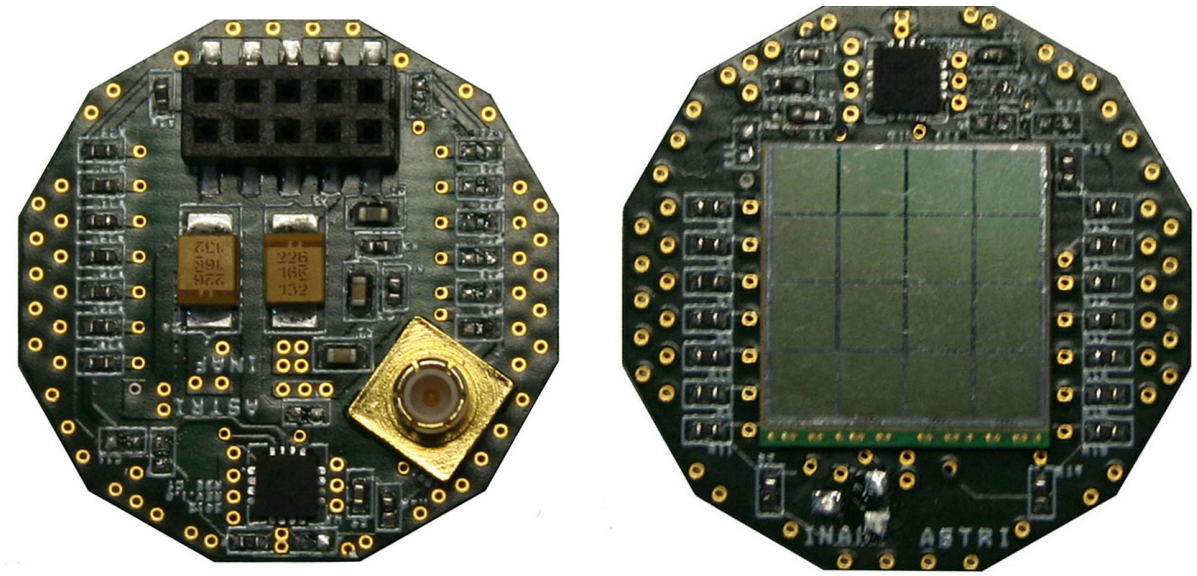

Figure 3.37: Board realized at COLD laboratory for PDE, dark cirrent measurements.

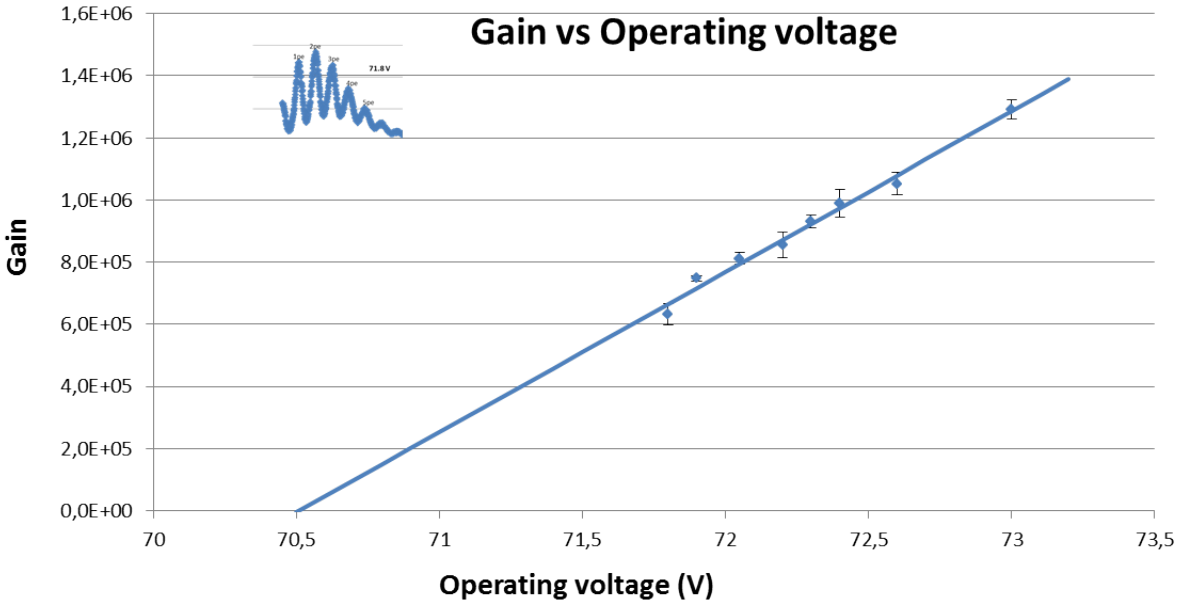

Figure 3.38: Gain as a function of applied voltage.

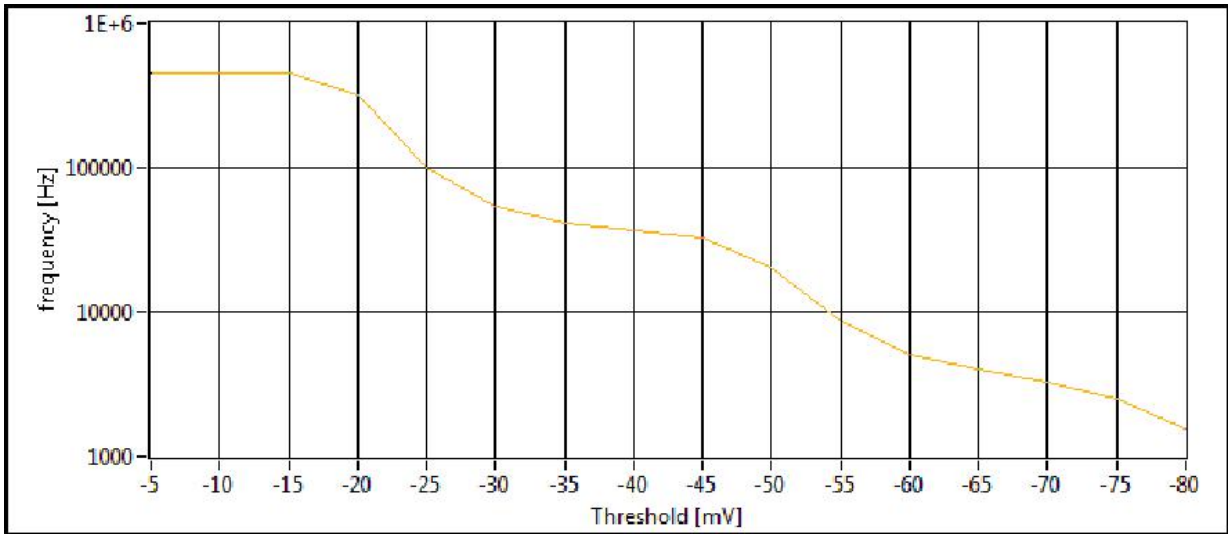

Figure 3.39: Stair of one of the ASTRI MPPCs.

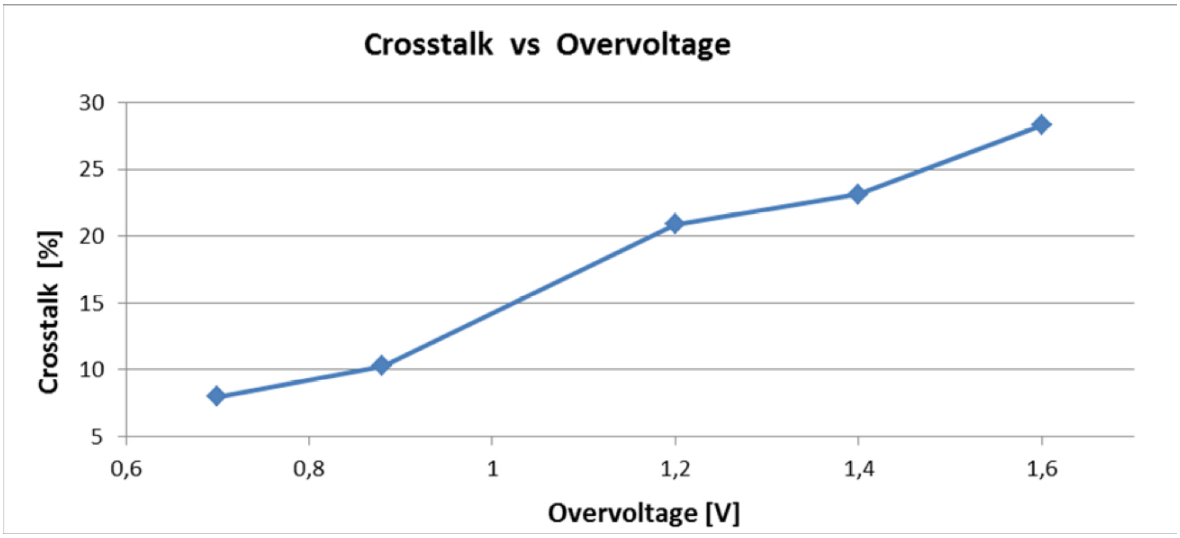

Figure 3.40: Cross–talk versus overvoltage.

have to be carried out with uncorrected signals at frequencies not higher than 2.5 MHz. The corresponding photodiode current is about 16 pA, sufficient to make measurements with small errors.

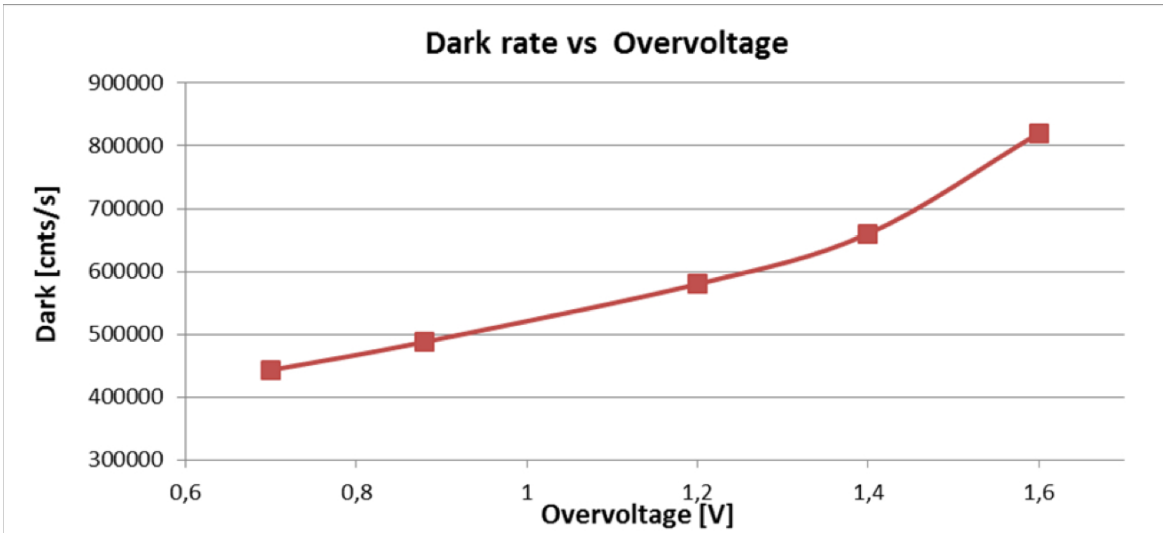

Figure 3.41: Dark count rate versus overvoltage with a temperature of 25–26° C.

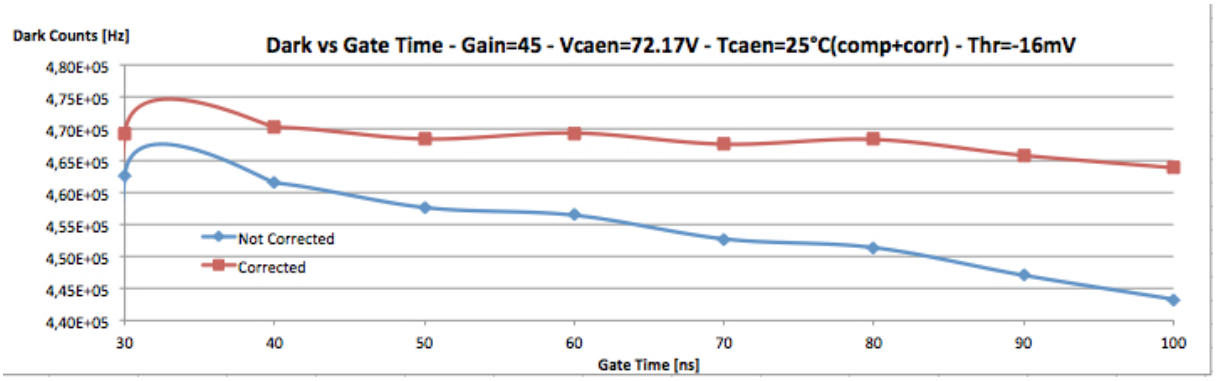

Figure 3.42: Dark count rate versus gate "hold–off" time at the Hamamatsu operating voltage.

PDE measurements at Hamamatsu operating voltage Measurements were performed at the voltage given by Hamamatsu and with a gate time of 70 ns. The plot (Figure 3.44) reports the PDE with values corrected for the Dead Time.

PDE (440 nm) versus Over–Voltage Measurements were performed at a wavelength of 440 nm and increasing Over–Voltage from 0.7 V to 1.6 V and gate time of 70 ns. In Figure 3.45 the PDE trend is shown and the operating voltage suggested by Hamamatsu is indicated by a red line.

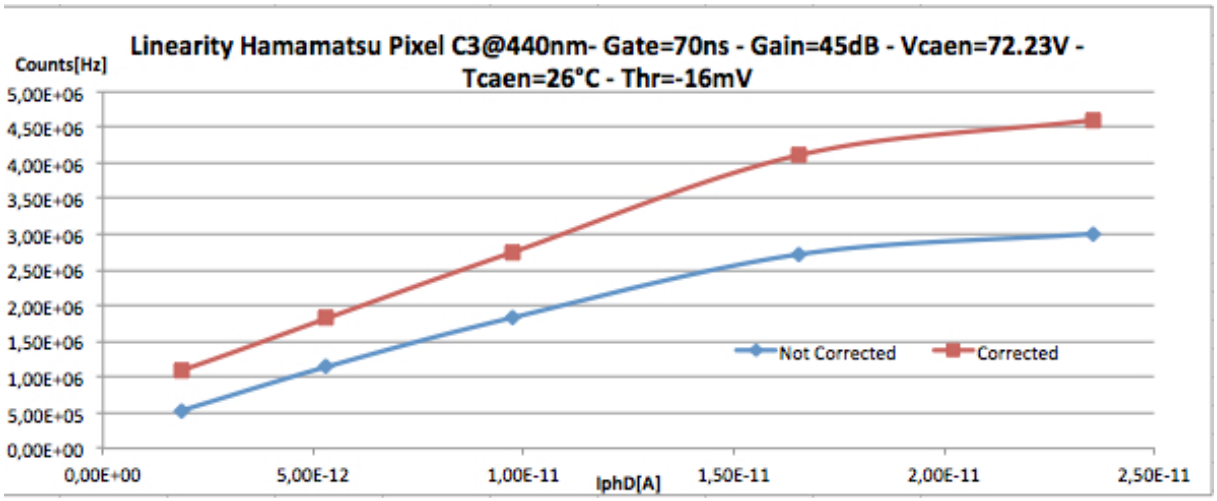

Figure 3.43: Linearity at 440 nm. Each signal rate is plotted with the corresponding value corrected for dead time.

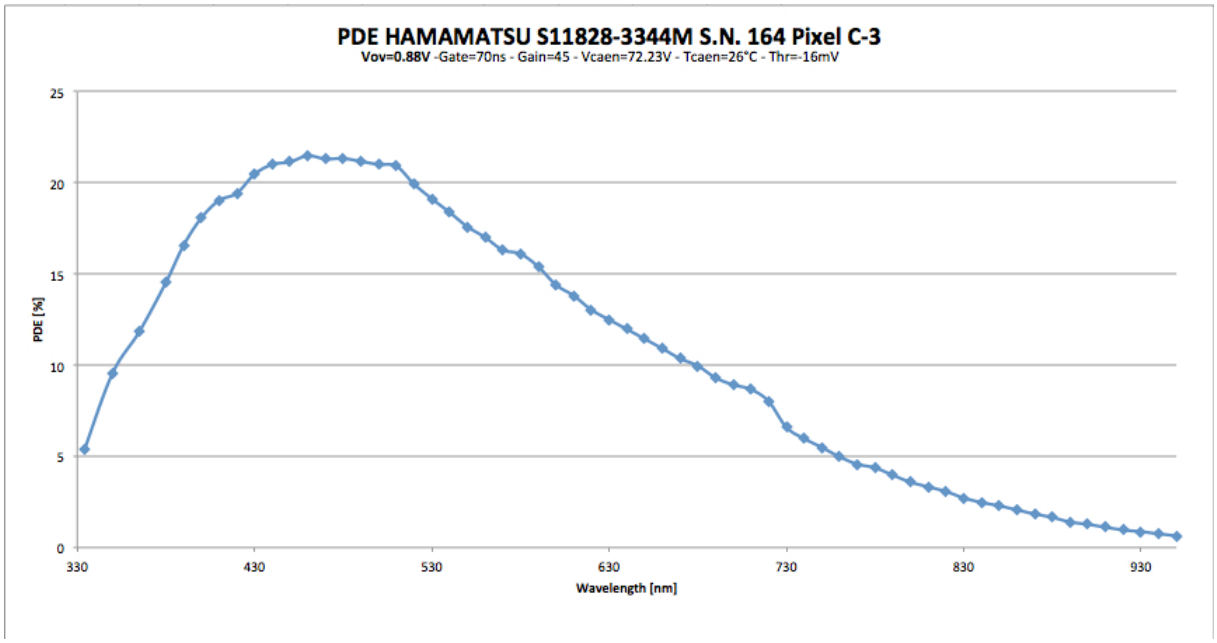

Figure 3.44: PDE measurement operating the MPPC at the voltage given by Hamamatsu, 26° C and with a gate time of 70 ns.

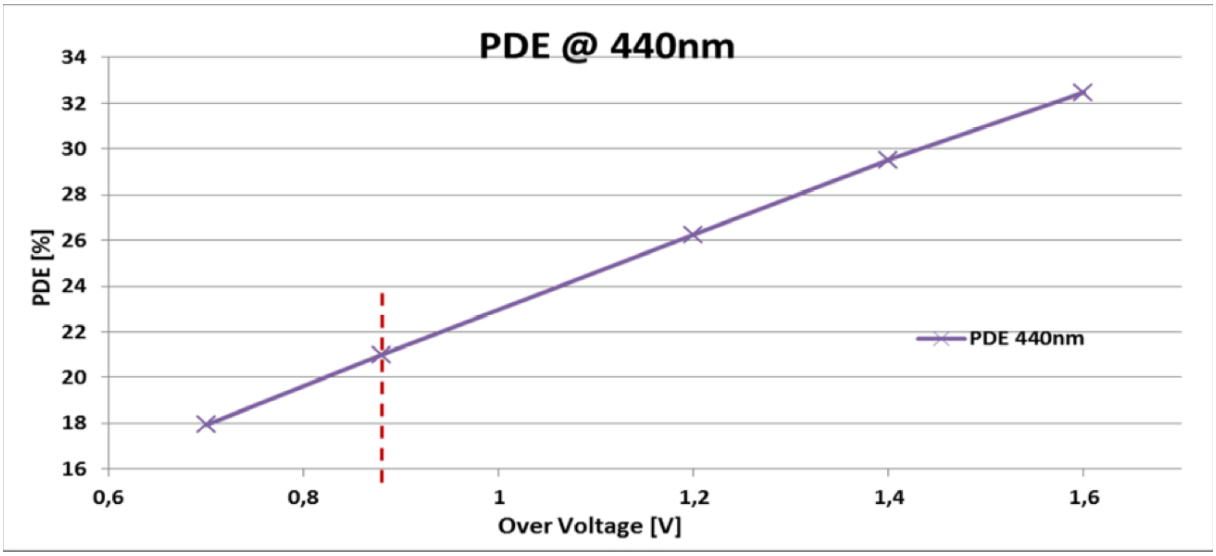

Figure 3.45: PDE at 440 nm versus the applied over–voltage.

PDE comparison and conclusions PDE measurements at the various Over Voltages are compared in Figure 3.46. As expected, the PDE increases with the Over–Voltage. Good operating conditions are obtained by operating at Vov = 1.2 V or even better at Vov = 1.4 V. At Vov greater than 1.4 V, the pixel is working near saturation. The error bars are to small to be visible. The cross–talk, even at levels of 25.2 %, doesn't affect the PDE measurements due to the method used for PDE evaluation. In fact, the threshold level is set to 0.5 photoelectrons and the second pulse due to the cross–talk is counted as one because it is simultaneous with the primary pulse.

3.7.3 Mechanical structure and cooling

ASTRI Camera Components

The ASTRI Camera is composed of four main blocks:

- Mechanical Components.
- Power Supply Components.
- Electronics Components.
- Thermal System Components.

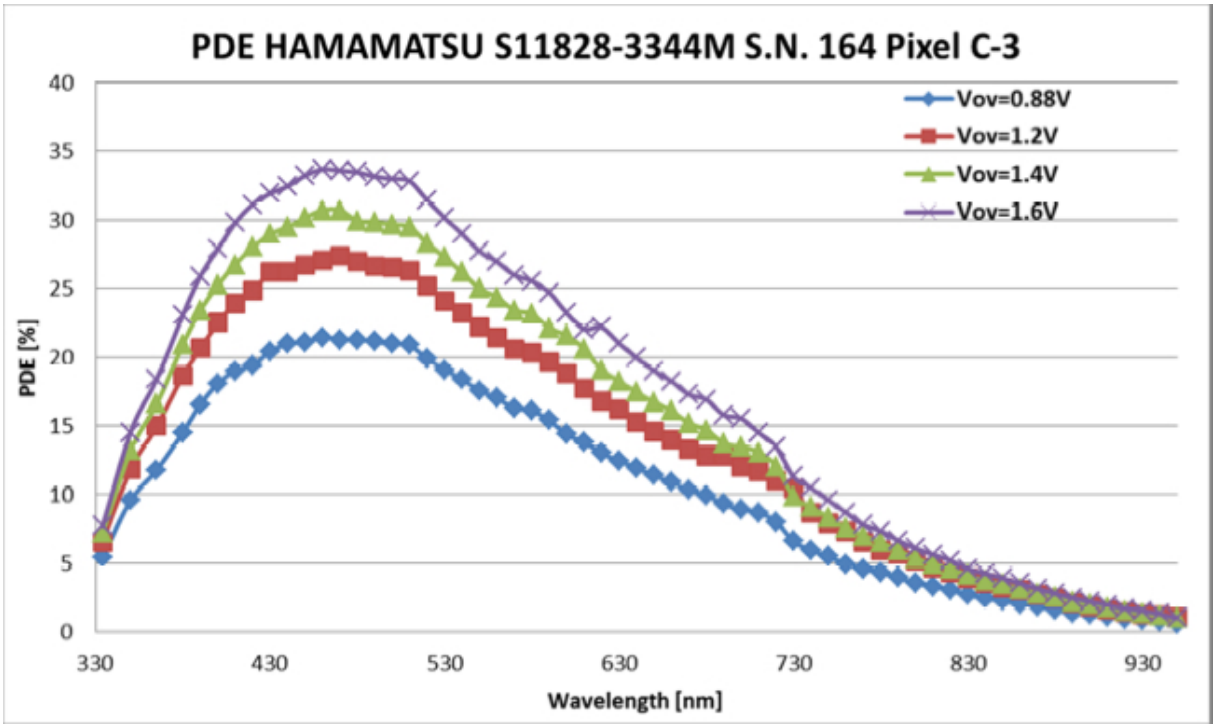

Figure 3.46: PDE shapes at different over voltage.

The Mechanical Components have the function of containing and supporting the camera electronics, including power distribution systems, cooling devices and fiber–optic calibration tools, as well as providing the mechanical interface to the ASTRI telescope. Components include the lids, poly–methyl methacrylate (PMMA) window and Photo Detection Module (PDM) support structure. The Figure 3.47 shows the camera breakdown at sub–component level.

The present 'opto–mechanical' weight estimate for the complete Camera is 46.0 Kg + 20 % contingency. The present baseline does not include the Back–End & Power Distribution cables and the connectors.

The PDM Support Structure and PDM module

The main support structure of the ASTRI Camera (also called the 'PDM support structure') is the spherical mounting shown in Figure 3.48 (*left side*). This structure will be machined from an aluminium plate, with a curvature radius of 1027.25 mm, an external diameter of 468 mm and with 37 holes machined to accommodate the PDM modules. The support will be mounted directly on the upper flange of the backbone structure via 8 M5 screws. The selected material for this component is Al Mg4,5 Mn0,7 – black anodized – (EN AW 5083 – PERALUMAN). The mechanical supports holding the PDM structure will be screwed from the bottom side of the FP structure via a dedicated support (see Figure 3.48, *right side*).

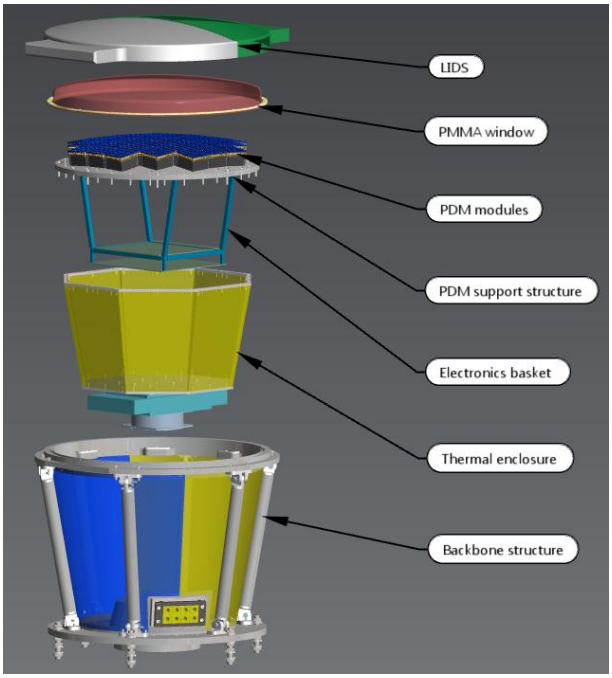

Figure 3.47: Breakdown of the ASTRI Camera.

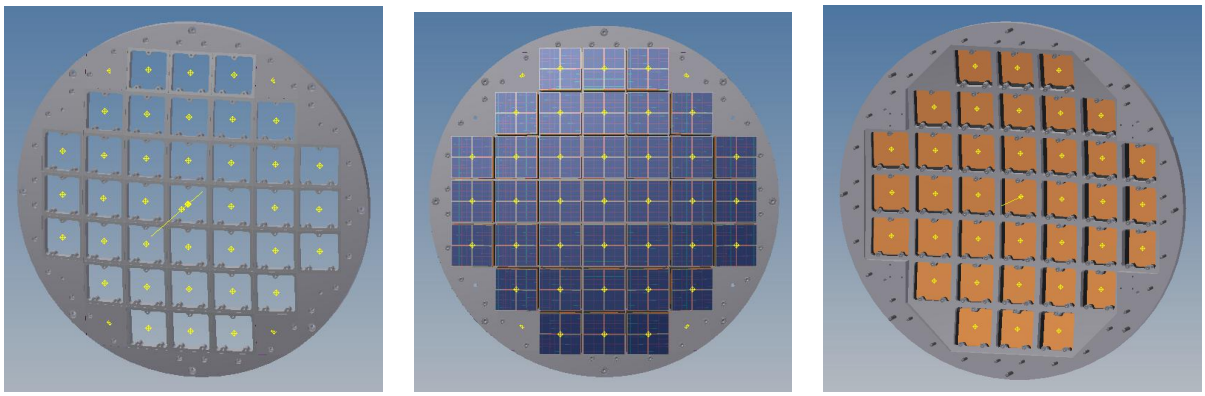

Figure 3.48: The FP structure (*left side*) and the FP with PDMs mounted (*right and central side*).

The PDM module is the mechanical unit consisting of MPPCs, FEE & PDM–FPGA Printed Circuit Boards (PCB) and PDM mounting. Figure 3.49 (*left side*) shows the breakdown of the PDM.

The selected material for the PDM mounting support is Al Mg4,5 Mn0,7 – black anodized – (EN AW 5083

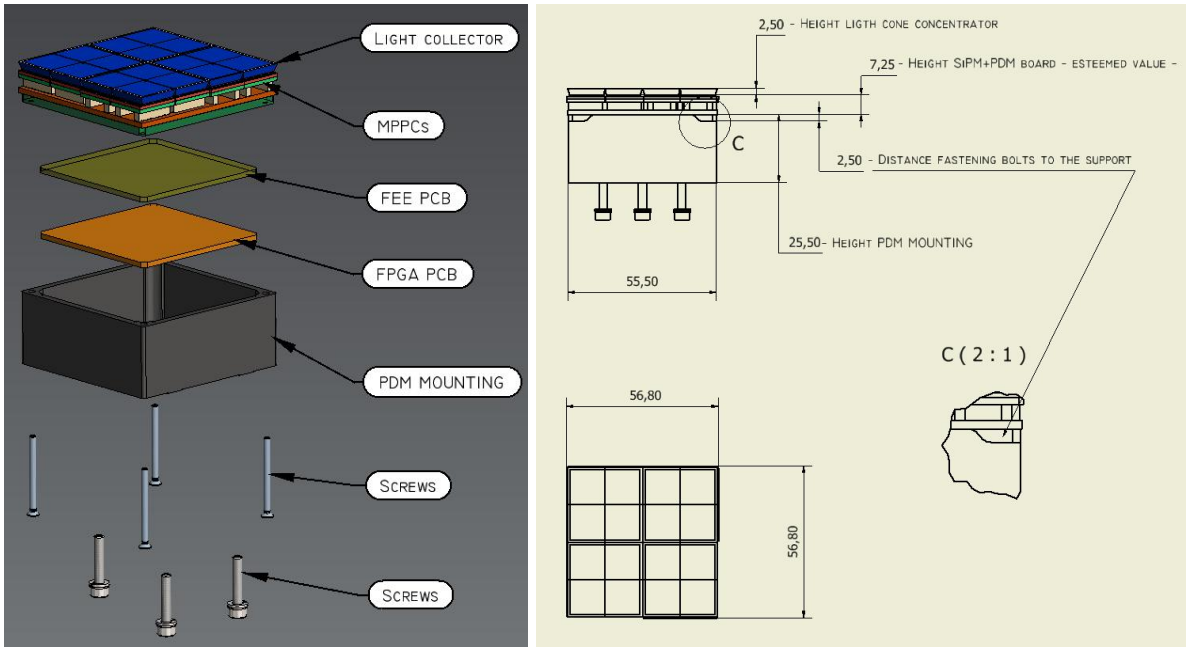

Figure 3.49: PDM Module breakdown (*left side*) and present dimensions of the PDM module (*right side*)

- PERALUMAN). The PCBs are mounted into the PDM by means of 4 screws. Each PDM module is mechanically interfaced to the PDM support structure through 3 bolts screwed from the bottom side. The present dimensions of the PDM Module are shown in the Figure 3.49 (*right side*).

The PMMA Window

In order to protect the camera sensors and electronics from the atmosphere, an optically transparent PMMA window will be mounted on the upper flange of the backbone support structure. As shown in Figure 3.47, the PMMA window has the same curvature radius as the focal surface. The thickness of the window is 3 mm. The window, with its aluminium ring, will be mounted on the backbone structure via 12 M3 screws.

The Back–end Electronic & Power Distribution Board

The purpose of this support (see Camera breakdown in Figure 3.47) is to mount on the camera the electronic boards and to permit easy access to the cables and wires coming from the PDMs. This box support will be screwed onto the bottom surface of the PDM support structure. The support – black anodized – will be made using a standard square 10 mm thick aluminium tube, linked with machined aluminium joints. The present dimensions of the electronic boards are:

- Back–end Electronic: 220 × 210 mm.

- Distribution Tensions: 240 × 210 mm.

Thermal Enclosure

The thermal enclosure will host the Peltier based thermal components, screwed onto its bottom surface. This structure is in thermal contact with the PDM support structure and is thermally isolated from the backbone structure using a synthetic flexible sheet – Nitrile rubber 25 mm thick. This structure will be made from 8 plates, one upper ring and a cold plate of aluminium, mated using screws.

The cold plate is designed to hold the Peltier based thermal components; 3 MIL connectors on this plate will allow for the feed through of the electronic cables. The selected Peltier cooler is the DA-160-24-02-00-00 PowerCool Series Direct–to–Air Thermoelectric Assembly, manufactured by Laird. It offers dependable, compact performance by cooling the camera via conduction/convection. Heat is absorbed through a cold plate and dissipated though a high density heat exchanger equipped with an air ducted shroud and brand name fan.

The thermal system ensures the proper working temperature of the camera electronics and in particular of the MMPCs. The thermoelectric system makes use of a Bi–Directional Thermostatic Controller that can operate in both heating and cooling modes and provides temperature control and system functions, including separate fan control, low voltage protection and an alarm.

The Camera Enclosure (Backbone Structure of the Camera)

The structure consists of two circular flanges (upper and lower) – machined out of a standard flat aluminium plate – and joined together with off–the–shelf circular aluminium tube (30 mm external diameter) via swivel joints. The Figure 3.47 shows the preliminary 3D layout for this structure and Figure 3.50 shows the present overall dimensions.

In order to permit the feedthrough of the Astri Camera cables (power line, ethernet, antenna and an RS232 for the thermal control system), Icotek solution (based on DOKU KEL16-8), has been selected. The material for the two flanges is Al Mg4,5 Mn0,7 – black anodized – (EN AW 5083 – PERALUMAN).

The calendered side panel, made of aluminium and painted black (TBC), will assure the external closure of the whole structure. This panel will be glued (with a 3M Scotch-Weld Epoxy Adhesive 2216 B/A) and riveted to the bottom and upper plates. The backbone body includes the interface to the mechanical structure of the ASTRI Telescope.

Camera Lids

In order to protect the PDMs from sunlight and to assist calibration, the camera will be equipped with a light–tight cover (see Figure 3.47). This structure will be composed of two lids, mounted on the upper flange of the Backbone Structure. The two lids are able to rotate in the range 0–270 degrees, powered by 2 DC servo motors (not shown in Figure 3.47). In this design, the baseline material used for the lids is aluminium.

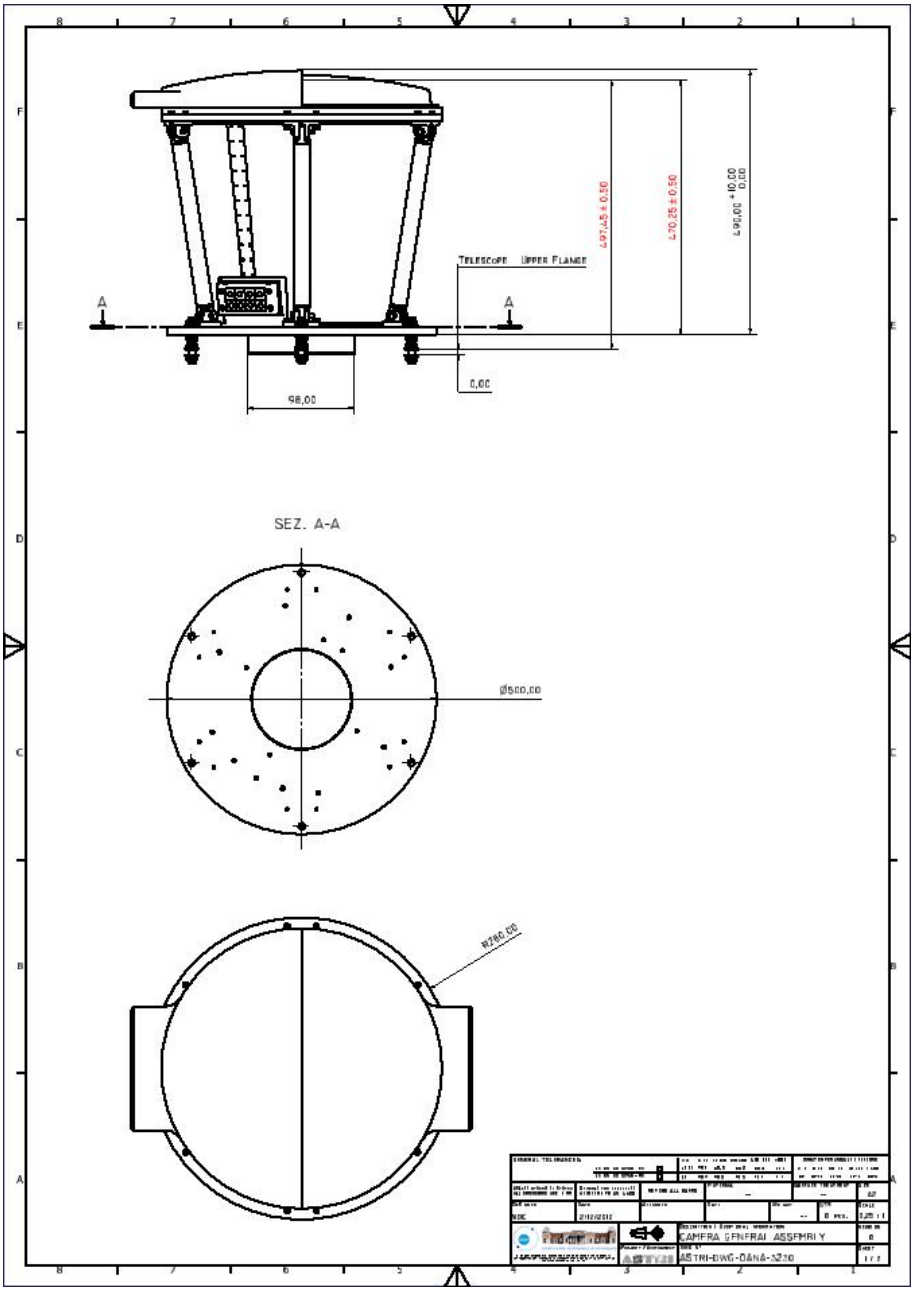

Figure 3.50: ASTRI Camera – overall dimensions

3.7.4 Electronics and Trigger

The ASTRI Camera Electronics is designed to record the pulses produced by the SiPM sensors of the focal plane, to generate a trigger, to manage these signals, to acquire and store the event data and to communicate with an external camera controller and data taking computer.

The detector used in the ASTRI telescope is the HAMAMATSU model S11828-3344M. This is a 16 channel (in a square 4x4 configuration) monolithic SiPM array mounted on a SMD package. Each channel (pixel) is made of 3600 cells (SPAD) in a square configuration array of 60 × 60, with a 50 μm pitch, hence covering a total photosensitive area of 3 × 3 mm^2. The resulting Fill Factor is 61.5 %. Typical Vbias is in the range of 70–75 Volts.

In order to match the required focal surface curvature, the detectors must be arranged in tiles. The best compromise is reached with tiles of about 6 × 6 cm, called Photon Detection Modules (PDMs). The ASTRI camera is formed of 37 PDMs.

The Camera Electronics is divided into two main systems: the Front-End Electronics (FEE) and the Back-End Electronics (BEE). Each PDM hosts the SiPM detectors and the Front End Electronics which is composed by the ASICs that provide the interface to the SiPM detectors plus four ADCs and a FPGA that manages the slow control of the ASICs, the capture of the events and the generation of a local trigger (PDM level).

The Back End Electronics (BEE) is hosted on a separate common board. The BEE is based on a FPGA that manages the setting and the communication between the external world and the 37 PDMs. The Figure 3.51 shows the basic ASTRI Camera Electronics block diagram.

The Front End Electronics

The PDM is composed of several parts:

1) A *SiPM Unit Board* on the top of which one SiPM is soldered (Figure 3.52). On the bottom are placed two connectors (to plug the SiPM Unit Board to the Connection Board), a temperature sensor and an RC circuit to locally filter the Bias Voltage. There are 16 SiPM Unit Boards on top of each PDM, in a 4 × 4 matrix.

2) A *SiPM/FEE Interface Board*, filled only with connectors, to interface the 16 SiPM Unit Boards to the FEE Board (Figure 3.53). On the top side of the board are the 16 SiPM sensors of a PDM. On the bottom side are two connectors for the connection to the ASIC Board. Here, the SiPM pixel signals are connected together in a 2 × 2 configuration; this means that the 256 physical pixels of the PDM are shrunk into 64 optical pixels (8 × 8) of 6.2 mm × 6.2 mm each, corresponding to an angular size of 0.17°. Thus, the total PDM angular size is 1.36°. This is done in order to obtain a pixel size comparable with the optical resolution and to reduce the number of channels required in the camera electronics.

3) An *FEE Board* that hosts two 32 channel front–end ASICs (EASIROC) plus 4 ADCs dedicated to the conversion of the two ASICs' Low Gain and High Gain channels (Figure 3.54).

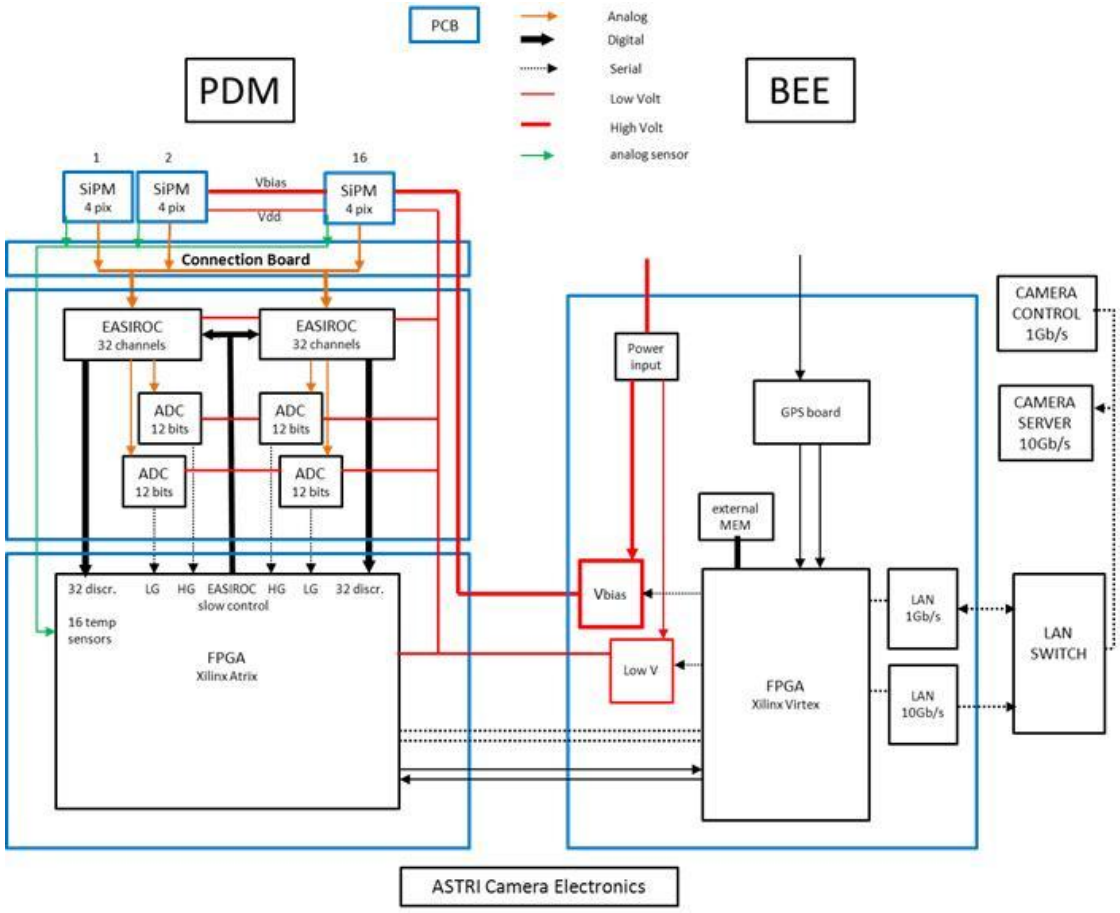

Figure 3.51: Block diagram of the ASTRI Camera Electronics.

The EASIROC is an ASIC specifically designed for the readout and powering of SiPMs. Usually, Cherenkov Telescopes are based on ASICs that sample the input signals with a rate of about 1 GHz. In contrast to this, the EASIROC is a signal shaper with selectable shaping time (25–175 ns) in which the peak of the shaper gives the amplitude of the input signal integrated in a specific time window for each pixel. In this way, the data rate is dramatically reduced as the event data are condensed into one value per pixel. The characteristics of the EASIROC chip are summarized below:

- 32 input channels: Voltage Sensitive Low Noise Preamplifiers.
- Double analog chain (preamp + shaper + track&hold): one for high gain and one for low gain.
- 1 high gain mux output (8 mV/pe).
- 1 low gain mux output (0.8 mV/pe).

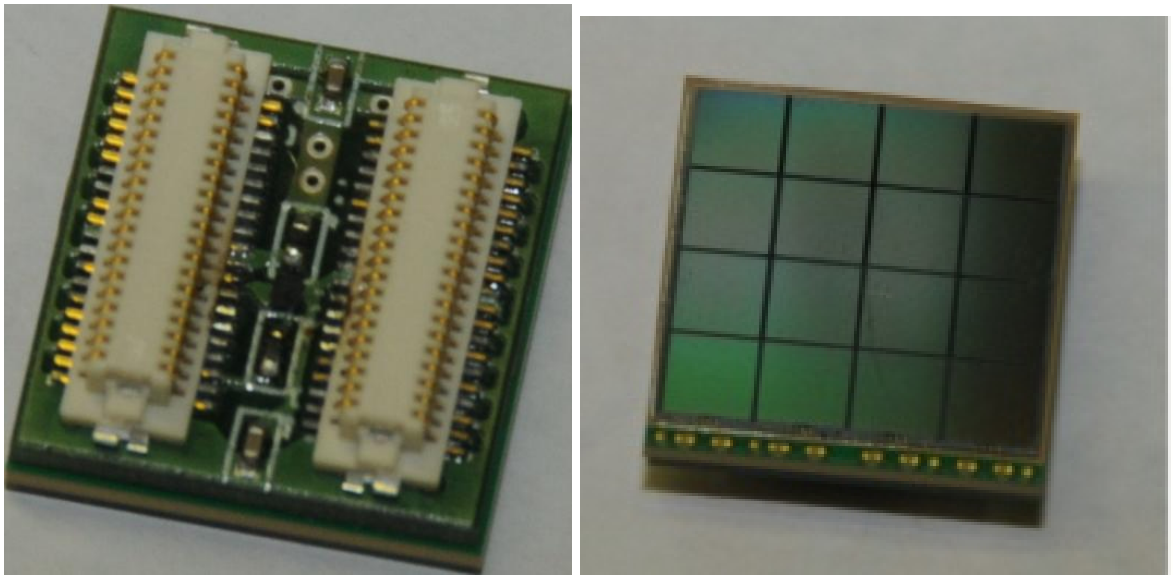

Figure 3.52: SiPM Unit Board of the ASTRI Camera.

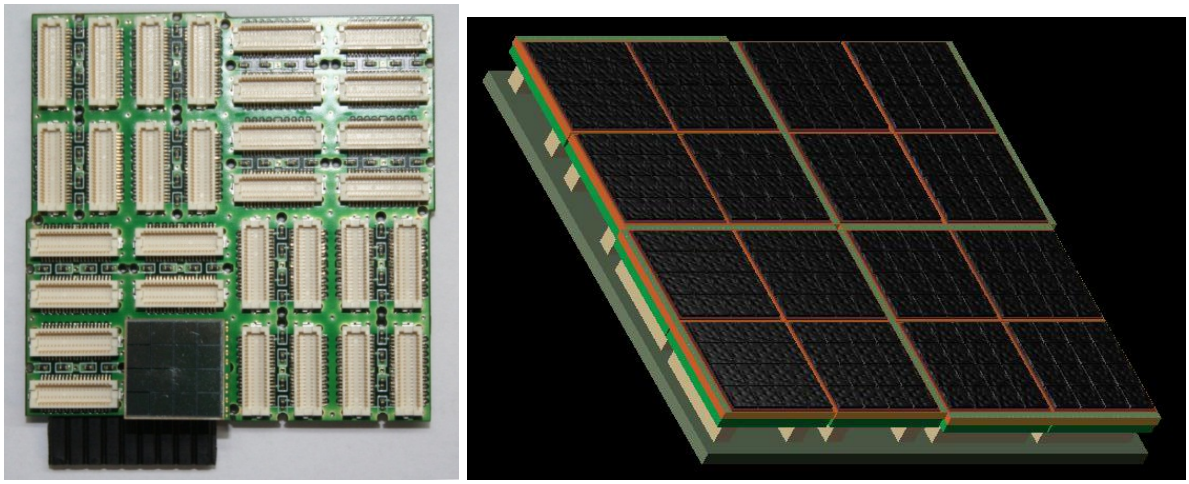

Figure 3.53: SiPM/FEE Interface Board of the ASTRI Camera.

- Adjustable Gain (common to all preamps) 4 bits (1–15 Low Gain, 10–150 High Gain).
- Electronic crosstalk : < 0.3 %.
- 32 8–bit DAC for individual SiPM bias adjustment (0–4.5 V) for fine gain tuning/equalization.

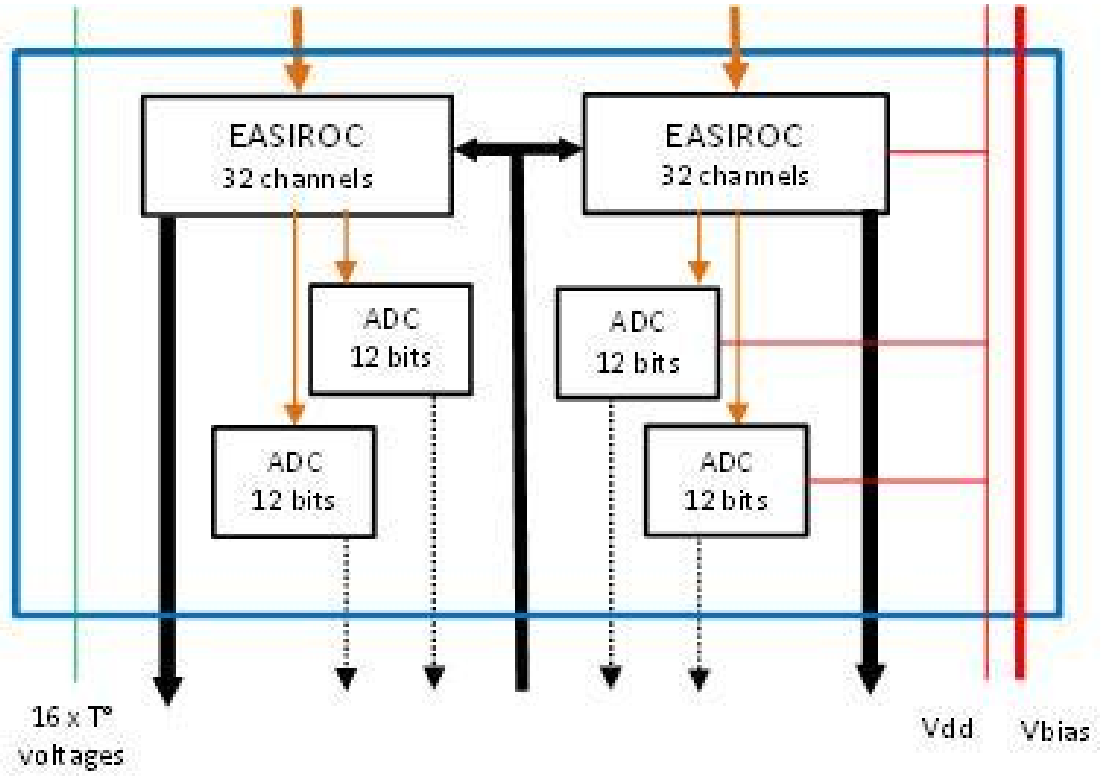

Figure 3.54: FEE Board of the ASTRI Camera.

- 32 trigger lines (fast shaper + discriminator) with 32 separate trigger outputs.
- 1 10–bit DAC to set a common threshold for all 32 trigger discriminators.
- 1 calibration input (enabled only one channel at time).
- 16 μs read–out of 32 channels.
- Power 5 mW/channel.

The most important characteristic of EASIROC is that it provides 32 trigger output lines, one per pixel. This allows the generation of the trigger (at PDM level) in a very smart and efficient way. Moreover, EASIROC provides 32 DACs to fine tune the SiPM bias of each individual pixel.

4) A *FPGA Board*, that hosts the FPGA that manages each single PDM. This allows the setting of the configuration of the two EASIROC chips through the slow control serial lines, the generation of the PDM level trigger and communication with the BEE.

5) A *PDM Box*, the electronics of the PDM and the SiPM detectors are assembled inside an aluminum box that is placed on the top of the focal surface mainframe.

The Back End Electronics

The Back End Electronics is the Read Out section of the ASTRI Camera Electronics. The heart of this module is a powerful FPGA that manages the Camera. The main tasks of the BEE are:

- Trigger signal routing.
- Clock (GPS)[4]
- Event Time Tag.
- Store events in a Local Memory.
- Data Packing and Transmission (to the Data Collection System).
- Voltage generation.
- HV/LV distribution.
- I/F to FEE.
- I/F to the external instrument console and Data Collection System (DACOS).
- Operating Modes

A block diagram of the BEE is shown in Figure 3.55.

Trigger Generation Strategy

Detecting Cherenkov events requires a smart trigger because the shower image is buried in the Night Sky Background and the detector dark noise. Pattern recognition algorithms must be used in order to efficiently reject accidental coincidences and these must be suitable for mplementation in the camera electronics.

The single pixel trigger rate is dominated by the NSB and detector dark noise. Increasing the threshold of each individual pixel discriminator eliminates most of the pixel accidental coincidence and hence decreases telescope trigger rate, but also limits drastically the dynamic (energy) range of the telescope (the signal to noise ratio decreases with decreasing energy threshold). A more effective way to limit the telescope accidental trigger rate, offering a less severe dynamic range limitation, is to trigger only on a selected pattern of pixels. This is possible as the shape of the characteristic Cherenkov event is elliptical and concentrated in a few tenths of a degree ($\sim 0.5^\circ \times \sim 0.3^\circ$). Requiring that an image event contains at least a few pixels, in a defined pattern, to cause a trigger, results in a reduction of the accidental trigger rate.

[4]The baseline for the ASTRI prototype is to perform synchronization using a GPS receiver installed in the telescope. The possibility of using systems like White Rabbit to time–tag camera data is under investigation.

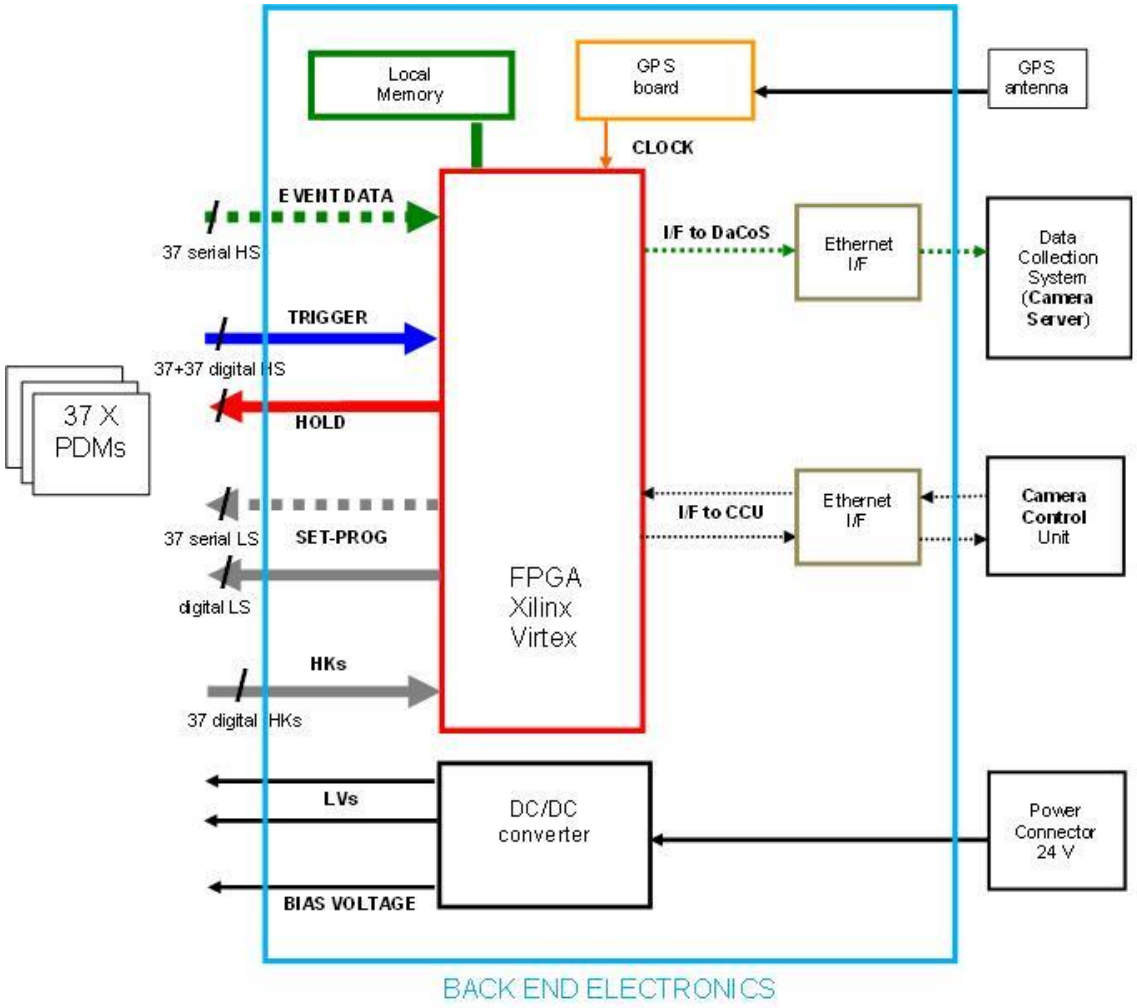

Figure 3.55: Block diagram of the Back–End Electronics of the ASTRI Camera.

After intensive simulation, it became clear that the most efficient trigger algorithm for the ASTRI telescope is based on a very simple rule: at least 4 adjacent pixels (any pattern) hit by a number of photoelectrons over a selected threshold in a time window of 15 ns.

This algorithm can be synthetized inside the ASTRI Camera Electronics thanks to the EASIROC front–end chip that provides a separate trigger line for each pixel. This feature is not available in the sampler chips usually selected for Cherenkov telescopes, where there are a limited number of trigger lines (only for groups of pixels).

The time window of 15 ns is imposed by the shaping time of the trigger channels inside EASIROC, but it is adequate for the Small Size Telescopes because high energy events last longer than low energy ones.

For the ASTRI prototype telescope, it was decided to generate a trigger only at PDM level, ignoring events that can switch on pixels in two adjacent PDMs. This could limit a little the trigger efficiency but only in the lowest part of the energy range.

The generation of the trigger is achieved with the help of the FPGA on the PDM. All 64 (32 + 32) trigger lines coming out of the EASIROC chips are connected to the FPGA. The logic inside the FPGA generates the trigger at PDM level. This trigger signal is sent to the FPGA located in the Back End Electronics that routes this signal to every PDM in the focal plane in order to stop acquisitions and start the ADC, hence saving the signal from every pixel in each relevant PDM. The converted data will, in turn, be transmitted to the Back End Electronics.

The delay introduced by the algorithm in the FPGA (on the PDM) plus that introduced by the routing of the trigger through the FPGA on the BEE is less than the delay between the trigger output lines in the EASIROC chip and the following peak of the shapers. In this way, the peak can be held and then converted.

Finally, the Back End Electronics receives event data from every PDM in the focal plane, tagging the events with the correct time and saving them in packets to be sent to the Camera Server that collects the scientific data.

3.7.5 Camera control software and Slow Control

ASTRI Camera Control System

The ASTRI Camera Control System (CCS) is shown in Figure 3.56 and consists of two main components: the *CDS* (Camera Detection Subsystem) and the *CAS* (Camera Ancillary Subsystems).

The *CDS* contains:

- A focal plane with 37 PDMs (Photon Detection Modules).
- A BEE (Back-End Electronics) module.
- A power board.

The *CAS* is composed of the following devices:

- A fiber–optic calibration subsystem (turns on and off the flasher).
- A lid control subsystem (actuates the opening of the lid).
- A thermal control subsystem (regulates the temperature via Peltier cells).
- Humidity & temperature secondary sensors (the primary sensors are located along the focal plane).

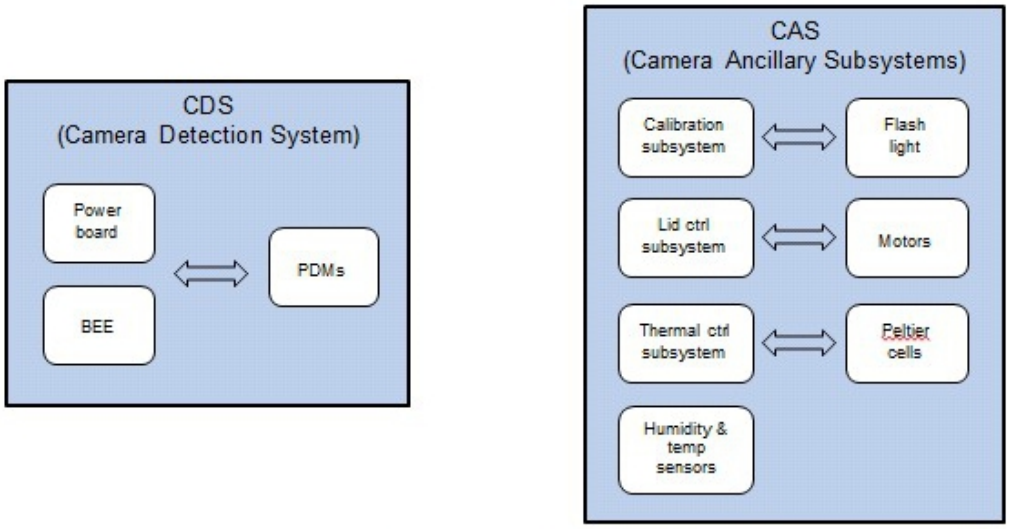

Figure 3.56: ASTRI CDS and CAS block diagram.

ASTRI Camera Slow Control

The operating logic of the Camera slow control is shown in Figure 3.57. The block diagram illustrates how the modules will communicate with each other. The ASTRI Camera Controller provides the slow control of the ASTRI Camera, i.e. configuration, command and HK (House Keeping) monitoring. The Camera Server receives bulk data from the Camera at two different levels: instrument level and observatory level. As shown in Figure 3.57, the interface between the user and the ASTRI Camera is realized through two further modules: the *DCS* (Detector Control Software) and the *CADC* (Camera Ancillary Device Control). These two modules are placed at an intermediate level and are completely transparent to the user.

Figure 3.57 shows the configuration foreseen for the integration and test of the Camera before delivery to the Observatory. Details on the configuration foreseen for Camera operations at Observatory level are given in the Control Software section (section 3.9).

The *DCS* module is responsible for handling the Camera Detection Subsystem, in particular it:

- Sets the SiPMs voltages after CDS bootstrap.
- Receives high–level commands from the user and converts them to low–level operations to be sent to the CDS in the various operating modes. e.g.:
  - Calibration mode;
  - Science mode;
  - Maintenance mode;

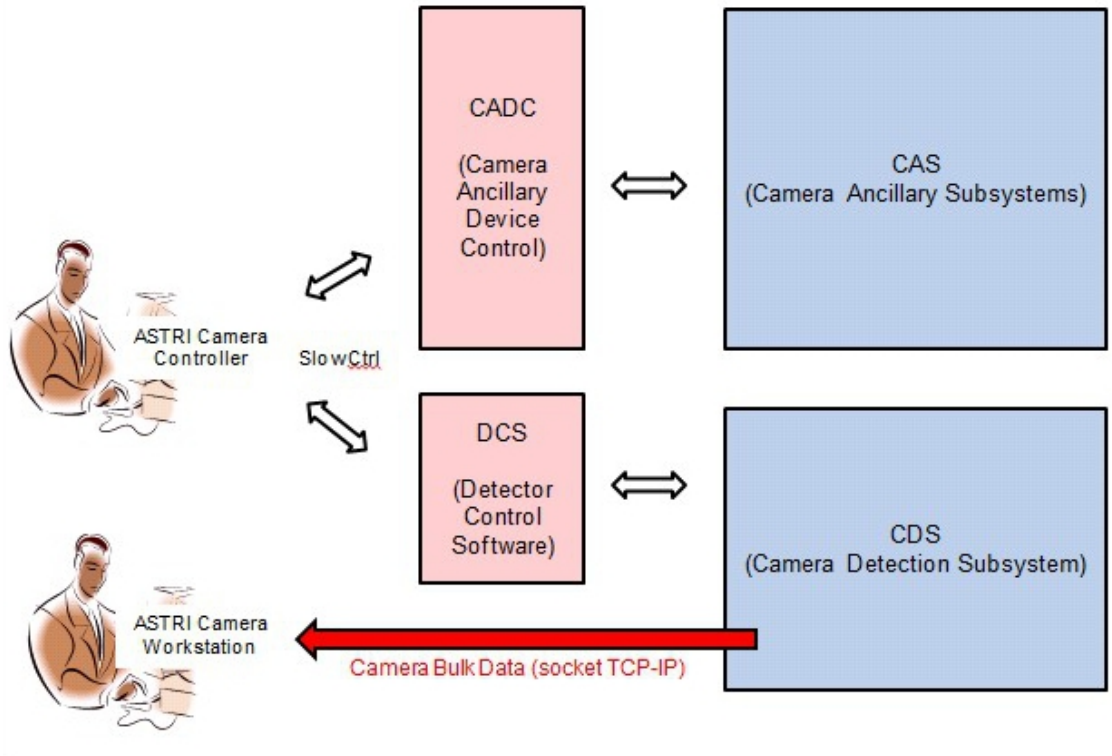

Figure 3.57: ASTRI Camera Slow Control and Data Acquisition block diagram.

  - Safe mode.

- Receives data from the CDS module; there are three possibilities:
  - single SiPM temperature (16x37 values);
  - average temperature for single PDMs (37 values);
  - average overall PDMs temperature (1 value).

The *CADC* module receives high–level commands from the user and converts them to low–level commands to be sent to the CAS, e.g.:

- calibration subsystem commands for turning on/off the fiber-optic flasher;
- lid control subsystem commands for opening/closing the lid;
- thermal control subsystem commands for temperature regulation of the Camera.

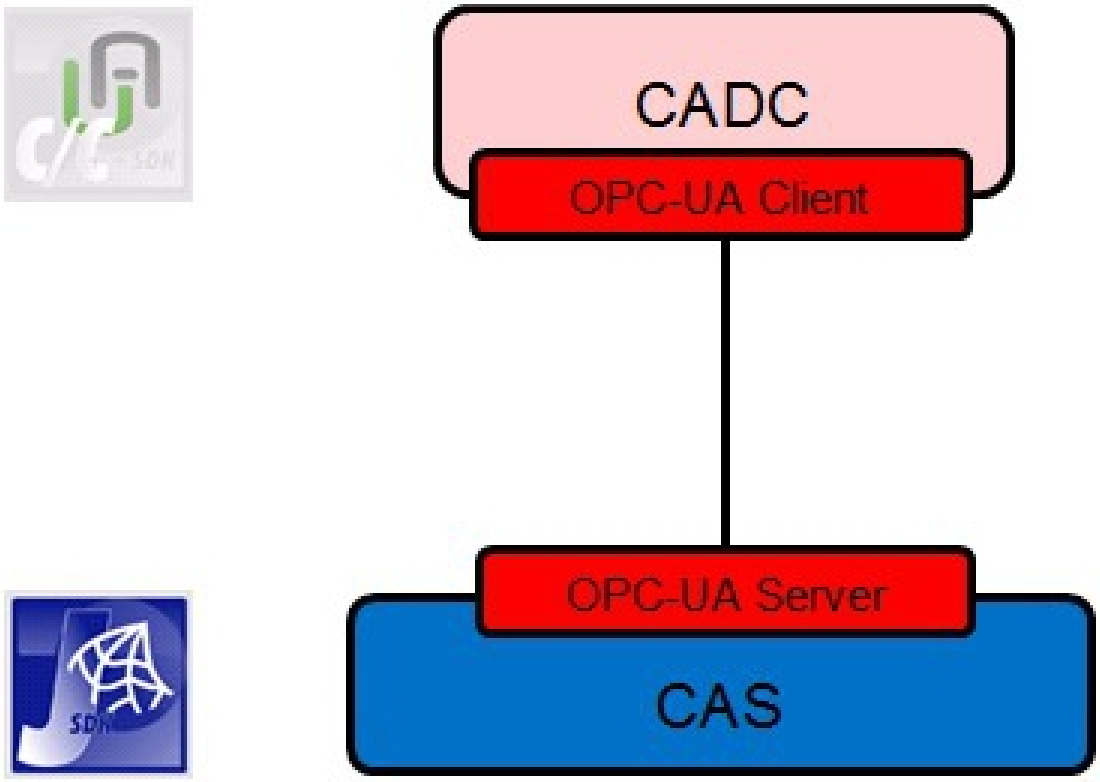

Figure 3.58: ASTRI Camera Software Infrastructure

The CADC also receives data from the CAS, in particular:

- flasher status (on/off);
- lid status (open/closed);
- humidity secondary sensors;
- temperature secondary sensors.

ASTRI Camera Software Infrastructure

The connection between *CADC* and *CAS*, as shown in Figure 3.58, could be realized through OLE for Process Control – Unified Architecture (OPC–UA) technology.

The OPC Unified Architecture (UA) is the next generation OPC standard that provides a cohesive, secure and reliable cross platform framework for access to real time and historical data and events. OPC UA is designed for high reliability and redundancy. Completely configurable timeouts, error detection, and recovery features allow OPC UA products to seamlessly deal with any error or fault conditions (such as the loss of network communication). The standard OPC UA model for redundancy allows applications from different vendors to be deployed.

Some tests

Some sample tests with OPC–UA architecture were performed, using:

- a Java OPC–UA console server from Prosys;
- a Java OPC–UA graphical client from UaExpert.

The first tests were encouraging, and the next test will be the data reading from the Serra La Nave weather station. Such data could be useful and integrated in the ASTRI Camera monitoring. The OPC–UA server could run directly on the ASTRI Camera, which is equipped with the ARM Cortex A9 CPU or similar, integrated on board the FPGA front–end module. The OPC–UA client should run on an external computer, that will coordinate all the Camera operations.

3.7.6 Reliability, Availability, Maintainability and Safety

For the RAMS of the ASTRI Camera the same observations of Section. 3.11 are applicable.

3.7.7 Test plan

The ASTRI Camera assembly will go through different levels of verification and tests before its integration on the telescope. The test flow can be summarized as follows.

- Characterization of MPPCs. Each SiPM will be tested and characterized in order to tune the best bias for best performance.
- Each PDM will be electrically tested before being integrated in the focal plane.
- A camera mock-up is actually under test in order to verify the thermal control system. The mock up is installed outdoors at the SLN site.
- The camera structure is under construction and will be tested mechanically.
- Interface test between PDM, BEE and VDS will be performed before integration of the Camera.
- Once integrated, the camera will be tested against the assembly requirements. Instrument slow control and Data Acquisition System (DAQ) interfaces will be tested at the same time. A secondary objective of the assembly test is to perform and validate the Camera operation procedures.

3.7.8 Maintenance and operation

The Operating Modes of the ASTRI Camera are summarized in Figure 3.59.

<table>
<tr><th>MODE</th><th>OPERATIONS</th></tr>
<tr><td>OFF</td><td>This state provides to the Camera an initial and stable state with all on-board equipment deactivated.
<table>
<tr><th colspan="6">VOLTAGE</th></tr>
<tr><th>MPCC</th><th>FEE</th><th>BEE</th><th>LID</th><th>CCD cameras</th><th>OPTIC-FIBER</th></tr>
<tr><td>OFF</td><td>OFF</td><td>OFF</td><td>OFF</td><td>OFF</td><td>OFF</td></tr>
</table></td></tr>
<tr><td>STANDBY</td><td>This is the default state. The BEE FPGA executes routine tasks such as housekeeping and sensors reading, command transmission tasks and power management. All the other functions of the BEE and FEE, except MPPC temperature sensors reading and HK, are also deactivated.
<table>
<tr><th colspan="6">VOLTAGE</th></tr>
<tr><th>MPCC</th><th>FEE</th><th>BEE</th><th>LID</th><th>CCD cameras</th><th>OPTIC-FIBER</th></tr>
<tr><td>ON</td><td>ON</td><td>ON</td><td>ON</td><td>OFF/ON</td><td>OFF</td></tr>
</table></td></tr>
<tr><td>SCIENTIFIC</td><td>This is the data acquisition state. In this state, the BEE is processing the image being acquiring from the FEE and manages the transmission to the Workstation-console. This state automatically switches to/from the calibration state to ensure the required accuracy on the final scientific data (TBC).
<table>
<tr><th colspan="6">VOLTAGE</th></tr>
<tr><th>MPCC</th><th>FEE</th><th>BEE</th><th>LID</th><th>CCD cameras</th><th>OPTIC-FIBER</th></tr>
<tr><td>ON</td><td>ON</td><td>ON</td><td>ON</td><td>ON</td><td>OFF</td></tr>
</table></td></tr>
<tr><td>CALIBRATION</td><td>Under this operational state, the FEE FPGA performs the required operations to assure the proper calibration procedures. This routine operation will consist on a set of measurements capable to verify the camera health (on line) and contemporarily store all the related information for further analysis (off-line). Depending on the calibration procedures, Lid has to be closed.
<table>
<tr><th colspan="6">VOLTAGE</th></tr>
<tr><th>MPCC</th><th>FEE</th><th>BEE</th><th>LID</th><th>CCD cameras</th><th>OPTIC-FIBER</th></tr>
<tr><td>ON</td><td>ON</td><td>ON</td><td>ON</td><td>ON/OFF</td><td>OFF/ON</td></tr>
</table></td></tr>
<tr><td>SAFE</td><td>All the subsystems are disabled and the BEE is monitoring the global Camera temperature sensors providing the necessary power to be active. The objective of this state is to perform an active thermal control and to implement FDIR.
<table>
<tr><th colspan="6">VOLTAGE</th></tr>
<tr><th>MPCC</th><th>FEE</th><th>BEE</th><th>LID</th><th>CCD cameras</th><th>OPTIC-FIBER</th></tr>
<tr><td>OFF</td><td>OFF</td><td>ON</td><td>ON</td><td>OFF</td><td>OFF</td></tr>
</table></td></tr>
</table>

Figure 3.59: Operating modes of the ASTRI Camera.

3.8 Telescope assembly

3.8.1 Preparation

The telescope shall be prepared with the following parts assembled:

1. Base Structure, Azimuth Column, Azimuth Fork, Elevation Bearings, Elevation Stow Pin, all together assembled with the Azimuth Stow Pin engaged.
2. Lower half Dish.
3. Upper half Dish.
4. Elevation Actuator.
5. Two Counterweights.
6. Arms of the Counterweight.
7. Central Tube with its M1 Dish Interface.
8. M2 Backup Structure, M2 Load Spreaders, M2 Dummy, M2 Covering and Optical Baffle.
9. Mast beams.
10. 18 Segment Triangles with their Support Spacers.
11. Power Cabinet with its support.
12. PLC and Interface Cabinet with its support.
13. Cables.
14. Spare parts.

The suggested personnel needed during the assembly consist of at least:

- 1 manager responsible for all elements provided by INAF, for the safety of the personnel and for the telescope, including the facilities needed during assembly and testing.
- 1 engineer from the supplier of the telescope to give information to the manager during all assembly and testing activities.
- 1 technician provided by the supplier of the telescope, for mechanical assembly and testing.
- 1 technician provided by the supplier of the telescope, for electrical assembly and testing.
- 1 or 2 technicians provided by INAF to support all activities during the assembly and testing.

The suggested lifting devices and platforms are the following:

- Crane with 20 t capacity, 10 m overhang, to rent for about a week.
- Forklift with 3 t capacity, 3m vertical stroke.
- Cherry picker.
- Hydraulic lift with 1 t capacity, 1.5 m vertical stroke.
- Platform adjustable from 1.5 m up to 3 m height, with ladder and protection.
- Lightweight platform, foreseen to be fixed to the azimuth fork and to the rear part of the dish, with protection.

3.8.2 Assembly on site

The mechanical structure shall be assembled according to the following outline:

- Azimuth column fixing to the foundation (time needed: 3 days).
- Integration of the elevation actuator (time needed: 0.5 days).
- Integration of the lower half of the M1 dish (time needed: 0.5 days).
- Integration of the upper half of the M1 dish (time needed: 0.5 days).
- Integration of the counterweights (time needed: 0.5 days).
- Integration of the central tube and the mast (time needed: 0.5 days).
- Integration of the M2 backup structure, load spreaders and baffle (time needed: 1 day).
- First movement of the elevation axis (time needed: 0.5 days).
- Integration of the M1 Segments support triangles (time needed: 3 days).
- Cabinets (time needed: 0.5 days).
- Cabling (time needed: 5 days).

The total time required for assembling and testing on site is two months, including 2 weeks as contingency.

The assembling procedures of all the structure items will be prepared and checked by the manufacturer before the telescope is delivered to the site. Afterwards, the results of the integration and test activities performed at the telescope site will be used to correct and update these procedures.

3.9 Control software

3.9.1 Introduction

The Context

In the framework of the ASTRI Project, the control software of the ASTRI SST–2M telescope is only a part of the Mini–Array Software System (MASS) that has the task of making it possible to achieve the goals stated in the ASTRI System Requirement Document (SRD), both for the single telescope and the Mini–Array, responding to the constraints and requirements contained in the ASTRI Operation Modes and User Requirements document [RD2]. Further, the design must be compliant with the CTA Data Management (CTA-DM) and CTA Data Acquisition and Array Control (CTA–ACTL) requirements and guidelines.

The MASS is being designed to allow a member of the ASTRI Collaboration (the user) to perform all the steps needed to prepare and execute a scientific observing run. The MASS will provide a set of tools to the user: to prepare an observing proposal, to perform the observations specified therein (after approval by the ASTRI internal Time Allocation Committee), to analyze the acquired data online and to retrieve all the data products from the archive. Also, the MASS will provide the software to manage and administer proposals, to schedule observations, to perform instrument operations and use the data archive.

Hardware Architecture of the Control System

The ASTRI SST–2M is a complex system including several subsystems, such as the telescope, camera and safety systems, that have to be monitored in order to get, in real time, the current status and availability of each component. Also, the different parts of the system have to be controlled in order to perform the operations requested by the user (astronomers, operators, engineers, etc.).

The ASTRI telescope Azimuth and Elevation servo systems are based on brushless motors. Absolute encoders monitor the position of the axes. A state of the art PC–based control technology is used to control the pointing and tracking of the telescope (the Telescope Control System (TCS) in Figure 3.3); this eliminates the need for complex and expensive special hardware (such as a PLC), since the functionality (control, regulation, motion control and visualization) of this hardware can be handled by the software. A fieldbus is used to connect the secondary servo systems, the Active M1 Mirror and the M2 piston/tilt control system as well as other I/O devices. A large number of temperature sensors, strain-gauges and accelerometers are distributed along the telescope structures, mirrors and mirror supports. Given the pointing requirements, $\pm$ 10 arcsec rms, up to 0.5° of zenith angle, two monitoring system are installed:

a) One wide field CCD camera ($\sim 10°$) mounted on the M1 support to obtain an astrometric solution for the parallactic angle useful for the pointing model (sampling rate of the images about 1 Hz).

b) Two 1–Gigabit Ethernet CCD cameras mounted on the ASTRI camera and 18 laser diodes (one for each M1 dish panel) using direct telescope optics to monitor panel and secondary flexures due to wind and gravity (sampling rate for images about 10 Hz).

The ASTRI Camera Back-End is in charge of delivering the Camera bulk data to the Camera Server through

a TCP/IP connection on a 1 (possibly a 10) Gbit fiber Ethernet LAN.

Figure 3.3 does not show several other auxiliary devices such as the Time distribution system, which will be based on a GPS receiver and NTP server (with possible use of the CERN White Rabbit technology for the mini–array, but not the first telescope prototype); the weather station; the fish–eye all–sky–camera (to record the cloud–cover), the Sky Quality Meter (SQM) instrument (to monitor the sky quality), the UVscope–UVSiPM complex (necessary for absolute calibration purposes and the measurement of the the Night Sky Background).

ASTRI SST–2M and Mini–Array requirements

The collection of sub–systems described above, must act in concert under the control of the MASS to achieve the goals stated in the ASTRI System Requirements Document (SRD) both for the single telescope and for the Mini–Array. In particular, the general operations that should be managed by the MASS software are given in the ASTRI Operation Procedures document [RD6] and User Requirements document [RD2]. The requirements listed in [RD1] and [RD2] are compliant with the CTA requirements.

3.9.2 MASS Design Concept

The MASS is being designed to manage the end–to–end flow of information from observing proposals to data delivery. The information flow that will be managed by the MASS (as derived from the list of requirements [RD2] and Operational procedures listed in [RD6]) is shown graphically in Figure 3.60.

The ASTRI Team user initiates the Observing cycle by preparing and submitting a proposal to the ASTRI Time Allocation Committee (TAC). After the proposal has been reviewed and accepted it is inserted in the ASTRI Data Archive. The user observation is then inserted in the Observation plan and in the long term Operations Plan.

The scheduling system will include the proposal in the nightly schedule and the observation will be performed by the MASS Observation Execution subsystem. The raw data collected during the observation will then be stored in a temporary archive and sent to the quick-look processing pipeline for system and data quality validation.

The results of the preliminary analysis can be used to process the next scheduled observation and/or to modify some of the system configuration parameters because of either changes in weather conditions or detection of errors in some subsystems (a halt to the schedule execution for maintenance actions can also be triggered at this stage).

After data quality validation, data will be stored in the on–site Observatory Database ready for post-processing and the delayed (next day) delivery to the off–site ASTRI Data Archive in Rome. The user will receive notice of the availability of the data and will be able to retrieve this data through a Web–based service and will be able to analyze the data using the Science Analysis tools.

This workflow shown in Figure 3.60 can be translated into the conceptual design of the MASS shown in Figure 3.61.

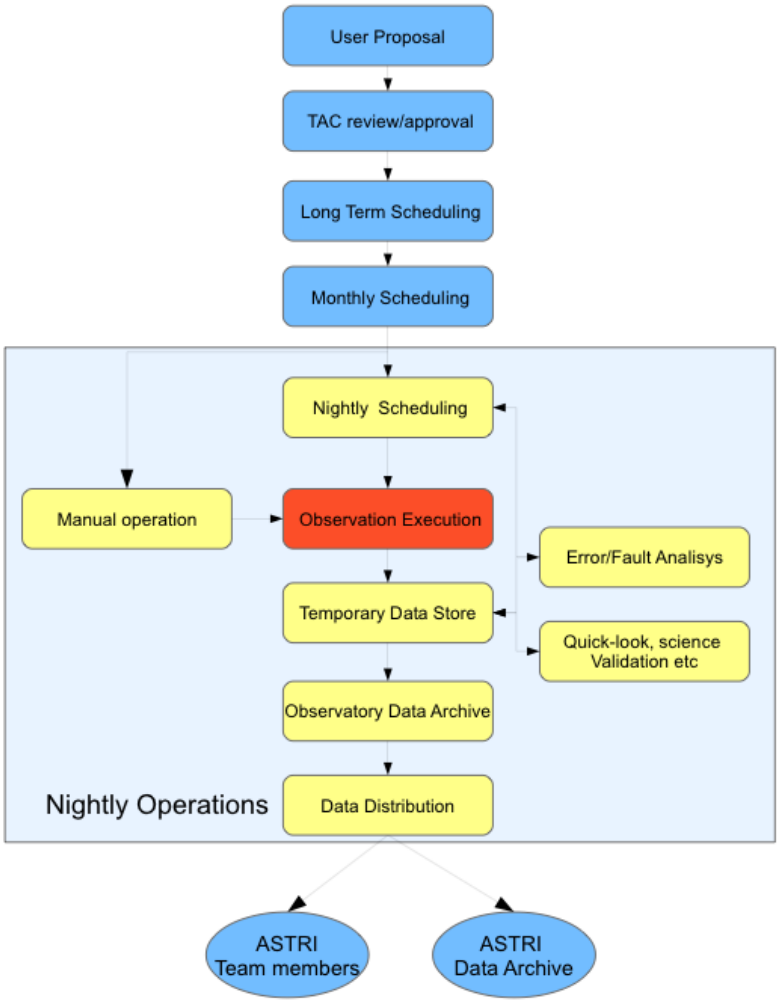

Figure 3.60: MASS information flow.

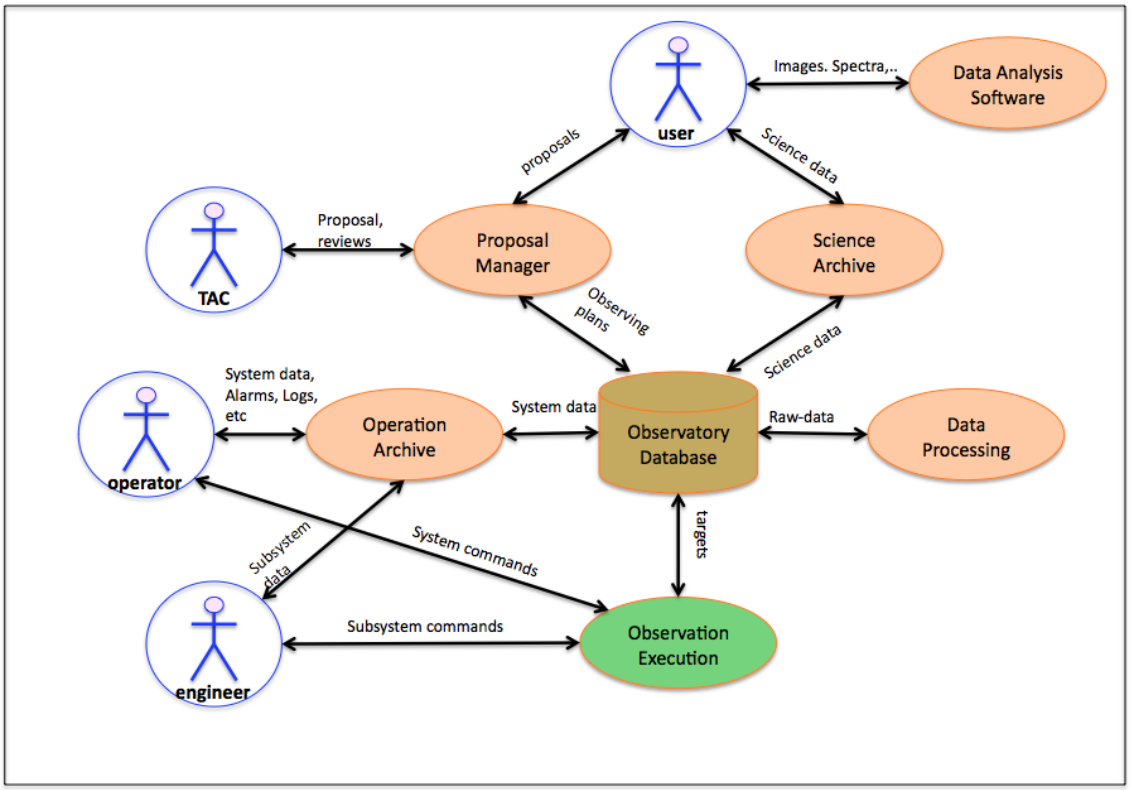

Figure 3.61: MASS Conceptual Architecture.

A central role in the design is assigned to the MASS Observation Execution (MASS–OE) subsystem, which is responsible for the actual observations requested by the user and approved by the ASTRI TAC. This subsystem controls and monitors all ASTRI hardware present at the site: Telescope, Camera, auxiliary devices, safety devices, etc. It can work automatically but an operator will normally supervise it.

3.9.3 The MASS Observation Execution Subsystem

The MASS–OE is a distributed system that, as in many of the most recent telescope control system designs, is composed of the following main components (see also Figure 3.62):

- The observatory control system (OCS).
- The telescope control system (TCS).
- The instrument control system (ICS).

- The data handling system (DHS).
- The Calibration/Auxiliary control system (CACS).

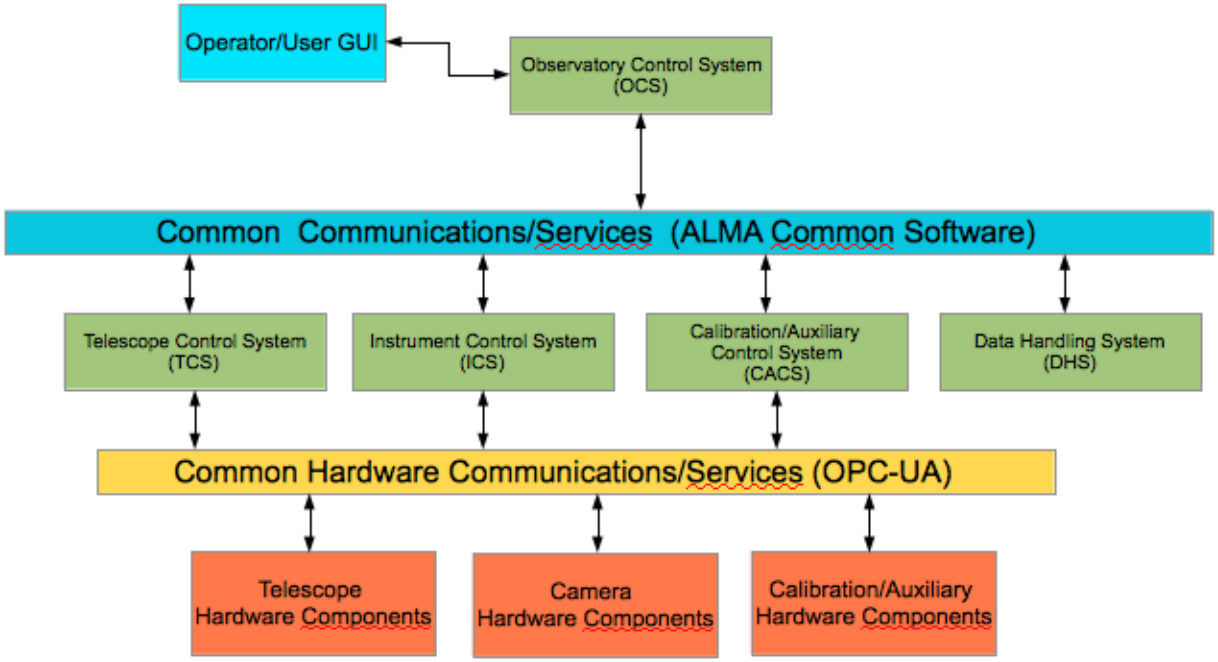

Figure 3.62: Main Components of the MASS–OE subsystem.

The CACS includes several components dedicated to monitonring and control tasks; at the Serra La Nave site, where the ASTRI SST–2M prototype telescope will be installed, the following auxiliary instrumentation is part of the CACS:

- The weather station and the rain sensor.
- The Time Synchronization and distribution system (GPS, etc.).
- The All–Sky Fish–Eye camera.
- The Sky Quality Meter (SQM).
- The UVscope–UVSiPM complex.
- Further devices now under investigation.

ALMA Software reuse in the MASS

From a communications and integration perspective, the MASS–OE is a distributed system. In other words, the system consists of a set of relatively autonomous software entities ("objects") interacting with each other through a software communications (middleware) backbone.

The wide use of uniform software frameworks in astronomical contexts has demonstrated their apability to simplify the development and maintenance of complex observatory control systems by providing a common programming environment and common services.

The MASS software will use the *ALMA Common Software* (ACS) framework, developed as the foundation for the software system for the Atacama Large Millimeter/submillimeter Array (ALMA). Furthermore, several aspects of CTA (and Mini–Array) system operations are nearly the same as those of ALMA. For instance, the control and synchronization of arrays of telescopes/antennas, the dynamic scheduling of observations, the acquisition of high–rate data and its storage in petabyte–scale archives, the monitoring, storage and analysis of data from hundreds to thousands of sensors mounted on telescopes and instruments, and the use of scripts to implement diverse observing modes.

Starting from these considerations an agreement for the sharing of the software developed by the ALMA Observatory with the ASTRI Project of Italy's Istituto Nazionale di Astrofisica (INAF) and the MST Project of Germany's Deutsches Elektronen–Synchrotron (DESY) and Humboldt University zu Berlin (HUB) has recently been signed.

With this agreement, together with the use of ACS as middleware, the MASS will be able to reuse additional ALMA software that, with modest refactoring, would be useful to speed-up the design and the development of the MASS. Among the ALMA software packages that will be adapted for use in the MASS are: the Operations Monitoring and Control (OMC) graphical interface to the system, the Operator's Shift Log Tool, the Telescope Monitoring and Configuration Database (TMCDB), the Control Command Language and other packages that may be mined for their algorithms rather than directly for their code. The ALMA Software System Architecture is described in [RD7], the OMC in [RD8], the Shift Log Tool in [RD9], the TMCDB in [RD10] and the Control Command Language in [RD11].

ALMA Common Software (ACS)

The ACS, developed by the European Southern Observatory for the ALMA project, provides the communication and coordination facilities for the main software components. It facilitates distributed development as well as distributed operations through a component-container paradigm. Individual developers concentrate on the creation and testing of components that, following a standard interface definition and protocol, are straightforward to integrate and test with other components in the system, for example, those developed at remote institutes.

Among the many advantages offered by the use of a common framework like ACS one of the most important is the possibility to have a clear separation of technical (*i.e.*,computer–science related) and functional details so that the developers can concentrate on applications, not on the underlying software infrastructure.

ACS is an optimal candidate for the standard framework for CTA, since it is successfully managing the 45 antennas that constitute the ALMA observatory (a number that will shortly rise to 66) and thus has proven itself capable in a distributed environment similar in topology and scale to that planned for CTA. The use

of ACS for ASTRI will enhance the role of the ASTRI project as a technological demonstrator also from the software point of view.

Applications are built with ACS as many independent components that communicate with each other using a number of common services. Typical technical aspects of system integration, such as distribution, deployment and location of other components, are hidden from the developers. All these technical issues are the responsibility of containers provided by the framework.

Among the common services provided by ACS that are also required by CTA, there are:

• Application communication handling: locate and connect to other applications in a distributed environment based on the CORBA standard [RD4].

• Event Handling: high-performance asynchronous messaging system.

• Command: client/service communication for application control.

• Logging: telemetry capture as well as collection, recording, distribution and analysis of messages.

• Persistent Store: hold system configuration information, calibration data, performance data, etc.

• Error/Alert Handling: monitor for improper behavior, report error conditions, and support recovery operations.

A complete description of the ACS software can be found in [RD3].

3.9.4 The Observatory Control System

The OCS is responsible for high-level ASTRI operations; it provides user interfaces, scheduling and execution of observations, system monitoring, and coordination of the TCS and ICS actions to acquire and monitor bulk data, which then will be stored and displayed by the DHS.

The OCS also provides high-level graphical user interfaces (GUIs) for system operators and observers, system status monitors, and environmental status monitors. A preliminary view of the main logical blocks of the OCS system is shown in Figure 3.63

Most of the software components of the OCS will be modified versions of the corresponding ALMA Software. In particular, most of the functions of the OCS Manager are those of the ALMA Executive software subsystem. Consequently, we are now working to remove all ALMA dependences from the ALMA OMC (that is the Operator Graphical User Interface) and the Operator's Shift Log Tool.

For the ASTRI SST–2M system, the Scheduling needs are very limited and we are planning a minimal implementation of this module concerning the "observation planning" part while we will implement the software modules that will allow observing in an automatic mode.

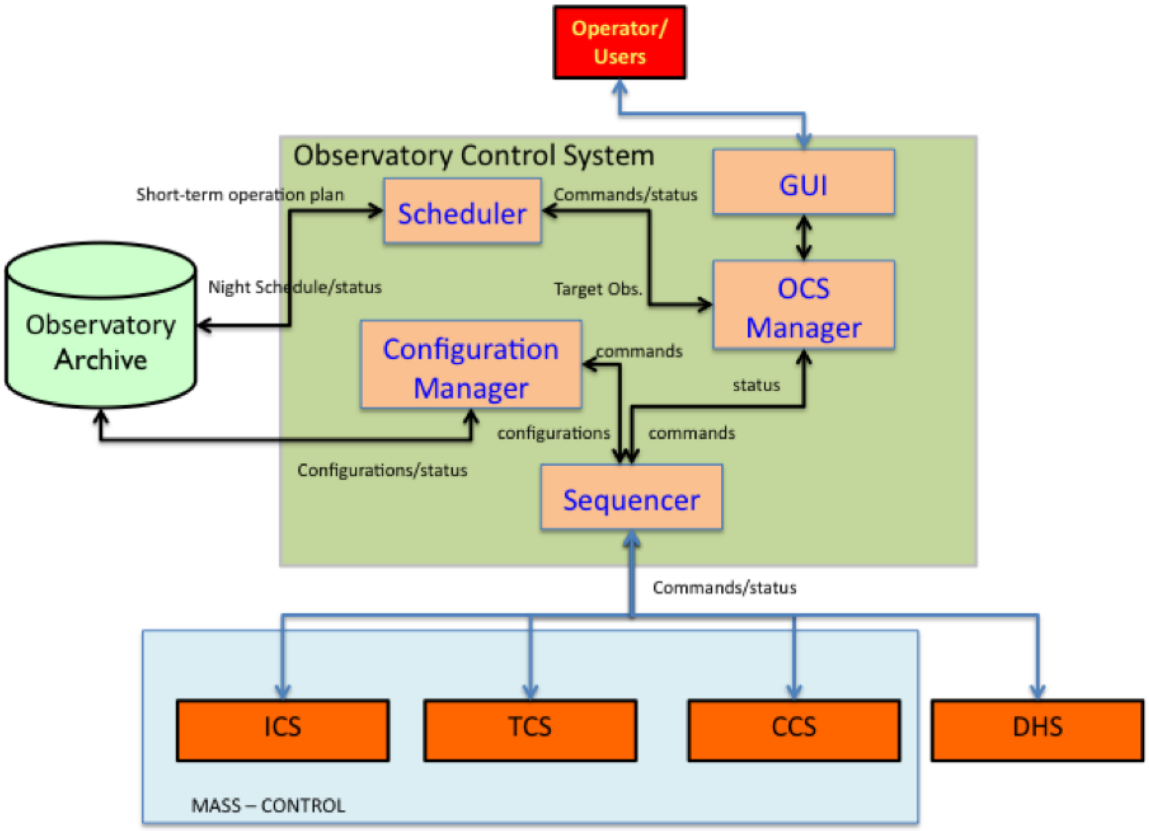

Figure 3.63: Main components of the OCS.

3.9.5 MASS–CONTROL

The TCS, ICS, CACS form the MASS–CONTROL subsystem of the MASS–OE, which is devoted to the monitoring and controlling of the ASTRI SST–2M telescope and to the execution of scheduled observation programmes. The ALMA Observatory, CTA and the ASTRI Mini-Array are arrays of telescopes and the ASTRI SST–2M is a prototype of one of the telescopes that will be part of the array. Because of their similarities and to accelerate the development phase of the MASS–CONTROL, we plan to modify and adapt to our scope several parts of the ALMA CONTROL software subsystem. This subsystem is already designed to monitor and control arrays of telescopes. Also, it can operate independently of all other software subsystems and offers a Control Command Language that allows direct access to all devices so that it is possible to write scripts to implement and test different operating modes (*e.g.* maintenance, engineering testing and debugging) and data–taking procedures.

Hardware Interface Layer: OPC–UA

With respect to the ALMA CONTROL software, a simplification introduced in the MASS–OE is represented by the use of the standard OPC (Open Productivity & Connectivity) -UA (Unified Architecture) [RD5] to access all telescopes devices. This will allow us to decouple high-level control software from the specific hardware device used and from proprietary communication protocols.

OPC–UA is designed to be independent of the operating system. It can be deployed on Linux, Windows XP Embedded, VxWorks, Macintosh OS X, Windows 7, and Classical Windows platforms. This also enables OPC to communicate over networks through Web Services. Client software is already available that enables access to OPC–UA servers by ACS components.

We have performed some tests using the Java OPC-UA console server and client from *ProSys* and a Java OPC–UA graphical client from *UaExpert*. The results of these tests were encouraging and OPC-UA will be used as the standard communication protocol to access all ASTRI SST–2M and Mini–Array devices.

The Telescope Control System

The scope of the TCS is to provide a high quality stable image of a specified point on the sky to the ASTRI Camera at the focal plane. The TCS does not include direct control of any ASTRI hardware; this is the responsibility of its subsystems, *e.g.* the Mount Control System and the Active Mirror Control System, which will communicate with the dedicated OPC-UA servers installed on the devices present on board the Telescopes.

The preliminary design of the TCS system is shown schematically in Figure 3.64.

The TCS coordinates and controls the activities of its subsystems under instruction from the OCS. Some of its functions are to:

- Point and track the telescope.
- Monitor and control the thermal loads on the telescope.

- Monitor and control the active optics systems.
- Control the pointing monitor camera.
- Provide interactive control for the observatory operators.

The TCS software package will run on a dedicated PC (TCS workstation) installed in one of the racks present in the control room. This PC will be never turned off.

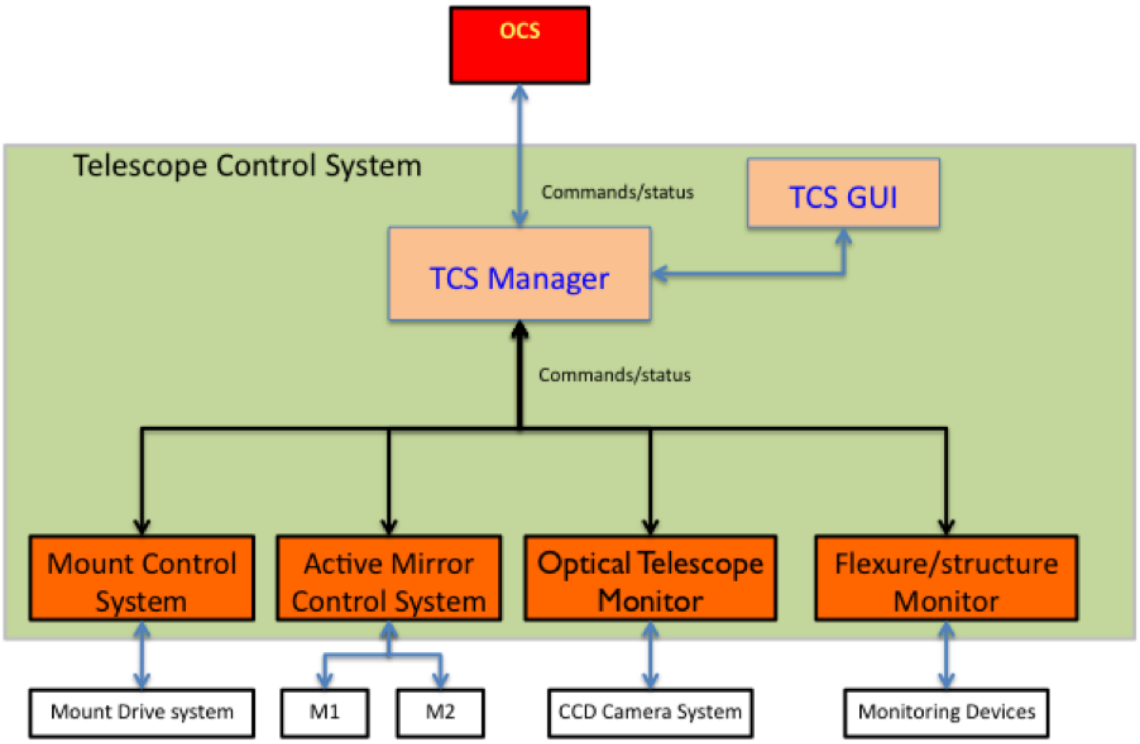

Figure 3.64: Main components of the ASTRI TCS.

Low level Control SW

The Mount Control System and the ACM System, as per Figure 3.64, have the responsibilities to steer the low-level software running on the Telescope Control Unit (TCU) and the Active Mirror Control Unit (AMCU). These two units correspond to dedicated PCs installed in the telescope.

Figure 3.65 shows the proposed deployment of the two main TCS subsystems dedicated to the pointing and tracking of the telescope, therefore to the TCU component. In this figure, the Mount Control system is resident on the TCU and its main responsibilities are:

- Controls the telescope mechanical components.
- Executes telescope motion operations on behalf of the TCS, OCS, and the operator.
- Sequence complex telescope operations.
- Monitors the state of the telescope.

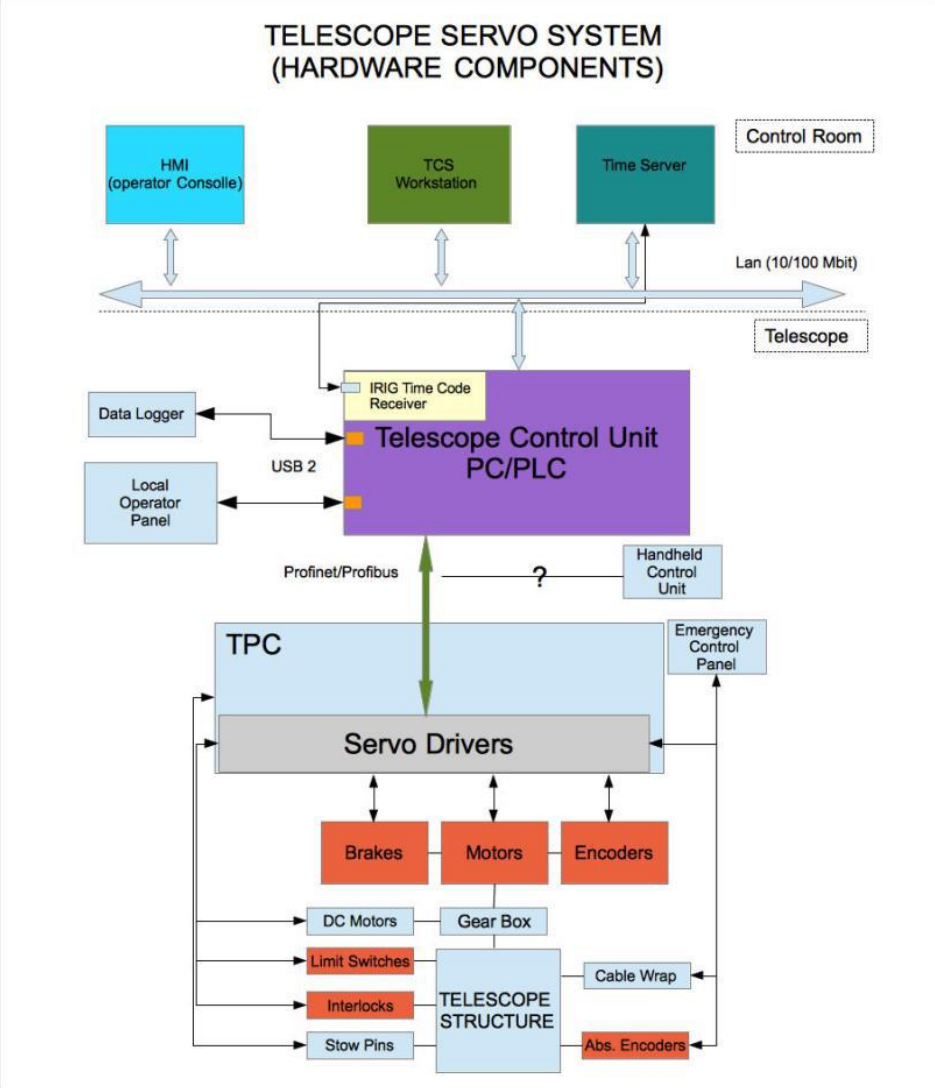

Figure 3.65: HW components of the Telescope Servo System

The other package present on the TCU is the AstroCoordEngine devoted to performing all the coordinate transformations needed to produce the required position of the telescope at a given time in mount coordinates (i.e. encoder coordinates). In our proposed approach, astronomical calculation shall be performed at the level of the servo system. This is not what is usually done to control the pointing of telescopes, where the requested position is sent to the telescope Motion Controller (PLC) by the software resident on the TCS workstation with a given frequency.

A similar approach is followed for the active surface which is controlled by the AMCU installed beside the TCU in the low power telescope cabinet. The Figure 3.66 shows the main subcomponents.

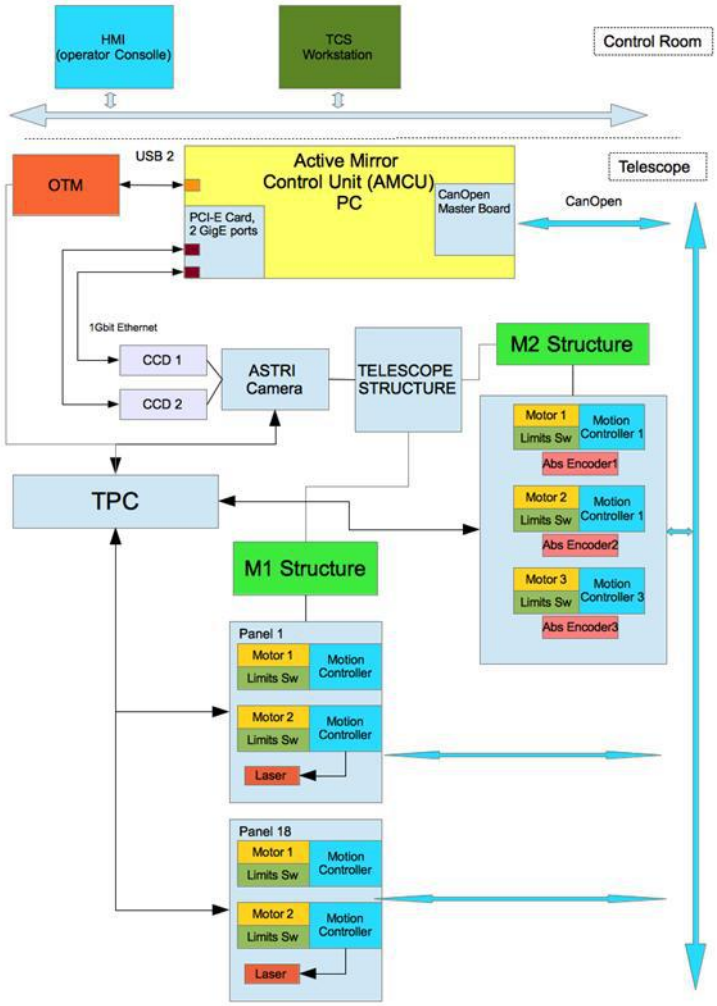

Figure 3.66: Main components of the ASTRI Telescope AMCU.

The Instrument Control System

The ICS provides all software components used to configure, control and acquire monitoring data from the ASTRI Camera. The Camera bulk data acquisition will be discussed in section 3.9.6.

The preliminary design of the logical blocks of the ICS system is shown schematically in Figure 3.67.

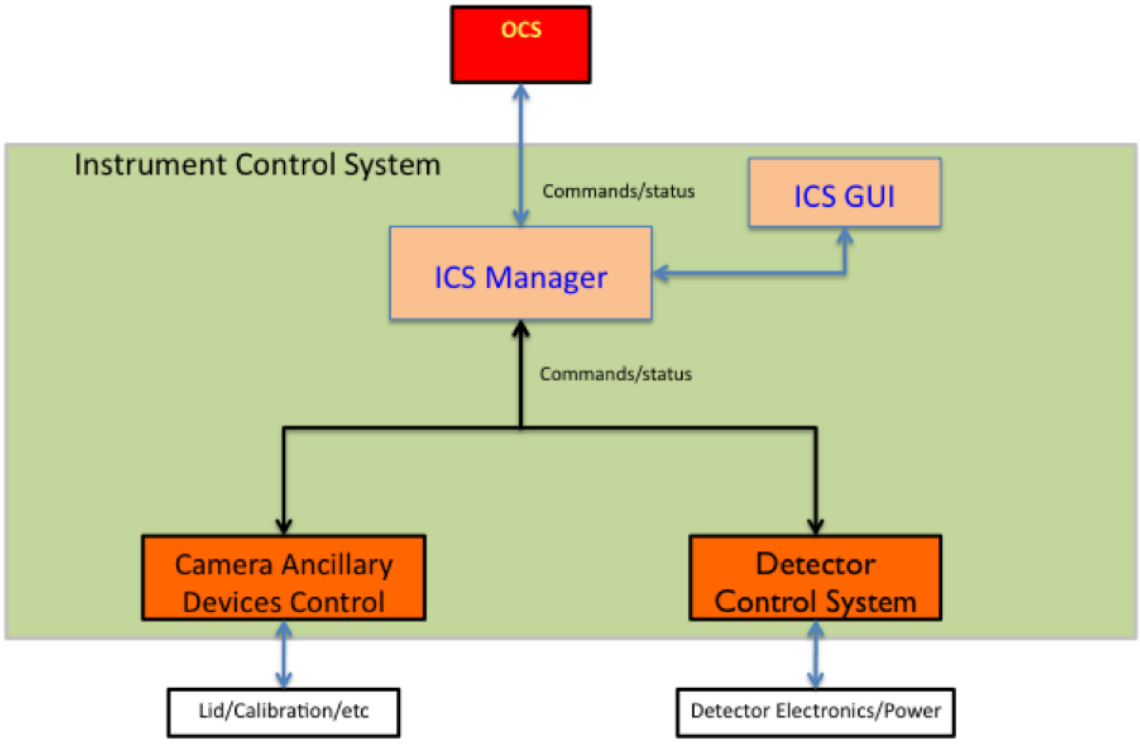

Figure 3.67: Main components of the ASTRI ICS.

The operating logic of the Camera slow control is shown in Figure 3.68. The block diagram illustrates the system, showing the way in which modules will communicate with each other. All devices will be commanded/monitored using an OPC–UA server running on an ARM Cortex A9 CPU (this is the current baseline), integrated on board the ASTRI Camera.

The ICS provides the capabilities for the slow control of the ASTRI Camera, *i.e.*, configuration, command and HK (House–Keeping) monitoring. A GUI that will be available as a plug–in to the modified version of the ALMA OMC will allow direct access to all devices controlled by the Detector Control System (DCS) and the Camera Auxiliary Devices Control (CADC). A more detailed description of the slow control is provided in section 3.7.5.

3.9.6 The Data Acquisition System

The ASTRI Camera bulk data are acquired and monitored by the ASTRI Data Acquisition system (DAQ).

The preliminary design of the DAQ system of the ASTRI Prototype is shown schematically in Figure 3.68. This design allows for a smooth transition to the mini–Array and CTA configurations.

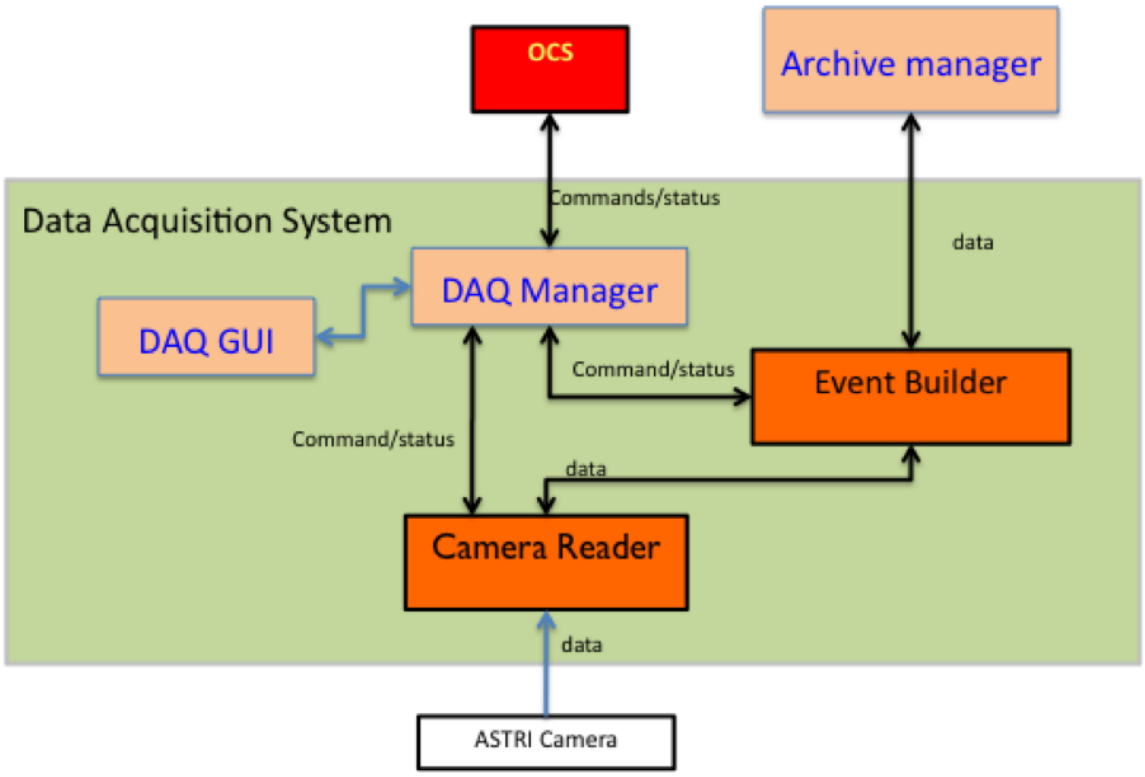

Figure 3.68: Main components of the ASTRI Camera Server

According to the CTA design principle, the ASTRI Camera shall be assigned to one machine, the ASTRI Camera Server, that shall run the Detector DAQ Software (DDS) in charge of collecting the data from the Camera Back End Electronics (BEE).

The Camera BEE shall implement an Ethernet based communication front–end on a Xilinx FPGA which shall send in near real time the Camera data to the Camera Server using jumbo frames and a TCP/IP protocol stack through a point–to–point fiber Ethernet cable.

The data stream sent by the Camera BEE to the DDS shall consist of structured packets with various layouts pertaining to the three main classes: notification packets, housekeeping packets, and science packets. A suitable packet header shall allow the various packet layouts to be distinguished.

The notification packets shall be aimed at notifying the DDS that the Camera operation mode changed from an operation mode that does not perform detector read–out (e.g. IDLE mode) to a mode that does, and therefore generates science packets.

The housekeeping (HK) packets shall host periodic housekeeping information (e.g. voltages, temperatures, ...) generated by the BEE and sent to the DDS in addition to the HK and monitor data sent by the Camera to the Camera Controller. The aim of these packets is to acquire and archive a full set of HK data at sample rates suitable for further on-line and off–line analysis.

The Camera Server will include a component that treats these HK data as individual ACS BACI properties, thereby enabling automatic alarms, for example, whenever a value goes out of its predefined range. In addition, the Camera Server will manage the archiving of these data in the same Telescope Monitoring and Configuration Database that holds all other ASTRI sensor data, following the same Monitor Collector/Blobber mechanism implemented for ALMA.

Each science packet shall host the read-out data corresponding to one "good" event, the trigger time stamp generated by the BEE, and additional ancillary information strictly correlated with the read-out. The size of each packet shall depend on the read–out mode and sub-mode, but will range from $\sim$ 2 Kbytes, in case of 9 PDMs per trigger, to 15.5 Kbytes, in case of 37 PDMs per trigger. Consequently, the data rate ranges from $\sim$ 0.2 Mbyte/s, in the case of 100 trigger/s, to $\sim$ 10.8 Mbyte/s, in the case of 700 trigger/s.

As sketched in Figure 3.69, during ASTRI Prototype nominal operations, the DDS shall implement the data transfer from the BEE memory buffer over the DDS Event Builder to the on-site archive storing the raw data products. In the current design, both TM raw data products and FITS raw data products are being evaluated.

In addition, the DDS shall support Commissioning and non-routine operations (*e.g.*, troubleshooting) by providing local data storage, processing and monitoring capabilities through a suitable operator GUI.

In the Mini–Array/CTA configuration, according to the CTA design, the DDS shall buffer the camera events coming from the ASTRI telescope in the computer memory for several seconds and thus implement a secondary buffer, as required to interact with the Central Trigger and the Array Event Builder (not shown in Figure 3.69). Indeed, this buffering is required in order to perform on each forthcoming "good event" the following procedure: 1) send the time tag to the Central Trigger and 2) wait to know whether to send the data read out to the Array Event Builder or to discard them.

Software prototyping is being carried out to develop DDS modules embedded into ACS components so that DAQ controls, configuration and errors can be handled by the MASS-OE at a higher control level.

3.9.7 The Data Handling System

The DHS is responsible for the management and on-site processing of the large amount of data produced by the ASTRI Camera during operation (of the order of 11 MB/s) as well as its delivery to ASTRI off–site archiving and analysis facilities.

A preliminary view of the MASS DHS system is shown in Figure 3.69. The main modules are the Data

Acquisition system (DAQ), the Archive Manager and the On–Site Data processing pipeline. In the logical design of the MASS, the DAQ discussed in section 3.9.6 is part of the DHS. In the CTA scheme the DAQ is part of the Array Control Software (CTA–ACTL). Independently of this logical aspect, the DAQ system is being developed following the CTA requirements.

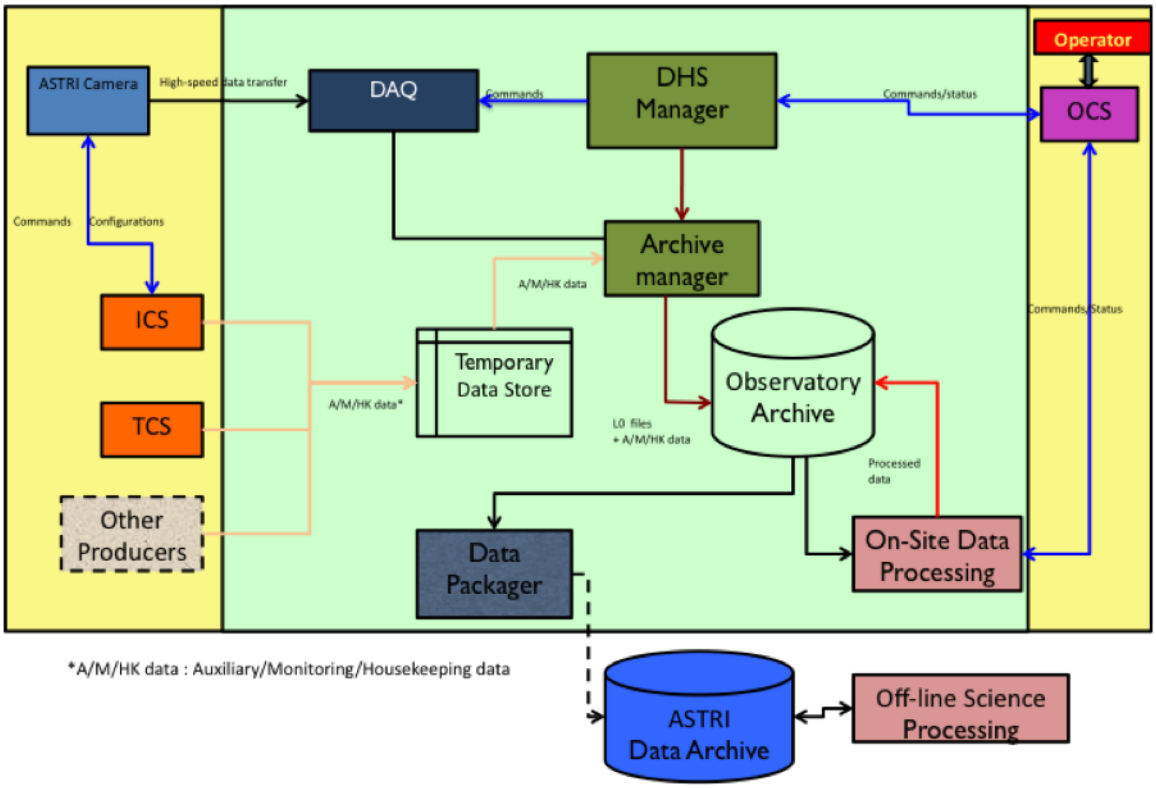

Figure 3.69: Main components of the ASTRI Data Handling System.

Data Archiving

The ASTRI SST–2M prototype is expected to produce a large amount of data (< 1 TB/night), while the mini–Array shall produce < 3 TB/night. This means that an efficient data management and archiving system must be implemented, together with all needed storage devices.

The MASS–OE is responsible only for the on–site Observatory Archive, which will temporarily contain the RAW data files produced by the DAQ, the engineering (HK and AUX) data produced by the MASS-CONTROL and the products of the on–site and online analysis. A fraction of the Monte Carlo data needed for the on–site data processing (see section 3.9.5) will be also stored in this archive.

The off–site ASTRI Data Archive (located in Rome and not part of the MASS–OE) will contain the RAW

data, the data Reduction products and the high–level scientific products.

The conceptual design of both the on–site and off-site ASTRI Archives is shown in Figure 3.70.

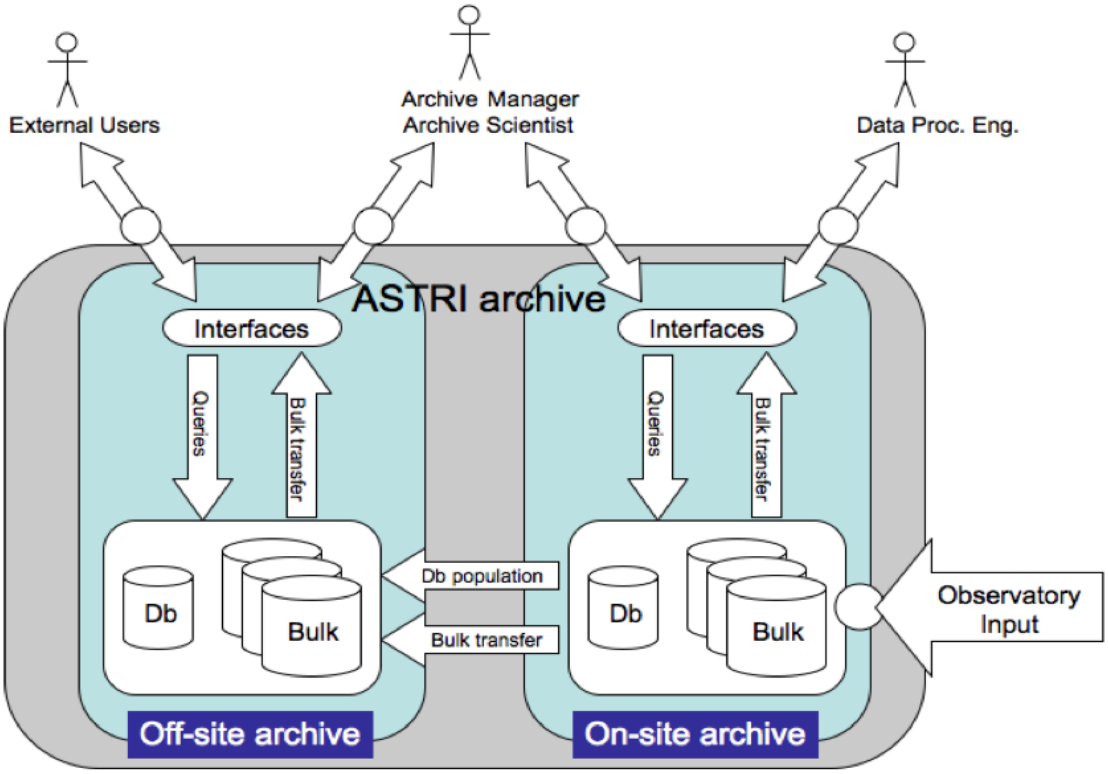

Figure 3.70: Conceptual design of the ASTRI Archive and its users.

The Figure 3.71 shows the logical structure of the ASTRI Archive. It is to be composed of four main logical levels:

• Raw Data archive. This contains the definitive archive of the RAW data produced by the Prototype and the mini-Array and a part of the data products generated from the reduction pipeline excluding L3 and L4 products (sky maps, lightcurves, spectra, see Appendix B).

• Engineering archive. This contains the archive of calibration data as well as the housekeeping and auxiliary information.

• Monte Carlo archive. This contains all the Monte Carlo events simulated for the Prototype and the SST mini-array configurations.

• Science archive. This includes reduced L3 data and L4 products as well as On–site and Real–time analysis

results.

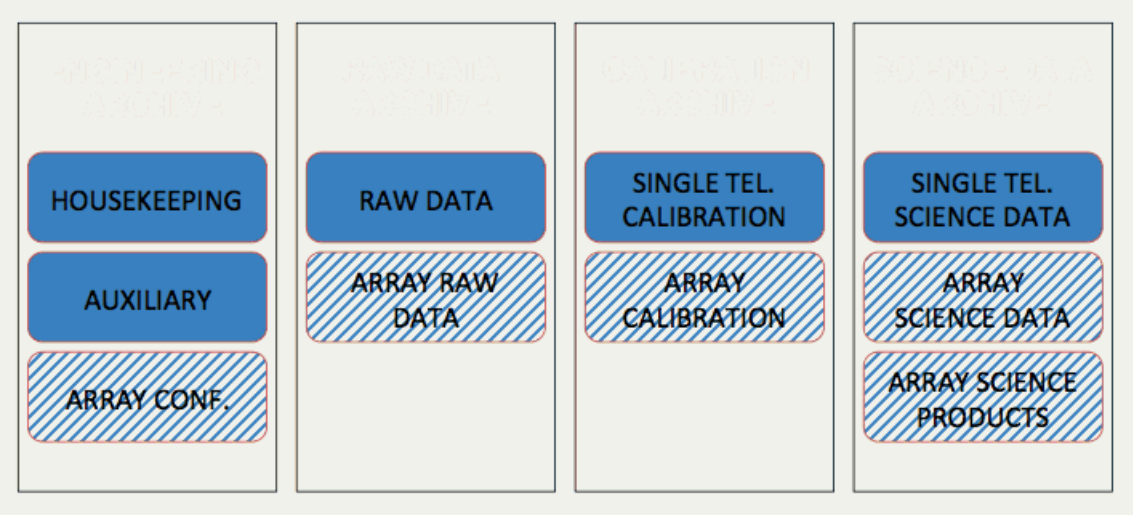

Figure 3.71: Logical structure of the ASTRI Archive.

A set of proper metadata will be defined and stored in a relational database in order to describe the archive content. For the ASTRI SST–2M we are evaluating the use of ORACLE in order to reuse several software components already developed for the ALMA Telescope.

The ASTRI mini–Array data archive will be used as a test bench for the CTA data archive.

On–site Data Processing

The DHS system is responsible for the on–site processing of the data collected by the system (Camera data, calibrations, housekeeping etc.).

Cherenkov telescopes are more complicated than any other instrument that takes direct images of the sky. They require an extensive processing chain to derive scientific information on the primary gamma ray from the Cherenkov images of the air showers as detected by the cameras. The data analysis chain will also critically depend on a wide range of parameters related to both the instrument configuration and the observing conditions. In advance, a complex set of simulations are also needed to calibrate data in order to estimate both the "hadroness" of the incoming primary particle and its energy. A brief summary of the analysis steps is reported in Appendix B.

We can distinguish different kind of analysis managed by the DHS System.

• **Quick–look analysis:** analysis aimed at providing basic monitoring quantities in (almost) real–time in order to let the operators check that the hardware/software subsystems are behaving properly.

• **Online analysis:** analysis aimed at providing basic scientific results from a given source (signal detection, skymaps, preliminary flux estimates) in (almost) real–time. This analysis is based on a reduction pipeline simplified with respect to that described in Appendix [A], with already implemented calibration responses (such as pixel calibration factors and already–analyzed Monte Carlo data). The results of this analysis are preliminary and subject to potentially large systematic errors. Nevertheless, they are very useful for giving clues to states of high source activity, hardware problems (in case of observations of known sources), etc.

• **On-site analysis:** complete analysis (see Appendix [A]) of recorded data done with the fully developed official data analysis software. This analysis is not meant to be a real time analysis but rather to provide already reduced data (on a time scale of a few hours) in order to make it possible to send data outside the observatory (the current baseline is data transfer to the ASTRI Data Archive on a daily basis). Due to bandwidth limitations, it will be not possible to directly send raw/calibrated data. The final steps of this analysis pipeline are not necessarily the scientific products, but rather middle-analysis-stage data whose size is reduced enough to make the data transfer possible (e.g. steps up to L1c/L2). This data reduction will be effectively done at the telescope also adopting new High Performance Computing technologies such as those based on Graphical Processing Units (GPUs).

The final data processing will be performed off–site based on the official full analysis pipeline (not part of MASS). The inputs to this analysis are the outputs of the on–site analysis sent from the observatory and its outputs are the high–level scientific products for the observed sources, which will be stored in the ASTRI Data Archive in Rome.

3.9.8 Software Development Infrastructure

All MASS components will be implemented adopting commercial and open source solutions that are already widely used in astronomy and industry:

3.10 Costs

In the following paragraphs the costs of the ASTRI prototype and for a single SST for the CTA array are presented. It should be noted that all the following costs are presented not including VAT (which must be applied according to national/international rules) and with a ± 10 % contingency.

Estimated Cost for Prototype The estimated cost of the mechanical structure of the ASTRI prototype is about Euro 270000 (Table 14). This value is calculated after a very detailed analysis of the single parts of the telescope. The cost details at subsystem level are presented in the following table (mirrors, camera and foundations are not included).

Two additional costs need to be added to this amount, for assembly and testing at the firm (before delivering the prototype to the site) and for the supply of all documentation related to the telescope. It is worth noting that the last of these additional costs is not needed for the CTA array, meanwhile the former is considered to reduce to half due to the assembly of subsystems instead of the entire telescope. All these costs are

Operating Systems	Scientific Linux 6.x - 64 bit Windows 7 - 32/64 Bit
Programming Language	C/C++ Java Python
Build and Tracking Tools	Jenkins Redmine
Software Documentation Tools	Doxygen
Software Repository	Git svn
Collaborative Tools	Twiki Redmine Saros

Item	Euro
Base structure	45121
Azimuth column	47587
Azimuth fork	53506
M1 Dish	34141
M1 segment support components	57945
Counterweights	8547
Central Tube	1752
Mast	4791
M2 Back-up structure	10180
Total	263570

Table 14: Detailed costs of the single items of the ASTRI Prototype.

illustrated in Table 15, including the amounts related to the unit cost of an array of 60 telescopes. Based on previous and similar industry contracts, a good estimate for the mechanical structure is about 200000 Euro.

Mirrors A similar very detailed analysis is done regarding the costs of the mirrors, including the scaled unit amount for an array of 60 telescopes. The totals for all the segments of the primary mirror and the secondary are presented in Table 16.

Item	Cost (Euro, 1 Unit)	Cost/Unit (Euro, 60 Unit)
Telescope structure and electromechanical parts	270000	200000
Assembly and test at firm facility	40000	20000
Documentation (including "as built" drawings, manuals, etc)	40000	-
Structure Total	350000	220000

Table 15: Total cost for the ASTRI structure prototype, including the delivery of technical documentation and test at the facility. Foundations are not included.

Items	Cost (Euro, 1 Unit)	Cost/Unit (Euro, 60 Unit)
M1 (all segments)	83000	60000
M2	35000	29000
Mirror Total	118000	89000

Table 16: Mirrors costs for the ASTRI prototype and the related scaled amounts for the 60 telescopes array.

Camera The camera costs are detailed in Table 17, including the unit amount calculated for an array of 60 telescopes. For the array production it is assumed that the new version of the Hamamatsu SiPM detector is used; in this way, the focal plane doesn't need the light collectors currently used to recover the dead area due to the edge contacts on the sensor.

Item	Quantity	Cost (Euro, 1 Unit)	Cost/Unit (Euro, 60 Unit)
SiPM (9.6° FoV)	496 mod.	70000	40000
Light collectors	496	7500	0
PCB + CAM mech. + Peltier	-	17000	12000
Front-end electronics	2,000 ch.	10000	7000
Power supply board	-	5000	3500
FPGA Triggers	-	6000	4200
Back-end electronics	-	5000	3500
Harness + data stor.	-	3000	2100
Camera Total		123500	72300

Table 17: Cost estimation for the ASTRI camera and the related scaled amounts for the 60 telescopes array.

Control system The costs of the control system are detailed in Table 18; it is worth noting that the estimate of the costs for the array units are rougher than the others presented so far.

Item	Cost (Euro, 1 Unit)	Cost/Unit (Euro, 60 Unit)
Hardware (PC, PLC, etc)	15000	10000
Drivers, amplifier, electronic controls, cabinet	27500	15000
Software Licenses (OPC-UA, Profinet, etc)	2000	
Control System Total	44500	25000

Table 18: Cost estimation of the ASTRI telescope control system and the related scaled amounts for the 60 telescopes array.

ASTRI prototype and large scale production total costs Based on the previous assumptions and calculations, all costs related to the production of the complete ASTRI telescope and the estimated amounts for a production of 60 units are presented in Table 19, including camera, mirrors and control system. Foundation costs are not included.

3.11 Reliability, Availability, Maintainability and Safety

At this stage all subsystems arew working to assure that RAMS issues are correctly addressed with an appropriate design. Most of the efforts regard the telescope subsystems (drive system and AMCU).

In particular the following actions have been considered:

Item	Cost (Euro, 1 Unit)	Cost/Unit (Euro, 60 Units)
Structure	350000	220000
Mirrors	118000	89000
Camera	123500	72300
Control System	44500	25000
Telescope Grand Total	636000	406300

Table 19: Cost estimation of the ASTRI telescope prototype and the related scaled amounts for the 60 telescopes array. Foundation are not included.

- The tilting system for the segments contains a high number of components so a particular effort to obtain high on reliability is being made.
- For each component, an accurate analysis of the Mean Time Between Failures (MTBF) has been taken into account and for those where the possibility of failure is high, easy access for maintenance has been considered in the design phase; for these elements the spare list will be evaluated to guarantee low cost maintenance and availability for the whole lifetime of CTA.
- Regarding the drive system, the access to the azimuth box is very easy, both for maintenance and for manual actuation in emergencies (loss of power). All parts are accessible from the ground, enhancing safety in emergency.

From the point of view of the safety, to assure easy access to mechanical and electrical components, a platform fixed to the fork is considered as an option that could be used during the assembly phase. This platform is fixed over the electrical cabinet, accessible by a portable ladder. In case of important maintenance interventions, parapets can be used. Moreover, the platform permits an easy access to the mirror cell for the insertion of the rods for segment mounting and removal. This platform also allows access to the manual emergency drive system of the altitude axis. In Figure 3.72, the design of the platform and how it is installed and operated at the telescope is shown.

3.12 Test plan

3.12.1 Verification Strategy

The overall verification approach on the ASTRI SST instrument is described in the Verification Plan, which presents at high level the verification strategy of the ASTRI SST system during the life of the project. With reference to the requirements extracted from the System Requirement documentation, the Verification Plan shall give to the AIV/AIT team the right tools and guidelines to perform the complete verification process.

An effective verification strategy shall be identified and followed during the entire execution of the project. The Validation process is the prerequisite for the verification. It is needed to identify all the requirements,

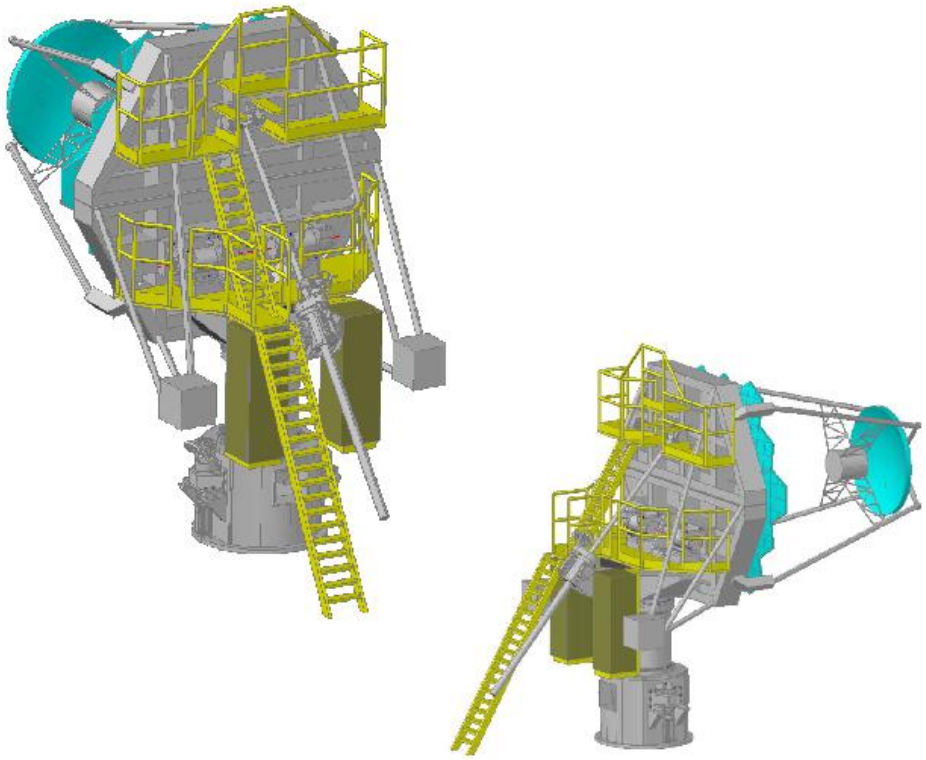

Figure 3.72: Accessing platform for important maintenance operations in the upper parts of the structure.

and only those, that ensure that the project is building the right instrument. Once the requirements have been identified, the Verification process shall demonstrate with objective evidence that the instrument is built in the right way.

The first step of the Verification Strategy shall be the Validation programme. Its output shall be the Verification Control Document (VCD), a living document that lists all the verifiable requirements; these requirements shall be first extracted from the System Requirement Specification document, which is the highest level description of the instrument. The VCD follows the verification status throughout the project's life: it will be kept updated by the AIV team and by the Configuration Manager, and also aligned with the ASTRI System Requirement Specification document. The objective of the validation process is also to have a list of requirements for which a trace to a Requirement document has been identified. Traceability is important because it enable checks that the list is complete (no missing requirements) and consistent (no repetition). The verification status of each Requirement shall be reported and, for each requirement, a suitable verification method (Test, Analysis, Review of Design, Inspection or Certification) shall be identified.

The second step of the Verification Strategy shall be the Verification programme, whose goal is to fill the VCD in all its fields in order to have a final and complete picture of the verification results. To this end, test is the preferred verification tool. Whenever this is not possible, an analysis will be conducted instead. Esamples of typical analysis that can be conducted during the Verification process are: Electromagnetic Compatibility (EMC) analysis, structural analysis, thermal analysis, optical analysis and FMEA (Failure Mode Effect analysis). Specifically for the latter, the ASTRI Project is preparing its FMEA using the guidelines required by CTA Project, which will be described in a document as normal deliverable of the Verification and Validation process. On the other hand, all the necessary Integration and Test activities will be organized in different Integration and Test Points, with the aim of verifying specific subsets of interfaces and requirements. In both cases, the following information will be provided: input needed (i.e. pre–requisites to be satisfied in order to start the activity); high–level description of the activity to be performed; interfaces to be verified; expected outputs and reference person. Unexpected events or problems can occur during all the Integration and Test activities. According to the relevance and type (time, quality, cost) of their impact on the project, these problems shall be classified as deviations, minor problems and major problems; minor/major problems may/must be reported in a Non–Conformity Report (NCR).

3.12.2 Integrations and Tests at sub–system level

In order to check the relevant interfaces and requirements, Integration and Test activities shall be performed at subsystem level before delivery to the installation site. These activities will involve the mechanical system, the optical system, the camera, the foundations, the auxiliary systems, the control system and the monitoring system.

3.12.3 Individual On–site Key Integration Points and Test Points at system level

The flow chart of the Key Integration Points (KIPs) and of the Test Points (TPs) at system level is shown in Figure 3.73. The integration and test of all the telescope items will proceed through the following steps:

- **KIP 1:** Mechanical integration of the telescope structure on the foundations.
- **KIP 2:** Electrical integration of structure, control room, harness and environmental & sky monitors; SW installation and configuration.
- **TP 1:** Functional test of the command procedures for the structure; test of the command procedures of the environmental & sky monitors; test of the control room monitor.
- **KIP 3:** Integration of the mirror servo mechanisms on the mechanical structure; integration of the mirrors on the mechanical structure (Integration of segments on M1 and integration of M2); integration of laser sub–systems.
- **TP 2:** Functional test of the mirror command procedures; test of the mirror configurations; monitoring of the mirror temperature in order to investigate the thermal stresses.
- **KIP 4:** Mechanical and electrical integration of the camera in the telescope.

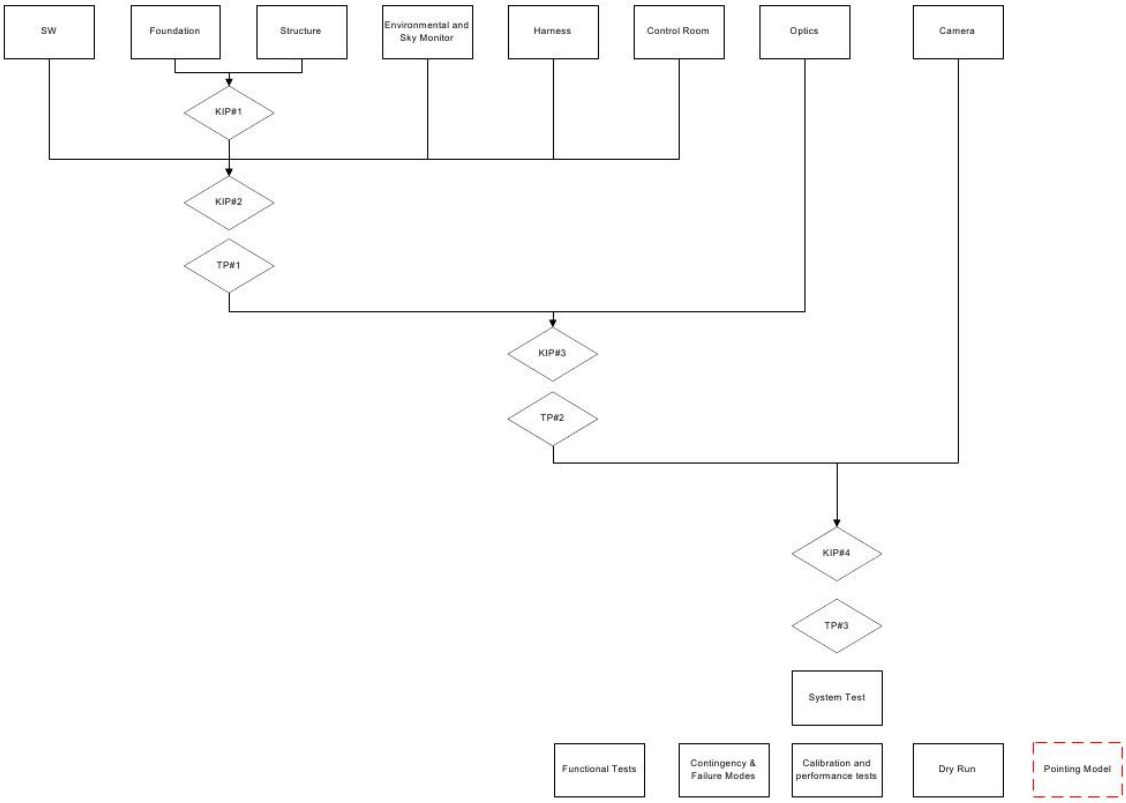

Figure 3.73: Flow chart of the Key Integration Points and of the Test Points at product level

- **TP 3:** Functional test of the command procedures of the camera and validation of the camera TM from the Control Room.

After the successful execution of all the previous activities, the whole telescope will be tested by performing the following operations:

- **Functional Tests:** test of the nominal command procedures of the telescope as a whole; test of the nominal configurations and operating modes.
- **Test of Contingency & Failure modes:** test of the health & safety command procedures to be used in case of anomalous or emergency situations; test of the configurations and operating modes to be used in the case of HW/SW failures.
- **Dry Run:** end–to–end simulation of a whole scientific observation: telescope switch–on, configuration of all the telescope sub–systems (structure, mirrors, camera, sky monitor, control system, monitoring system, ...), calibration, data acquisition.

- **Calibration & Performance Tests:** characterization of all the telescope parameters which are involved in obtaining a target observation.

3.12.4 Deliverables

The following documents will be delivered as outcome of the AIV activity:

- Completed VCD.
- Operation User Manua.l
- Maintenance Manual.
- Installation Manual.
- Test Reports.

3.13 Site consideration

ASTRI is compliant with all site and infrastructure requirements. Nevertheless, there are a few considerations that deserve some explanation.

Transport ASTRI baseline is to ship the telescope in small containers (6 meters). This will minimize transportation problems if steep roads or narrow turns are present in the selected site.

Foundation As the site has not yet been selected, the soil typr in which the foundation will be erected is not known. Without knowing the correct soil type, only a rough estimate of the foundation's dimensions can be made. For the ASTRI telescope, a reinforced concrete foundation $4 \times 4 \times 1.5$ m^3 can be envisaged for "normal" soil.

Installation As in the related chapter where the integration procedure is listed, ASTRI does not need an integration hall to mount the telescope. It will be integrated on the spot once the foundation is ready.

Power At the moment, as suggested by CTA, the ASTRI Project is considering the possibility to install a "supercap" battery to handle the peak power needs of the telescope itself.

3.14 Drives

The control system of the two main axes of the telescope shall be capable of good performance both in pointing conditions and during tracking. The selected drive component is a state of the art Commercial Off-The-Shelf (COTS) component in order to fulfill all the reliability and maintainability requirements from CTA.

The actual baseline solution is a mixed configuration:

- Control hardware (PC, PLC, Interlocks) – Beckhoff that corresponds to the TCU.
- Drive Amplifiers and Motor – Siemens.

The two components use the Profibus field bus to communicate. The baseline solution appears to be the best compromise between performance and cost. The control systems of both axes have three closed loops: the torque closed loop; the velocity closed loop and the position closed loop. All loops will accept the calibration of proportional, integral and derivative control parameters, in order to obtain the best performance.

For the active mirror components, the chosen solution is also mixed between DPB stepper motors and Nanotech controllers, and Beckhoff for the PLC system (basically the AMCU). The chosen field bus is a CAN open bus.

3.15 Power requirements

The ASTRI power budget is described in table 20. The budget has a margin of 10 % to cover hardware installations that have not yet been selected and lists the maximum power needs in order to ensure correct specification of the power grid.

The baseline power distribution which will be used for the prototype will use an automatic switching cabinet before the grid. In the case of power outages, this will switch on a diesel generator. On telescope dedicated UPS components will also be installed in order to guarantee no power off of basic components (this will be included in the Telescope Control cabinet).

These main components are:

- Telescope control unit (the unit in charge of the servo major and Telescope health check).
- Ethernet switch (to keep communication with Computer room).
- Cherenkov Camera (in order to complete data transfer).

In normal operation, the estimated power consumption is 2.5 KW per telescope.

For CTA installation, the telescope will use a different strategy. In order to guarantee the availability of peak power spikes, the baseline is to use a supercapacitor (Supercapacitor Systems – Maxwell). These systems

Name	**Power (Watt)**	**Notes**
Auxiliary Assembly	250	Monitoring components
Major Drive Components	8300	Peak Power during Slew with max wind during operational condition
Active Surface Components	260	Movement of the Active surface (all segments)
Camera Assembly	350	Thermal component included in Budget
TCS Cabinet Components	700	Electronic/PLC/UPS in charge of control/monitoring/communication of the telescope
Optical Calibration Components	110	Lasers and control electronic
Total x Telescope (ROM Budget)	9970	Max power worst case

Table 20: Power Budget

require less maintenance than a UPS and can sustain also the peak power consumption of the major servo drives.

3.16 Maintenance and operation

The ASTRI telecope is designed to have as low a maintenance requirement as possible and when maintenance is unavoidable this is designed to be as simple as possible (e.g. positioning of servo motors). Components of the Telescope are selected not just for their performance but also taking in account their MTBF in order to minimize the maintenance.

The ASTRI telescope shall operate during the night, the maximum period of observation being the time interval between end and start of astronomical twilights, although reduced by initial, intermediate and final operations (e.g. pre– and post–calibrations). The astronomical twilights in Serra La Nave will be automatically computed and made available on an ASTRI web–page where additional information will be available to the Collaboration (e.g. moonlight, ...). The general operational rule is that the ASTRI prototype will perform regular data–taking unless the weather does not allow it. Temperature, humidity, high winds, rain, snow and lightning storms are the main weather conditions under which normal operations could be stopped or not started at all: for this reason some auxiliary assemblies, e.g. weather station, rain meter and lightning detector, must be operational even before any regular ASTRI prototype operational phase. If the sky is cloudy or the atmosphere is not completely clear, normal data acquisition is performed anyway (the atmospheric conditions are always registered in the archive for the data reduction and analysis steps).

The procedural steps needed in order to regularly operate the ASTRI prototype can be summarized as follows, without forgetting that a continuous monitoring of all the key environmental and safety parameters

is mandatory to ensure that they remain within the telescope limits:

1. Pre–operation Check: this includes the presence of all the required "crew" and the absence of critical/emergency conditions. The fulfillment of the pre–operation requirements is mandatory before cotinung to the following actions. (Transition from OFF to SAFE)
2. Telescope Start–up: all the ASTRI telescope components must be active and verified together with the parameters of the auxiliary sub-systems needed to perform the planned operation(s). (Transition between SAFE to STAND BY)
3. Data–taking: the series of necessary modes is applied to achieve operation (e.g. pre–calibration, data taking, post–calibration); the data–taking operation might be designed for special calibration purposes. (Either in SCIENCE, CALIBRATION or MAINTENANCE modes)
4. Telescope Shutdown: all the ASTRI telescope components are switched–off as well as the auxiliary instrumentation not required to be kept active outside ASTRI data–taking. All the ASTRI system parameters must be verified together with those from the active auxiliary sub–systems. (Transition from STAND BY to OFF).

From the instrumental point of view, the control of the data-taking quality and of the ASTRI system performance will be done through the health monitoring; all the functions in the different control subsystems will be monitored through the Operator Console. Any anomalous conditions and remedial actions shall be documented in the proper electronic logbooks, hereafter named "e-log".

The Figure 3.74 describes at very high level the Telecope modes and basic transitions between modes:

OFF Mode: telescope is in safe position (Stowed) and no system is on.
SAFE: the telescope is in safe position (Stowed). Communication components are on. Camera BEE is on. TCU is on.
STAND BY: All assemblies are on, telescope can be in any position (unstowed). Drives are on.
LOCAL: This mode can be accessed only locally. In this mode all the functions of the telescope can be enabled and disabled for testing/debugging purpose. This is the only mode in which the return to SAFE is not controlled by a watch–dog in case of any alarm. To reach the SAFE mode, the telescope needs to be again in stand–by or it has to be manually moved to the safe position as explained in Cap. 3.2.2.

OPERATION MODES (All components are on and some specific procedure is being executed)
MAINTENANCE: For instance telescope is operating a specific procedure to check the optical alignment.
CALIBRATION: Any calibration needed is performed in this mode. For instance calibration of the camera is performed in this mode.
SCIENCE: The telescope is commanded to make science observation and produce science data.

3.17 Summary

In this Chapter we presented the activities related to the development of the ASTRI SST–2M end-to-end prototype that will be installed and operated during Spring 2014 at the INAF Observing Station in Serra

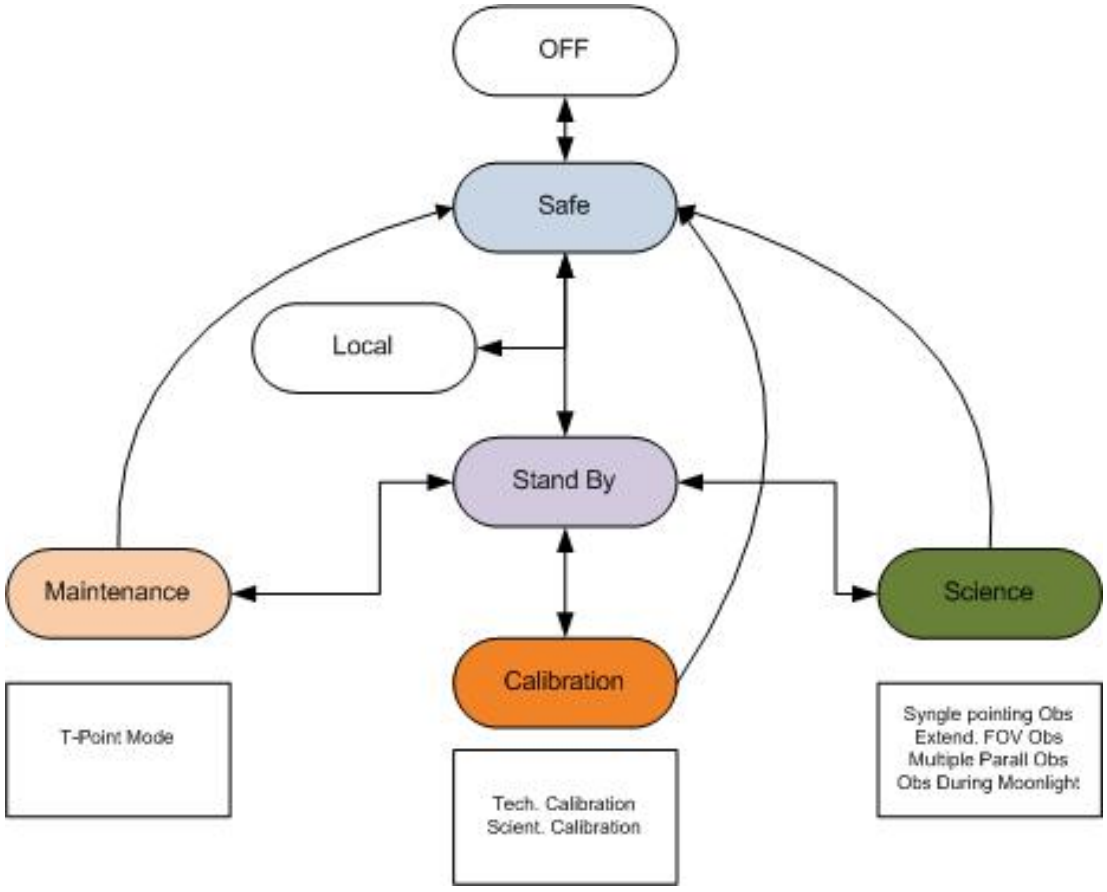

Figure 3.74: ASTRI Telecope modes and basic transitions between modes.

La Nave, Sicily. The ASTRI prototype performance will provide crucial information on several topics, such as the dual-mirror Schwarzschild-Couder optical design, the SiPM-based focal plane and the software/data-handling architecture, all of whc=ich are innovative with respect to the current IACT design. Moreover, the prototype site will allow us to obtain a direct measurement of prominent γ-ray sources, such as the Crab nebula, MRK 421 and MRK 501. THe data from these bsevations will be compared with simultaneous observations from other IACT telescopes, allowing for cross-calibration.

4 GATE

4.1 Introduction

The SST-GATE is a Schwarzschild-Couder (S-C) telescope developed at the Observatoire de Paris in Meudon. The first design of the SST-GATE was produced by the University of Durham, and this has now been optimized by the Meudon team. The mechanical structure, the software architecture and the control and command programming is designed by the Observatoire de Paris. The camera is being developed by an English-Japanese-US team through the CHEC (Compact High Energy Camera) project.
Since the last review in October 2011, the mechanical design has been changed in order to (1) take account of the specific CTA requirements and (2) to build a light and versatile telescope so as to ease assembly and maintainability.

The SST-GATE telescope is defined by the Product Breakdown Structure in Figure 4.1. In summary, the telescope is composed of:

- The FSS (Foundation and Slab Structure) which supports the telescope weight and provides the torque resistance.
- The AAS (Alt-Azimuthal Structure) which allows telescope to point in any direction on the sky and to track any scientific sources with the required accuracy within the limits of the specified environmental conditions (wind speed up to 50 km/h). It also has the function of supporting the optical part of the telescope.
- The MTS (Mast and Truss Structure) which connects the AAS to the optical sub-systems. The AAS is connected to the M1 mirror through the MTS support and the AAS is linked to the M2 mirror and the camera via the truss tubes, assembled in a Serrurier configuration.
- The mirror M1 is supported by a dedicated dish linked to the AAS through the MTS.
- The mirror M2 is supported by a dish connected to the MTS triangular support and holding the camera removal mechanism.
- the camera is supported by arms connected to a triangular MTS support behind M2.
- The TCA (Telescope Control and Alignment) which controls the science operation of the telescope.
- The SDS (Software Data System) which operates the telescope, the data storage and all the alignment systems.
- The PSS (Protective Shelter Structure) which protects the telescope during the Assembly, Integration and Test (AIT) phase and afterwards during the use of the telescope.

	SST-GATE Prototype	SG-SST
1	Telescope Mechanical Structure	SG-MEC
	Foundation and Slab Structure	SG-FSS
	Alt-Azimuthal Structure	SG-AAS
	Mast and Truss Structure	SG-MTS
2	Telescope Optics	SG-OPT
	Primary Mirror Structure	SG-PMS
	Secondary Mirror Structure	SG-SMS
3a	Scientific Detector (Cherenkov)	SG-SDT
	Focal Plane Instrumentation	SG-FPI
	Camera Alignment System	SG-CAMS
	Mechanical Interface between Camera and the scientific camera Holder	SG-MCH
	Data Acquisition Hardware	SG-CAH
	Supplies	SG-SUP
3b	Optical camera	SG-FEC
	Detector	SG-DMS
	Supplies	SG-SUP
	Mechanical Interface between Optical camera and Scientific camera Holder	DG-IOS
	Data acquisition Software	SG-MOH
4	Telescope Control and Alignment System	SG-TCA
	PLC	SG-PLC
	Monitoring	SG-TMP
	Driving	SG-TDP
	Alignment	SG-TOP
	Safety	SG-SAF
	Weather Station	SG-WSA
	Technical Archive	SG-TAR
5	Protective Shelter Structure	SG-PSS
	Shelter	SG-SHL
	Shelter Control	SC-SCT
6	Maintenance Devices	SG-MAD
	AIT Facilities	SG-AIT
	Maintenance	SG-MAI
	Global Safety	SG-SAV

Figure 4.1: PBS of the SST-GATE telescope

4.2 Structure

Several changes have been made to the design presented at the last review Figure 4.2. Section 4.2.1 describes these changes. The second section (4.2.2) presents the detailed mechanical design. The last section (4.2.2.2) focuses on the validation of this complete design to check that it fulfils the required specifications.

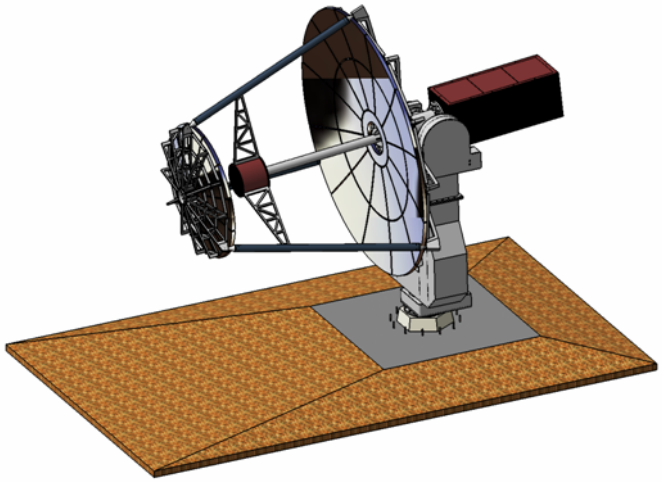

Figure 4.2: SST-GATE design issue Oct. 2011

4.2.1 Conceptual design

When different technical solutions were possible for an assembly or a component of the PBS, these technical solutions were first identified then compared using a decision matrix with the help of a scoring system based on 3 marks and 3 weights. The procedure and the conclusions of this analysis are detailed in the trade-off files.

4.2.1.1 Alt-Azimuthal Subsystem The Alt-Azimuthal Subsystem (AAS) is made of several parts:

- Pedestal, tower.
- Azimuth Drive.
- Forks (lower and upper fork).
- Elevation Drive.

4.2.1.1.1 Lower fork The original design used a long steel fork which allowed the use of the camera electronics as a counterweight. It is now clear that the camera electronics are smaller and less massive than originally assumed, so a new design with a shorter and stiffer fork became possible. Mechanical behaviour calculated by FEA (Figure 4.3) of an AAS with a long and a short fork made with beams and plates of the same dimension and subjected to the same external load, modelling the combination of wind and elevation subsystem mass, is reported below. We deduce from this comparison that the short fork is lighter and less expensive than the long fork while also being stiffer.

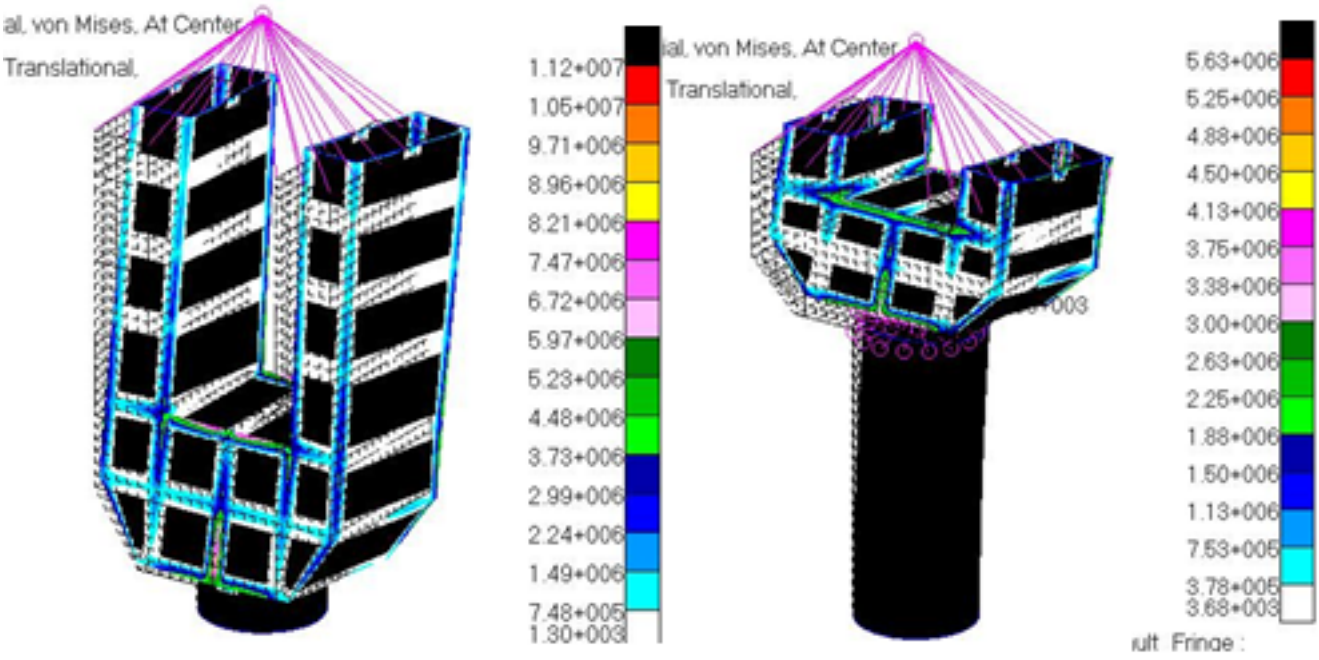

Figure 4.3: Axial bar stresses calculated by FEA of an AAS with a long (left) and a short (right) fork. The masses of these designs are respectively 1.9 and 1 ton.

All the criteria identified in the trade-off analysis concerning the length of the fork (cost, mechanical behaviour, impact on the global accuracy of the telescope, ease of assembly, mass, maintainability) lead to the choice of a short fork.

The shape and concept of the lower fork has also been slightly modified (Figure 4.4). The new fork consists of an assembly of beams covered by plates. This structure fulfils the requirements even if the CoG of the Elevation Subsystem is slightly decentred. Nevertheless, it will have to be modified slightly to match recent progress with the Elevation Subsystem.

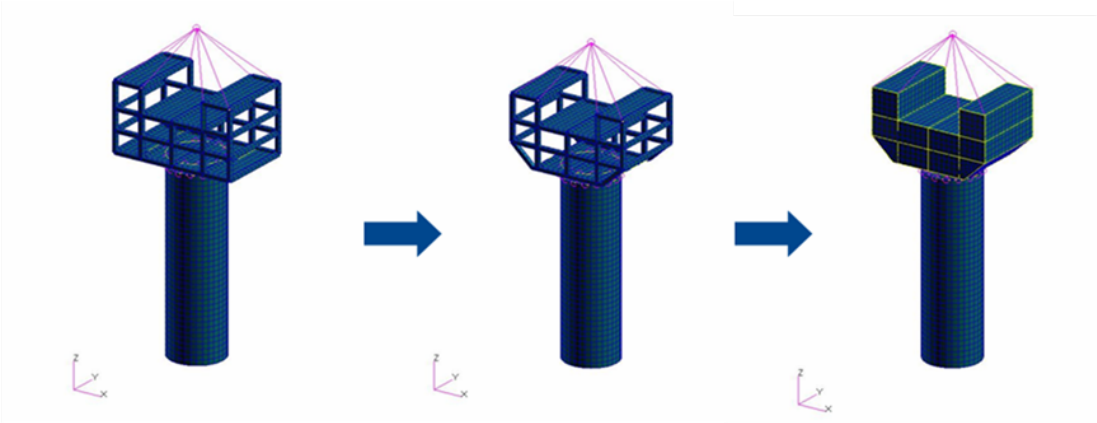

Figure 4.4: Evolution of the design of the lower fork.

4.2.1.1.2 Tower The diameter of the tower is constrained by that of the azimuth bearing (outer diameter 470 mm). Its thickness is first determined analytically by considering the compression due to the mass of the elevation subsystem, the bending related to wind loads and buckling. Detailed calculations show that a minimal thickness of 10 mm is necessary to fulfil the requirements; i.e. to avoid buckling and to keep bending and compression stresses below admissible values. Moreover, this analytical study shows that the thickness of the tower increases with the square of the wind speed, and so does its cost if we take into account only the material cost.

We studied the possibility of putting the azimuth motors inside the tower. This solution requires an aperture inside the tower to give access to the motor (see Figure 4.5). This aperture decreases strongly the stiffness of the tower and requires a more complex design to keep the required stiffness. For this reason, we choose to mount the azimuth motor outside the tower.

4.2.1.2 Mast and Truss Structure (MTS)

4.2.1.2.1 Material The material (steel or aluminium) constituting the MTS is defined by a trade-off. The performance of both materials is similar, so we choose steel for its greater ease of assembly.

4.2.1.2.2 Camera mount The camera moount was studied in the trade-off and all details related to this item can be found in section 4.4.2. We deduced from the analysis of several constraints (removal mechanism, stiffness) that fastening the camera to M2 is a better solution than a connection to the MTS tubes or to M1.

4.2.1.2.3 Tube assembly Using a Serrurier-like assembly instead of the previous tripod strongly improves mechanical performance. The dynamic behaviour is strongly improved because the first mode is no

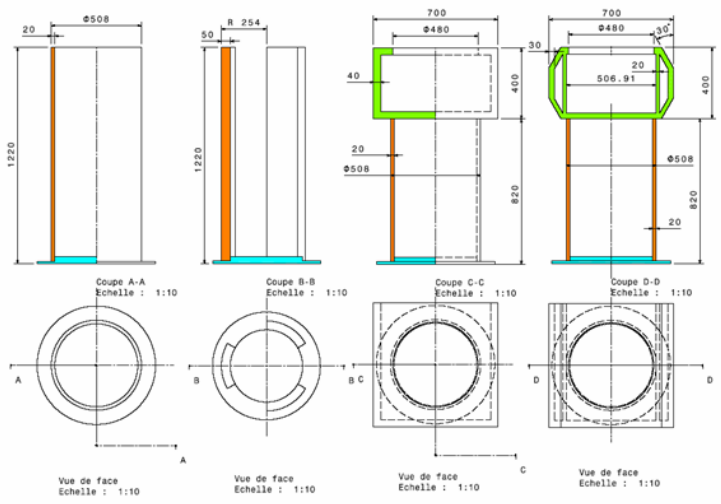

Figure 4.5: Conceptual designs of towers of AAS without (left) and with an aperture

longer a bending mode, which induces a tilt of M2 and the detector and so harms the telescope performance, but becomes a torsional mode, which does not effect mirror/camera tilts and deviations (see section 4.2.2.2.2). We discarded a four-arm Serrurier structure because this would not allow the possibility of removing the detector through the MTS tubes. Moreover, the structure would have been hyperstatic (i.e. the alignment more difficult to realize) for no improvement in stiffness. For these reasons, a three-arm Serrurier structure is preferred (Figure 4.6).

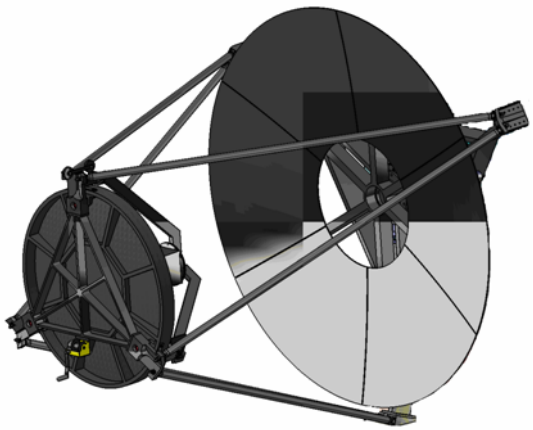

Figure 4.6: Three-arm Serrurier MTS.

The optimization of tube geometry is performed using FEA with a model of the MTS supported by an

infinitely rigid primary dish in order to minimize the obscuration. These results are reported in the table 21 and Figure 4.7.

	Tripod	Serrurier (same geo.)	Serrurier (opt. geo.)
Mass (tons)	2,4	2,5	2,5
Tube geometry (ext. diam. thickness)	100x3	100x3	70x8
Impact on obscuration of M1 (%)	2,6	9,3	6,5
Dev. M1 M2 (mm)	44,9	0,19	0,19
Dev. M2 Cam (mm)	15	0,6	0,6
Tilt M2 (arcsec)	0.78	0.03	0.03
Tilt Cam (arcsec)	0.93	0.03	0.03
1st bending mode (Hz)	2,3	11,7	11,3

Table 21: Comparison of performance of tripod and Serrurier MTS structures at an elevation angle of 90°.

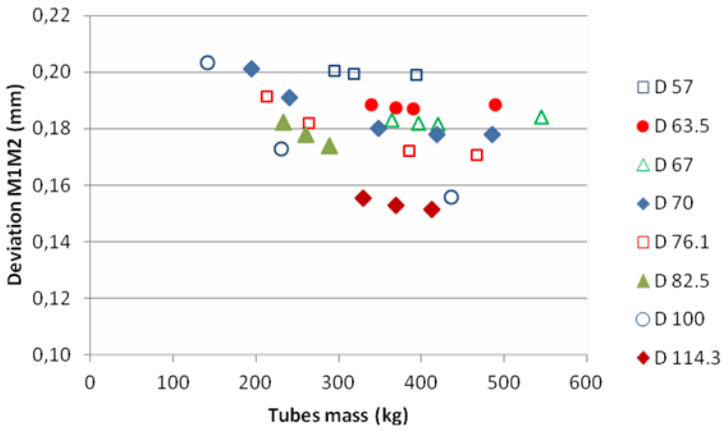

Figure 4.7: Influence of the tube geometry for a Serrurier assembly supported by an infinitely rigid primary dish calculated by FEA on the deviation M1 M2

The impact on the obscuration is deduced from the ratio of projected areas of the beams to the M1 surface (with central hole). These magnitudes can be compared to the obscuration by the tubes in HESS, about 11%, and to the obscuration caused by M2 and the detector on M1, about 16% to first order.

4.2.1.2.4 MTS Support The previously discussed deviations are on-axis deviations. Deformations of M1 become huge close to the fixation points of the truss tubes. Indeed, the primary dish in this conceptual

design has two functions: supporting the panels of M1 and the whole MTS (including M2 and the detector). Separating these two functions allows the decrease of the deformations of the primary dish. The additional stiffness required to increase the stability of the MTS may be added to a second structure without the need to respect the constraints related to M1 curvature. This leads to add a new component of the MTS responsible for supporting M2 and the camera. The only function of the primary dish is then to support the M1 panels.

The geometry of this new component, named the MTS support, is deduced from topological optimization performed by FEM (Sol 200, MD.Nastran) of an annular plate clamped at its centre and subjected at its external diameter to three torques equivalent to the action of MTS tubes. Topological optimization consists of removing the unnecessary material in the structure as regards to the mechanical stiffness and with the objective of mass reduction [NAST]. This analysis led to a three-arm structure with some reinforcements. Further simulations were performed to optimize the shape of these beams. "T beams" lead to good behaviour, but may not be easily available commercially. This is the reason we chose rectangular beams. In Figure 4.8, 4.9, 4.10 is shown the evolution of the deviation M1 M2 calculated by FEA for several geometries of MTS support beams and with the previous secondary dish design.

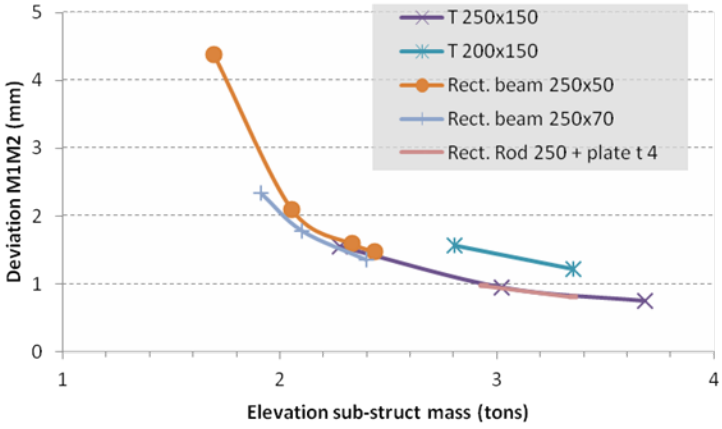

Figure 4.8: Effect of the beams geometry on M1 M2 deviation calculated by FEA.

Moreover, rotating the outer part of these arms improved the stiffness of the MTS. The detailed design of the MTS Support is presented in section 4.2.2.

4.2.1.2.5 Central Axis The Central Axis is a critical part of the new configuration because it supports most of the components of the MTS. Since its length has increased in the new design, it may bend more easily. There are several solutions to improve this behaviour: increasing its thickness or outer diameter, reducing its length, or adding reinforcement beams. These solutions are being investigated.

4.2.1.2.6 Conclusion A Serrurier-like structure strongly increases the stiffness and the performances of the M2/camera support structure compared to the previous tripod design. Finally, separating the functions

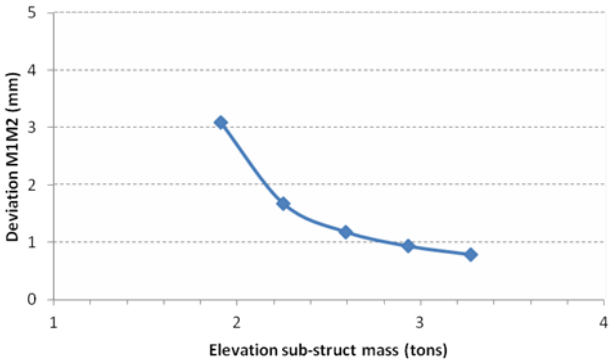

Figure 4.9: Effect of the dimensions of rectangular beams on M1 M2 deviation calculated by FEA.

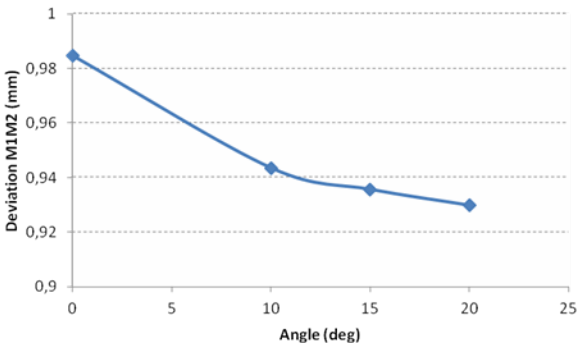

Figure 4.10: Effect of the inclination of the outer part of the MTS support arms on M1 M2 deviation calculated by FEA.

of the supprts for the primary dish and the truss assembly strongly improves the off-axis performances of M1. This last item allows a lighter primary dish while improving the optical quality.

4.2.1.3 Primary Mirror Structure and Primary Dish The Primary Mirror Structure (PMS) consists of:

- The Primary Tesselated Mirror.
- The Primary Alignment Subsystem (PAS).

As we will see further (section 4.3), we propose to tessellate the primary mirror in 6 panels instead of 24 as in the first design.

The Primary Dish bas been redesigned in order to optimize the mass of this component and to give easier access to the actuators during AIT. This component is in steel and is made from an assembly of beams. The geometry of these beams has been optimized using FEA with respect to changes in elevation angle and wind loads in critical (stresses) and operational (stresses and deviations) conditions.

4.2.1.4 Secondary dish This component has to support the secondary mirror. Because of similar consderations to those for the MTS Support, we also adopt for the secondary dish a structure with three arms and reinforcements. FE optimization of these arms is currently in progress.

4.2.2 Detailed design

Having fixed the new general concept for SST-GATE, we here describe the mechanical design of the telescope by taking into account the conceptual options. This description will begin with the fastening elements on the ground and will end with the mechanical fixing of the camera.

4.2.2.1 Alt-Azimuth Structure

4.2.2.1.1 Tower The tower is the only stationary part of the telescope. It is the link between the ground and the azimuth drive. It consists of a tubular body with an outer diameter of 470 mm and thickness of 35 mm (see Figure 4.11) and a ground interface flange (thickness 20 mm) which allows the use of 16 safety stud anchors (diameter 20 mm).

The upper part of the tower is a flange which will support the azimuth drive system. The different parts of the assembly are welded. The colour of the tower and the telescope structure is the red (RAL 3016).

4.2.2.1.2 Azimuth drive The azimuth drive will be fixed on the upper face of the tower. The mechanical design uses an irreversible worm gear and crown (figure 2-12). The supplier of the wheel and worm is ROLLIX. The reference of the crown is 06-0574-04 (see appendix C.2) and that of the worm gear is 05-0070-00 (see appendix C.3). The choice is based on calculations of stresses induced by the wind and the weight of the telescope and is also related to the available space for implementation in the telescope.

The crown is fixed on a flange attached to the tower, and the engine assembly with the worm gear moves around the azimuth axis and is linked to the fork. The advantage of this solution is that it reduces the space constraints for the mobile elements needed during elevation. The goal is to create a system that can also be used for the elevation drive (see section 4.14).

4.2.2.1.3 Fork This element is the link between the azimuth drive and the elevation drive (Figure 4.13). Even if its external shape is defined, it has to be optimized by calculations to ensure its performance is adequate and to get the best stability and rigidity possible. The dimensional constraints on the fork result

Figure 4.11: View of the tower (3D CATIA).

from its attachemt to the azimuth drive, the space necessary for the counterweight and the interface to the elevation drive.

4.2.2.1.4 Elevation drive The design of the elevation drive is progressing. We are using two systems similar to those in the azimuth drive for cost and maintenance reasons. One of these will be composed of the worm gear and the motors, the other one will be composed of the crown and the bearing.

4.2.2.1.5 Mast and Truss Structure (MTS) There are two major changes in the mechanical design of the MTS. As was described in the Conceptual Design, we have modified the tripod to use a Serrurier-like hexapod. The second strong change is that the primary mirror dish and the arms of the hexapod are independent, so that the constraints on the arms do not affect the M1 shape.

Each arm of the hexapod will be a tube (external diameter 70 mm, thickness of 6.3 mm and length of 4190 mm) with two adjustable end parts to alter the length between the joint interfaces with the base of the MTS and the secondary mirror support.

The joints will be made using an HPC hinge (CSS-30). This accepts an angle variation of 17° and is able to resist a static load of 25400 N (cf. Figure 4.14).

To decouple the MTS support from the primary mirror support, we use a spider with three arms. This element will be fixed on a flange which is a part of the central axis. The central axis provides the interface to the elevation drive.

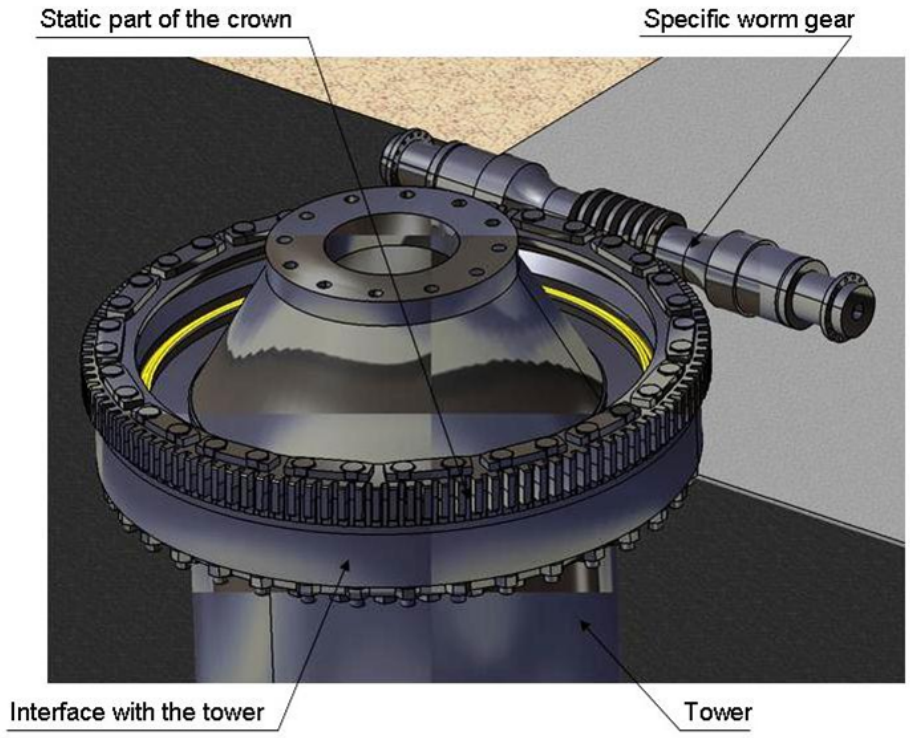

Figure 4.12: View of mechanical parts of azimuth drive.

The MTS support has yet to be optimized for cost, but the size of the arms should not change. The section will be a rectangular shape (250 mm x 50 mm with a thickness of 5 mm) as shown in Figure 4.15). At the edge of the triangle (reinforcement), the three plates are bent by 20° because FEM simulations show that it decreases constraints in the rectangular beams

4.2.2.1.6 Primary Mirror Structure The primary mirror structure will be fixed on a flange on the MTS structure. The primary mirror structure is hexagonal. Each verticex of the hexagon is an interface flange for the support structure of an M1 panel. The positions of the vertices of the hexagon correspond to the centre of gravity of the M1 panel and its support structure. The beams used for the hexagonal structure have a rectangular section (160 mm x 80 mm, thickness of 8 mm).

Each panel of the primary mirror is supported by a triangular structure. The shape of this structure is defined. We have yet to optimize the section of the beams to get the lightest structure possible (Figure 4.16).

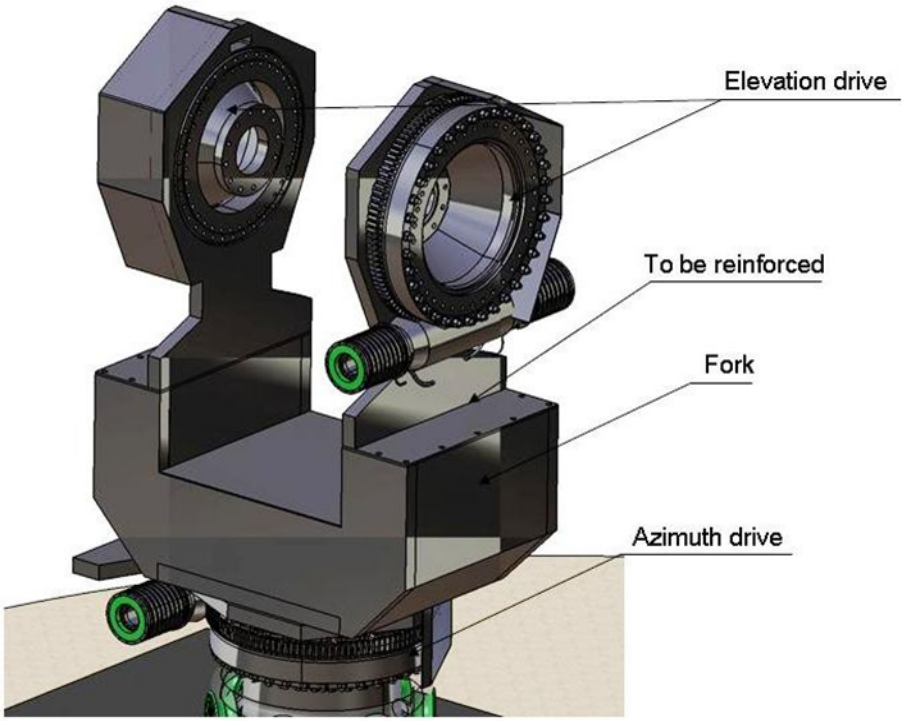

Figure 4.13: View of the Fork

4.2.2.1.7 Secondary Mirror Structure In the secondary mirror structure, we distinguish two different elements: the interface, made of three connectors and a support structure (see Figure 4.17).

The interface satisfies three functions: the attachment of the secondary mirror via three actuators, the connection with the MTS and the attachment of the camera support. We are waiting for an interface control document with the camera to optimize the latter.

The support structure must connect the three interface parts. The structure will be optimized and finalized once the interface with the M2 mirror is defined with the CEA IRFU (M2 manufacturer).

4.2.2.1.8 Counterweight The counterweight should balance the telescope. It is fixed on a flange at the end of the central axis. Its shape is not yet defined precisely because this depends on the weight of the different elements and the needs of the alignment procedure. The goal will be to position the centre of gravity of the counterweight as far as possible from the elevation axis to decrease the mass of the counterweight. It will be formed of an assembly of separately mounted weights to allow adjustment of the mass of the counterweight.

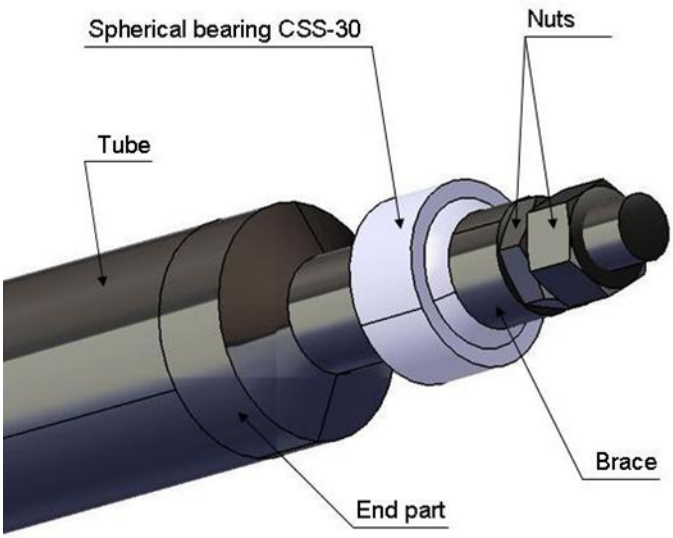

Figure 4.14: View of the end part (3D CATIA).

4.2.2.2 FE validation of the structure Validation of the design detailed in the previous section is described here. This analysis is based on theoretical analytical or numerical calculations. FE models are performed under MD.Nastran. COTS are modelled by single points located at their CoG (Detector, M2) or by MPCs (Multi-Point-Constraints) (Azimuth crown, Upper Fork). Actuators are modelled by MPCs. The counterweight is not considered. The primary mirror is modelled by an aluminium plate of constant thickness and with the proper mass. The FE model of the telescope is shown in Figure 4.18.

The foot of the tower is clamped rig rigidly to the ground. Static calculations are made with a linear static solution (Sol 101) while modal analysis is made with sol 103 (normal modal analysis). No non-linear analysis has been performed as yet.

4.2.2.2.1 Gravity loads The influence of the elevation angle on the behaviour of the MTS is summarized in table 22. Results are calculated at the theoretical centre of M1 and of the CoGs of M2 and the Detector with a model of the MTS. The evolution of the M1 M2 defocus in mm vs the elevation angle follows the relationship:

$$\text{M1M2 defocus(mm)} = 0.3476\cos(\text{Elev.angle}) + 0.002$$

4.2.2.2.2 Modal analysis Modal analysis of the current version of the full telescope at an elevation angle of 0° is reported in table 23.

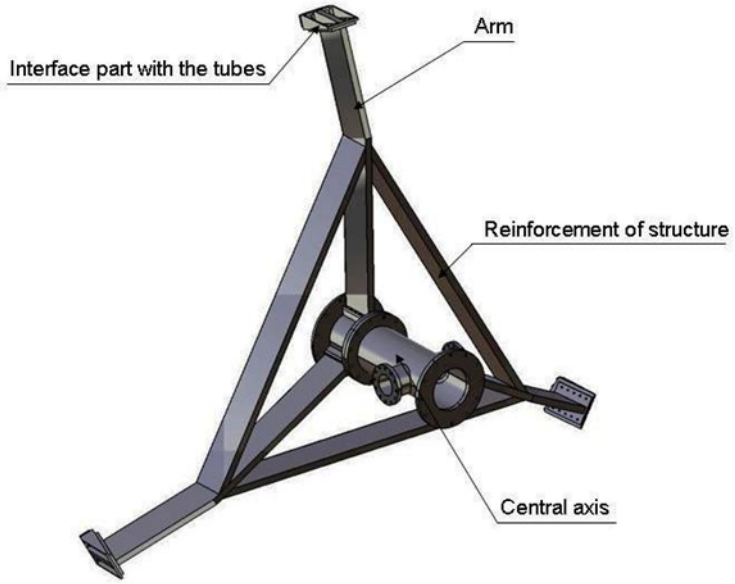

Figure 4.15: View of the MTS support (3D CATIA).

Elevation angle [°]	M1M2 defocus [mm]	Tilt y M1 [arcsec]	Tilt y M2 [arcsec]
0	0.35	-0.7	0.4
30	0.3	8.6	10.1
45	0.25	12.4	14
60	0.18	15.5	17
90	0.17	18.2	19.4

Table 22: Influence of the elevation angle on M1 M2 defocus and tilts of M1 and M2 calculated by a FEA of MTS

Modes 1, 2 and 7 to 9 are associated with deviations or tilts of the optical elements. Two of them occur below 10 Hz. These, shown in Figure 4.19, correspond to a bending of the central axis. They are also associated with a bending of the telescope as shown by the corresponding effective mass fractions in rotation which are about 76%. Improving the stiffness of this element as suggested in section 4.2.1.2.5 may increase these frequencies. The thorough study of this component is currently in progress.

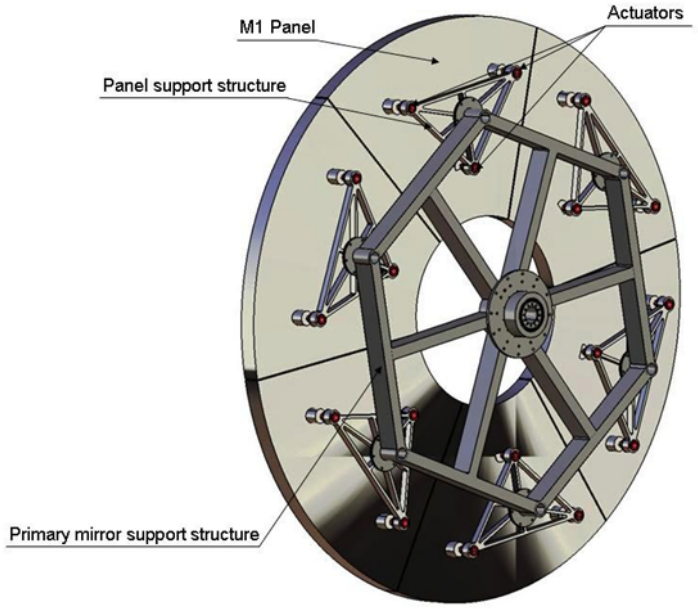

Figure 4.16: Back view of the PMS (3D CATIA).

Number	Frequency [Hz]	Description
1	4.5	Bending of the Central Axis
2	4.7	Bending of the Central Axis
3	10.2	Torsion of the Central Axis
$4 \rightarrow 6$	$13.8 \rightarrow 14.4$	Local bending of Serrurier tubes
7	16.5	Tilt of Primary Dish and Mirror
8	17.0	Tilt of Primary Dish and Mirror
9	18.1	MTS elongation associated with M2 piston
10	18.3	Local bending mode of Serrurier tubes

Table 23: First ten eigenmodes of the telescope calculated by FEA.

4.2.2.2.3 Wind Loads The wind velocity is a combination of a steady-sate or mean velocity and turbulence or gusts. The operational wind speed will impact the telescope pointing and tracking ability while the survival wind speed will define the strength of the telescope and of the foundations [20]. In this section, we consider only the steady-state component. Analysis of the turbulent component is currently in progress.

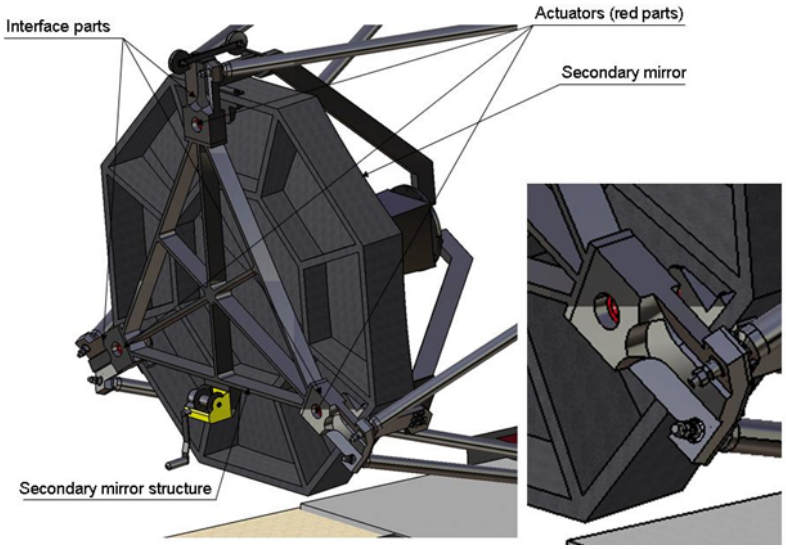

Figure 4.17: View of the Secondary Mirror Structure (3D CATIA).

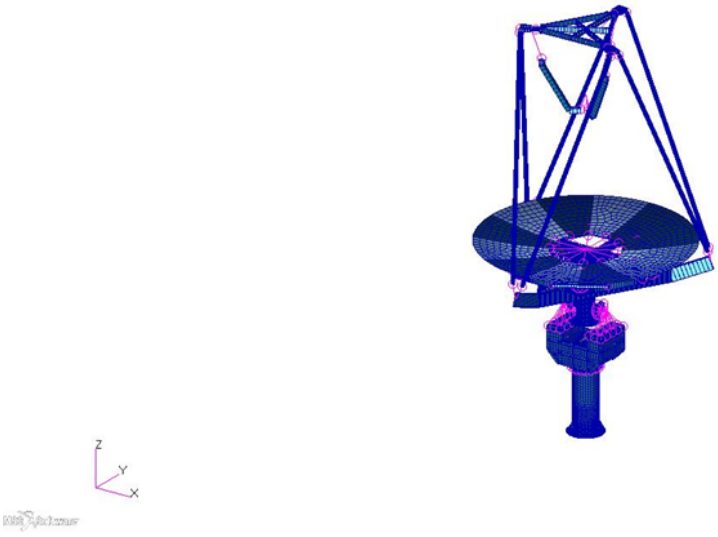

Figure 4.18: FE model of SST GATE.

From the mean wind speed, we can deduce the wind load f,

$$f = \frac{1}{2}\rho C_D A u^2,$$

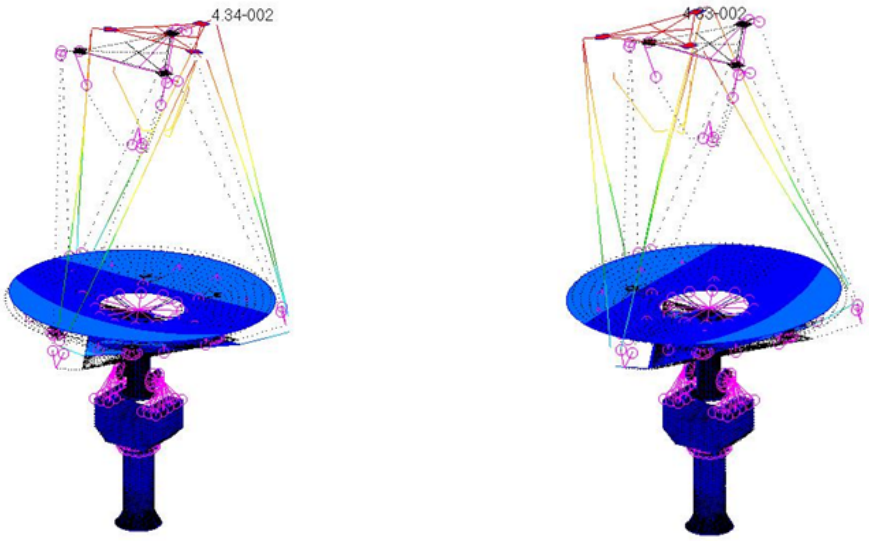

Figure 4.19: Eigenshapes of modes 2 (left) and 3 (right) of the telescope calculated by FEA

where ρ is the air density (1.3 kg/m^3), C_D is a drag coefficient (1.2), A is the projected area and u is the mean wind speed. We consider the telescope in its horizontal position at an elevation angle of 90° at which the projected area is maximal. Wind load is applied on M2 and on the primary mirror (pressure) backwards and forwards in observing and survival conditions. Lateral wind loads are not studied since we have no data about the thicknesses of the mirrors. As Meudon's environmental requirements are more constraining than CTA's for the survival wind speed (150 km/h [21] instead of 120 km/h (A-ENV-0730, [20]), Meudon's maximal wind speed will be applied for the survival conditions of SST-GATE. Deformations of the structure in operating conditions are reported in table 24 while figure 2-20 shows the stresses in the structure in survival conditions. As for the influence of the inclination, the results are calculated at the theoretical centre of M1 and of the CoGs of M2. Deformations will have to be refined by a dynamic analysis; nevertheless, a damping of the structure may contribute to reduction of the amplitude of these deformations as we will see in section 2.2.2.2.5 concerning seismic analysis. There are some differences between winds from the and the back. The stresses in the structure remain below the maximal admissible stresses since yield stresses for aluminium alloys (for instance AU4G) and carbon steel are about 400 MPa. The highest stresses are about 100 MPa and are observed at the interface between MTS support arms and the central axis. These stresses are related to the modelling of the interface (screws) by point contacts and are for that reason probably overestimated. A lower boundary of the real value may be calculated by assuming linear contacts. Moreover, the gaps between M1 titles, not modelled here, will contribute to a decrease in the wind pressure on this mirror.

Conditions	M1M2 defocus [mm]	M1 decenter [mm]	Tilt M1 [arcsec]	Tilt M2 [arcsec]
Back wind	0.05	1.29	-8.9	-9
Front wind	0.04	1.26	-8.5	-9.1

Table 24: Wind effects on M1 deformations and stresses in the PAS and Primary Dish.

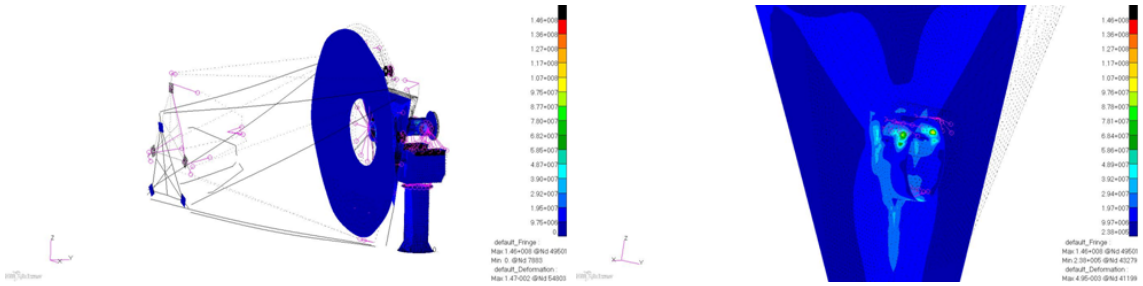

Figure 4.20: FE Stress analysis of SST-GATE in survival conditions for a wind blowing on the backs of M1 (back wind). Left: Model of the telescope. Right: Maximal stresses at the interface between the central axis and the arms of MTS Support.

4.2.2.2.4 Thermal analysis We present in this section an analytical transient analysis performed to estimate the magnitudes of the distortions due to temperature effects. Since we assume that the thermal behaviour of the AAS will not harm the performance of the telescope, this analysis was only applied to the MTS. The procedure of a thermomechanical analysis consists of calculating the temperature of the components resulting from the application of thermal loads, then using these temperatures to calculate the expansions. This analysis was applied to two subsystems:

- Primary Dish, PAS and PMS.
- MTS Support and Serrurier beams.

The MTS central axis is the mechanical interface between these two subsystems. M1 is assumed plane; no deformations parallel to the optical axis will be calculated. The honeycomb at the back of M1 can be simply taken into account by using an adequate density for M1 [18]. We assume that the Secondary Dish is not sensitive to the temperature and is infinitely rigid and, because of the lack of current data, M2 is not taken into account. These results will be further refined by FEA. Thermal loads applied to the telescope are listed below:

- Solar flux.
- External temperature.

- Convection.
- Heat dissipated by electronic devices (actuators, motors).
- Ground (concrete slab) radiation.

As CTA requirements [20] are more constraining than those of the Meudon environment (table 25), CTA requirements will be used instead of Meudon's for thermal analysis of SST-GATE. Moreover, in order to analyse the worst case, the wind related to heat dissipation by convection is not taken into account in this analysis. An analytical calculation of the magnitudes of heat dissipated by actuators and of ground radiation is given in table 26. It shows that the heat dissipated by the actuators can be neglected. A similar assumption was also used in the thermal analysis of TMT [25]. Ground radiation will also not be taken into account. The initial temperature of the structure is assumed to be 20°C.

Requirement	CTA [20]		Meudon	O-day	Sh-day	Sc-day
Operating conditions						
Min/Max temperatures [°C]	-10 / +25	A-ENV 0210		-+8 / +22		
Temperature gradient [°C/h]	±5	A-ENV 0230		+5.6/-3.3	+5.6 / -3.3	+5.6 / -3.3
Survival conditions						
Min/Max temperatures [°C]	-20 / +40	A-ENV 0220	-10 / +35	-20 / +40	+10 / +40	-20 / +40
Thermal shock (24h) [°C]	±30	A-ENV 0240	±20	±30	±30	±30
Solar flux [w/m^2]	1200	A-ENV 0810	920	920	1200	1200

Table 25: Thermal requirements. O-day, Sh-day and Sc-day describe a typical day in operating conditions, in survival conditions (hot) and survival conditions (cold), respectively.

Source	Power [W/m^2]
Maximal solar flux [20]	1200
Ground radiation	200
Dissipated heat per actuator	1

Table 26: Comparison of heat magnitudes

The time-dependent behaviour of the temperature was deduced from temperature surveys in Meudon and led to the definition of three typical days, which fulfil CTA requirements, defined in table 2-5. The time-dependant behaviour of the solar flux was deduced from surveys of the sun position [24]. The Figure 4.21 shows the evolution of the temperature in survival heat conditions and of the solar flux which were used for the calculations [18]. These results ware obtained at an elevation angle of 90°.

Expansion of the Primary Mirror's panels corresponds to an expansion of 1.6 mm per petal. As this expansion is less than the initial gap between the panels (10 mm), no damage is caused by the thermal expansion.

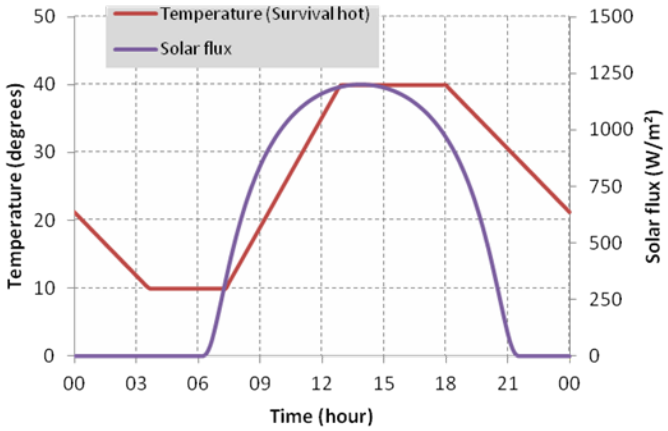

Figure 4.21: Evolution of the temperature during one day used for thermal analysis [COS 13].

Expansion of the Primary Dish is mainly a radial deformation leading to an expansion of the Primary Mirror by increasing the spacing of the petals without any rotation of the titles. The maximum value of this expansion is 0.5 mm and corresponds to a maximum increase of the inter-petal gap of 0.56 mm per petal. The effect of this increase on the PSF is currently being determined. The tilt of M2 is the sum of two contributions: the expansion of the MTS support and the expansion of the Serrurier assembly. The evolution of these magnitudes versus time is shown in Figure 4.22. The maximal tilt of M2 is 0.0126°, i.e. 45 arcsec.

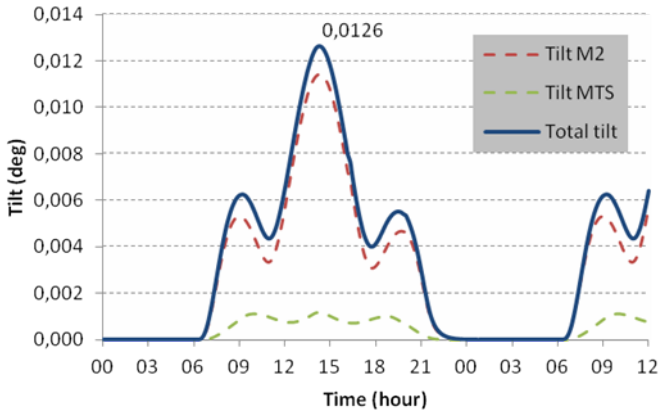

Figure 4.22: Evolution of the thermal tilt of M2 [18].

4.2.2.2.5 Seismic analysis We present here only an overview of existing possibilities in seismic design applicable to SST-GATE. An earthquake is caused by a sudden release of energy in the ground which may be absorbed by the structure, may go back in the ground or damped by dampers. In the first case, if the stiffness of the structure is sufficient, the structure suffers no damage and the energy is sent back to the ground, otherwise, the structure is damaged. The acceleration may be horizontal or may also have a vertical component if the earthquake occurs close to the epicentre. The vertical component is more dangerous and is defined as 1.2 times the horizontal component [19].

4.2.2.2.5.1 Seismic design

Many technical solutions may be used to reduce the vibrations of a structure in response to an earthquake.

- Oversizing. The stiffness of the structure is increased in order to resist the maximal load. When the maximal load is reached, the structure breaks. Moreover, this solution is expensive and requires a heavier structure.
- Seismic isolation. Devices are set up under the structure and decouple the structure from the ground. During the earthquake, the structure has only rigid motions and suffers reduced deformation.
- Damping. Dampers are set up in the structure. Different kinds of dampers can be used: viscoelastic materials, viscous fluid dampers, magnetic dampers etc. Earthquake energy is dissipated by the damper. This solution may be appropriate for vertical waves depending on how the dampers are set up. This technique increases the damping of the structure and will also reduce the amplitude of the displacements caused by the wind at resonance. It is possible to set up joint or interface dampers at the connection between two pieces of the structure.
- A TMD (Tuned Mass Damper) offers high damping for a single mode. The mass and stiffness of the system must be chosen to make the natural frequency of the TMD match the problematic, resonant mode of the structure. This splits the problematic mode. It acts only at a defined frequency. Multiple TMDs with distributed natural frequencies can be set up in the same structure. This technique is commonly used in civil engineering for tall buildings [23] or for bridges.

4.2.2.2.5.2 Application to SST-GATE

Seismic design aims to protect the structure especially its fragile or sensible components. Oversizing leads to heavier and more expensive structures. Moreover, if the new allowable stress is exceeded, the structure is damaged. Seismic isolation may harm the performance of the telescope during light wind by enhancing displacements of the structure and is not appropriate for vertical waves. It is possible to set up one or several dampers combined to multiple TMDs inside the structure of SST-GATE to prevent against seismic hazard. These solutions may also improve the behaviour of the telescope for windy conditions. These solutions will be investigated after analysing by FEA the behaviour of the structure when an earthquake occurs.

4.3 Mirrors

The SST-GATE optical design provides a very good PSF on-axis as shown in Figure 4.23.

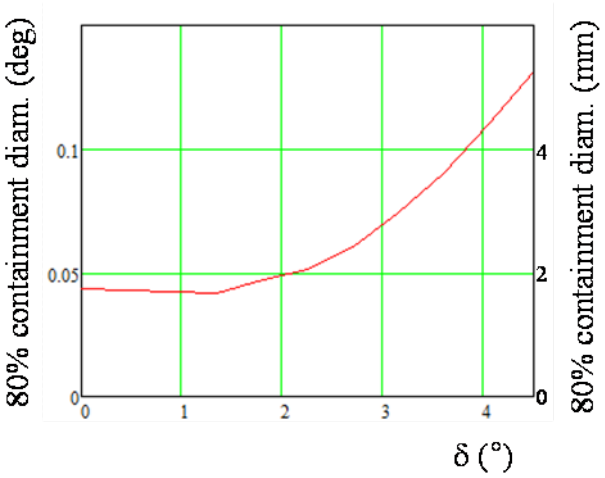

Figure 4.23: PSF versus FoV.

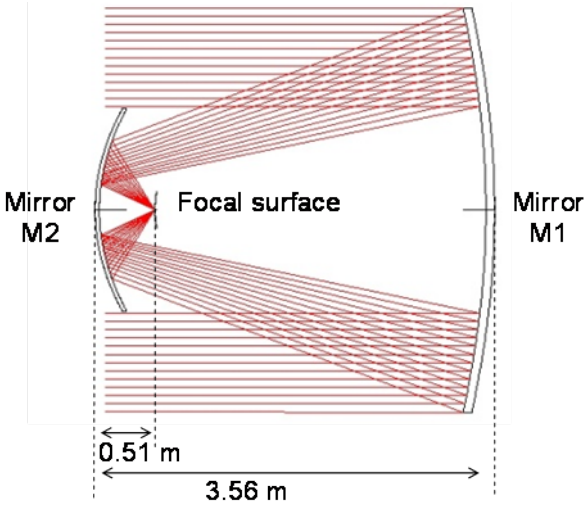

Figure 4.24: The SST-GATE design

The Figure 4.24 shows the optical design composed of two mirrors, M1 and M2, and the camera is located in between. M1 collects the incoming light and redirects it towards M2 which focuses the light onto the detector.

4.3.1 Manufacture of M1

M1 has an aspherical concave shape and is 4 meters in diameter. The optical design has been calculated with Zemax. The mirror's shape is described by a polynomial curve with the coefficients presented in table 27.

Coefficient	M1 mirror
α_1	−5.4280255e-05
α_2	-3.3912879e-13
α_3	1.3451359e-18
α_4	-1.290035e-24
α_5	6.8508142e-31
α_6	-2.0059722e-37
α_7	3.0563336e-44
α_8	-1.8853301e-51

Table 27: Polynomial coefficients describing the mirror M1 shape (altitude versus radius) the formula is $z = \alpha_1 x^2 + \alpha_2 x^4 + ... + \alpha_8 x^{16}$

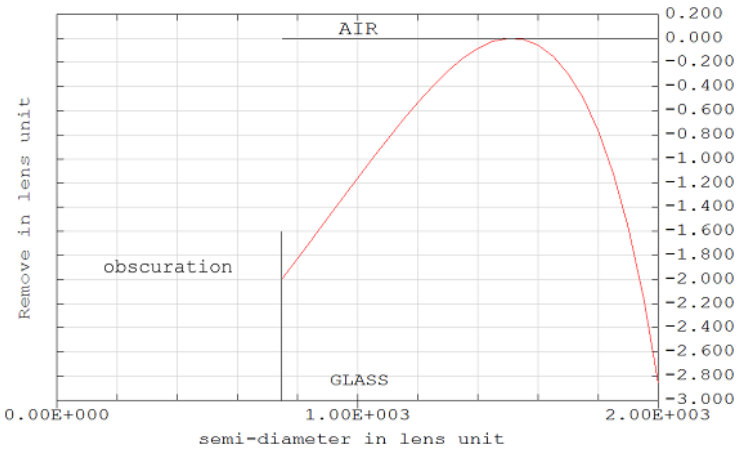

Figure 4.25: The red curve is the gap between M1 and the best sphere fitting the polynomial definition of M1 (value in mm).

The primary mirror is aspherical. The radius of the sphere which most closely fits the mirror shape is 9667.8410 mm. The deviation from this perfect sphere is shown in mm Figure 4.25 by the red curves. Due to the location of M2 and the camera in front of M1, there is a hole in the centre of the M1 of radius is 650 mm.

M1 will be constructed of 6 identical panels (Figure 4.26). This tessellation corresponds to the manufacturing

capacity of industry, and allows us to use the minimum number of actuators behind each panel. The Figure 4.27 shows an M1 mirror panel and its actuators.

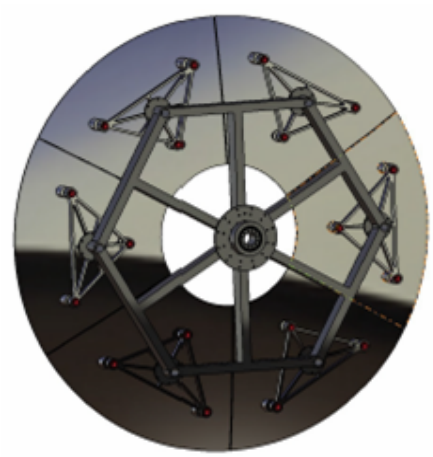

Figure 4.26: Mirror M1

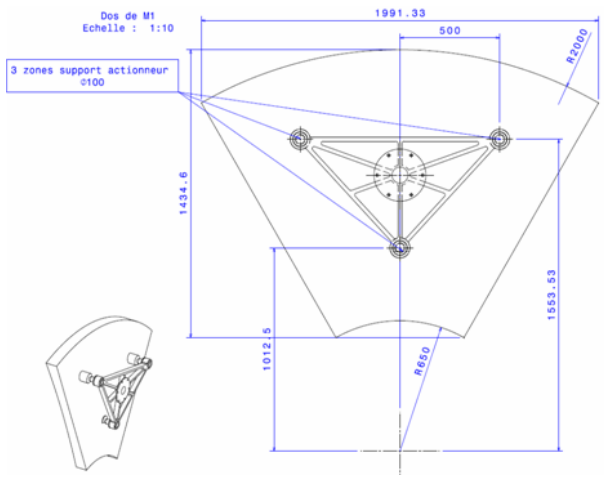

Figure 4.27: One panel of mirror M1 and its actuators.

The prototype will use M1 panels made of aluminium. The specifications required to make mirrors from aluminium bulk substrate are summarized in table 28.

The manufacturing of the panels with this surface roughness requires that the work be split between several firms. The first will machine the panels with the appropriate aspherical surface and with a roughness down to 0.8μm. Then the mirror finishing, a roughness of Ra 0.02μm, will be achieved by polishing by a second

	Tolerance
Flatness	$\pm 50\mu$m TBC
Waviness	20μm rms
Irregularity	0.02μm
Mean transmission	$> 83\%$

Table 28: Specification for M1 manufacture.

firm. The last step will be the coating of the mirror with a layer based on aluminium in order to guarantee reflectance above 83% and to protect the surface from corrosion. The choice of aluminium class is 5083, as it satisfies the criteria for machining, polishing and coating and will survive the environment in which it will be used. The back of M1 will be structured to achieve a weight of 20 kg/m^2 (CTA requirement), so the panel will have a weight of 40 kg and the total weight of M1 will be 225 kg. The mechanical interface consists of 3 actuators that link the back of the mirror to the triangular support structure (see Figure 4.27).

The collaboration with the three companies needed to construct M1 is being finalized. To ensure the feasibility of the construction, the three steps will be tested on small substrates having the petal shape and a size of 180 x 220 mm^2 (see Figure 4.28). The machining of six petals like this will allow us to test the alignment procedure on an optical bench.

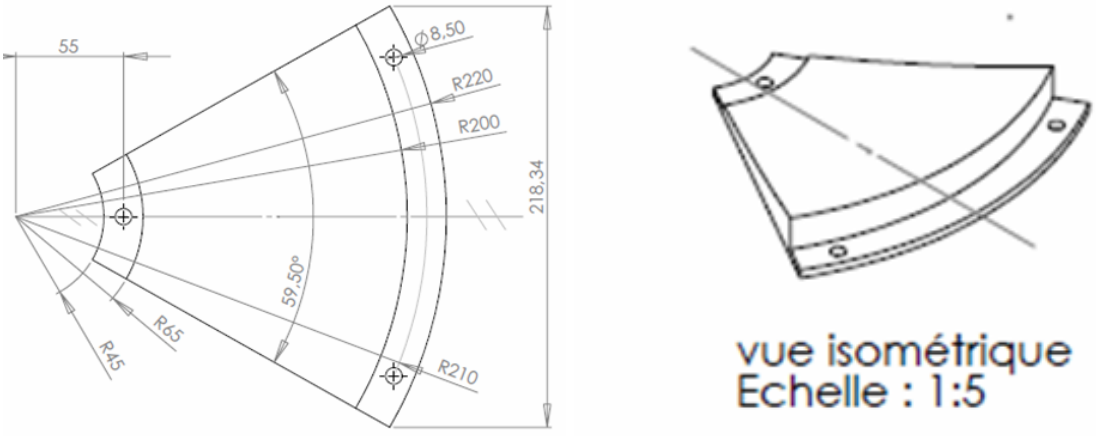

Figure 4.28: Panel test

The machining and polishing test will be completed by the end of spring, and the primary mirror will be manufactured in the summer.

4.3.2 Primary Alignment Sub-System

The M1 actuators will be supported by a mechanical structure similar to that used for the Hess I Mirror Unit and developed by ECAP at Erlangen. This component could be manufactured by moulding for large scale production and by an assembly of flat bars for prototyping. Six are required for one telescope. The material will be the same as for M1, or will have a thermal expansion similar to that of M1. As we plan to use an aluminium primary mirror for the prototype, this component will also be in aluminium. The geometry of this structure has been optimised by FE with respect to changes in the elevation angle and the wind loads under operational and survival conditions in order to check that displacements and stresses fulfil the requirements.

Sensors will be absolute. The final motor choice is still to be made, but devices from Nexeya and Canary are under consideration. The control-command system will be provided by Nexeya. Actuators and sensors are being chosen taking into account the site considerations listed in the CTA requirements level B and the accuracy needed to align the M1 tiles.

4.3.3 Manufacture of M2

M2 is 2 m in diameter and is aspherical. The radius of the sphere that best fits the mirror shape is 2.114.7610 mm. The deviation in mm to this perfect sphere is given in Figure 4.29 by the red curves.

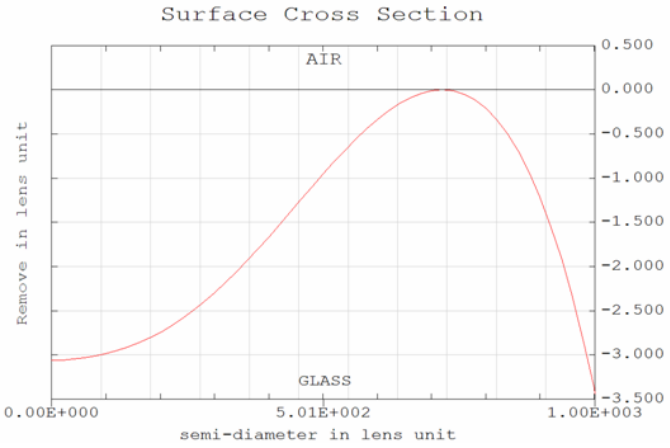

Figure 4.29: The red curve is the gap between M2 and the best fit sphere (value in mm).

This mirror will be monolithic and will be manufactured by CEA IRFU. The process used is cold slumping, but in order to achieve the high curvature needed in the S-C design, the process is augmented by reducing the thickness of the glass material and using reinforced glass (a patent is being filed by CEA). Thanks to the decrease of the thickness, the strain of curvature is decreased and a small radius of curvature can be achieved. However, due to the curvature, folds are created due to an excess of material; hence the solution

validated by CEA consists of creating small cuts at the corners of the glass mirror to prevent the folds. The mirror is curved onto a mould having the required shape; the remaining gap at each glass corner cut is filled with an appropriate resin. IRFU proved the feasibility of this process by producing a 1.5 m radius of curvature mirror (see Figure 4.30).

M2 will be made by following this process. As M2 is too large to be produced in one piece using this method, it will be constructed in 9 panels, one in the centre and 8 identical panesl for the outer ring. These panels will be assembled to form a monolithic mirror as presented in Figure 4.31.

Figure 4.30: Mirror curbed to radius 1.5 m.

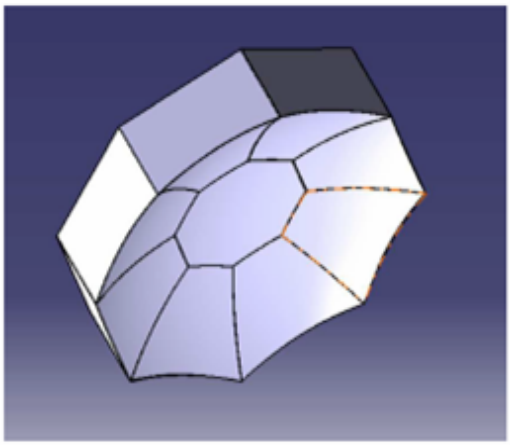

Figure 4.31: Plan of the M2 assembly

Currently, the assembly step is being checked using dummy mirrors. The mould for the tiles of the outer

ring is under manufacture and the eight tiles will be made by the end of the summer. A dedicated mould for the central tile has yet to be manufactured to complete M2.

4.4 Camera options and interface

The CHEC camera has been designed for the SST-GATE prototype and a CHEC camera will be used to equip it. Discussions with the Leicester team about the interface are underway. Nevertheless, we have already taken into account the camera's needs in our telescope design (mechanical structure, electrical and fibre interfaces). As our M1 and M2 mirror can translate, no camera movement is needed to place the focal plane onto the detector plane. Finally, it will also be possible to adjust the camera tip-tilt.

4.4.1 Mechanics

The camera is fixed by three arms which connect the back of the camera to the MTS tubes. The back of the camera is a circular flange. The mechanical fastening of the camera at the back allows the same interface to be used to the ASTRI telescope. The three arms are connected by ball joints to the MTS triangular support on which the M2 dish is supported. The mechanical design of the camera supporting structure is shown in Figure 4.32.

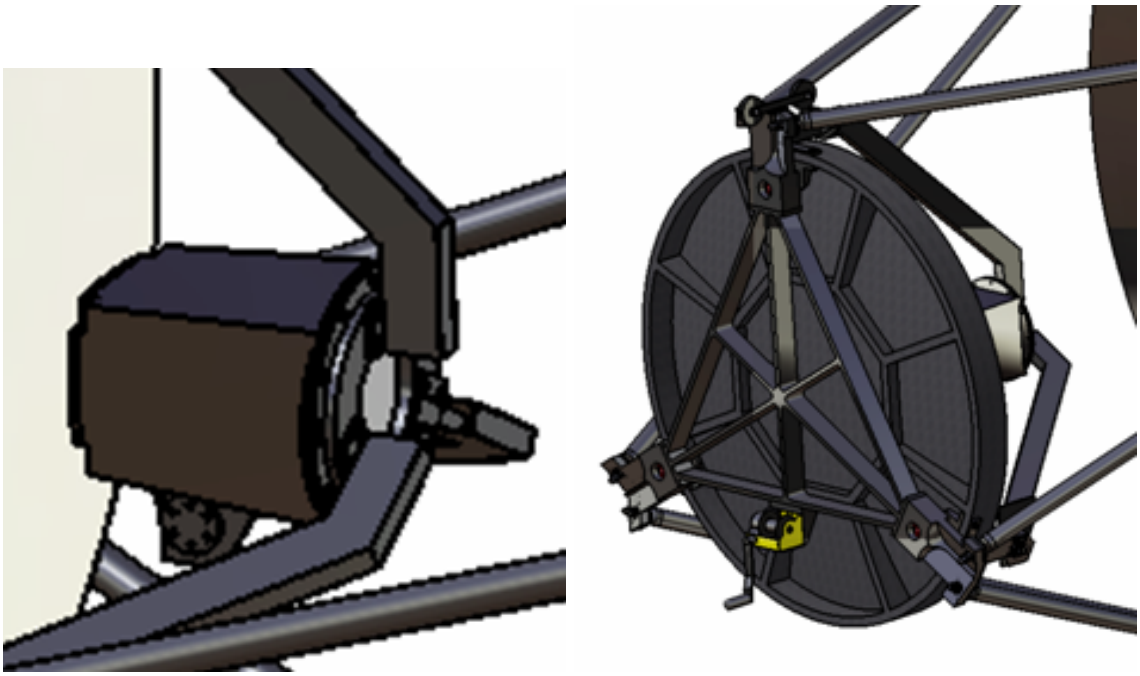

Figure 4.32: Supporting structure of the camera with M2 simulated with circular edge.

This mechanical support fits the CHEC camera volume. The weight of this structure made in aluminium is 52 kg.

The geometry of the mechanical components of the camera fastening have been obtained from a topological optimization made by FEA (Sol 200, Nastran) and take into account recent evolution of the CHEC mechanical interfaces (see Figure 4.33). This optimization, performed from a rough structure studied at several elevation angles, leads to the illustrated preliminary design. The implementation of this design in the telescope structure is in progress.

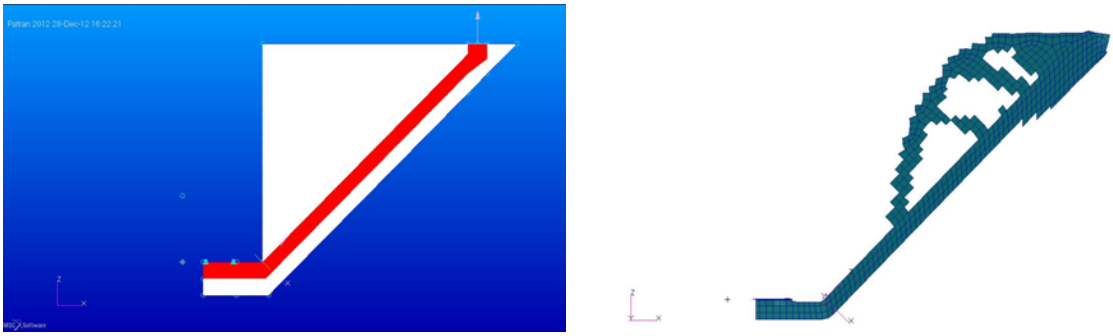

Figure 4.33: Preliminary design of mechanical link of the camera deduced by FE optimization.

4.4.2 Camera removal mechanism

At the beginning of 2012, we proposed to the camera community to use the SST-GATE as a test bench for cameras. For this purpose, we investigated several solutions to allow easy removal of the camera in order to change it rapidly and without damage. This design phase led us to propose an ingenious removal mechanism that allows the rotation of the camera along a horizontal axis in order to place the camera at about 1 meter height (first stage) or on the ground (second stage). The former is interesting for camera maintenance and the latter well suited to camera removal. This system is illustrated in Figure 4.34.

The upper arm seen on Figure 4.32 is fixed to the MTS triangular support by a locking system such as a clamp that can be easily locked and unlocked by one person. When unlocked, the upper arm is free to rotate. The horizontal axis for the rotation is given by the base of the triangular support of M2; the two arms closer to the ground rotate to move the camera. The movement is controlled by a cable passing through the upper arm; the rotation is driven by a pulley system. The drive system, which could be either manual or powered, will be finished after the completion of the ICD with the M2 structure. The return to the proper location of the camera is ensured mechanically with an accuracy of 0.2 mm.

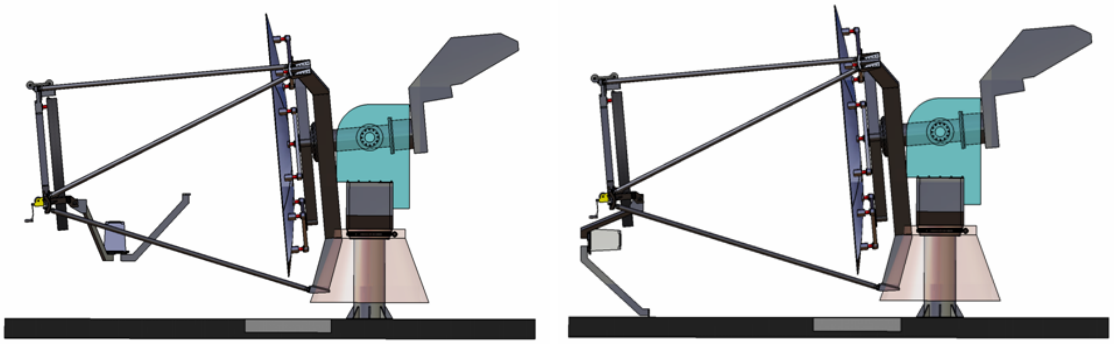

Figure 4.34: Camera removal mechanism.

4.4.3 Power and network supply

A power supply of 25 V is required for the CHEC camera and will be available on SST-GATE. The connector is not yet defined but can be easily plugged at the electrical cable.

The amount of data of the camera can be larger than 1 Gbit/s. We took into account this constraint by providing 12 optical fibres from the telescope to the control room, each one having a 10 Gbit/s bandwidth. The fibres used are multimode and will be connected to the camera by FC connectors. These screwed connectors prevent unwanted disconnection and provide better protection against external damage. LC connectors remain possible if needed.

4.5 Telescope assembly

Telescope assembly starts by attaching the tower to the foundation. This is done with 16 M20 screws with a double nut system to tune the horizontal plane once the azimuth ball bearing is fastened on the top of the tower. An inclinometer will help to ensure the axis is vertical and provide information on residual errors to the telescope control software. The assembly of the azimuth elements (encoders; fixed and movable parts) is under development; some parts will be mounted in the lab and then attached to top of the tower via the flange. Once characterization is done, the fork will be installed with the elevation drives. The same assembly process will be used for the elevation and the azimuth systems. The mounting of the fork on the azimuth bearing can be done with a reasonably sized crane as it is possible to hold the structure between the beams and its height is less then 3 m.

The next element is the central tube which is connected to the elevation drives. Half of counterweight is fixed to one end and the MTS dish to the other. This element will be mounted on the top of the fork. In the central tube will be placed the alignment elements (e.g. the laser). Half of the counterweight will then be assembled. The counterweight will be composed of a set of separate boxes. These boxes will be filled to give

the counterweight a mass of 2.8 tons (see mass budget). This scheme allows the balancing of the telescope as it is assembled.

The MTS is composed of several parts that can be easily assembled on the ground. The supporting MTS (on which will be fixed the M1 dish) will be manufactured separately. It will be mounted on jack stands, whcih will help to hold it during mounting on the telescope. We can mount the MTS dish using 3 3 m crane. By the same procedure, the M1 dish will be assembled and mounted on the telescope structure. The counterweight has to be adjusted and filled in order to prepare for the mounting of the dish and the other parts of the MTS. To ensure an appropriate balance during the whole operation, the structure will be secured by tie-down straps; studs will be provded on the slab for this purpose. On the ground, we will attach the MTS tubes to the triangular MTS support on which will be mounted M2. We will fix the whole MTS on the telescope structure using the 3 m crane. The counterweight then has to be further filled.

The next step is to mount the M1 tiles. Thanks to the rotation of the M1 dish, it is easy to mount all tiles while from the ground. Then, the sky camera will be placed behind the M2 dish and will be aligned in order to observe the telescope axis. The second half of the counterweight will be mounted to balance the telescope. Once M1 is aligned, the M2 mirror will be mounted. The counterweight has to be further filled tol reach its nominal mass. The mirror M2 will then be aligned following the alignment procedure. In the, t final step, the arms holding the camera will be installed on the back of M2.

For steps 1 and 2, alignment is performed to minimize the difference between nominal and real angles. The discrepancies will be measured with the appropriate accuracy (better than1 arc minute in all cases) in order to use Wallace's method [Wallace et al].

The main assembly of the telescope will be made close to the slab, whereas some specific mountings such as the azimuth and elevation sub-systems will be made in the lab. A free space all around the telescope is available in Meudon and should be available on the CTA site. The elements will be delivered by trucks so enough room has been defined in order to let trucks move around and close to the slab. Considering a truck of 8 m, the surface for a half rotation is 400 m^2 (estimation of surface with a turning radius of 12.5 m).

In terms of AIT equipment, a first list of items has been purchased. This is mainly equipment to lift to the proper height the telescope's parts and the persons doing the mounting. The maximum height is 3 m due to the ingenious design used. For instance, the M1 tiles can be mounted while the person is on the ground. The equipment purchased is:

- A crane to deliver elements from the truck to the ground, considering our light design, the max weight shall be 2 t and the height is 3 m.
- A working platform, with a maximum working height of 4.2 m.
- A step ladder.
- A pallet truck,
- 4 load rollers to move heavy item.
- 4 pallet jack stands to mount above the ground the different elements such as the MTS tubes.

The assembly will be made on our slab which is dimensioned for the largest assembly of the telescope, the 4 meter M1 dish. We double this size to allow space to move around so the ideal slab dimension for the SST-GATE assembly is 8 x 8 m^2.

4.6 Control software

4.6.1 Overall design considerations

The software is divided into two main parts: the telescope software and the remote software. The telescope software is built to be operated either in a stand-alone mode or – thanks to the OPCUA server used as a gateway with the remote software and other possible clients – in an array. The remote software allows high level orders to be given to the telescope – a basic control panel being provided at the foot of the telescope for manual operations – and provides a user-friendly view of the telescope parameters. The programming language is LabVIEW. Available routines in C are also used, e.g. in the pointing and tracking module. Three main users are defined:

- Observer (possible actions described in Figure 4.35): a trained astronomer, most important user. Their knowledge level of telescopes may be from novice to expert.
- Engineer (actions described in Figure 4.36): has built part of the telescope (hardware or software). Responsible for maintenance and enhancements, they respond on short notice to irrecoverable failures, monitor key telescope values and define telescope configurations. They also have all the rights of an Observer.
- Administrator: has the ability to add and remove users, change their type and manage their passwords.

4.6.2 Communication architecture

The whole communication architecture (Figure 4.37) is based on two flavours of Ethernet: Internet and EtherCAT. The fibre link for the camera is shown in red.

4.6.3 OPCUA client-server

The OPCUA server is started at the initialization phase of the telescope software. All the files defining the OPCUA server (configuration, address space and constants) follow an XML scheme. There is no issue about the configuration file, as it contains little data (names, paths, port, policies...). On the other hand, the address space file is large. To ease the creation and the population of the server, its XML structure follows the LabVIEW OPCUA objects classification: root, folders, items, and properties. The constants file follows a simpler scheme, providing only a full node path and its associated constant value.

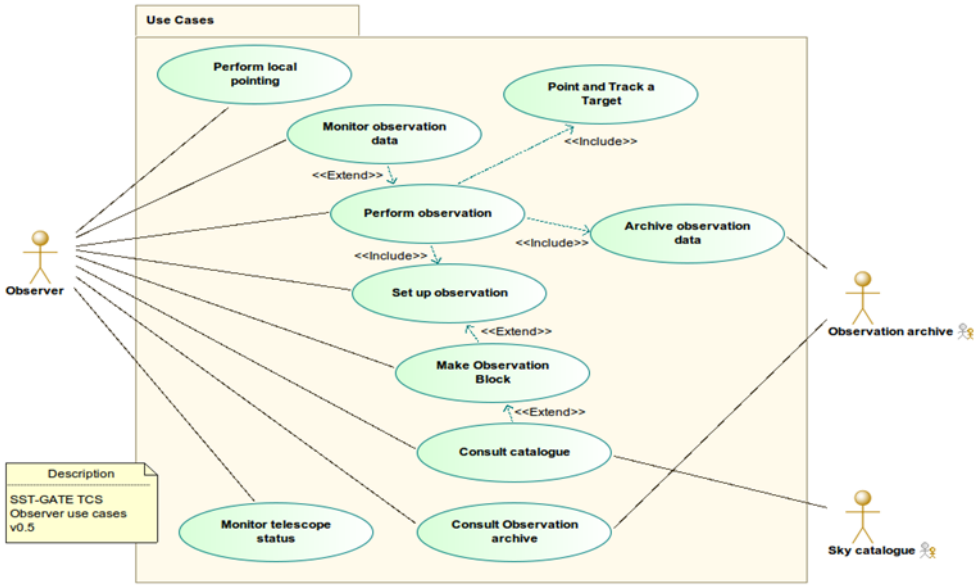

Figure 4.35: Observer actions

4.6.4 Telescope software core

The core of the telescope software is implemented as a state machine called supervisor. The supervisor manages all the software modules and gathers all the required information or orders to switch to the required mode. The supervisor's modes are (see Figure 4.38):

- Warm-up: Initial mode; start all usual processes and wait for stable operation.
- Observation: Main mode for the Observer.
- Maintenance: Access restricted to Engineer; all processes started/stopped at will; calibration constants may be modified.
- Warning: Automatic mode; keep all running processes.
- Fail-safe: Automatic mode (has priority over Warning); park telescope; stop all motion processes.

The modules managed by the supervisor are:

- RT control automation (pointing and tracking software and drive control).
- Slow control automation.

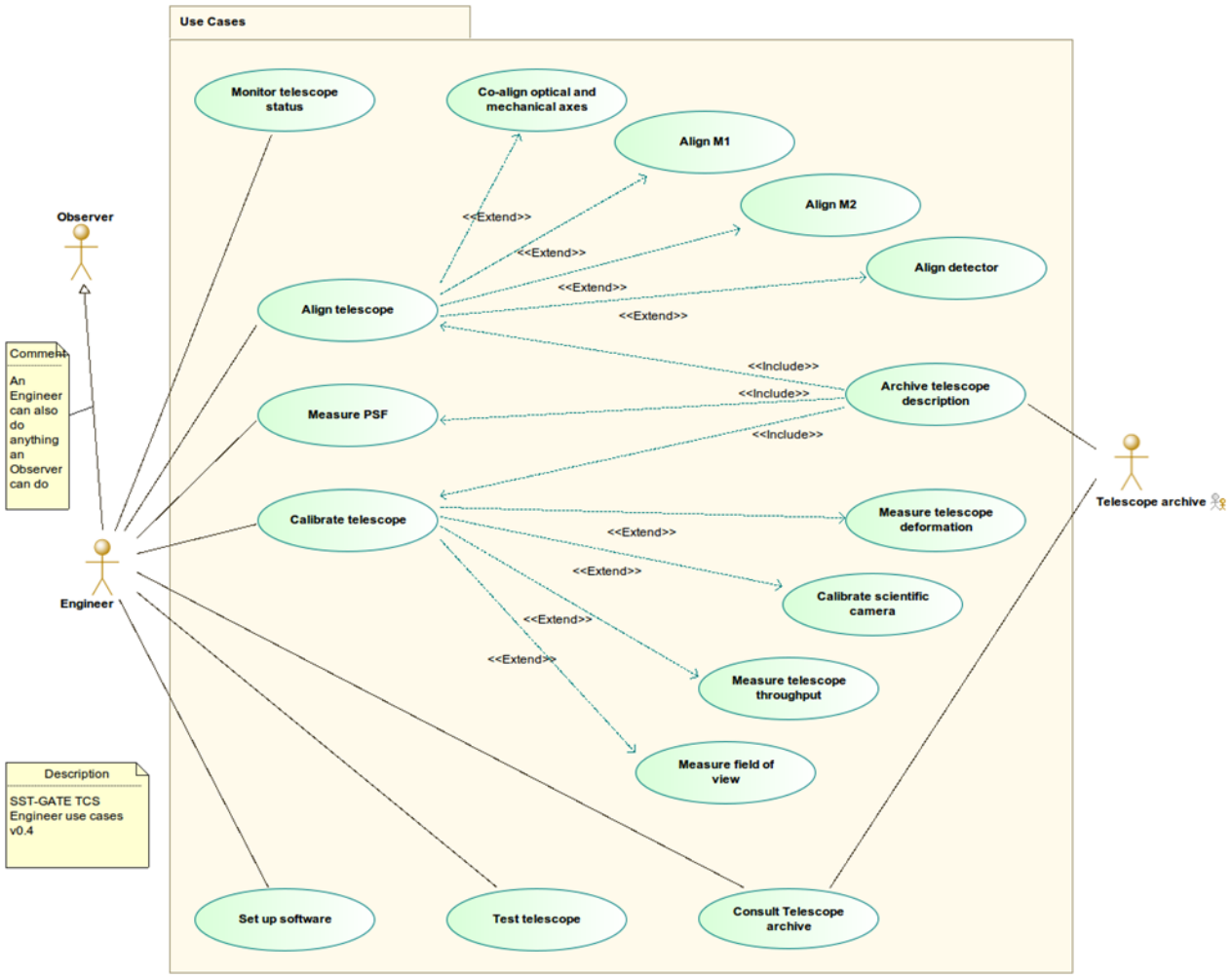

Figure 4.36: Engineer actions

- Command manager.
- Main PLC event logger.
- Error manager.
- Main PLC resources manager.
- Background built-in test (BIT).
- Handshake – with the safety PLC – manager.

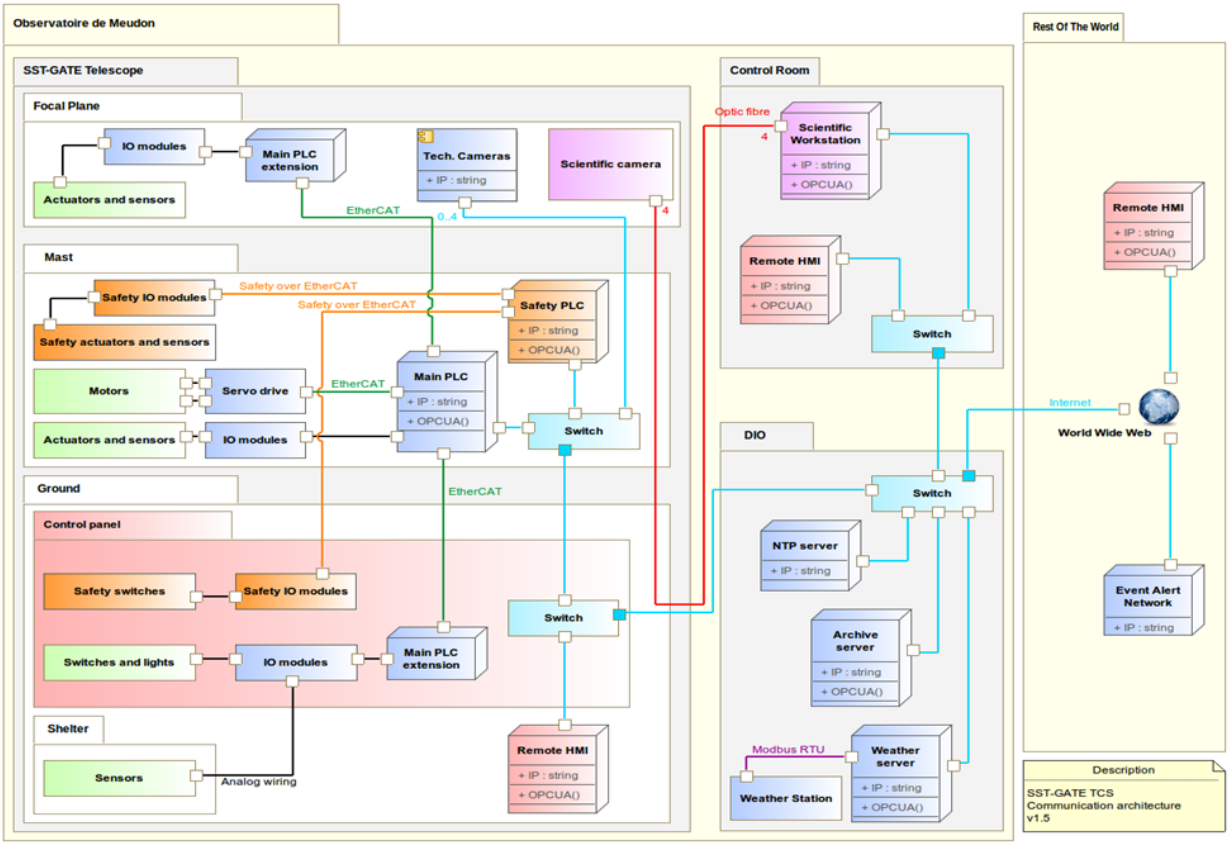

Figure 4.37: SST-GATE communication architecture

- OPCUA client manager.

4.7 Pointing and tracking software

The pointing and tracking software is a stand-alone module. Given a target, a starting time and the duration of the observation, the module computes the required transformations to obtain the full required trajectory the telescope axes have to follow. This trajectory is then forwarded to the drive system to control the telescope axes in real-time. The main PLC clock will be synchronized via a daemon with a secondary (stratum 2) NTP time server provided by the Paris Observatory. The frequency of synchronization is still to be decided, depending on the required time accuracy and the main PLC clock accuracy with an operating temperature range of -10°C to +25°C during observations.

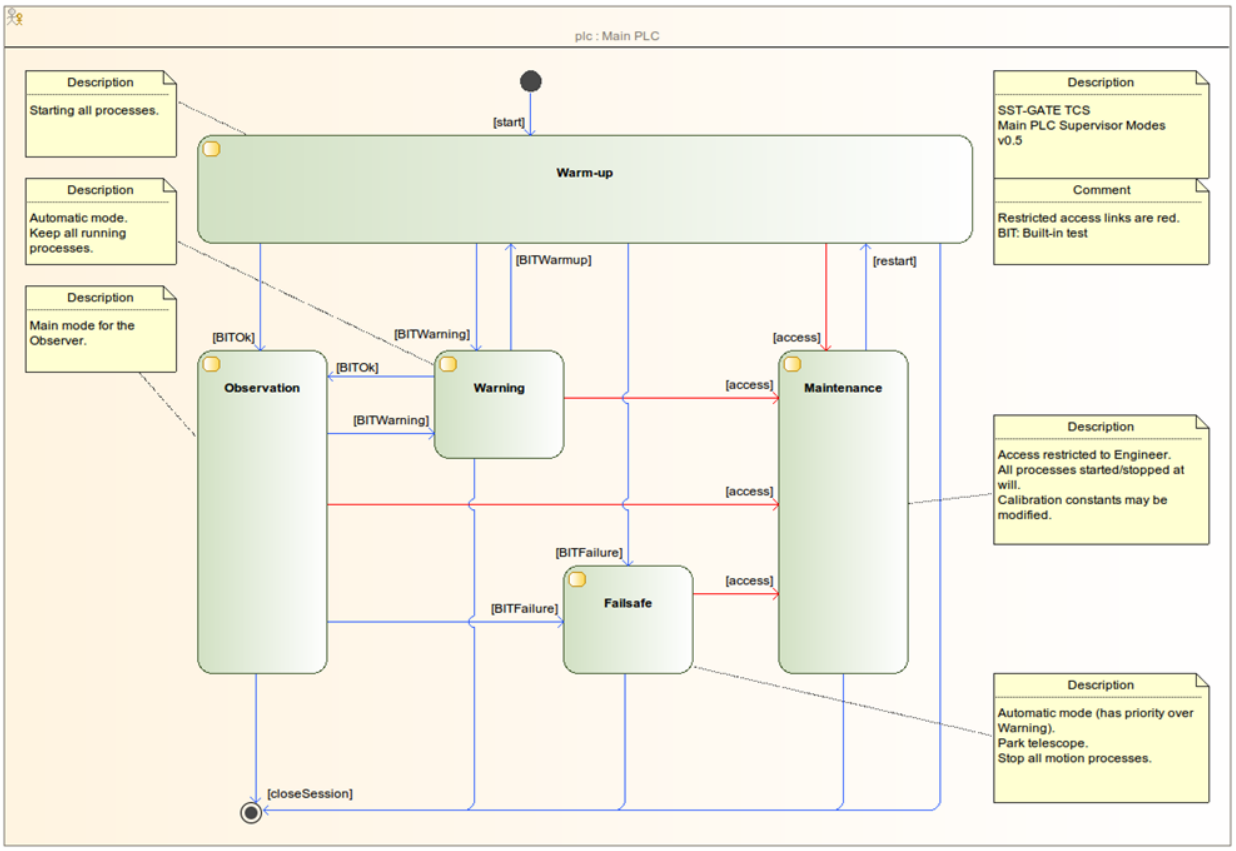

Figure 4.38: Main PLC supervisor modes

4.7.1 Drive control software

The drive software is split into two main parts: the trajectory software module and the servo software module (Figure 4.39). Two kinds of trajectories are involved: a low frequency trajectory is made in the pointing and tracking module from the provided observation data and the shaper module transforms this into a sequence of target positions – with zero velocity. On the other hand, the online trajectory module's purpose is to provide, at the servo rate, target points (position and velocity) to ensure a smooth motion while taking into account the low level systems' limits (velocity, acceleration and jerk). The algorithm used here is taken from the robotic company Reflexxes. The software will be located in the main PLC and, thanks to the EtherCAT link and the main PLC's operating system, a full real-time motion will be performed.

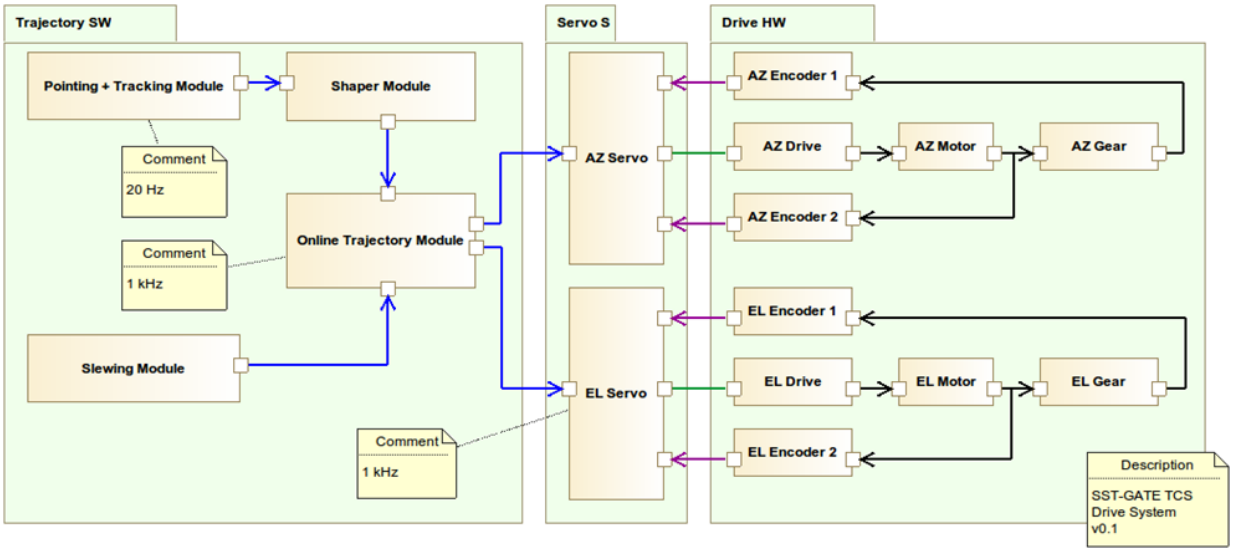

Figure 4.39: Drive system software and hardware elements.

4.7.2 Software implementation

The telescope software is implemented in the main PLC. This PLC will be a CompactRIO, from National Instruments: a rugged PLC family featuring a real-time OS (VxWorks) and a FPGA backplane enabling great versatility in software implementation. The model is not yet defined – a NI cRIO 9074 is currently being used to perform tests and define the required disk, memory and FPGA sizes. A safety PLC – most likely from Beckhoff, for field bus consistency – will be used to manage all safety-related sensors and actuators. The remote software is implemented in a workstation. Thanks to the Ethernet-based architecture, the workstation may be located either in the control room or in any place provided with an internet connection. Regarding the file formats, the OPCUA server address space file XML scheme is fixed.

The successful implementations already performed are:

- Communication between an OPCUA server implemented on a cRIO and a third party OPCUA client on a distant workstation.
- Synchronization of the cRIO with a NTP server (time delivering).
- Weather station readout via a Modbus RTU link.

The work in progress includes:

- The pointing and tracking algorithm.

- The drive control algorithm.
- The GUI prototype.

4.8 Costs

The goal of SST-GATE is to build a telescope which respects the cost requirement of CTA and the SST-GATE budget. The cost of an SST telescope in the industrialized phase and with contingency is 420 k€. SST-GATE is mainly funded by the Region Ile-de-France through the SESAME funding scheme. This funding has been obtained by the GATE consortium which is composed of five French laboratories situated in Paris. All of them are working on the CTA preparatory phase. The Observatoire de Paris is the only one focused on the SST and proposing a full telescope prototype. The budget for SST-GATE (equpment only) is 280 k€. Some additional funding is available from the Observatoire de Paris. This is used mainly for travel and to purchase the infrastructure equipment or civil works needed to install the telescope. Last year an amount of 35k€was received. This year a larger budget scould be obtained as the SST-GATE project is strongly supported by the administration.

The overall budget for the SST-GATE telescope can only be estimated at this stage. The design is still undergoing final optimisation and the mechanical plans are not yet entirely fixed. However, the philosophy of the SST-GATE design is to fit the industrial capacity by using beams, plates, and tubes with existing dimensions. For instance, the tower has been adjusted in diameter in order to fit the usual standard. Concerning the actuators and sensors, we are directly working in collaboration with industry. For instance the actuators will be from Nexeya, who were involved in the project since the beginning of the mirror design. We try to design with COTS (commercial off-the-shelf) in order to decrease the cost by using standard elements, and to ensure the maintainability of the telescope. Table 29 summarizes the cost estimated for the Meudon site and for mass production. As regards the infrastructure etc. on site, this will depend on the chosen location for the southern observatory.

4.9 Reliability, Availability, Maintainability and Safety

4.9.1 Risk analysis

The project is currently at the preparatory phase. For this phase and following the CTA RAMS plan, a preliminary risk analysis was done. The policy for managing SST-GATE project risks is described in the SST-GATE risks management plan. The preliminary risk analysis process includes five steep as shown in the Figure 4.40.

Risk Analysis allows identification and assesses the risks of any kind incurred by the project; all risks are organized in different domains:

- management
- system

	Meudon site	Mass Production
Infrastructure	32 k€	?
Network	4 k€	?
Mechanical structure	130 k€	80 k€
Control software	30 k€	25 k€
Alt-azimuthal sub-system	40 k€	30 k€
Mirror M1		
actuating	15,3 k€	12,5 k€
mirror	100 k€	60 k€
transport	1,2 k€	?
Mirror M2		
actuating	2,6 k€	2 k€
mirror	0	6 k€
shelter	45 k€	35 k€
Camera	CHEC	CHEC
Cables, fastenings	55 k€	50 k€

Table 29: Cost breakdown

- foundation and Slab Structure
- alt-azimuthal Mechanical Structure
- azimuth Drive
- elevation Drive
- mast and Truss Structure
- primary Mirror Structure
- secondary Mirror Structure
- front End Camera
- telescope Control and Alignment System
- software Data System
- protective Shelter Structure
- safety

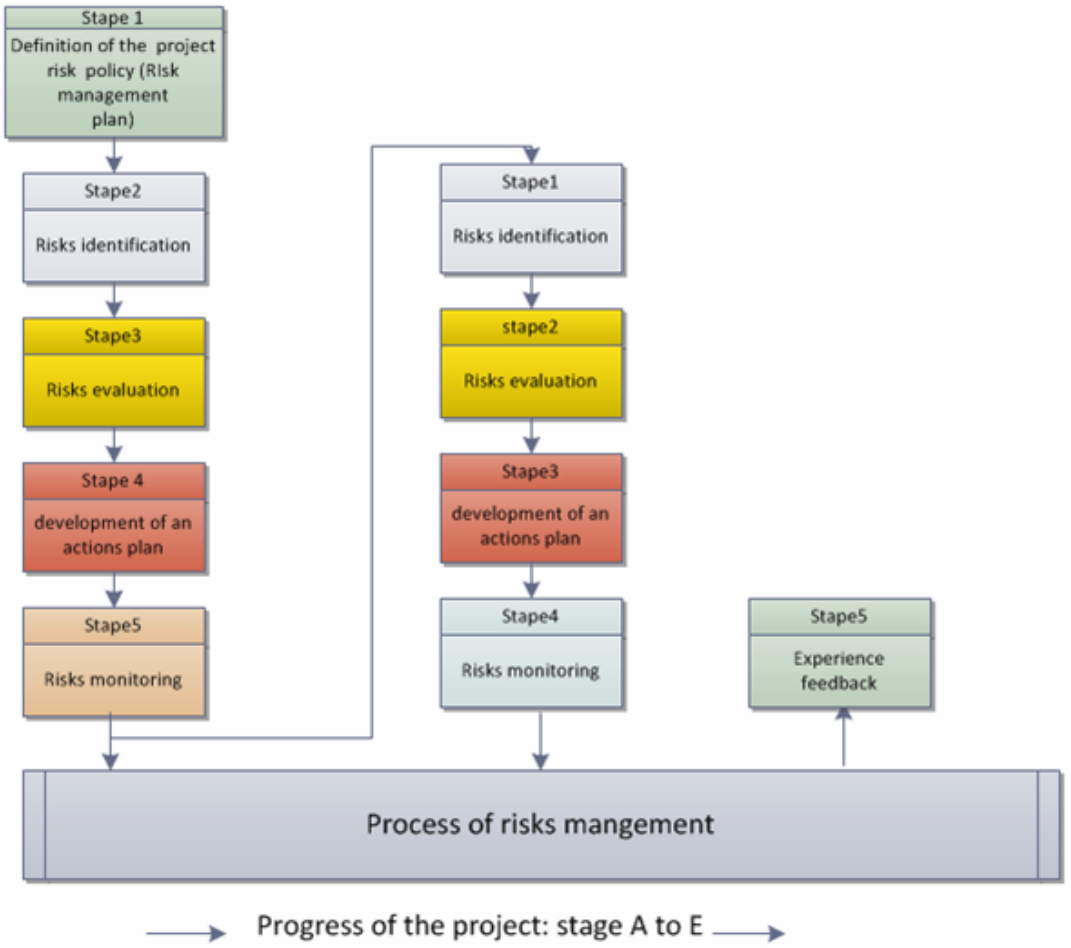

Figure 4.40: Preliminary risk analysis

- AIT
- maintenance
- environment

Functional analysis started at the beginning of the project and is currently under up-date; therefore, FMECA is also under review. FMECA and SST-GATE risk analysis was discussed during the CTA quality meeting in Heidelberg and in Milan.

4.9.2 Behaviour in case of emergency

In case of emergency for CTA, an inverter will be used (1) to detect the loss of electrical power, (2) to close the current activity, (3) save files and (4) move the telescope back to its parking position. In the SST-GATE telescope, passive return is always provided for safety reasons, so even in the case of emergency failure, the telescope will be brought back to its parking position by the passive return. However, to save files and switch off properly the PLC, an inverter will be used. The assessment of the appropriate inverter will be made considering the power for the electronics (2 kW). So the inverter is 3 kVA, the autonomy of the battery is 8 min at 100% and 20 min at 50% which is enough to shut down the PLC.

If at the same time, CTA preferred that the telescope moves back to its parking position using the AAS motorization, a global assessment can be made. Considering the maximum power of 10 kW, the inverter must be of 16 kVA. In this case, the battery autonomy is 24 min at 100% and 55 min at 50%, so this time is far enough to switch off everything and park the telescope.

4.9.3 Safety

Safety conditions described in the French and European standards will be respected for the preparation and the installation of the telescope at the MEUDON site, Meetings were held with the safety engineer of the Paris Observatory to implement preventive actions concerning the safety of persons and the handling of heavy loads, etc. Safety equipment for the AIT phase has been purchased: helmets, additional lighting, gloves and goggles are provided. Moreover, two stop buttons will be provided close to the telescope in order to switch off all electrical systems and movements in case of problems.

4.10 Calibration and alignment

4.10.1 Philosophy

All the SST-GATE alignment elements will have absolute sensors to allow retrievl of their position even after a power failure. This will also reduce the overhead due to finding the end-switches to perform a calibration of each movement and will ensure the required accuracy. In SST-GATE, each alignment sub-system (i.e. the primary and the secondary mirrors) will have its own group of three actuators and sensors to provide 6 degrees of freedom. Two actuators would have been enough to align the mirrors, but the camera would then need a moveable support. To save weight and volume around the camera, we choose to use a third actuator for each tile. Hence, by moving both the M1 and the M2 mirrors in the same direction, it is possible to move the focal plane forwards or backwards without any additional sub-system. This simplifies the camera removal mechanism; it saves cost and eases the AIT of the camera. Another advantage of this philosophy is that it makes the alignment independent of the mechanical mounting or any further change in the design. Indeed, the actuator's stroke (30 mm) ensures it is possible to place the tiles at the required position whatever the design.

4.10.2 Movement calibration

The calibration will be performed rarely, at a rate of onece per year, to measure possible mechanical shifts or ageing for the azimuth and the elevation movements. The procedure will consist of making half and complete turns (for the azimuth) at different elevation angles and 90 degree movement (for the elevation axis). The exact angle will be determined by selecting several pairs of stars (one for each end of the movement). The results will be compared with the initial calibration in order to update the telescope parameters in the software. Concerning the sensors, we will use absolute ones in order to get the real position each time the telescope is switched on. This solution avoids the need for accurate end-switchs or an accurate zero-position.

4.10.3 Alignment of the telescope

The telescope alignment consists of two items. The first is devoted to the alignment of the optical elements of the telescope so that it will be able to focus onto the focal plane and at the proper position the image of the showers. The second is the alignment between the mechanical axis and the optical axis. The alignment procedure must include a method to determine the angle between the mechanical and optical axes to make the telescope able to point its optical axis at any point in the sky with the proper accuracy. Moreover, the procedure must allow monitoring of the possible shift of the different optical elements of the telescope in order to determine when a re-alignment is required.

All the details about the telescope alignment will be available in the report [503-AIV-GEPI-PR-0001]. We only tackle in this section the main lines of this procedure.

An optical bench is usually mounted on a rigid table which plays the role of reference. For the mounting of a telescope, we must find another mechanical reference as the ground can not play this role. We chose to use the mechanical centre of the M1 and the M2 dishes. A target will be mounted at their centre with a mechanical accuracy of 0.1 mm. The line passing through these two centres will define the mechanical axis of the telescope. A laser installed on this axis and behind the M1 mirror will make this visible. The goal of the procedure is to align the optical axis along the mechanical one. We first intend to install the M1 tiles with a mechanical accuracy of less than 1 mm. This is sufficient for the x, y and z position as well as the z-axis rotation [see ref Julien Rousselle presentation in Amsterdam and the Denis Savoie's simulations hereafter]. The S-C optical design with an M1 split into tiles suffers from a degeneracy between the effects of x, y movements and tips/tilts of the tiles. It is not possible to distinguish one from another by the use of the PSF positioning. Nevertheless, in the SST-GATE case, we alleviate this problem by having a positioning accurate enough to have only the tip-tilt to take into account during the alignment. Recent thermal and mechanical simulations showed that we can rely on a mechanical accuracy of 1 mm. The obvious second step is to place the M1's tile PSF at the proper position on the M1's focal plane. The latter is located with the help of the laser and by placing a flat screen at the theoretical focal distance of M1. Then, a camera with a mirror fixed at its back is installed at the top of the M2 mechanical mount. The mirror will be tuned on a test bench so that its axis is parallel to the camera optical axis. The laser allows the orientation of the camera with respect to the mechanical (and the optical) axis. We can now install the M2 mirror so that its centre corresponds to the impact of the laser on it to ensure a proper position (x, y). The three M2 actuators will ensure the z and tip-tilt position (the laser beam must be reflected onto the laser). As the M2 is symmetric along the z-axis, no alignment is required for this degree of freedom.

One (small) section of each tile will be sacrificed to have a flat area capable of reflecting the light emitted by a source at the back of the telescope (possibly the counterweight). The movement of the light spot on a camera close to the light source will detect any tile movement. The actuators will be used to perform an alignment if the detected movement is considered significant.

4.11 Pointing

The pointing system is not being developed by SST-GATE. We plan to use the pointing system of the Dutch team. We collaborate on the definition of the telescope specifications which constrain the pointing system. We are waiting for the ICD to integrate the system to our telescope.

4.12 Test plan

The test plan is a complex document that has yet to be completed.

First of all, the telescope will be tested to check its behaviour in case of hazards. The telescope will then be forced into error situations, such as forbidden movements, or motor failures. This will allow checks of the safety end-switches and safety PLC. A full list of hazardous actions will be made in order to check all eventualities.

Then, we will validate the global mechanical system by testing the pointing and tracking positions. This step will help us to define the drive systems and check the accuracy of the software requirements and the telescope movements. The tests will be performed by observing stars having different motion speeds in the sky.

Once the movements of the telescope have been competed, we will be able to measure the optical quality. The goal will be to measure the PSF versus the elevation angle and versus the FOV. This step will allow us to validate the optical performance. This test could be done by measuring, for instance, the alpha polaris star. To do so, we will just need a CCD camera (e.g. PHOTONLINES).

The final test will then be done in order to fully characterise the mechanical structure of the telescope. The eigenfrequencies will be measured as well as the displacements during wind loading and due to thermal effects. For this purpose, dedicated sensors that will not be part of the mass production telescope will help in understanding the telescope behaviour.

4.13 Site considerations

In this part, we aim to summarize all specific characteristics of the SST-GATE prototype infrastructure in order to give the information needed to choose the future CTA site. We list below the equipment needed in terms of infrastructure, electrical and Ethernet supplies, and shipment. The first requirement for the assembly has already been discussed in section 4.5.

4.13.1 Control and security of the telescope

Several non electrical equipment items have been defined in order to control and secure the telescope. Close to the telescope screwed on the slab will be placed the switchgear cubicle, where the cable of 10 kW (see the paragraph on power below) will be connected. The cubicle is protected against dust and rain (IP 65). Five additional plugs will be placed on it, one of 400 V and 4 of 230 V. In order to guarantee a good operation of the electrical network, several elements will be provided:

- 1 sensor to measure the global power consumption (sensors can be placed on dedicated cables to measure properly the power, for instance for the camera and AAS motors).
- 1 stop button on the cubicle.
- Circuits breakers: 1 general and 7 on each section of the electrical board.
- 1 lightning arrester.
- Voltage transducer: 3 transducers from 400 V to 230 V, and 1 from 400 V to 24 V.

In terms of safety risk, pictograms of electrical risk will be placed on the cubicle and electrical board. A fire extinguisher (CO2) must be placed close to the cubicle. Two other stop buttons will be placed on the telescope in order to switch off the telescope in case of emergency.

4.13.2 The control room

The control room of the telescope must take into account several requirements as the scope of such a room is to house the remote HMI and the scientific workstation. As the control room does not have a direct view of the telescope (that will also be the case in CTA), a webcam will be installed in order to monitor movements. The switching on of the telescope will not be possiible if the shelter is closed. Dedicated position sensors will be placed on the shelter. The opening and closing will be done close to the telescope (A Meudon requirement is for public/educational tours). This could be changed for CTA and can be done at distance. The available control room for SST-GATE is about 20 m^2 and as we are placed inside the observatory all other facilities such as offices, meeting rooms, dining facilities are provided. For the CTA site, the same surface for the telescope control could be sufficient, but rooms for conferences, meetings and all others facilities must be foreseen. Accommodation is also available close to the observatory and at Meudon.

4.13.3 Ethernet communication between equipment

The SST-GATE control and command system has been developed using standard solutions from the industry. The communication architecture is based on an Ethernet low-level layer and OPC-UA as a software layer. So the communication is based on RJ 45 wires. The architecture is then composed of:

- 1 main PLC.

- 2 main PLC extensions.
- 1 safety PLC.
- 2 remote stations for day to day scientific use of the telescope.

The main PLC, its extensions and the safety PLC are placed on the telescope. However the main remote HMI will be placed in the control room for scientific use and night observations. In addition, a remote station such as a laptop could be used close to the telescope, for instance during the maintenance phase or in the case of Meudon public and educational tours.

In SST-GATE, 5 IP addresses are needed for the telescope control. To secure the communication, they must be connected to the same switch. In addition, external equipment must be connected to the telescope software such as:

- Weather station.
- Archive server.
- NTP server.

All these are located in another computer room at the observatory; communication between this equipment and the telescope software is through standard Ethernet wires with RJ45 connectors.

The standard data transfer rate at the Paris Observatory is 100 Mbits/sec inside the building and 1 Gbit/sec between the buildings. For the performance of the SST telescope, these characteristics are sufficient.

However, the scientific camera developed for Cherenkov astronomy can need a higher data rate. As the telescope SST-GATE has been proposed as a camera test bed, a fibre link of 10 Gbits/sec has been installed between the telescope and the control room. The proposed equipment is:

- Optical fibre: unique length to avoid losses in switches and to secure data. The optical fibre is composed of a 12 element fibre so 6 pieces of equipment can be connected: 2 for the camera, 1 for the trigger and some spares; the fibres are multimode 50/125 in OM3 standard.
- 2 connectors: the fibre will be connected to the Ethernet bay placed on the slab, the connection with the camera is made by a FC screw connector. The same connector will be used inside.

The bay on the slab is composed of:

- Electrical unit for the plugs.
- 1 empty unit for electrical wires to be connected.
- Optical rack : 1 unit.
- 1 unit for patch panel to connect RJ 45 based wires.

- 1 unit for the cable grommet.
- 1 unit for the Switch HP Procurve 2510-24 with 2 plug 1 1 Gb/s and 24 plugs 100 Mb/s.

The final choice of the bay will be 12 U in order to have some margin for expansion.

4.13.4 Shipment

Transport will be by road and sea. The main goal is that all equipment can be transported on conventional trucks and boats. The SST-GATE telescope is composed of several sub-systems that can be assembled on site; the partitioning of the elements and the assembly and integration plan is currently being written. Currently, it seems that the maximum load will be 500 kg and the maximum height could be around 2 m.

First discussion with our partner Ulisse at the DT-INSU give the following conclusions:

- Standard container 2.40 x 6 m.
- Transport by sea is risky as it presents risks of corrosion, a dedicated protective layer must be provided, in addition to the box which is not secured at all.
- The protective systems (such as absorbers and wrapping layer) must be provided considering the fragility of each telescope part.

The main parameters to define for each element in order to find the best appropriate protective layer are:

- Maximum acceleration accepted by the component.
- Temperature and humidity.
- Mass, volume, fragility.
- Mechanical points on wich the element can be supported.

For the most fragile parts, a shipment by airplane must be envisaged, for instance part of the camera.

4.14 Drives

The drives system consists of a motor, its drivers, the mechanical gear (if required) and the sensors needed to operate the drive. Considering the CTA requirements, our design is made of ETEL motors both for azimuth and elevation because they can ensure high and low speeds while no torque is available when the power supply is off. This eases the return system design.

We have estimated the torque our telescope drives must provide for various situations (wind speeds and elevations). The maximum torque is 3,000 Nm with 15% margin. We add a security coefficient before choosing the ETEL motor (TMB0140-150). The data sheet of the torque motor is given as an appendix C.4

Encoders must fit two constraints: the volume available and the accuracy they must provide. During CTA operation, an accuracy of one arc minute should be enough. Nevertheless, as SST-GATE is a prototype, we will equip the telescope with an enhanced encoder to reach 3 to 5 arc-seconds. We chose to have an over-accuracybecause it will help us to understand the telescope and to split the mechanical and the optical elements that are involved in possible discrepancies. We are in contact with HEIDENHAIN for providing and defining the most suitable encoders for our application.

The detailed design is subject to change in function of the type of encoders we choose.

To provide the autonomous return, we will use a second torque motor for the azimuth motion and for the elevation motion. A safety power supply will be implemented close to the tower of the telescope.

The CAD image presented in Figure 4.41 shows the configuration and details without the encoders.

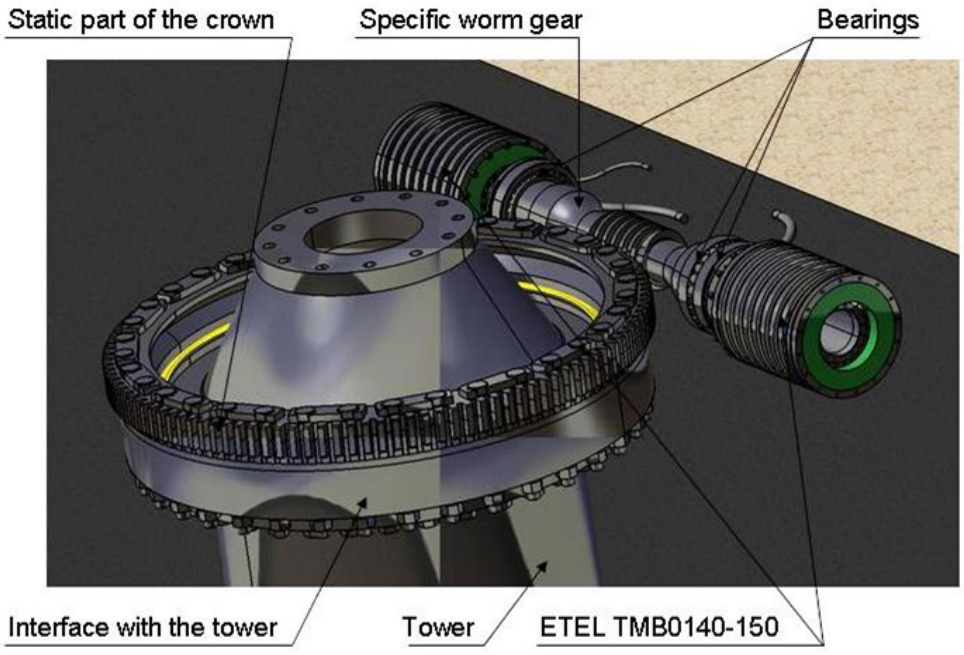

Figure 4.41: View of azimuth drive with motors

4.15 Power requirements

The power requirement has been established following the different uses of the telescope. The items consuming power in the telescope are the following:

- The motors of the shelter (automatic opening) 5 kW.
- The motorization system of the telescope: 2 kW for each elevation system and azimuth systems.
- Mirror alignment: 0.6 kW.
- Camera optical: 0.1 kW and scientific: 1 kW.
- Control and command of the telescope: 0.6 kW.
- Ethernet bay: 0.1 kW.

In terms of equipment needed during the assembly, integration and test phases, three kinds of equipment are taken into account as regards their power consumption, namely:

- Small equipment (a laptop for instance): 1 kW.
- Medium equipment: 2 kW.
- Large equipment: 4 kW.
- Lighting by LED: 0.2 kW.
- Additional plugs 400 V: 3 kW.

Normally, these items will work on their own batteries, however, to ensure their operation, the possibility to plug them while they are used is taken into account.

The different uses of the telescope are now listed together with the equipment operating. Only the PLC and Ethernet switchgear cubicle will be running continuously.

- The opening and closing of the shelter: automated using two motors; only the lighting is switched on when the shelter is opened or closed. Total power: 6.9 kW.
- Switching on of the telescope: only the webcams operated at this stage. Total power in this case: 3 kW.
- Motorization testing, the elevation and azimuth motors are operating. Total power in this case: 7.9 kW.
- The alignment phase: camera, lighting and maybe some AIT equipment are used. Total power in this case: 8.4 kW.

- Observations: motorization, camera and maybe small AIT items will work at the same time. Total power in this case: 6.8 kW.
- The maintainenance phase: can be made with the motors switched on and all AIT equipment running, in this case the total power is 10.9 kW, however it seems very rare that both the large and medium equipment as well as the 400 V plug will be used at the same time so the total power is less than 10 kW.
- The assembly phase: we can imagine that all AIT equipment will be working; in this case the total power is 10.3 kW.
- No working use of the telescope: everything is shut down except the PLC and Ethernet bay; total power in this case: 0.7 kW.

Following the previous list, the maximum power is fixed at 10 kW including a margin of around 3 kW for the main phases of telescope use.

4.16 Maintenance and operation

4.16.1 Maintenance

Maintenance will be driven by (1) the MTBF calculations and (2) the results of preventative maintenance. The MTBF of a system can be estimated by the datasheets of the different modules that are parts of the system. As one CTA requirement is a lifetime of 30 years (87,660 hours, assuming a duty duration of one third) we have selected the aforementioned parts (motors, ball bearing...) wherever possible with the MTBF needed to give an adequate lifetime, taking into account the cost. When this was not possible, we added sensors to the design to allow preventative maintenance and the MTBF calculations gave us the number of spares required for a lifetime of 30 years. As an example, the PLC we chose for SST-GATE has a lifetime higher than 250,000 hours and has an operational range larger than the CTA requirements (-40°C to +70°C). Preventative maintenance consists of using sensors to measure a physical characteristic that will help us to anticipate a failure. As an example, accelerometers on a ball bearing will give the vibration frequencies and their amplitude. With the help of tables, it becomes possible to schedule a maintenance – which can take a long time for the azimuth ball bearing – well before failure occurs. This philosophy is extremely interesting for elements that are very expensive (i.e. having spares may cost a lot). Our list of these elements is:

- Azimuth and elevation ball bearings.
- Azimuth and elevation motors.

For these items, accelerometers (for ball bearings), current sensors (for the power consumption of the motors and/or the drivers) and torque sensors (for the torque transmitted to the ball bearings) are foreseen in the SST-GATE design.

For the actuation systems of the M1 tiles, which consist of actuators, drivers and sensors, we follow the same approach. These elements will not work for a long time, since the alignment will take no more than one

hour on each occasion, giving a maximum of 1,500 hours for the 30 years lifetime of the telescope, assuming a re-alignment each week. In this case, no maintenance is foreseen, but spares will be provided taking into account the relevant MTBF.

The mirror lifetime will strongly depend on the site conditions (sand, wind, hail...) and will impact on the re-coating phases needed for 30 years. We have designed the mirror support structures so that removing a mirror is a rapid operation (we expect 2 hours per tile with its realignment). Indeed, the whole M1 mirror can turn around its optical axis, thanks to mechanical marks, in order to place the tile to be changed close to the ground. This makes the operation quicker as operations are made on the ground and not at an altitude of 5 meters. It will also decrease the risk of damage and mirror breaking. Once the mirror is changed, the M1 mirror is turned to its initial position and rotation is locked. Hence, we ensure both an easy mirror change and an alignment operated in the observation condition as the tile is situated at its definitive place before its alignment. On the prototype site, the telescope will be protected by a shelter in order to decrease the number of re-coating operations. The shelter, provided by Losberger, is a dome with a PVC membrane giving natural light inside and providing protection from animals, vandalism and weather. The shelter is shown in Figure 4.42.

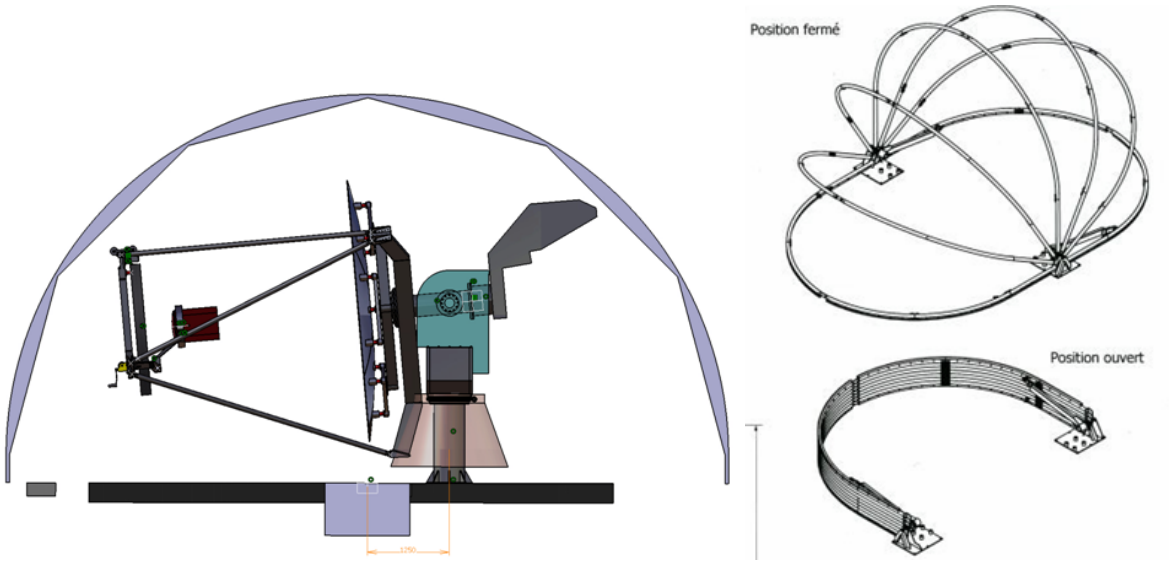

Figure 4.42: Shelter

4.16.2 Operation

Operating the telescope means getting it to point at a source and tracking the source with the accuracy needed to perform good science (i.e. the PSF is on the central pixel for an on-axis observation). This assumes that all the movable parts are available, the PLC (main and security) are running and that all security and housekeeping sensors return an OK status. All this information will be gathered and sorted by

the SST-GATE software (see Figure 4.43 for its GUI). It will be able to raise any error to the operator who will decide, in the case of a major error, what to do.

Figure 4.43: Observation tab of the GUI prototyppe

4.17 Summary

We designed our telescope with its functions as independent as possible to make a light and versatile structure. Example include the camera removal mechanism, the rotation of M1 that helps to mount the tiles without the help of a crane and the separation between the M1 dish (which supports the tiles) and the structure which supports the MTS to prevent the latter warping the former and hence decreasing the optical quality of the telescope. Changes in the design occurring since the previous review are all the result of an optimization of the telescope structure to fit both the CTA requirements and to make easier the operation and maintenance processes. The Figure 4.44 shows the telescope SST-GATE with the latest optimizations that are detailed in this document.

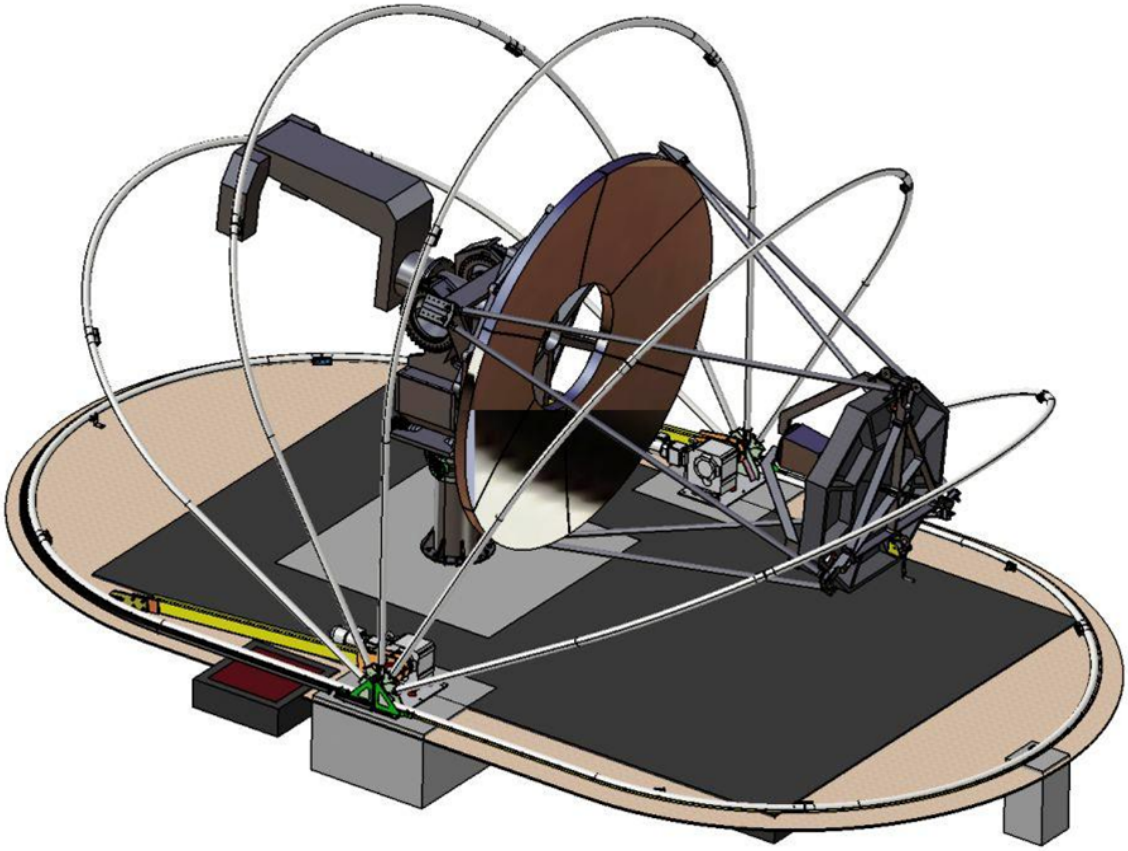

Figure 4.44: Telescope SST-GATE.

4.17.1 Compliance Matrix

The SST-GATE design takes into account all the CTA quality requirements as summarized in the compliance matrix in (Figure 4.45).

4.17.2 Performance

The performance of the telescope can then be summarized in these two figures representing the mass budget and the performance budget.

The mass budget is presented in table 30. The overall weight of the telescope is 6.9 tons. The small weight is a strong advantage of our design. This reduces the requirements on the foundation and eases the transport and the assembly phases.

Sub-systems	Mass [kg]
Tower	528
Fork	596
Azimuth part	510
Elevation part	915
Central tube	206
MTS	905
Dish M1	610
Mirror M1	250
Dish M2 and removal mechanism	270
Mirror M2	45
Counterweight	2800
Camera support	55
Camera	54

Table 30: Mass budget

The performance budget is presented in Figure 4.46. It includes all parameters, mechanical and optical, the uncertainties linked to all sub-systems and this budget is updated automatically when values are changed so that the system engineering is reactive to any changes in the design. This performance budget shows that SST-GATE fits the CTA requirements with a certain margin.

4.17.3 Perspectives

The first elements of SST-GATE have been delivered and have been mounted at the Meudon site (see Figure 4.47). The electrical and Ethernet supplies and optical fibres are installed on the slab to connect the telescope and the camera to the control room (see Figure 4.47)

The next step in the assembly process will be the mounting of the azimuth sub-system. Once the elevation sub-system and the fork mechanical simulation are done, we intend to finalize the formal analysis of the overall structure before completing purchasing. The mirror M1 construction process is currently under test and the manufacturing of the six petals will follow the test phase, so that the complete mirror could be mounted by the end of this year. At the same time, the mirror M2 will be received and so they could be both assembled on the telescope and correctly aligned in order to accomplish the final test of the telescope at the beginning of 2014. The mechanical test phase will be performed as the telescope is built (the required software is split into dedicated sub-programs) for instance measurement of the telescope parameters (non-

verticality, non perpendicularity) etc. This will also ease the software validation. This partition gives also the advantage to share the work and allows collaboration with the DT-INSU and the training of students. The test on the finalized structure and with all the software will be made in 2014. The CCD camera placed on the focal plane will allow testing of the optical quality and the measurement of the PSF versus FoV. The CHEC camera should be delivered by the end of 2014, by which date the telescope will be fully mounted and tested. The final test will be made thanks to the CHEC camera by observing Cherenkov light in the Meudon sky.

In Figure 4.48 are shown two examples for air showers seen with SST-GATE and a CHEC (MaPMT) camera. The images are simulations of the Cherenkov light from showers triggered by gamma-rays of 20 TeV and 100 TeV, assuming a night-sky background typical of sites where Cherenkov telescopes operate. Observations in Meudon will be mostly restricted to air showers from cosmic rays, and will be characterized in the next months.

CTA Quality Plan RED	Reference GATE (PAP)	Conformity		Comments
		Yes	No n	
3.1 Design				
3.1.1Design input (specifications)	2.1.2 Design :a Design input	x		
3.1.2 Design output (specifications)	:b Design output	x		
3.1.3 Design review	:c Design review	x		
3.1.4 Prototype validation	3.1.3 Documentation	x		
3.1.5 Technical Interfaces	3.1.3 Documentation	x		
3.2 Procurement				
3.2.1 Suppliers selection	3.4.1 Selection of providers	x		
3.2.2Procurement specifications	3.4.2 Provider documents	x		
3.3Manufacturing, assembly, integration and tests phase				
3.3.1Manufacturing	3.5 Quality assurance during manufacture and AIT/AIV	x		
3.3.2 Incoming control	3.1 General requirements Incoming control	x		
3.3.3 Assembly, integration	3.5 Quality assurance during manufacture and AIT/AIV	x		
3.3.4 Traceability	3.5 Quality assurance during manufacture and AIT/AIV	x		
3.3.5 Manufacturing tests	3.5 Quality assurance during manufacture and AIT/AIV	x		
3.4 Handling, packaging, storage, transportation, delivery and acceptance				
3.4.1 Handling, packaging, storage and transportation	3.5.6Handling, packaging, storage and transportation	x		
3.4.2 Delivery	3.1.3 Documentation	x		
3.4.3 Acceptance of the product	3.6 Acceptance of the product	x		
3.5 Installation, maintenance and decommissioning				
3.6 Specific documentation for Hardware products (deliverables)	3.1.3 Documentation	x		
4 , 4.1, 4.2, 4.3, 4.4, 4.5	**Under definition**			

Figure 4.45: ComplianceMatrix

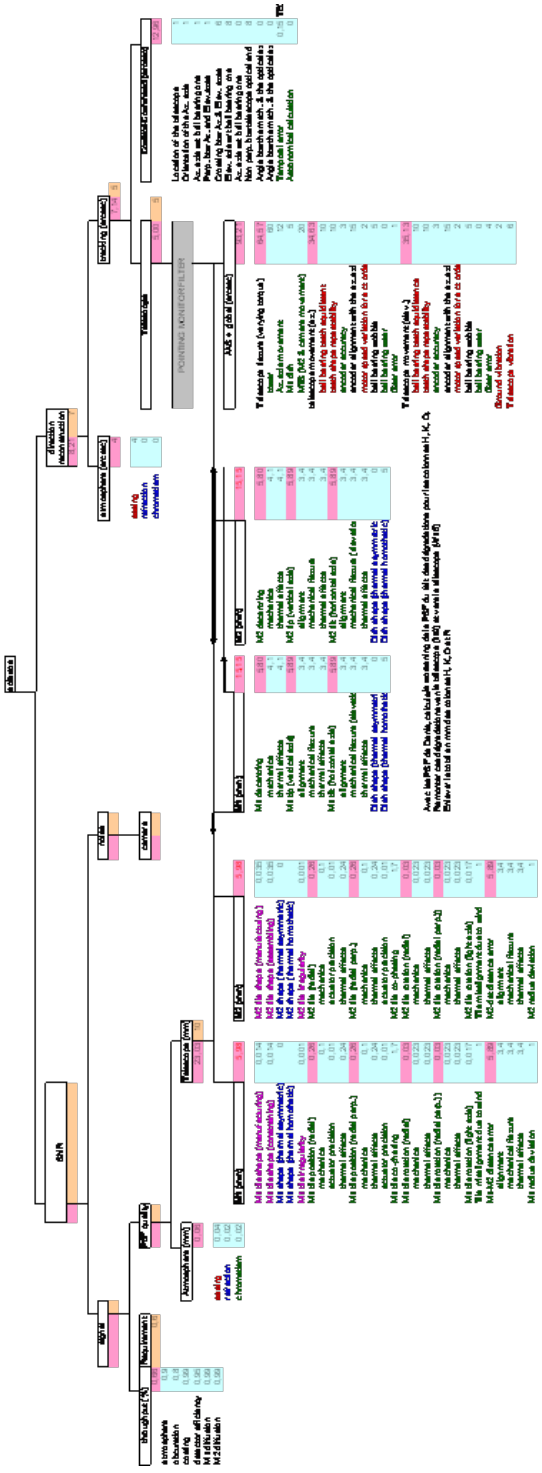

Figure 4.46: PerformanceBudget

Figure 4.47: Progress on the telescope SST-GATE.

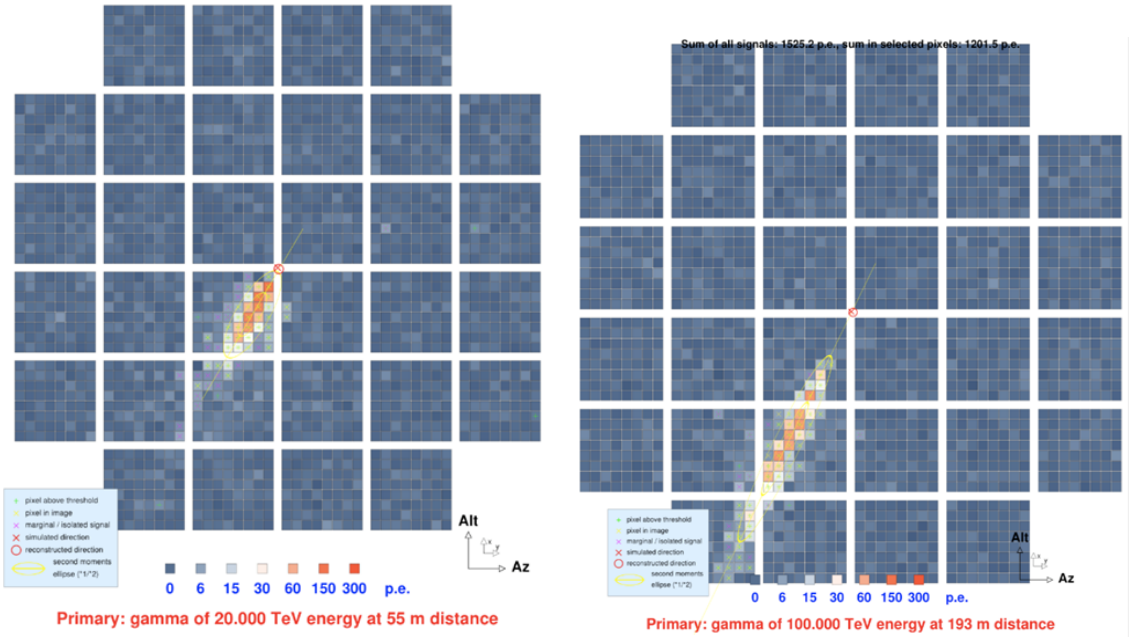

Figure 4.48: Simulation of the Cherenkov light from showers triggered by gamma-rays of 20 TeV and 100 TeV, assuming a night-sky background typical of CTA sites.

5 The Compact High Energy Camera (CHEC)

5.1 Concept

The Compact High Energy Camera (CHEC) is a camera-development project for the SST-2M. Two CHEC prototypes, based on different photosensors are funded and will be assembled and tested in the UK over the next ≈18 months. CHEC is designed to record flashes of Cherenkov light lasting from a few to a hundred nanoseconds, with typical RMS image width and length of $\sim 0.2^\circ \times 1.0^\circ$, and has a 9° field of view. The physical camera geometry is dictated by the telescope optics: a curved focal surface with radius of curvature 1 m and diameter ∼35 cm is required [26, 27]. CHEC is designed to work with both the ASTRI and GATE SST-2M telescope structures. The first CHEC prototype will be based on multi-anode photomultipliers (MAPMs) and as referred to here as CHEC-M. CHEC-M will be installed on the ASTRI prototype on Mt. Etna in Autumn 2014. The second CHEC prototype (CHEC-S) will be based on silicon photomultipliers (SiPMs or MPPCs) and will be ready ∼6 months after CHEC-M. Installation of one of these cameras or possibly a 'dummy' CHEC camera on the GATE structure is under discussion. The CHEC architecture is shown in Figure 5.1, with the principle components and functions described below.

1. **Photosensors -** MAPMs and SiPMs will be used for CHEC-M and CHEC-S respectively. In both cases 32×64-pixel modules of size $\sim 52 \times 52$ mm are envisaged.
2. **Preamplifiers -** Signal amplification and shaping to optimise camera triggering and readout, implemented on 16-channel boards. A single preamplifier module will serve 64 sensor channels.
3. **TARGET Modules -** 64-channel signal capture modules based on the TARGET ASIC for data digitisation, read out, pixel-level triggering and slow control. The camera will contain 32 such modules.
4. **Backplane Board -** All 32 TARGET Modules plug direclty into a large backplane PCB that provides: camera-level triggering, clock distribution, communication with the TARGET Modules and routing to the DACQ board.
5. **DACQ Board -** High-speed serial data from the TARGET Modules are routed to a DACQ board, connected to the backplane. This board thus provides data acquisition from the TARGET Modules, the interface to the outside world for the data stream, and control for camera 'peripherals' such as the lid and calibration systems.
6. **Mechanics -** The internal support structure, cooling system, enclosure and lid/shutter.

In addition to the elements labelled in Figure 5.1 CHEC will contain a (self-)calibration system based on LED flashers, reflecting light from the secondary mirror. More details on all elements are given below.

5.2 Trigger and Readout Simulations

The optimisation of the CHEC trigger is complete assuming MAPMs as sensors. The exercise is currently being repeated assuming SiPMs as sensors. Optimisation of the readout scheme will start soon.

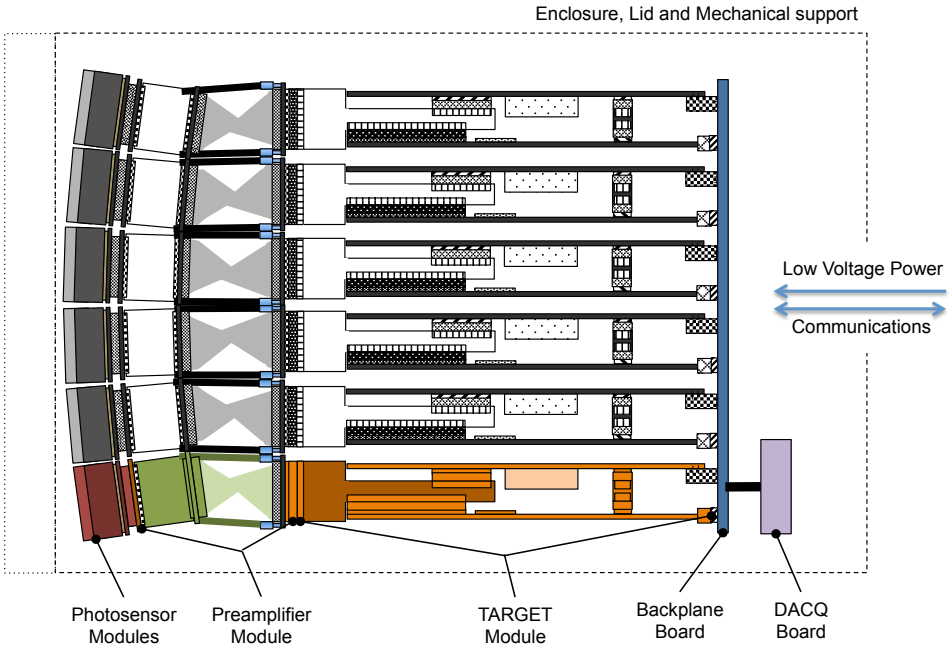

Figure 5.1: A schematic showing the principle elements of the CHEC camera.

Air showers and Cherenkov light production are simulation using CORSIKA with output in the form of photoelectron (pe) lists, which are converted to a ROOT-based image format assuming (for the moment) perfect optics. An electronics and readout simulation (developed independently at Leicester) is then applied. A camera of 32×64 pixel modules is assumed in all cases. The simulated signal and noise pulse height distributions (including after pulses) for MAPMs are based on a study by Homeschandra and Hinton in 2010. Pixel-level thresholds are derived by requiring an accidental camera trigger rate of 200 Hz at double the nominal night-sky-background level, which corresponds approximately to the 'safe' trigger definition of the Monte-Carlo working group. A digital pulse based on a pixel (or combination of neighbouring pixels) exceeding this threshold is assumed to be sent to the camera-level trigger where a neighbour requirement is applied. Trigger scenarios were constructed for the analogue-sum of 4 MAPM pixels, and 16 MAPM pixels, amplitude clipping of individual pixel signals pre-sum was also investigated. Figure 5.3(left) shows the trigger rate for these scenarios as a function of trigger threshold.

The goal of this study was to demonstrate that the basic SST requirements for triggering (efficiency of triggering Cherenkov images with intensity of 100 pe is greater than 50%, B-SST-1230) can be met. Figure 5.3(right) shows the trigger efficiency as a function of minimum image amplitude. Trigger efficiencies for

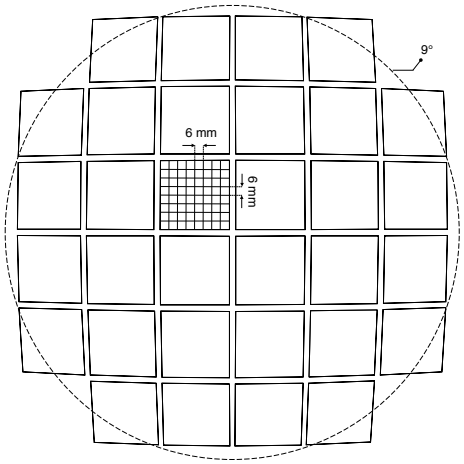

Figure 5.2: Layout of the CHEC focal plane.

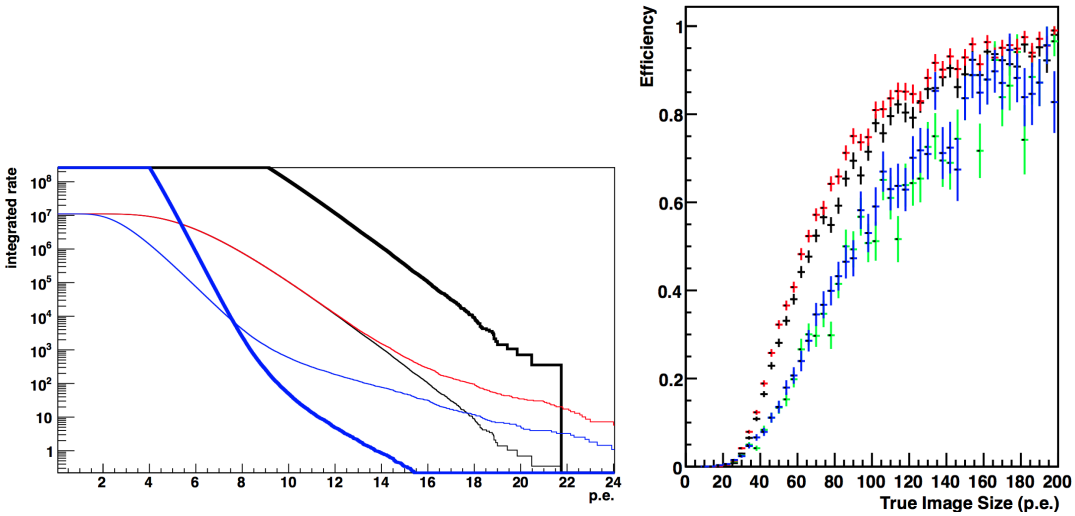

Figure 5.3: *Left:* The rate for a trigger based on 4-summed MAPM pixels is shown by the thin blue line. The corresponding camera rate based on 2 neighbouring patches of these pixels is shown by the thick blue line. The rate for a trigger based on 16-clipped and summed MAPM pixels is shown by the thin black line with clipping of individual pixels at 9 pe (and without clipping by the thin red line). The corresponding camera rate based on any patch of these pixels triggering is shown by the thick black line. *Right:* Trigger efficiency for gammas (red & black) and protons (blue & green) for camera triggers based on 2-neighbouring patches of 4-summed MAPM pixels (red & blue) and any patch of 16-clipped and summed MAPM pixels (black & green). A coincidence window of 9 ns and a pulse FWHM of 6.5 ns are used in all cases.

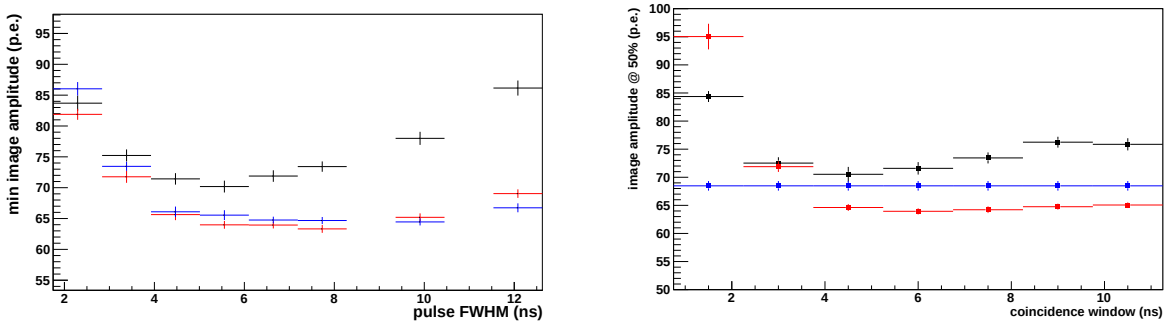

Figure 5.4: *Left:* Image amplitude for 50% trigger efficiency as a function of pulse width (FWHM) for coincidence windows of 3 ns (black), 6 ns (red) and 9 ns (blue) based on 2-neighbouring patches of 4-summed MAPM pixels. *Right:* Image amplitude for 50% trigger efficiency as a function of coincidence window for configurations that include gaps between MAPM modules for: 2-neighbouring patches of 4-summed MAPM pixels (red), any patch of 16-summed MAPM pixels (blue) and any 2-neighbouring MAPM pixels (black).

plausible CHEC-M configurations reach 50% at a threshold of (60 - 70) pe, well below the requirement, and meets the goal of 80 pe (B-SST-1240). In addition the triggers perform well at large energies and impact distances. Figure 5.4 shows the impact of pulse shape changes on trigger performance and illustrates that the trigger efficiency is relatively insensitive to the coincidence window between pixels. Gaps of 1-pixel width between MAPM modules in the camera have a significant negative effect on performance (at the ≈15% level), but the performance requirements can still be readily met.

Adding electronic noise at the expected level of 0.4 pe (rms) to the simulations results in a ∼10% increase in the image amplitude required for 50% trigger probability. Electronics noise levels significantly greater than 0.4 pe (per pixel rms, corresponding to 0.8 mV in our baseline operation mode) are therefore undesirable on the trigger (and indeed readout) path.

It is also clear from Figure 5.4 that a requirement of two neighbouring patches of 4-summed MAPM pixel pre-trigger (the baseline trigger scenario) has superior performance to a neighbour requirement applied to individual MAPM pixels. Furthermore, a simple trigger with no neighbour requirement, based on a 16-pixel analogue sum, has a performance approaching that of the baseline trigger scenario. No gain in performance was found for 3 different clipping levels tested for 2-neighbouring patches of 4-summed MAPM pixel trigger. However for any patch of 16-summed MAPM pixel trigger, clipping looks very promising, and may make this style of trigger very powerful. Figure 5.5 shows the impact of trigger time jitter and gain variations on the performance. Gain variations of $< 20\%$ rms have a modest ($< 10\%$) impact on performance. Time jitter on the inputs to the camera level trigger is acceptable up to ~ 2 ns rms when a ~ 10 ns wide gate is used.

In summary, the following specifications are used for CHEC-M to meet the requirements for triggering:

Pulse Shape (after pre-amplifier/at TARGET input): 10-90% rise-time 3.5-6.0 ns, and FWHM 5.5-10.5 ns.

Trigger logic: analogue sum of 4 pixels, discriminated and sent to the camera trigger where a neighbour

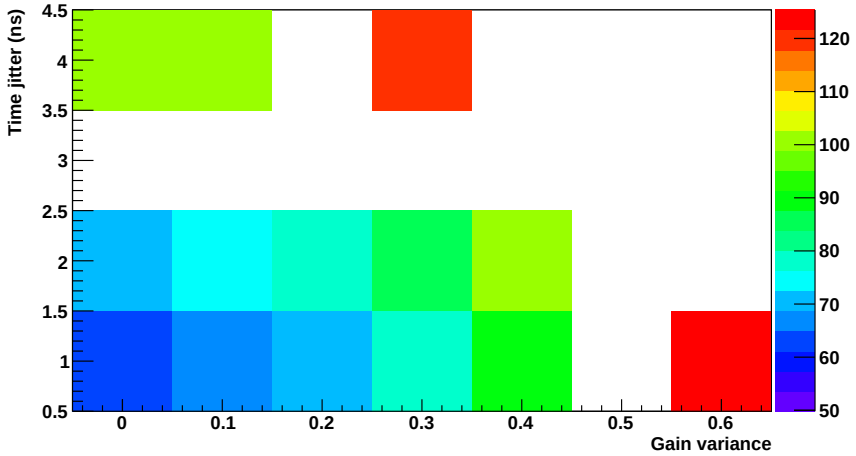

Figure 5.5: Minimum image amplitude (50% trigger efficiency) versus gain variation and time jitter for the merge- 4/multiplicity-2 configuration for a coincidence window of 10ns.

requirement and a minimum multiplicity of 2 is applied within a coincidence window.

Camera Trigger Coincidence Window: $6 - 10$ ns.

(a simple OR of all discriminated 16-pixel sums is attractive particularly with clipping, but has inferior performance at larger impact distances at least when no signal clipping is applied.)

Time jitter on digital inputs to camera trigger: < 2 ns for a 10 ns coincidence window, < 1 ns for a 6 ns window.

Electronic Noise: < 0.5 mV rms per pixel on the trigger path.

Pixel to pixel gain variations: $< 25\%$ rms (4-pixel sum), $< 35\%$ (16-pixel sum)

Gaps: < 1 pixel=6 mm gaps between MAPMs (including glass thickness).

This exercise is currently being repeated for CHEC-S, using SiPMs. Some idealised, preliminary, results are included here. Figure 5.6 shows the assumed SiPM pulse height spectrum for several levels of optical cross talk (OCT) between micro-cells. Figure 5.7(left) then shows the trigger rate as a function of threshold, and Figure 5.7(right) shows the resulting trigger efficiency as a function of minimum image amplitude. These idealised cases do not include any jitter or electronic noise and are performed at modest NSB. Once more detailed simulations have been completed, the tolerable level of OCT can be assessed. The simulations were performed assuming signal shaping to the idealised shape indicated by the MAPM trigger simulations and a trigger gate of 6 ns. A dead time per SiPM micro-cell of 150 ns was assumed. The assumed trigger is based on 2-neighbouring patches of 4-summed 6 mm SiPM pixels (i.e. the baseline CHEC-M trigger scenario).

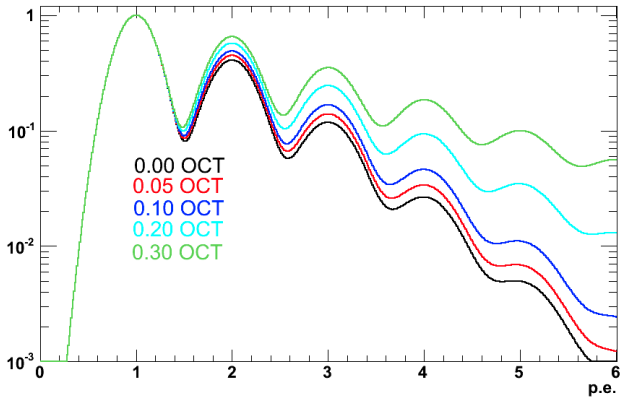

Figure 5.6: The SiPM pulse-height spectrum for varying levels of OCT.

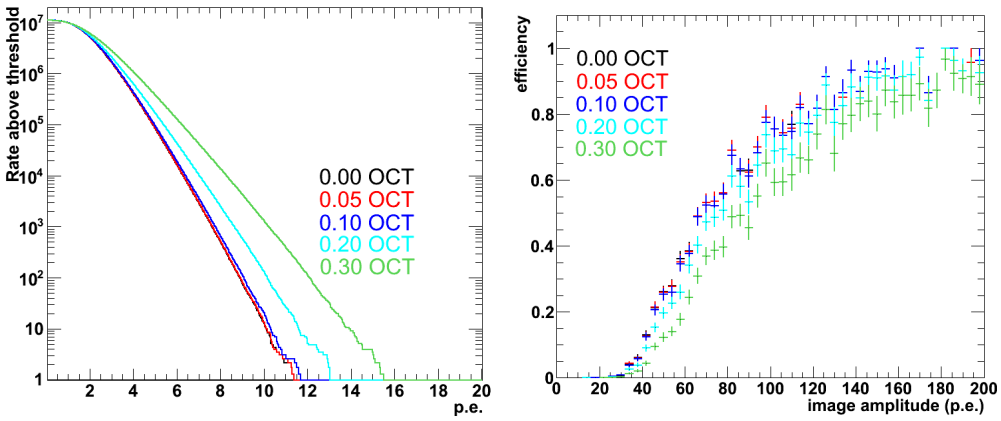

Figure 5.7: The camera trigger rate (*left*) and trigger efficiency for gammas (*right*) based on 2 neighbouring patches of 4-summed SiPM pixels for varying levels of OCT.

Different realisations of the SST-2M camera electronics, to explore the available parameter space (such as bandwidth and different trigger schemes) have been implemented and will be launched as part of the CTA *Production-2* simulation. Together with the trigger and readout study, this will allow the finalisation of the specifications for the CHEC prototype.

5.3 Photosensors

5.3.1 MAPMs

The CHEC-M detector plane contains 32 H10966 MAPMs, rotated and tiled to approximate the 1.0 m radius of curvature optical focal plane. The maximum deviation from the ideal pixel position is then 0.5 mm at the corner of the MAPM, within the required tolerance.

The Hamamatsu H10666 each contain 64 pixels of size $\approx 6 \times 6$ mm^2. This corresponds to an average angular size of 0.19° when installed on the ASTRI structure, and 0.17° when installed on the GATE structure. In both cases, the requirement of $< 0.25°$ (B-SST-1150) is clearly met. The PSF (θ_{80}) for the SST-2M design is smaller than 6 mm over the full CHEC field of view in both ASTRI and GATE. A gap of ∼2 mm between MAPMs is required to accommodate the depth of ∼25 mm. When combined with the dead space at the edges of each MAPM, a total maximum dead space of ∼5 mm (corresponding to the diagonal gaps) is achieved.

The field of view of CHEC-M is $\sim 9°$ on ASTRI and $\sim 9°$ on GATE, thereby meeting requirement of 8° (B-SST-1130), and the goal of 9° (B-SST-1140).

Detailed qualification of H10966 MAPMs has taken place as part of CHEC in Leicester and for the SCT in Santa Cruz. There are several aspects of MAPM performance that were of initial concern:

1. **Dynamic Range -** Figure 5.8(left) shows the dynamic range and of a single H10996 channel. By 1000 pe the response is 20% non-linear. The dynamic range needed to meet the charge-resolution requirements (B-SST-1010, B-SST-1020) is not yet clear. As CHEC will provide full waveform data, useful information can still be extracted from saturated channels via pulse fitting (to within 5% accuracy at 1000 pe assuming complete saturation at 650 pe for example).

2. **Angular Response -** The SST-2M optics result in off-axis angles of up to 70° onto the focal plane. Figure 5.8(left) shows the dynamic range and angular response of a single MAPM channel to illumination by a beam much wider than a pixel. At 70° ∼30% of the light is lost.

3. **Uniformity -** Time-stable gain variation across the MAPM that can not be removed (as each MAPM receives a single HV supply for 64 channels) affects the dynamic range of a channel, as the digitisation range of the TARGET ASIC is fixed. Gain variations of up to a factor of 2 across the 64-channels have been noted. These will be included in upcoming simulations to properly understand the consequences .The affect on charge resolution is not expected to be significant, as the gain of each channel need only be measured to within ∼5% (as indicated in [28]). Such variations also affect the trigger threshold of the camera. One solution may be to include a variable input amplifier stage in the TARGET 7 ASIC.

4. **Ageing -** The gain of the MAPM pixels is expected to decline over time in relation to the integrated anode current in the device. Tests at UCSC have shown that for the expected operating voltage and NSB level, this effect is at an acceptable $< 20\%$ level over a decade of operation.

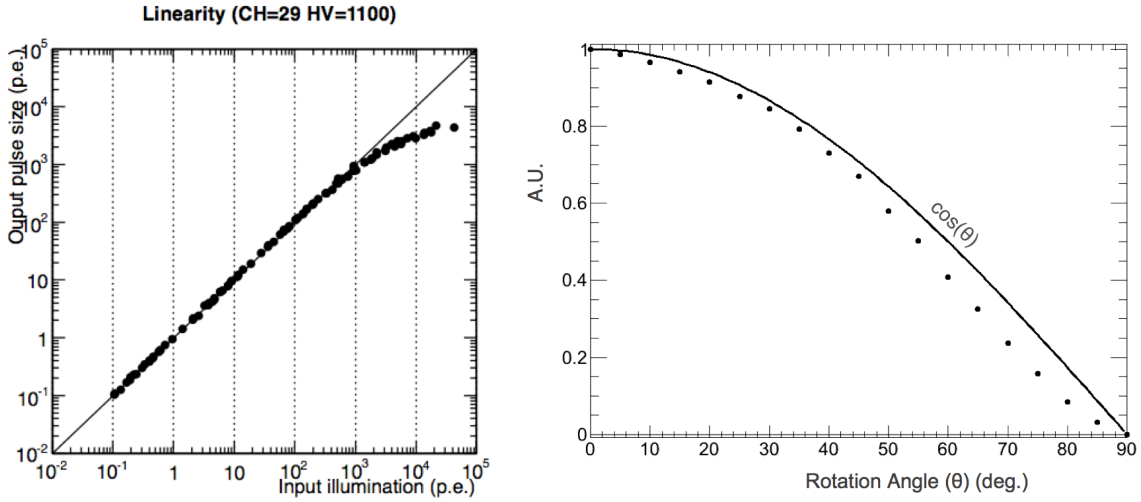

Figure 5.8: Results from MAPM testing for a single channel of the 64 channel device: dynamic range (left) and angular response (right).

In addition, the pulse shape was measured to provide input for the preamplifier design. It is assumed that the MAPMs will be operated at a gain of 8×10^4. The average efficiency of the focal plane detectors weighted by the reference Cherenkov spectrum in the wavelength range 300-550 nm, including dead space is required to be at least 13% (B-SST-1170). Dead space corresponds to ∼20% of the total area of the focal plane, and initial results indicate an average detection efficiency for the MAPM of ∼23.5, therefore the average detection efficiency across the focal plane is ∼19, and B-SST-1170 is met. Off-axis, the MAPM is up to 30% less efficient, but the incidence-angle averaged photon detection efficiency is expected to be comfortably above the required 13% over the whole required camera FoV.

The exact model of MAPM chosen for CHEC-M is the H10966B with Super-Bialkali photocathode, and without UV-transmitting glass. All 32 devices have been ordered and will be delivered by May 2013. Qualification of these devices for CHEC will proceed following delivery.

5.3.2 SiPMs

The choice of SiPMs for CHEC-S will be made in Autumn 2013. Initial tests have been performed on the Hamamatsu S11828-3344M. Samples from Excellitas and SensL have also been obtained. Further tests scheduled for this spring.

Testing has proceeded under the operational concept that by using the digitised waveforms taken during normal operation, a pulse height spectrum for each pixel can be constructed on timescales short compared to factors affecting the gain. The bias voltage can then be corrected to stabilise the gain. Testing has therefore focused on determining the operating temperature over which the bias voltage can be changed to stabilise the gain and parameters such at the dark count rate (DCR) and the OCT are at an acceptable level. As shown in Figure 5.9 and 5.10 , initial tests indicate that the DCR is below the expected NSB rate (which will be ∼30 MHz for SiPMs on the SST-2M). However, at some bias voltages, OCT reaches a level that could be unacceptable (as discussed in Section 5.2). Further simulations will reveal the consequences of large amounts of OCT, and development in SiPM technology are expected to significantly reduce the OCT on an appropriate timescale for CHEC-S.

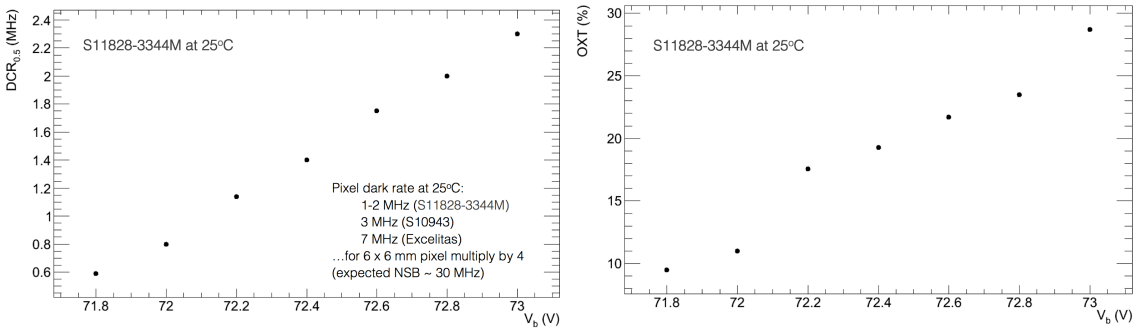

Figure 5.9: Initial test results for the S11828-3344M showing DCR (left) and OCT (right) at room temperature.

5.4 Signal Amplification and Shaping

The MAPMs must be operated at relatively low gain due to the high background rate associated with exposure to the night sky. Preamplifiers are required in close proximity to the photosensors to minimise electronic noise and to shape the output signals to match the optimal shape specified in Section 5.2).

The requirements for the CHEC-M preamplifiers have been completed followed by an initial design stage. This resulted in three design concepts that have now been qualified in lab tests with the MAPM. A design from the three candidates was chosen and further developed. The resulting design meets the requirements (with ≈8 ns FWHM, ≈3.5 ns rise time, RMS noise ≈0.4 mV) and the pulse shape can be seen in Figure 5.11 for various input illuminations. Saturation occurs above 1.3 V (the maximum input voltage of TARGET, see Section 5.5).

The preamplifier is currently being incorporated into a 64-channel preamplifier module consisting of 4 x 16 channel boards. Once this is complete the preamplifier module will be assembled with the MAPM and tested with the first TARGET Module in April 2013. A final design iteration is scheduled to follow testing of the 64-channel preamplifier module. The preamplifier module is shown in Figure 5.12 attached to the MAPM and TARGET Module (see Section 5.5). The preamplifier module consists of the preamplifier boards themselves,

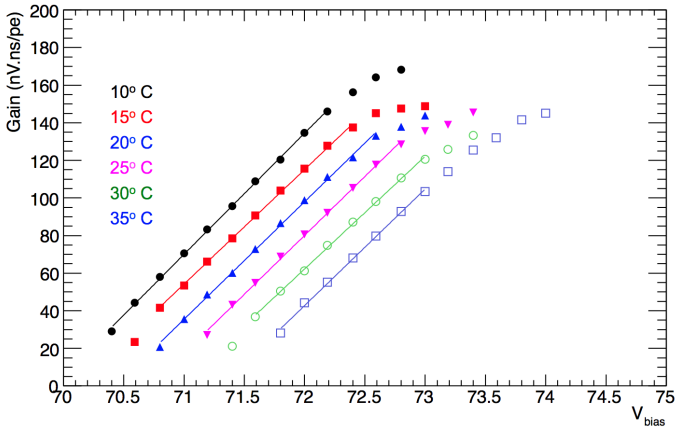

Figure 5.10: Initial test results for the S11828-3344M showing the temperature dependence of the gain with bias voltage. Clearly the bias voltage could be adjusted with changing temperature to stabilise the gain.

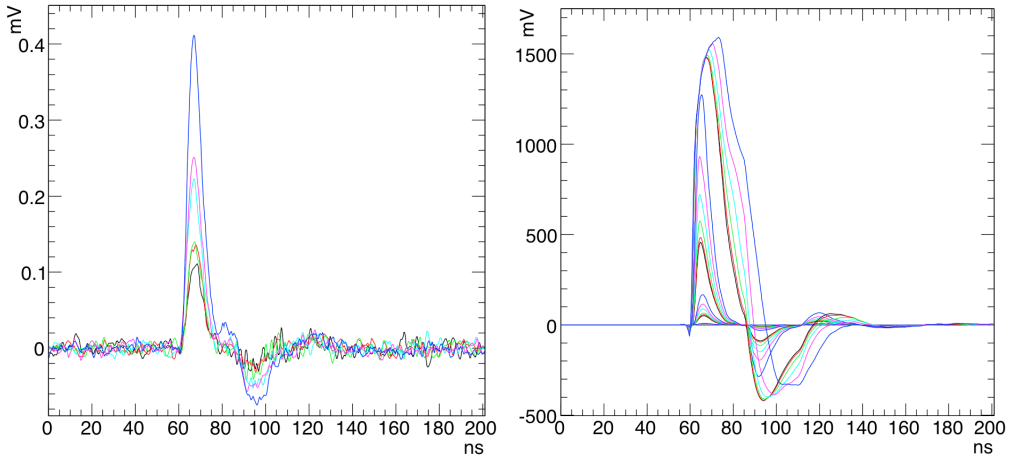

Figure 5.11: Resulting MAPM pulse shapes at the output of the first version of the CHEC-M preamplifier for low (left) and high (right) average illumination levels. The low illumination level reaches a maximum of ∼0.2 pe, and the high illumination level reaches a maximum of >2000 pe, beginning to saturate at around 50% of that level. These pulses are averaged over 1000 waveforms. The RMS noise is ≈0.4 mV.

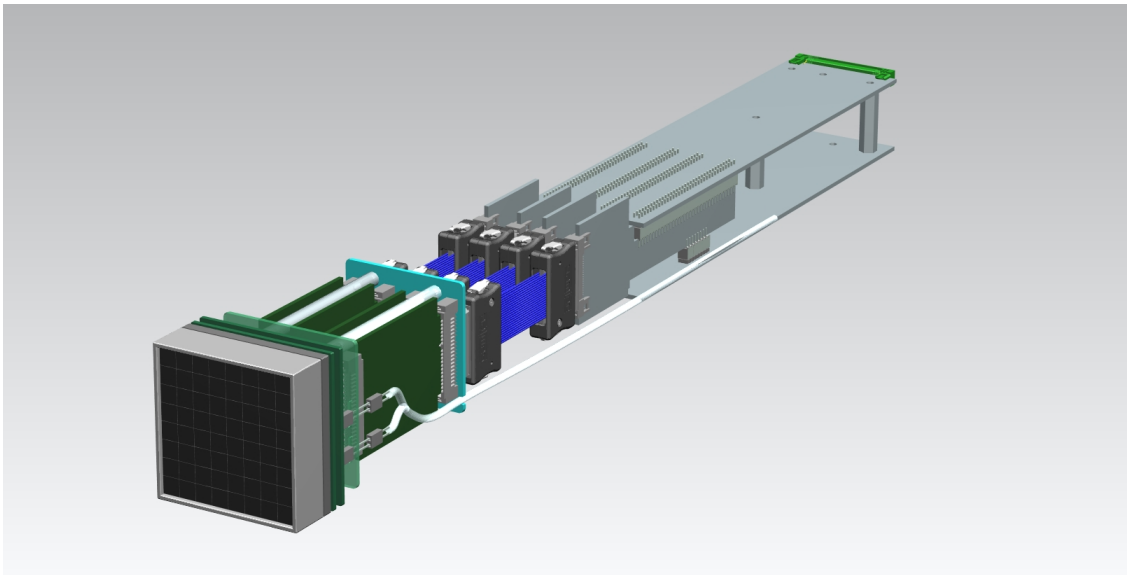

Figure 5.12: Model of the TARGET module attached to a preamplifier module and MAPM

connected to PCBs for mechanical attachment of the MAPM (see Section 5.9), and flexible, Samtec coaxial ribbon-cables. These cables remove the curvature of the focal plane, allowing the TARGET Modules to be located in a parallel manner.

CHEC-S will require a different preamplifier circuit to shape and amplify SiPM signals to the required range. This development will begin in full once the SiPM for CHEC-S has been selected, but initial work implies that a zero-pole device could be suitable.

5.5 Digitisation

Digitisation of the amplified and shaped analogue signals will be performed by the TARGET Modules developed at SLAC. Each TARGET Module will be connected to a preamplifier module via the 4 short Samtec coaxial ribbon-cables. Figure 5.12 shows a 3D CAD representation of the TARGET module attached to a preamplifier module and MAPM.

Each TARGET Module will supply a single MAPM with high voltage, digitise the signals from all 64 channels, and provide these digitised signals together with trigger information to the Backplane. These modules are based on the TARGET ASIC.

It is envisaged that the TARGET ASIC used in CHEC will operate over a range of ∼0-1.3 V with 12 bit resolution, and an RMS noise of ∼0.5 mV. A single pe at the TARGET input will have an amplitude of ∼2 mV and correspond to ∼6.3 digital counts. The signal will therefore saturate at ∼650 pe. The shaped

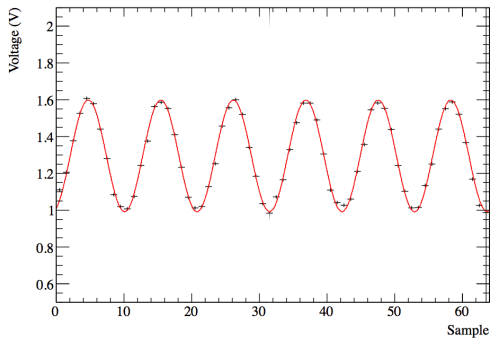

Figure 5.13: Sine wave input as sampled by TARGET 5 at 1 Gsps.

signal will have a FWHM of ∼6 ns and be digitised at 800 MSa/s over ∼100 ns. The goal readout window for this camera of 80 ns is therefore reached (B-SST-1220).

The dead time incurred by the TARGET ASIC for conversion and readout over the ∼80 samples is ∼ 20 μs. The expected camera trigger rate is ∼200 Hz, and therefore this dead time is negligible.

Combining the various sources of fluctuations in quadrature indicates that with this configuration, the required charge resolution is met across the full range of pe. Above saturation the pulse area can be recovered by fitting the digitised waveform, to an accuracy of ∼5% at 1000 pe.

Each TARGET Module contains four TARGET ASICs, which are read out to an on-board Xilinx Spartan 6 FPGA. The FPGA controls the ASIC and prepares the data for transmission to the Backplane (see Section 5.7). The TARGET ASIC is currently in design iteration 5. Test results from TARGET 4 and 5 show a dramatic improvement from TARGET 3. Figure 5.13 shows the digitisation of a sine wave using TARGET 5, which appears to meet the majority of requirements for CHEC. See [29, 30] for more details.

There is expected to be one further iteration of the ASIC for ./CHEC/SCT (TARGET 7). Various additional features for inclusion in TARGET 7 are currently under discussion. An interface control document (ICD) between CHEC and the TARGET Module has been agreed and signed. The first two TARGET modules (using TARGET 5) are due to be delivered to Leicester in April of this year 2013 for lab testing. Following this testing and feedback to SLAC a second design iteration of the TARGET Module is envisaged late next year using TARGET 7. Adaptations to the TARGET Modules will be needed for CHEC-S, however some of the required functionality has already been included in the current module. The CHEC-S TARGET Modules are also expected to be based around TARGET 7 and the goal is to have modules identical to those used for the SCT.

5.6 Trigger

The TARGET ASIC provides the first level of triggering for the camera. The trigger consists of the analogue sum of 4 neighbouring pixels, which is then discriminated. This has been shown to be a suitable trigger

scheme in Section 5.2. Each TARGET ASIC outputs 4 digital trigger signals, which are routed through the TARGET Module to the Backplane, resulting in 16 differential LVDS trigger signals per module.

As described in Section 5.2, a trigger threshold of ∼9 pe (18 mV) results in a minimum image amplitude well below the required 100 pe with 50% trigger efficiency. Tests are underway to see if this is achievable with TARGET 5, or if modifications are necessary for TARGET 7.

The 16 trigger signals from each of the 32 TARGET Modules are routed on the Backplane to a Xilinx Virtex FPGA. The FPGA forms a camera trigger by requiring any 2 neighbouring trigger patches be present within a programable coincidence time. The trigger signal formed in the Backplane FPGA is then routed back to the TARGET Modules to initiate a full camera readout. External inputs to the FPGA from the DACQ board will allow the camera to be artificially triggered.

Due to the relatively low event rate per telescope (∼200 Hz), no inter-telescope hardware array trigger is envisaged. When a telescope triggers, all data is read out to the central location over ethernet. Triggers are compared at the central location for several telescopes to decide whether to write the data to disk. To make this possible an accurate array-time distribution / event tagging scheme is required, and we envisage that such a system will be provided by ACTL for the final SST. Within the CHEC prototype we plan to include an internal clock distribution and event-time-stamping system.

In the current Backplane architecture, clocking and wall clock time (i.e. the absolute time from the last array event marker) synchronisation is accomplished via a High Speed Deterministic Time Data Link (HSDTDL) utilising a SERDES IC. This IC will use a 62.5 MHz reference clock to derive its bit rate and word rate clocks. The 62.5 MHz clock must be provided externally to the camera. For example via a centrally located GPS receiver reference clock.

Wall clock time marker information will be sent to the camera over the HSDTDL. The Backplane will utilize a Programmable Quad Clock Generator to generate a 125 MHz clock from the 62.5 MHz reference signal for distribution to the DACQ board, trigger FPGA and TARGET Modules. Each of 4 outputs is phase programmable in 20 ps increments and will be routed to a 1:16 fanout buffer, specified to introduce no more than 25 ps delay between the outputs. Assuming matched copper trace pair lengths and capacitance load, the 125 MHz clocks at the TARGET Modules will be at least 400 ps edge accurate, even without tuning the delays using the 20ps resolution. This leads us to believe that the internal camera clock distribution scheme will not be the limiting factor in meeting the goal rms inter-telescope time accuracy for events of 2 ns (A-PERF-0610).

The clock/array interface will be implemented on a daughter board and connected directly to the Backplane. This provides flexibility for changing the interface at relatively low cost to match the final solution (and/or try other options). For example, we are also considering the inclusion of a White Rabbit interface board.

Figure 5.14 shows a recent version of the Backplane and DACQ board. The design is being led by Wash U., and is rapidly evolving. An ICD between CHEC and Wash U. will be agreed for both the Backplane and the DACQ board prior to manufacture. These boards will also be utilised for the SCT camera (with some small alterations / changes to physical layout).

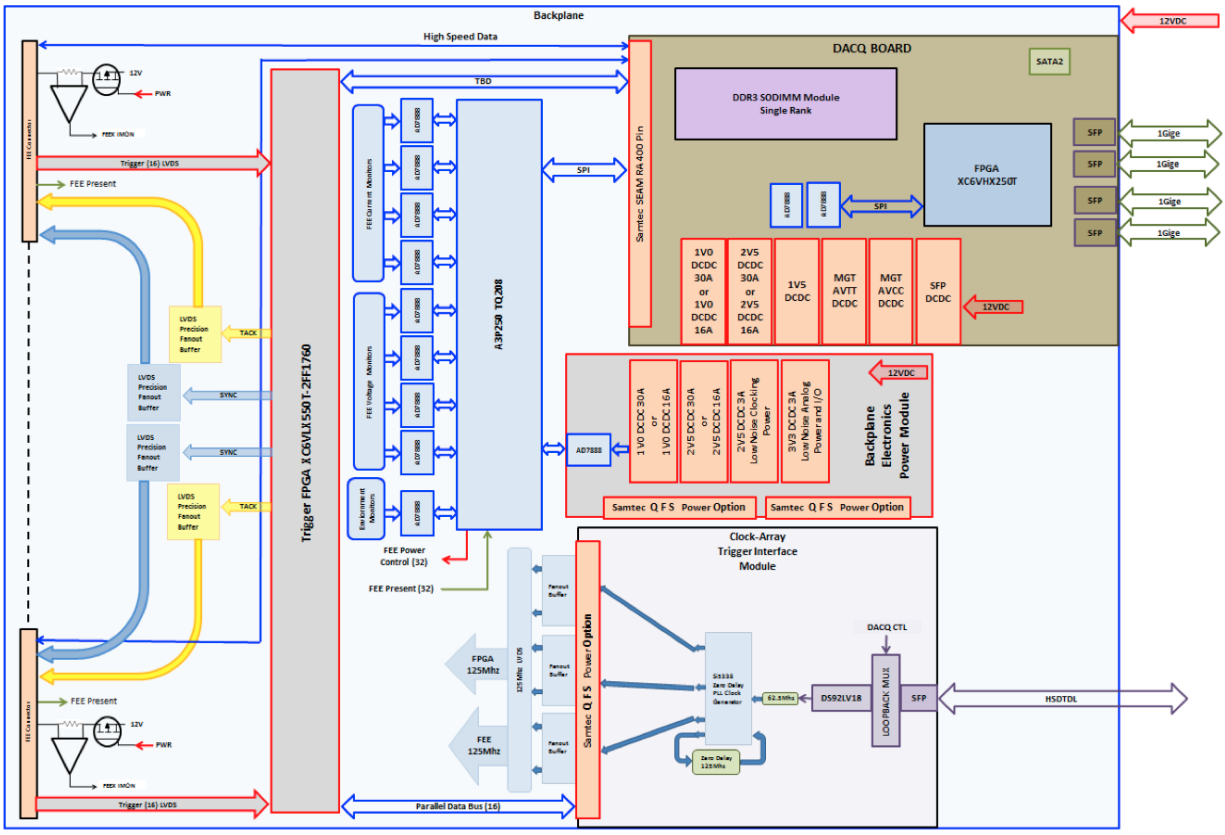

Figure 5.14: A recent schematic of the current Backplane and DACQ boards.

5.7 DACQ and Control

The Spartan 6 FPGA on each TARGET Module serialises event data for output to the Backplane via a high speed data link (HSDL) that is comprised of 2 differential CML pairs (RX and TX) on GTP I/Os running at 1.25 Gbps (2.5 Gbps TBD). Serialisation and readout of 64 channels in this way minimises the connections to modules, but could incur an additional $\sim 10-20$ μs dead time. When combined with the conversion time this translates to a dead time well below the required 5% (B-SST-1260) at the required event rate of 300 Hz (B-SST-1280), and even at the goal rate of 660 Hz (B-SST-1290). Both event data and control commands will be sent via this HSDL. Command traffic is likely to be simultaneous to all TARGET Modules.

The 32 RX and TX HSDLs from the TARGET Modules are routed to the DACQ board via the Backplane. The DACQ board is designed around an Xilinx XC6VHX250T-2FFG1154 FPGA. The 1154 pin package has 48 GTX 6.6 Gb/s transceivers, and 320 I/O pins. As currently captured, there are 4 SFP connectors for Gigabit Ethernet, a SATA2 connection, a 204 pin DDR3 SODIMM socket for up to 1 Gbit RAM,

a TARGET Module compatible connector for serial protocol development testing, an expansion connector (TBD) for future growth, 2×12 bit ADCs for DACQ power monitoring, clock fanout buffers, local oscillators, and DC-DC converters for the DACQ FPGA and onboard resources. Of the 48 GTX transceivers, 32 are dedicated to the TARGET Modules, one to the SATA2 connection, 4 for SFP transceivers, one for backplane trigger FPGA communications, one for the TARGET Module development connector and 8 are routed to the expansion connector. The final form of the DACQ board will likely be much more minimal than is currently envisaged, however this solution provides flexibility and assurance for the CHEC prototype development.

In the current model, the interface from the DACQ board to the 'world' would be one of the four available SFP Gigabit Ethernet connectors, providing sufficient resource for all data and control signals.

The proposed operation sequence for data acquisition is shown in Figure 5.15, and proceeds as:

- The DACQ commands TARGET Modules to arm (prepare to start acquisition).
- The DACQ issues *START_ACQ* signal to the Backplane FPGA.
- The Backplane synchronises *START_ACQ* to the 125 MHz clock.
- The Backplane FPGA tells all 32 TARGET Modules and DACQ to start acquisition simultaneously via *SYNC* discrete signal. This also acts as a marker (*AcquisitionZero*) for the upcoming event.
- When a camera trigger occurs, *TACK* (asynchronous to the 125 MHz clock) is sent immediately to all 32 TARGET Modules and the DACQ.
- *TACK* tells the TARGET Modules to pause acquisition. The TARGET Module FPGA controls the ROW information of the TARGET ASIC so it knows which rows of samples correspond to the event trigger, and initiates the analogue to digital conversion and readout of these. The TARGET Modules will also send the event number associated with the event sample data. All pixels of the camera are read out for each event in accordance with requirement B-SST-1250.
- TBD time later, the Backplane trigger FPGA issues a *SYNC* pulse (synchronised to the 125 MHz clock) to the TARGET Modules to resume acquisition.
- The DACQ receives the same *SYNC* signal, and calculates the time difference between the *AcquisitionZero* signal and the block of sample data from the TARGET Modules.
- At the end of the observation period the DACQ commands the TARGET Modules to stop acquisition.

This system will therefore be able to continuously monitor the dead time of the camera as required (B-SST-1270).

5.8 Calibration

CHEC includes an internal calibration system to flat-field the camera across a large full dynamic range of illuminations. A light pulse width of 3-4 ns (FWHM) at short (blue) wavelengths from 0.1 pe, for absolute

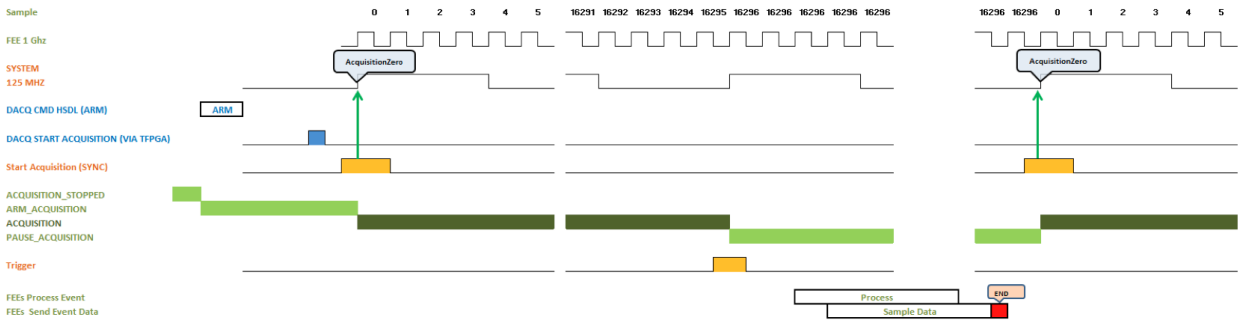

Figure 5.15: The DACQ process.

single-pe calibration measurements, up to 1000 pe, to characterise the camera up to and at saturation is required. To achieve this CHEC will be equipped with flasher units containing multiple LEDs placed in the corners of the focal plane to uniformly illuminate the sensors via reflection from the secondary mirror as illustrated in Figure 5.16 (left). Each unit will contain multiple LEDs.

The speed at which an LED can output light is driven by internal capacitance and transit time effects in the depletion layer. Commercial pressures in the LED industry mean that developments for blue LEDs are increasingly concentrated toward steady illumination sources rather than fast pulses. This makes it challenging to provide light pulses that are both bright and fast and so sophisticated electronics design is needed to both turn on and turn off the LED very quickly. The CHEC calibration system has the additional constraints that it will need to be mounted on a potentially large number of telescopes, meaning the system needs to be inexpensive, reliable and easily operated.

Tests of candidate LED driver circuit designs along with a number of candidate LEDs have been performed with an MAPM to determine the light pulse width suitability and a successful combination, along with a back-up solution if needed, has been selected. Several potential fast circuit designs were considered as possible solutions. The selected design (which we refer to as the simple gate, SG) is the most simple and inexpensive, consisting of a fast gated TTL drive pulse, but has the requirement of finding a suitable LED with a self-capacitance that allows it to reach the necessary speeds. Tests of 5 mm LEDs showed them to be inadequate for our purposes (with light pulse FWHM of $\sim$10 ns) (Figure 5.16 (right), red), but 3 mm Bivar UV3TZ-XXX-XX series LEDs had a suitable FWHM of $\approx$4.5 ns (Figure 5.16 (right) blue). A back-up design (known as the bipolar technique, BP) makes use of commercial video line amplifiers to manipulate both the anode and cathode signal to boost both the speed and illumination level, this was able to achieve light pulse FWHM of $\approx$3.5 ns even with 5 mm LEDs (Figure 5.16 (right), green).

Given the SG circuit can satisfy the design requirements it has been selected to be used for CHEC due to the low cost, simplicity and small circuit footprint. There is obviously a risk that such an LED may be discontinued during the lifetime of CTA, so further tests of available LEDs will be ongoing, the back-up solution of the BP design and the final system will have sufficient spare capacity to be able to switch systems with only minimal modifications needed.

The flasher system has been integrated into the camera mechanical design and an initial attempt at board size has been made, see Figure 5.17.

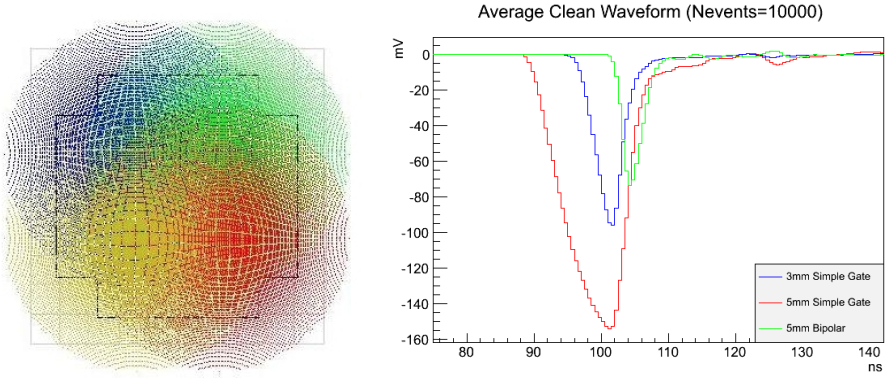

Figure 5.16: *Left:* The optical scheme for an indirect off-axis illumination calibration light source showing the footprint of the illumination in the detector plane after reflection from the secondary mirror. *Right:* Pulse shapes for various LEDs and driver circuits as recorded by an MAPM.

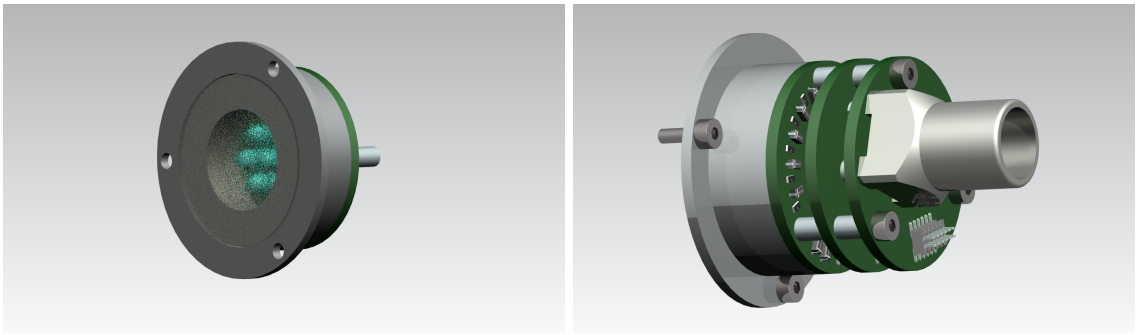

Figure 5.17: An initial concept for the LED flasher unit, including a 1 inch diffuser and mount, and several PCBs with preliminary ideas for signal and power connection.

5.9 Mechanical structure and cooling

The mechanics for CHEC consist of: a focal-plane positioning plate, internal 'rack' mechanics, an adjustable interface plate for mounting to the telescope, and the external shell. Figures 5.18-5.20 shows the mechanics including components such as MAPMs, PCBs and TARGET Modules.

The focal-plane positioning plate located at the front of the camera is responsible for the accurate positioning of the sensors. The TARGET Modules with preamplifier modules attached, are slotted through this plate

and into the rack. The front-most preamplifier module PCB does not go through the focal-plane positioning plate, but rather sits in a recess flush to the surface where it is secured using screws. The MAPMs are then attached. The retention of the MAPMs will be provided by the 4 × 34 pin connectors reinforced with removable glue. A removable sealant will be used between each MAPM once they are attached to increase the retention and provide a seal against the elements.

The interface plate at the rear of the camera will provide manual adjustability in tip/tilt and de-center to postion the camera on the ASTRI structure to within the required tolerance. An error-budget has been initialised, and will be completed once the accuracy of the ASTRI central tube structure is known. An ICD has been drafted and will be agreed upon before the interface plate design is finalised.

The camera shell may be constructed from carbon fibre using existing facilities at Liverpool University. The exact shape of the shell is not yet finalised, the current concept is depicted in Figures 5.18 and 5.19.

For CHEC-S an 'MAPM-like' module will be constructed, to minimise changes to the mechanics. The pitch of the camera can be easily changed to accommodate different physical sized sensor blocks of 64 pixels due to the flexible ribbon cables used to remove the radius of curvature between the preamplifier and TARGET Modules.

Sizing calculations have been carried out for the thermal control system. Driving requirements are that it should be able to extract heat dissipated in the CHEC electronics to a suitable sink whilst maintaining the electronics (and all other hardware) below a suitable upper limit. Total dissipation within the CHEC camera is expected to be 400 W (including thermal control system fans). The thermal control system is designed to meet requirements at the upper operating temperature of the camera which is assumed to be 37°C. The resulting thermal control system consists of a 4 fans coupled to a large water cooled heat sink. The fans, together with a system of baffles provide a recirculating airflow within the sealed camera enclosure. The maximum air temperature within the enclosure is predicted to be 45°C, with operating board temperatures predicted to be in the range 70-80°C. Sizing approach and temperature predictions will be validated using a 4 module 'demonstrator' model incorporating a scaled down thermal control system.

5.10 Reliability, Availability, Maintainability and Safety

The RAMS process for the CHEC prototype is ongoing, here we summarise some of the primary considerations and implications for the SST camera design.

The maintenance and availability requirements for the SST (A-RAMS-0040, A-RAMS-0110) are demanding. Clearly prototyping is required to demonstrate that these requirements can be attained, but there are several reasons why we believe that the reliability and maintainability of a CHEC-like camera will be superior to that of current IACT cameras:

- **Removable Camera** as maintenance concept. The estimate weight of a CHEC camera is 40 kg and the GATE and ASTRI telescopes designs are being developed to ensure the replacement of a camera is straight-forward. The use of spare cameras and the ability to inspect all elements of a camera for maintenance in an electronics workshop environment will allow repair of multiple issues simultaneously (and additional preventative maintenance) once a threshold in the number of inoperable pixels is

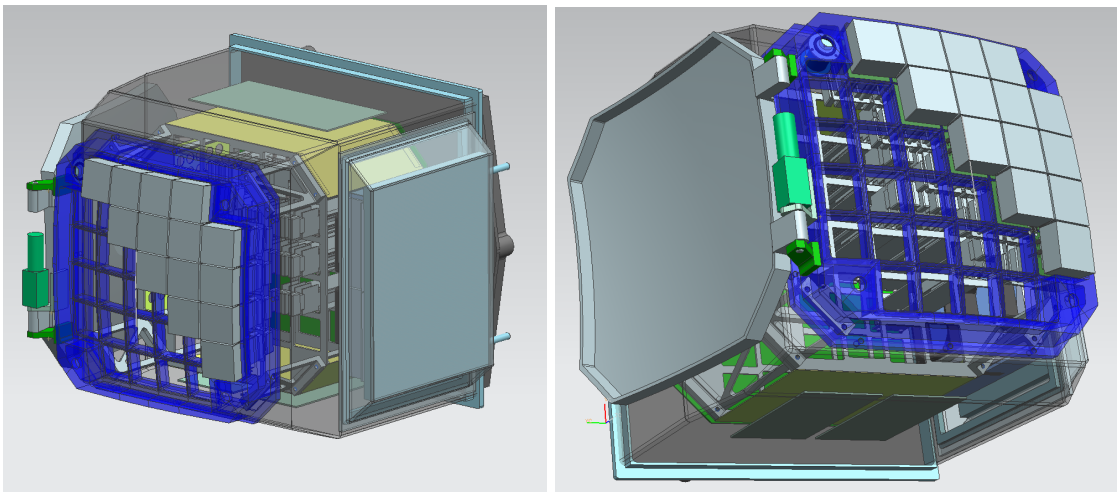

Figure 5.18: The current version of the CHEC-M mechanical concept. Half of the MAPMs (grey) are shown positioned in the focal-plane plate (blue). The heat-exchange unit can be seen to the right of the picture. Note that the shutter and motor shown are simple place holders.

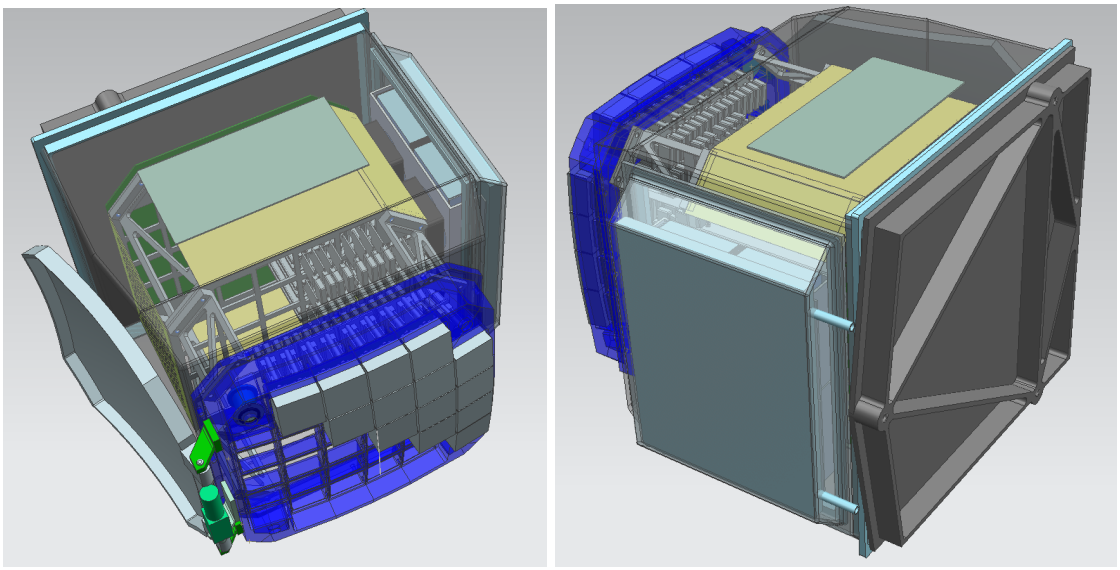

Figure 5.19: The current version of the CHEC-M mechanical concept.

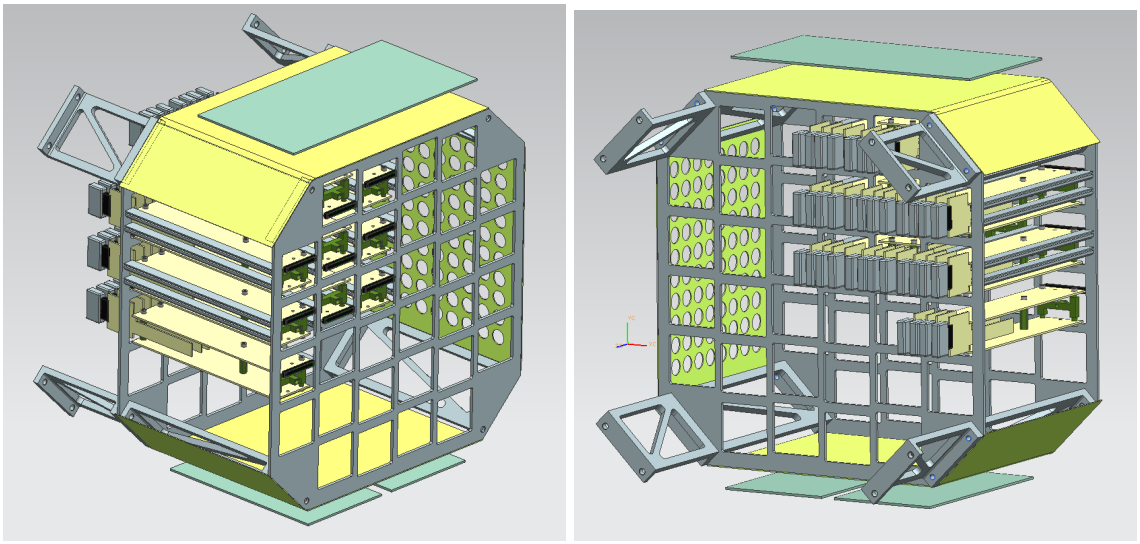

Figure 5.20: The current version of the CHEC-M mechanical illustrating the internal rack mechanics. Several TARGET Modules can be seen placed in the rack. The baffles fro air flow are shown in yellow. A place holder for the DACQ PCB is shown in green at the top of the picture. This would connect to the Backplane located at the rear of the rack (not shown) via a cable.

reached. Our design therefore sacrifices the ability to easily remove sections of the front-end electronics in-situ (the *drawer* approach) to reduce cost and complexity, in favour of higher reliability which is inherent to lower complexity systems.

- **Sealed system**. The cooling solution for CHEC does not involve circulation of air drawn from the external environment. The ingress of dust into the system is therefore prevented. The compact design of CHEC and the absence of fans drawing in air also make it much easier to prevent the entrance of water/moisture into the system.
- **Space instrumentation approach**. The engineers responsible for the overall CHEC mechanical structure, cooling system, preamplifier boards and all electro-mechanical interfaces, come from a space instrumentation background, where extremely high reliability and maintenance-free operation are essential, and are applying the same rigorous design principles to CHEC.
- **Extensive testing** at the prototyping stage. The test plan for CHEC is being designed to ensure that flaws in the design become apparent pre-mass-production. The accelerated ageing of electronics and vibration and environmental testing of the camera as a whole (including water-spray, salt-fog, hailstone impact tests, and thermal cycling) will identify weaknesses in the design.

High impact failure modes identified so far include: cooling failure - resulting in potential damage to electronics, mitigated by a monitoring/control loop and fail-safe power-down of the camera; accidental operation

of MAPMs at high light-levels (see below); water ingress (see above); solar damage (mitigated at the telescope/drive level); and freezing of the chilled water supply (backup power to water chiller/heater, additives to water supply).

5.10.1 Safety

The primary risk to human safety in the camera identified in the CTA RAMS requirements is High Voltage (A-RAMS-0350). CHEC-M will be designed such that access to the interior of the camera is possible only with special tools, preventing access to the system in the operating state by untrained personnel. The use of a photodiode to ensure HV is turned off when a given light-level is reached, is under consideration to ensure the safety of the instrument. In the CHEC-S solution HV is absent. The camera will close the lid and switch off HV if contact is lost with ACTL (following A-RAMS-0330).

Further risks to the safety of the instrument include the ingress of water and the failure of the cooling system as discussed above, and the installation/replacement of the camera. The ∼40 kg and height of the camera in the Safe position necessitate the definition of a well-defined procedure which minimises the impact of human error. This procedure must be defined together with the telescope groups and will take place over the next few months.

A full risk analysis clearly requires the development of a more detailed operational/maintenance concept, and this will occur over the next 6-9 months.

5.11 Current Plans for Prototype Testing

Planning for the testing of the camera module, consisting of the sensor, preamplifier and TARGET module has started. These tests will be performed in the laboratory using the calibration system described in Section 5.8 to provide fast light pulses with a time structure and intensity similar to those of the Cherenkov showers the camera will ultimately have to record. In order to determine the performance of the module in the presence of background, these flashes will be supplemented by low level constant illumination that gives pixel hit rates similar to those that will be caused by NSB when the camera is in operation. The frequency and intensity of the flashes provided by the calibration system will be varied, as will the background light level, allowing the response of the module to be determined and its limitations, e.g. in terms of the tolerable NSB rate, to be mapped out.

Facilities for the testing of the camera housing have already been identified at the Centre for Advanced Instrumentation in Durham, for example a climate chamber of the required size and apparatus for measuring the IP ratings for water and dust tightness. Tests designed to simulate the impact of hailstones have been devised.

Once a complete camera has been assembled, this will again be tested in the laboratory, using the above-mentioned calibration system. Planning of these tests is underway as are preparations for testing of the complete camera on a prototype telescope. These latter tests will take place on the ASTRI telescope installed at the INAF Catania Astrophysical Observatory in Sicily at a height of about 2000 m above sea

level on Mount Etna.

5.12 Concept for Maintenance and Operation

No in-situ maintenance is envisaged for CHEC. Once a camera reaches the point where it is deemed that maintenance is required, it is expected that the camera will be removed and dismantled under electronics workshop conditions. Due to the low cost of the camera, potentially a spare camera could instantly replace the one undergoing maintenance. This maintenance concept clearly implies a highly-reliable camera.

The operation of CHEC will be defined in conjunction with the telescope operation over the course of prototype development, however the currently envisaged statedgy involves the autonomous operation of the camera during normal observations. At the beginning of each evening, the camera will be illuminated with the lid open by the internal LED flashers at the single pe level whilst the telescope (primary mirror) pointing at the ground (park position). During normal observations calibration will be performed continuously for flat-field and dynamic range/linearity monitoring using the LED flashers. It is not expected that the CHEC lid will be closed whilst moving the telescope between targets.

To operate, CHEC requires power (12 V) and a chilled water supply. Both of these will be house in a 'cabinet' located on the telescope structure (as described in the ASTRI documentation). A single multi-core fibre will carry data, control and clock signals. The software process controlling the camera is envisaged to run in a (ACTL) rack in control building.

The philosophy of whether to allow the camera to be switched on during the day-time whilst in situ has not yet been determined. For CHEC-M this presents a significantly higher risk than for CHEC-S.

5.13 Preliminary Cost Estimate

Here we briefly summarise current estimates of the cost of a CHEC-like camera for the SST in the construction phase, assuming the construction of 70 identical cameras. More detailed cost information is in preparation.

5.14 Project Organisation

The Principle Investigator (Hinton) has overall responsibility for the project. CHEC coordinator (White) maintains the projects schedule, keeps track of milestones and ensures the smooth running of the project on a day-to-day basis. Oversight of the STFC-funded CHEC-M is performed by an oversight committee which meets every 6 months and assess progress and can recommend the release of contingency. The following work packages were defined in our proposal to STFC, and form the basis for our project organisation:

- **WP1: Optimisation via simulations.**
- **WP2: Data processing.**

Item	k£	Type
MAPMs	67	Estimate
Preamplifier Modules	8.2	Quote
TARGET Modules	32	Estimate
Backplane Board	6.5	Estimate
DACQ Board	2.2	Estimate
Calibration System	0.8	Estimate
Lid & Control System	1.5	Guess
Internal Cooling System	0.7	Guess
Internal Mechanics	2	Guess
Focal Plane Plate	0.85	Quote
External Mechanics	3	Guess
External Cooler	3	Estimate
External Power Supply	0.5	Estimate
Misc.	1	Guess
Total k£	**129**	
Total kEuro	**152**	

Figure 5.21: Preliminary cost estimates for CHEC based on 70 cameras.

- **WP3: Camera Design and Prototype Construction.**
- **WP4: Camera Test and Calibration System.**
- **WP5: Evaluation of Camera Prototype.**

Each technical work package has a coordinator (WP1: Hinton, WP2: Osborne, WP3: White, WP4: Daniel, WP5: Greenshaw), and the coordinators provide regular updates / progress reports. A detailed project schedule has been developed in Microsoft Project, Project milestones are defined and provide the primary mechanism for monitoring project progress internally and for reporting progress to the (STFC) Oversight Committee. Effective internal project communication is guaranteed via weekly telephone calls (bi-weekly with US partners) and regular face-to-face meetings. See Section 5.15 for Gantt chart and milestones table.

A draft agreement with ASTRI exists, with the goal of merging of the SST-2M camera projects for the next (post- current prototype) phase.

5.15 Summary

In summary, two CHEC prototypes will be constructed using almost identical electronics and different photosensors. Figure 5.22 shows the overall project schedule for CHEC-M. CHEC-M will be installed on the ASTRI prototype structure in late 2014. CHEC-S will be ready ∼6 months later. CHEC will include an internal LED flasher system for calibration of the camera. CHEC-M is on schedule 10 months in to a 36 month programme, and work on CHEC-S has begun. Crucially, the development of CHEC includes simulations of the trigger and readout performance to establish the specifications for hardware such that the CTA requirements are met.

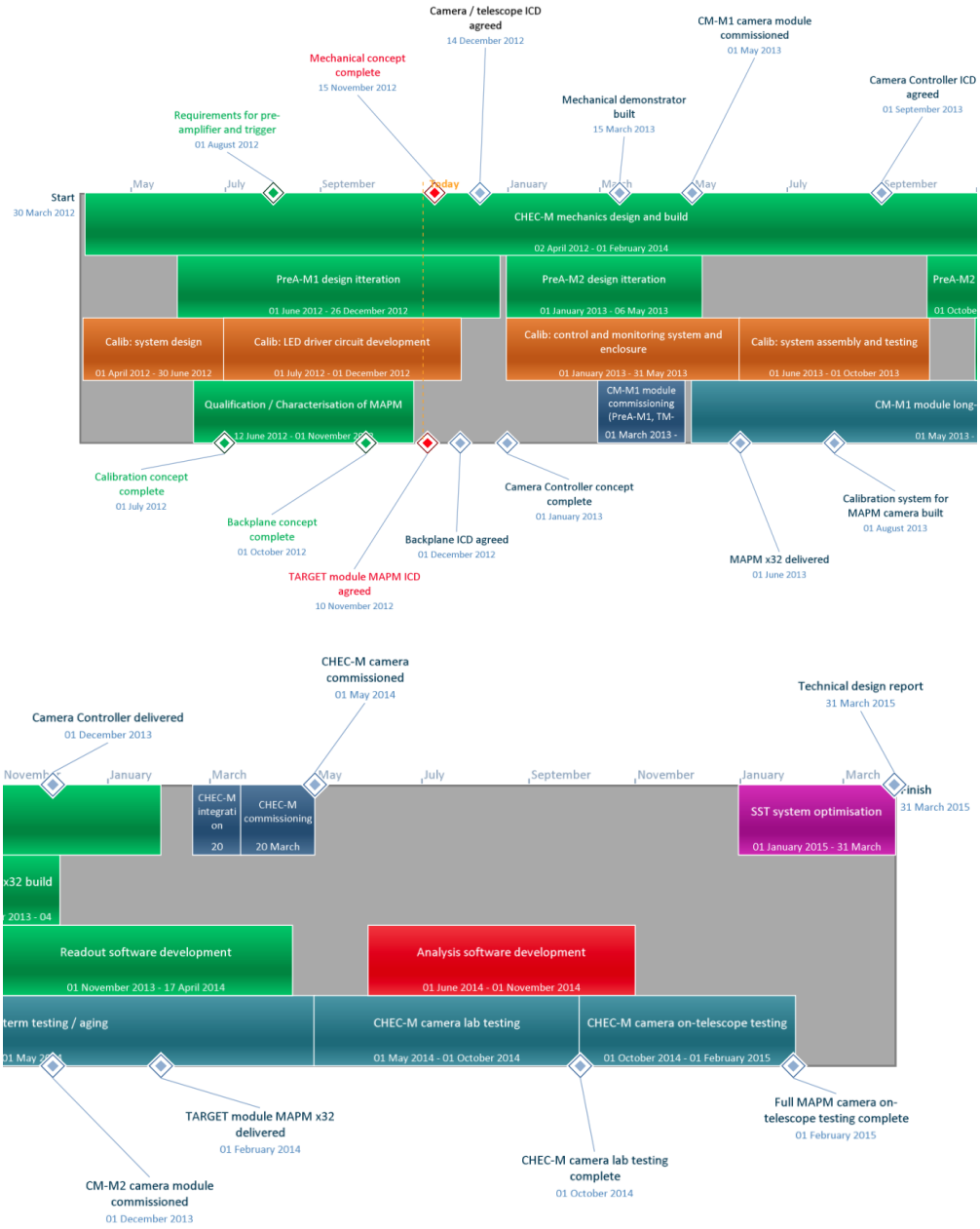

Figure 5.22: The current CHEC-M project schedule.

6 Overall Summary

CTA realised in 2010 that the cost of a Davies-Cotton (D-C) Small Size Telescope (SST) with a conventional photomultiplier- (PM-) based camera of a size similar to that needed for the Medium Size Telescope (MST), the solution proposed for the high energy section of the array until that point, would be dominated by that of the camera. Reducing the cost of the SSTs thus required that alternative camera, and hence telescope, designs were explored. It was recognised that there were two possible solutions to this: to use a dual mirror (2M) telescope with a compact camera using commercially available multi-pixel detectors, or to develop a silicon PM (SiPM) based camera and use it in a single mirror SST (1M-SST). This led to the investigation of 2M designs by ASTRI (telescope and SiPM-based camera) and SST-GATE (telescope). Work on a further camera design, able to use either multi-anode PMs (MAPMs) or SiPMs, was started in 2012 by the Compact High Energy Camera (CHEC) consortium. In the same year, work also started on the second option for a low-cost Small Size Telescope, the 1M-SST, led by groups in Switzerland and Poland.

Progress with all these projects has been rapid, as is reported in this document. For example, at the time of the last review, it was not clear whether the small radius of curvature aspherical mirrors needed for the 2M designs were feasible. Test mirrors and first prototypes have now demonstrated that this radius of curvature can be obtained either by modifying the glass slumping process to include a "hot" step, or by using very thin reinforced glass samples with cutouts. Prototypes constructed using the first of these techniques have demonstrated that the required asphericity can also be obtained, with the needed precision. Cameras for the 2M telescope are being designed and elements of these, the sensors and parts of the electronics chain, have already been tested. For example, both MAPMs and SiPMs have been studied and an improved understanding of their behaviour obtained; both look to be viable alternatives for the 2M-SST camera. The 1M-SST studies, for which funding was only recently obtained, have moved very rapidly. The Polish groups who were previously working on a 7 m diameter D-C telescope, designed to accept an "MST-like" camera, were able to use their expertise to quickly produce a design of a 4 m structure suitable for a SiPM-based camera. Development of the camera for this telescope has been similarly rapid. A large SiPM (or Gieger-mode avalanche photo-diode - GAPD) has already been developed and first promising tests performed. This device allows the group to use "open" Winston cones, rather than the closed cones necessary for the FACT camera (the first SiPM-based camera used on an Imaging Atmospheric Cherenkov Telescope, which is currently operating successfully in the Canary Islands), making the use of the mass-production techniques necessary to reduce costs much simpler. The 1M-SST group has made significant progress in this direction through the design and study of cones that can easily be assembled into modules that can form the focal plane.

The goal of the SST group is to test the first 2M prototypes in 2014. The results of these tests, and the studies made in developing the prototypes on which they are performed, will lead to the development of a single 2M-SST design for CTA. The same process will take place for the 2M-SST camera. The groups involved in these projects will then work together to develop a complete 2M-SST for CTA, the first versions of which will form the "mini-array" on the CTA site. This will be used to test both the telescopes and the algorithms and software necessary to operate the array for scientific observations. The 1M-SST development will be reviewed on the same timescale and, if it achieves the required performance, will offer CTA a further option for the high energy section of the array.

Constructing the number of SSTs required by CTA within the desired time-frame requires that they can

be assembled at a rate of about one telescope every two weeks. Studies of the effort levels and equipment needed to achieve this are now starting, and telescope designs reflect the need for easy assembly, particularly on site. Similarly, operating the telescopes reliably over the 30 year lifetime of CTA requires that possible failure modes are understood and either designed out, or appropriate maintenance scenarios developed, as is described for the telescope designs in this document.

Realising the SST on the timescale foreseen by CTA requires that the rate of progress achieved since the last SST review and described above be maintained. We welcome the assistance of the reviewers in helping us to achieve this goal.

References

[1] Aharonian et al. A&A, 437, 95 (2005)

[2] Aharonian et al, Nature, 440, 1018 (2006).

[3] Aharonian et al, ApJ, 664, 71 (2007)

[4] *Basic Definitions*,MAN-PO/120726

[5] *Science Requirements for CTA* , SCI-LINK/121120

[6] *Level-A Preliminary CTA System requirements*
TPC-SPECS/110331 ED 1/0 June 7, 2011

[7] *Level-B Preliminary CTA Sub-System requirements*
TPC-SPECS/110331b ED.1.0 0 June 7, 2011

[8] *SST Requirements*
MAN-PO/120808 v1.1 November 16, 2012

[9] *Performance Requirements*, MAN-PO/121004

[10] *SST-DC Mirror requirements*
L. Wisniewski, L. Platos, M. Karyzewski, K. Seweryn, available on request.

[11] *Mirror Draft Specifications* M. Doro, A. Forester, ref.: xST-OPT, version: 1.0; Jan. 18, 2012.

[12] *FlashCam: a camera concept and design for CTA telescopes*
xST-CAM/120403b , v2.4 April 2012

[13] *Stereo Imaging of VHE Gamma-Ray Sources* F.A. Aharonian, A.K. Konopelko, arXiv:astro-ph/9712044

[14] K. Bernlohr, Astropart.Phys. 30 (2008) 149.

[15] W. T. Welford, R. Winston *The optics of nonimaging concentrators:Light and Solar Energy*, Academic Press Inc (1978) ISBN-10:0127453504 ISBN-13: 978-0127453507

[16] A. Okamura *Optimization of the collection efficiency of a hexagonal light collector using quadratic and cubic Bzier curves* Astroparticle Physics 38 (2012) 18-24, DOI:10.1016/j.astropartphys.2012.08.008

[17] Cerruti et al, 5th international meeting on HE gamma-ray astronomy, AIP conference proceedings, 1505, 635 (2012).

[18] Costille C. Etude thermomécanique d'un télescope de 4 m, Internal Document SST-GATE, 503-THM-GEPI-TN-0001

[19] Eurocode 8: Design of Structures for Earthquake Resistance – Part 1: General Rules, Seismic Actions and Rules for Buildings. EN 1998-1

[20] Hinton J, Bernlöhr K. SST Requirements, Issue 1.1. Document CTA, MAN-PO/120808, Nov 2012

[21] Metéo France. Weather Forecast in Ile-de-France surveys, 2011

[22] MSC Software. MSC Nastran 2012 Quick Reference Guide. MSC Software Eds

[23] Sadek F, Mohraz B, Taylor AW, Chung RM. A Method for Estimating the Parameters of Tuned Mass Dampers for Seismic Applications. Earthquake Engineering and Structural Dynamics, Vol. 26 p614-635 (1997)

[24] www.sunearthtools.com

[25] Vogiatzis K. Thermal Modeling Environment for TMT. Proc. SPIE 7738. Modeling, Systems Eng. and Project Management for Astronomy IV, Aug 2010

[26] Schmoll, J. A study of the optics of a 4m dual-mirror SST. Internal Note, CTA-MC-Note-6, March 2011.

[27] Conconi, P. et al. A Status Report on TARGET-5. https://portal.cta-observatory.org/WG/SST/SiteAssets/SitePages/Home/INAF-ASTRI-OpticalDesign_rev3.pdf, 2012.

[28] Ohm, S. and Hinton, J. Impact of measurement errors on charge resolution and system performance. Internal Note, SCI-MC/121113, November 2012.

[29] K. Bechtol, S. Funk, A. Okumura, L. L. Ruckman, A. Simons, H. Tajima, J. Vandenbroucke, and G. S. Varner. TARGET: A multi-channel digitizer chip for very-high-energy gamma-ray telescopes. *Astroparticle Physics*, 36:156–165, August 2012.

[30] Okumura, A. A Status Report on TARGET-5. https://www.cta-observatory.org/indico/getFile.py/access?contribId=122&sessionId=5&resId=0&materialId=slides&confId=115, November 2012.

A SST Requirements document

SST Requirements

Responsible Editor:

J. Hinton University of Leicester

Approved By:

- Preliminary - Approval Pending

Applicable Documents:

MAN-PO/121011 The CTA Observatory

MAN-PO/121004 Performance Requirements for CTA

MAN-PO/121018 RAMS Requirements for CTA

MAN-PO/120918 Environmental Requirements for CTA

SCI-LINK/121120 Science Requirements for CTA

History:

1.0	2012-11-15	First released version
1.1	2012-11-16	Minor revisions
1.2	2012-11-27	Incorporated comments from TG and GP
1.3	2012-12-14	Modified mirror requirements and cost comments
1.4	2013-01-15	Version for submission to the STAC

Distribution: Open

CONTENTS

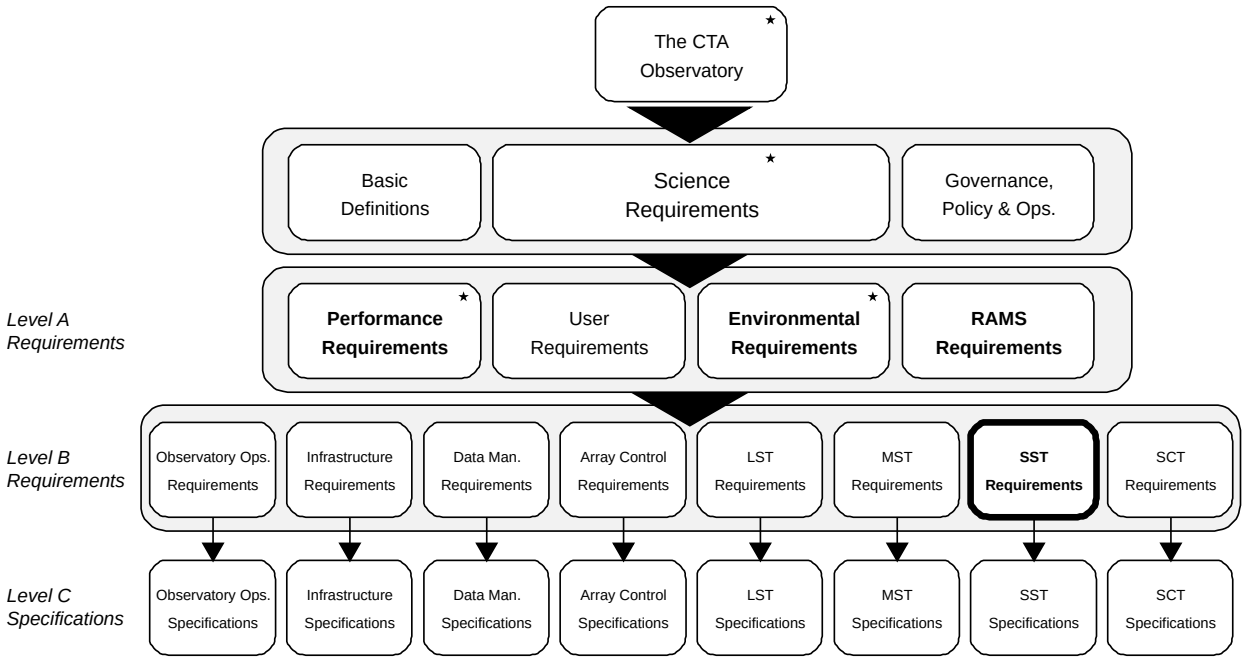

Figure 1: Structure of the high-level documentation of CTA, highlighting the place of this document (in bold, thick outer line) in the structure. Documents containing higher-level requirements from which the requirements given here are derived are marked with a star. Source documents for requirements included here are shown here with titles in bold.

1 HISTORY AND CONTRIBUTORS

This document is derived from on the earlier document [1] and includes substantial contributions from the Monte Carlo work package and its coordinator Konrad Bernlohr. It incorporates input from an internal review of CTA requirements in March 2012.

2 SCOPE

This document provides the requirements for the small-sized telescopes (SSTs) of CTA, including requirements for camera, structure and drive systems. In the current CTA cost model the average capital cost (escalated assuming a build phase from 2014-2019) of a single SST telescope is assumed to be 420 keuro.

The relationship of this document to the remaining CTA requirements documentation is shown in Figure 1.

3 REQUIREMENTS DEFINITION

3.1 Environment

Environmental requirements are summarised in the following. All requirements are associated with a specified State of the System or Product.

3.1.1 Conditions

A-ENV-0010 CTA must meet all performance requirements for Observations, during the conditions frequently encountered at the sites in each hemisphere.
R, motivated by: CTA-100, CTA-070 *Applicable States: Observing*

A-ENV-0020 CTA must not incur damage beyond the SL state during the transitions between Observing and Safe states during conditions outside those acceptable for Observations.
R, motivated by: CTA-100, CTA-070 *Applicable States: Transitional*

A-ENV-0030 CTA must not incur damage beyond the SL state during conditions expected to occur with a probability of ∼2% per annum at the sites in each hemisphere.
R, motivated by: CTA-100, CTA-070 *Applicable States: All*

3.1.2 Geography and Topography of Site

A-ENV-0130 The altitude of the sites (and at which all CTA Products must meet all requirements) above mean sea level will be **1500 - 3800 m**.
R, motivated by: CTA-010, CTA-020 *Applicable States: All*

Details of the site specifications can be found in the document: *The generic site infrastructure 1. Definition*, OBS-INFRA/120928a.

3.1.3 Ambient Temperature

The air temperature referred to below is that measured outside at 1.5 m height above ground level.

A-ENV-0210 The ambient air temperature during observations will be **-10 to +25 °C**.
R, motivated by: A-ENV-0010 *Applicable States: Observing*

A-ENV-0220 The extreme air temperature range where telescopes and buildings must suffer no damage will be **-20 to +40 °C**.
R, motivated by: A-ENV-0030 *Applicable States: Safe*

A-ENV-0230 The range of air temperature gradient at night time will be ± **5 °C/h**.
R, motivated by: A-ENV-0010 *Applicable States: Observing*

A-ENV-0240 The natural temperature variations within 24 hours will be less than **±30 °C**.
R, motivated by: A-ENV-0030 *Applicable States: Safe*

3.1.4 Relative Humidity

A-ENV-0310 The relative humidity for observations is in the range **4-95 %**.
R, motivated by: A-ENV-0010 *Applicable States: Observing*

A-ENV-0320 The relative humidity for survival in safe state is in the range **2-100 %**.
R, motivated by: A-ENV-0030 *Applicable States: Safe*

A-ENV-0330 The telescopes must operate with un-misted mirrors when the dew point temperature is at least 2°C higher than the ambient temperature. This requirement is effectively an upper limit on relative humidity which is a function of the ambient temperature as shown in Figure 2.
R, motivated by: A-ENV-0010 *Applicable States: Observing*

3.1.5 Rain

A-ENV-0410 The maximum rain precipitation in 24 hours is **200 mm**.
R, motivated by: A-ENV-0030 *Applicable States: Safe*

A-ENV-0420 The maximum rain precipitation in one hour is **70 mm**.
R, motivated by: A-ENV-0030 *Applicable States: Safe*

A-ENV-0430 The assumed wind speed for blowing rain is **90 km/hour**.
R, motivated by: A-ENV-0030 *Applicable States: Safe*

A-ENV-0440 The sizes of the droplets during precipitation with maximum intensity are **0.5-4.5 mm**.
R, motivated by: A-ENV-0030 *Applicable States: Safe*

A-ENV-0450 No rain will be present during Observations
R, motivated by: A-ENV-0010 *Applicable States: Observing*

A-ENV-0460 During transitions the maximum rainfall is **0.5 mm/minute**.
R, motivated by: A-ENV-0020 *Applicable States: Transitional*

3.1.6 Snow and Hail

A-ENV-0510 No snow will be present on the ground during Observations.
R, motivated by: A-ENV-0010 *Applicable States: Observing*

A-ENV-0520 Damage beyond the SL level must not be incurred during Safe state for a snow accumulation of the ground of **<50 cm**.
R, motivated by: A-ENV-0030 *Applicable States: Safe*

A-ENV-0530 All elements of the system must be undamaged in their Safe positions by the impact of hailstones with diameter **<20 mm**.
R, motivated by: A-ENV-0030 *Applicable States: Safe*

A-ENV-0540 The CTA sites must have a probability that hailstones with a diameter of > 20 mm should occur with a frequency **<0.03 year^{-1}**.
R, motivated by: A-ENV-0030 *Applicable States: All*

3.1.7 Ice

A-ENV-0610 No ice will be present on any surfaces during Observations.
R, motivated by: A-ENV-0010 *Applicable States: Observing*

A-ENV-0620 Damage beyond the SL level must not be incurred during Safe state for an ice thickness (on all surfaces) of **<20 mm**.
R, motivated by: A-ENV-0030 *Applicable States: Safe*

The density of ice can be assumed to be 900 kg/m^3

3.1.8 Wind

Unless otherwise stated, the wind speeds referred to are at 10 metre height above ground (this corresponds to the Mean Wind Velocity as defined in *Eurocode 1 - Part 4*).

Wind profile
The external wind speed as a function of the height h above ground is: $V(h) = V(10\,\mathrm{m})\ln(h/z_0)/\ln(10\,\mathrm{m}/z_0)$ (for $h > z_{\min}$) and $V(h) = V(z_{\min})$ (for $h < z_{\min}$) where V is the average wind speed, z_0 is the roughness length and can be assumed to be 0.3 m, and $z_{\min} = 5$ m.

Conversion between average and gust wind speeds
The conversion from mean wind velocity (averaged over time T) to maximum wind velocity including gust (of duration t) is: $V_{\mathrm{gust}} = V_{\mathrm{mean}} \times G(T,t)$ where $G(T,t) = 1 + 0.42 \times I \times \ln(T/t)$ is the gust factor and I is the turbulence intensity, with I=25%.

Wind Spectrum
The model describing the wind dynamic characteristics is the Von Karman model. The Von Karman model describing the (one-sided) Power Spectral Density of the longitudinal wind speed temporal variation is:

$$s(f) = (IU)^2 \frac{4L/\bar{U}}{(1 + 70.8(fL/\bar{U})^2)^{5/6}} \quad (1)$$

With parameters defined as follows: f: frequency (Hz), I: turbulence intensity, $\bar{U}$: mean wind speed (m/s), L: integral length scale (m), and with I=25% and L=50 m.

A-ENV-0710 During observations the 10-minute average wind speed is **<36 km/h**.
R, motivated by: A-ENV-0010 *Applicable States: Observing*

A-ENV-0720 During transitions (telescopes moving to the Safe state), the 10-minute average wind speed is **<50 km/h**.
R, motivated by: A-ENV-0020 *Applicable States: Transitional*

A-ENV-0730 Telescopes and buildings must not incur damage beyond the SL level whilst in the Safe state for 1-s gusts of <200 km/hour or 10-minute average wind speeds **<120 km/h**.
R, motivated by: A-ENV-0030 *Applicable States: Safe*

3.1.9 Solar Radiation

A-ENV-0810 The maximum solar radiation is 1200 W/m^2 (survival condition).
R, motivated by: A-ENV-0030 *Applicable States: Safe*

A-ENV-0820 All components exposed to direct solar radiation must be UV resistant (survival condition).
R, motivated by: A-ENV-0030 *Applicable States: Transitional Safe*

3.1.10 Dust and Sand

A-ENV-0910 The natural cleanliness class of the site at 3 m above ground should be better than ISO-Class 8 (according to ISO14644-1) for 90% of the time (survival condition). This ISO-Class 8 corresponds to a limit of 29×10^3 particle of 5μm per m^3 of air.
R, motivated by: A-ENV-0010 *Applicable States: All*

3.1.11 Aggressive Atmosphere

A-ENV-1010 The following aggressive atmosphere concentrations should not be exceeded: NO <3 ppb, NO_2 <3 ppb, SO_2 <3 ppb (Survival conditions).
R, motivated by: A-ENV-0010 *Applicable States: All*

3.1.12 Earthquakes

A-ENV-1110 Damage Limitation requirement: Peak horizontal ground acceleration $< 0.25g$ and peak vertical ground acceleration $< 0.22g$ with 10% probability of exceeding these figures within 10 years (reference return period 95 years). With these conditions, all system shall meet the Damage Control Limit requirement as defined in [2].
R, motivated by: CTA-100 *Applicable States: All*

A-ENV-1120 Collapse Prevention requirement: Peak horizontal ground acceleration $< 0.5g$ and peak vertical ground acceleration $< 0.44g$ with 10% probability of exceeding these figures within 50 years (reference return period 475 years). With these conditions, all systems shall meet the Collapse Prevention Limit state as defined in [2].
R, motivated by: CTA-110 *Applicable States: All*

3.1.13 Electromagnetic Environment

A-ENV-1210 The site will be subject to lightning. It will be considered a lighting protection zone (LPZ) 0A and have lightning current parameters corresponding to the lighting protection level (LPL) I, as defined in EN 62305:2011.
R, motivated by: A-ENV-0030 *Applicable States: Safe*

3.1.14 Background Light

The telescopes will observe during astronomical darkness and during partial moonlight. The ambient night sky background (NSB) light level during observations is expected to be in the range given, with a spectrum of the form shown in Figure 3, in the wavelength range 300-650 nm [3, 4, 5].

A-ENV-1420 The ambient (night sky background, NSB) light level during observations is expected to be in the range given, with a spectrum of the form shown in Figure 3, in the wavelength range 300-650 nm. The nominal NSB level corresponds to the lowest end of this range, with partial moonlight observations as the upper bound [3, 4, 5]. **0.24-1.2 $\mathbf{ns^{-1}\ sr^{-1}\ cm^{-2}}$**.
R, motivated by: A-ENV-0010 *Applicable States: Observing*

A-ENV-1430 Illumination of telescope components and in particular of cameras by (non-calibration) artificial light sources on or near the site must not exceed 10^6 photons ns^{-1} sr^{-1} cm^{-2}, and must occur <once per week for any given telescope.
R, motivated by: CTA-100 *Applicable States: Observing*

3.2 RAMS

3.2.1 Procedure

A-RAMS-0010 CTA RAMS activities must be carried out according to the RAMS Plan [6].
R, motivated by: CTA-70, CTA-90, CTA-100, CTA-110

A-RAMS-0015 All CTA activities with implications for RAMS must be carried out in a manner consistent with the Quality Plan [7].
R, motivated by: CTA-70, CTA-90, CTA-100, CTA-110

A-RAMS-0017 All CTA Products must be fully documented to ensure effective and safe operation.
R, motivated by: CTA-90, CTA-100, CTA-110

3.2.2 Availability

Many of the following availability requirements apply to the availability of system elements during Observations (i.e. the time in which conditions are suitable for Products to enter the Observing state). As maintenance during the night (when Observations are taking place) is not foreseen, failure of an element during Observations will normally imply the loss of ∼half of one night's data (assuming failure at a random time during observations), assuming that repair can be conducted during the next day. For example, a Product that fails 5 times per year and is always fixed during the next day will have an availability of ≈ 99%. The availability and maintenance requirements apply only to the Operations phase of CTA.

A-RAMS-0040 The availability of each SST telescope during observation time must be **>97 %**.
R, motivated by: SCI-120, CTA-100 *Applicable States: Observing*

3.2.3 Maintenance

The maintenance effort expressed in terms of person-hours in this section refers to an estimate averaged over one year of operations. The work required for upgrades or extensions after the commissioning of the observatory is not included.

A-RAMS-0100 Provision must be made for access and lifting points for safe assembly, maintenance and disassembly as an integral part of the design of telescopes. .
R, motivated by: SCI-120, CTA-110 *Applicable States: All*

A-RAMS-0102 For components where corrective maintenance proceeds via exchange, a sufficient stock of spare components must be in stock on site. The number of spares must be matched to failure rates and the time needed for repair or production of replacements. The observatory must keep an inventory of spares.
R, motivated by: CTA-100, CTA-90 *Applicable States: All*

A-RAMS-0110 The maintenance of a single SST telescope on site must on average require **<3 person-hours/week**.
R, motivated by: SCI-120, CTA-100 *Applicable States: All*

3.2.4 Safety

A-RAMS-0160 The telescope position in the Safe state (the *parking position*) must be chosen to avoid damage by the Sun (normally anti-solar pointing at noon).
R, motivated by: SCI-120 *Applicable States: Safe*

A-RAMS-0170 The telescope must be able to return to the Safe state in Normal and Critical conditions (see [2]) within **5 minutes**.
R, motivated by: CTA-100 *Applicable States: Transitional*

A-RAMS-0180 Construction, operation and decommissioning of the CTA systems must comply with European or host country regulations, whichever is more stringent, concerning health, human safety, as well as with the health and safety requirements described in sections 1, 3, 4 and 6 of Annex I of the directive 2006/42/EC on machinery.
R, motivated by: CTA-110 *Applicable States: All*

A-RAMS-0190 No single failure of hardware or software must have either critical or catastrophic consequences.
R, motivated by: CTA-110 *Applicable States: All*

A-RAMS-0200 No reasonably foreseeable human error must have either critical or catastrophic consequences.
R, motivated by: CTA-110 *Applicable States: All*

A-RAMS-0210 The telescope must never be in the state where it can move in an uncontrolled manner.
R, motivated by: CTA-110 *Applicable States: All*

A-RAMS-0275 Hazard analysis and safety practices will be governed by the following order of precedence:

- Design for minimum risk: The primary means for mitigation of risk is to eliminate the hazard through design.
- Incorporate safety devices: protective devices are used in conjunction with the design features to attain an acceptable level of risk. Provisions shall be made for periodic functional checks as applicable.
- Provide warning devices: When neither design nor safety items can effectively eliminate or reduce hazards, devices shall be used to detect the condition, and to produce an adequate warning to alert personnel of a hazard.
- Procedures and training: only where it is impractical to substantially eliminate or reduce the hazard or where the condition of the hazard indicates additional emphasis, special operating procedures and training shall be used.

R, motivated by: CTA-110 *Applicable States: All*

A-RAMS-0300 The entrance control device to restricted areas must not impede the exit from them, nor must this exit be dependent on electric supply or electronic and software systems.
R, motivated by: CTA-100, CTA-110 *Applicable States: All*

A-RAMS-0310 Each telescope must have all the safety subsystems and signaling needed to prevent human injuries.
R, motivated by: CTA-110 *Applicable States: All*

A-RAMS-0330 The telescope must transition from Observing to Safe (telescope to a secured *parking position*, camera to the Safe state) if the communication with Array Control is lost during observations.
R, motivated by: CTA-110 *Applicable States: Observing*

A-RAMS-0335 Transition from Safe state to Observing state and back to the Safe state must not require any manual intervention in the field (such as manually opening locks, powering up telescopes, etc.).
R, motivated by: CTA-110, CTA-090 *Applicable States: Transitional*

A-RAMS-0340 Drive control systems must be provided with safety interlocks that prevent injury to personnel or damage to telescope that might result from inadvertent operation, human error or mechanical or control system failure.
R, motivated by: CTA-110 *Applicable States: All*

A-RAMS-0350 High voltage systems must be provided with safety interlocks that prevent injury to personnel that might result from inadvertent operation, human error or mechanical or control system failure.
R, motivated by: CTA-110 *Applicable States: Observing*

A-RAMS-0360 During observations telescopes must never point in a direction where, in case of breakdown, the rising Sun could cause catastrophic damage in the time needed after the beginning or civil twilight to reach the telescope and to move it manually to the Safe position.
R, motivated by: CTA-110 *Applicable States: Observing*

3.2.5 Reliability

A-RAMS-0400 CTA elements must provide detailed performance monitoring information (or provide data which allow this information to be generated by higher-level systems) which can be used to identify emerging problems and ensure the reliable functioning of the instrument.
R, motivated by: CTA-100 *Applicable States: All*

A-RAMS-0410 Comprehensive logging of conditions, actions, incidents, errors and warnings must take place to ensure that problems and failures can be analysed and avoided in the future.
R, motivated by: CTA-100 *Applicable States: All*

A-RAMS-0420 Information on the status of CTA elements (down to at least assembly level) must be provided in a readily comprehensible manner to array operators, to ensure that problems and failures are rapidly identified.
R, motivated by: CTA-100 *Applicable States: All*

A-RAMS-0430 Appropriate measures must be taken to ensure that the probability of complete loss of a significant fraction of acquired data is extremely low, for example through storage of multiple copies of observation data.
R, motivated by: CTA-100 *Applicable States: All*

3.3 System Performance

Requirements related to the performance of the entire array of telescopes at the northern or southern site of CTA are given below. Unless otherwise specified the performance must be met under optimum observing conditions and relate to the detection of γ-ray initiated air-showers.

3.3.1 Inter-telescope Timing

A-PERF-0610 The goal rms inter-telescope time accuracy for events (for use in event reconstruction) is **2 ns**.
G, motivated by: A-PERF-0100 *Applicable States: Observing*

3.4 Sub-System Performance

In the following requirements the word sensitivity is used to denote the differential sensitivity in 5 independent logarithmic bins per decade in energy.

3.4.1 SST sub-system

A-PERF-1210 The SST sub-system sensitivity must be within a factor of 2 of that required for the system as a whole, see Figure 4, at all energies above 10 TeV.
R, motivated by: SCI-180 *Applicable States: Observing*

A-PERF-1220 The SST sub-system sensitivity above 100 TeV must be within a factor of 1.5 of that required for the system as a whole, see Figure 4
R, motivated by: SCI-180 *Applicable States: Observing*

A-PERF-1230 The goal SST sub-system collection area at 100 TeV is **>7 km^2**.
G, motivated by: SCI-180 *Applicable States: Observing*

A-PERF-1240 The goal SST sub-system sensitivity above 50 TeV is equal to that required for the system as a whole , see Figure 4.
R, motivated by: SCI-180 *Applicable States: Observing*

3.5 Telescope Performance

This section describes the required properties and capabilities which are common to all the Telescopes of CTA. Telescope-type specific requirements are described at Level B.

3.5.1 Product

This section includes requirements on CTA telescopes as a whole, rather than assemblies such as cameras, which are given below. The overall optical efficiency of the system for signal photons $\varepsilon_{\rm sig}$, referred to below, is defined as $\varepsilon_{\rm sig} = \int_0^\infty F(\lambda)\varepsilon(\lambda)d\lambda / \int_{300{\rm nm}}^{550{\rm nm}} F(\lambda)d\lambda$, where $F(\lambda)$ is the nominal Cherenkov spectrum shown in Figure 3 and ε is the probability that a photon of a given wavelength, incident on the primary mirror and parallel with the optical axis, results in the generation of a detectable photoelectron. This efficiency therefore includes the reflectivity of mirrors, of light concentrators if present, camera dead space and the quantum and collection efficiencies of photosensors. The optical efficiency for background, $\varepsilon_{\rm bg}$, is defined in a similar way but weighted by a spectrum $F(\lambda)$ given by the NSB curve in Figure 3.

A-PERF-2020 The overall optical efficiency of the telescope to signal photons, $\varepsilon_{\rm sig}$, must be **>11 %**.
R, motivated by: A-PERF-0100 *Applicable States: Observing*

A-PERF-2025 The overall optical efficiency of the telescope to background light (including night sky background and albedo), $\varepsilon_{\rm bg}$, must be such that $\varepsilon_{\rm sig}/\sqrt{\varepsilon_{\rm bg}}$ is **>0.3** .
R, motivated by: A-PERF-0100 *Applicable States: Observing*

A-PERF-2050 The systematic error on the measurement of the absolute intensity (i.e. photons per square metre) of Cherenkov light (post-calibration) at the position of each telescope must be **<10 %**.
R, motivated by: A-PERF-0260 *Applicable States: Observing*

A-PERF-2060 The goal systematic error on the measurement of the absolute intensity of Cherenkov light at the position of each telescope is **5 %**.
G, motivated by: A-PERF-0260 *Applicable States: Observing*

3.5.2 Structure, Drives & Optics

A-PERF-2110 The elevation range of the telescope during observations must be at least **25-91 degrees**.
R, motivated by: SCI-130, A-PERF-0720 *Applicable States: Observing*

A-PERF-2120 The azimuth range of the telescope during observations must be at least **540 degrees**.
R, motivated by: SCI-130, A-PERF-0720 *Applicable States: Observing*

A-PERF-2130 The telescopes must be able to track any target in the positioning range for observations for elevation angles smaller than **89.2 degrees**.
R, motivated by: SCI-130, A-PERF-0720 *Applicable States: Observing*

A-PERF-2140 The telescopes must be able to track any target in the positioning range for observations with a precision in each axis of **<0.1 degrees**.
R, motivated by: A-PERF-2010 *Applicable States: Observing*

3.5.3 Camera

A-PERF-2250 The fraction of the time that an individual telescope is unavailable for recording of events (due for example to inefficiency in data collection, transport and storage) during observations must be **<8 %**.
R, motivated by: SCI-120 *Applicable States: Observing*

A-PERF-2260 The camera must survive undamaged illumination of any or all pixels for up to 10 seconds at an intensity of $\mathbf{10^6\ ph.\ ns^{-1}sr^{-1}cm^{-2}}$.
R, motivated by: A-ENV-1330 *Applicable States: Observing*

3.6 Product

3.6.1 Positioning

For the purpose of telescope design it is acceptable to assume that the post-calibration pointing precision of a telescope will be smaller than the raw mis-pointing arising from structural deformations due to wind and gravity by a factor 30. A factor of ten improvement is assumed to be possible with a predictive model for the deformations, with the remaining factor of 3 improvement due to monitoring with one or more guide cameras or other real-time monitoring devices.

B-SST-0020 The rms space-angle post-calibration pointing precision of the Product, i.e. the precision with which a physical position in the camera can be mapped to a celestial coordinate at a given time, must be **<7 arcseconds**.
R, motivated by: A-PERF-0230 *Applicable States: Observing*

3.7 Telescope

3.7.1 Optics

The optical point-spread function (PSF) is defined in terms of θ_{80}, the angle around the spot centroid at a given off-axis angle, within which 80 percent of the light reflected on to the camera falls. The mirror reflectivity is defined as the fraction of photons incident on the primary, unaffected by shadowing, which are reflected onto either with camera or the secondary mirror, as appropriate.

B-SST-0110 The effective mirror area of the SST, corrected for the effect of shadowing by the camera and its support structure (and if present the secondary mirror), must be **>5 m^2**.
R, motivated by: A-PERF-2010 *Applicable States: All*

B-SST-0130 The telescope must focus light (over 80% of the required camera field of view diameter) with an optical PSF θ_{80} of **<0.25 degrees**.
R, motivated by: A-PERF-2150 *Applicable States: Observing*

B-SST-0140 The telescope must focus light (over 80% of the required camera field of view diameter) with an rms optical time spread of **<1.5 ns**.
R, motivated by: A-PERF-2070 *Applicable States: All*

3.7.2 Positioning

B-SST-0210 The telescope must be able to rotate to any point in the sky above 30° in elevation in at most **90 s**.
R, motivated by: A-PERF-2040 *Applicable States: Transitional*

B-SST-0220 The goal time for the telescope to rotate to any point in the sky above 30° in elevation is **60 s**.
G, motivated by: A-PERF-2040 *Applicable States: Transitional*

3.8 Camera

3.8.1 Assembly Performance

The measurement of the time-integrated Cherenkov intensity is the most critical task for the camera pixel hardware and/or off-line analysis. The total charge collected (Q) can be expressed as a number of photo electrons (p.e.) and should be close to proportional to the Cherenkov light intensity in the pixel. The rms charge resolution (σ_Q) has contributions from Poisson fluctuation in the number of p.e. generated by the incoming (signal and background) photons, the intrinsic excess noise factor (ENF) of the photo sensor (typically in the range of 1.1-1.2), and additional noise sources associated with the electronics and signal capture (for example digitization errors). The methods used to derive the required and goal curves given below are described in [8].

B-SST-1010 The required fractional charge resolution for Cherenkov signals under dark sky conditions is given in Figure 5
R, motivated by: A-PERF-2220 *Applicable States: Observing*

B-SST-1020 The goal fractional charge resolution for Cherenkov signals under dark sky conditions is given in Figure 5
G, motivated by: A-PERF-2220 *Applicable States: Observing*

B-SST-1030 The goal rms time resolution for signal amplitudes of more than 5 photoelectrons is **2 ns**.
G, motivated by: A-PERF-2240 *Applicable States: Observing*

3.8.2 Focal Plane Detectors

The field of view diameter is defined as the average distance of an outermost pixel edge to the camera centre, in addition the focal plane must be fully instrumented up to 85 percent of the required field of view radius. The angular size of pixels is given in terms of a flat-to-flat distance under the assumption of hexagonal pixels. For square pixels the appropriate number is approximately 10 percent smaller for the flat-to-flat distance, corresponding to the same solid angle subtended.

B-SST-1110 The focal plane positioning precision in the directions perpendicular to the optical axis should be **<0.06 degrees**.
R, motivated by: A-PERF-2030 *Applicable States: Observing*

B-SST-1120 The focal plane positioning in the direction along the optical axis should be such that defocusing does not increases the θ_{80} of the optical PSF beyond the requirement B-SST-0130.
R, motivated by: A-PERF-2150 *Applicable States: Observing*

B-SST-1130 The field of view diameter of the camera must be **>8 degrees**.
R, motivated by: A-PERF-0020 *Applicable States: All*

B-SST-1140 The goal field of view diameter of the camera is **9 degrees**.
G, motivated by: A-PERF-0020 *Applicable States: All*

B-SST-1150 The angular size of pixels in the camera must be **<0.25 degrees**.
R, motivated by: A-PERF-2210 *Applicable States: All*

B-SST-1160 The largest dead spaces (non-photosensitive surfaces) must be narrower than $\theta_{80}/4$ at any place within the required FoV.
R, motivated by: A-PERF-2020 *Applicable States: All*

B-SST-1170 The average efficiency of the focal plane detectors (i.e. conversion efficiency from photons to photoelectrons), weighted by the reference Cherenkov spectrum (see Figure 3) in the wavelength range 300-550nm, including deadspace and the efficiency of any focal plane optics/windows etc, must be **13 %**.
R, motivated by: A-PERF-2020 *Applicable States: Observing*

3.8.3 Data Capture

The time duration of the Cherenkov light signal as seen in a camera depends on the distance to the shower core, and on the type and energy of the primary particle. The duration of the Cherenkov signal in an image is in general larger than the duration within a single pixel due to image time gradients which are significant at impact distances beyond the Cherenkov light pool radius. The integration window requirements given here are therefore the result of a compromise between charge collection efficiency from air shower signals and noise contribution from the NSB, taking into account the different expected impact distance distribution for the different telescopes. The goal for the readout window aims for an improvement in the fraction of Cherenkov light recorded and a potential reduction in the integrated noise, resulting possibly in improved charge resolution. For these benefits to be felt a sampled waveform would need to be provided by the data capture electronics. The integration window is defined here as the time interval over which photons arriving at the photosensor contribute at least half of their signal to the integrated charge, as compared to photons for which the signal arrives centered with respect to the window.

I_{thresh} is defined as the mean integrated Cherenkov light intensity that is needed to generate a local camera trigger with a probability of 50 percent over 90 percent of the camera field of view (diameter) and any image orientation. The average trigger probability should be calculated for gamma-ray showers with a differential energy spectrum following a power law with a photon index of 2.5 and for a uniform shower impact position distribution. For proton initiated showers a factor of 1.5 higher I_{thresh} is acceptable.

B-SST-1210 The cameras must allow operation with a pixel integration window fixed with respect to the local camera trigger time. For small signals up to about 100 photo-electrons an integration with fixed window width within the following range is required: **20-30 ns**.
R, motivated by: A-PERF-2230 *Applicable States: Observing*

B-SST-1220 The goal readout window for this camera is **80 ns**.
G, motivated by: A-PERF-2230 *Applicable States: Observing*

B-SST-1230 The Cherenkov light intensity that is needed to generate a local camera trigger with a probability of at least 50 % over 90 % of the camera field of view (diameter) and with any image orientation, must be smaller than: I_{thresh}/ (NSB per pixel / 0.12 ns^{-1})$^{1/2}$ photoelectrons, or I_{thresh} if NSB < 0.12 ns^{-1}. The value of the threshold image size I_{thresh} must be **<100 pe**.
R, motivated by: A-PERF-1210, A-PERF-0100 *Applicable States: Observing*

B-SST-1240 The goal value of the threshold image size I_{thresh} is **80 pe**.
G, motivated by: A-PERF-1210, A-PERF-0100 *Applicable States: Observing*

B-SST-1250 The camera readout system shall be able to deliver information from all camera pixels in each event, unless it can be shown that for a given partial readout scheme, using end-to-end simulations, that the achievable sensitivity is not reduced by more than **2 %**.
R, motivated by: A-PERF-0100 *Applicable States: Observing*

B-SST-1260 The fraction of the time during a continuous observation, at the minimum event rate, that the camera is unable to identify or record events (the *deadtime*) must be **<5 %**.
R, motivated by: A-PERF-2250 *Applicable States: Observing*

B-SST-1270 The deadtime of the camera must be continuously monitored. The availability for trigger or readout of an individual camera in any given event must be derivable
R, motivated by: A-PERF-0410 *Applicable States: Observing*

B-SST-1280 The camera must be able to readout events (whilst meeting the deadtime requirement) arriving at random with a rate of **>300 Hz**.
R, motivated by: A-PERF-1210, A-PERF-0100 *Applicable States: Observing*

B-SST-1290 The goal rate to read out events is **600 Hz**.
G, motivated by: A-PERF-1210, A-PERF-0100 *Applicable States: Observing*

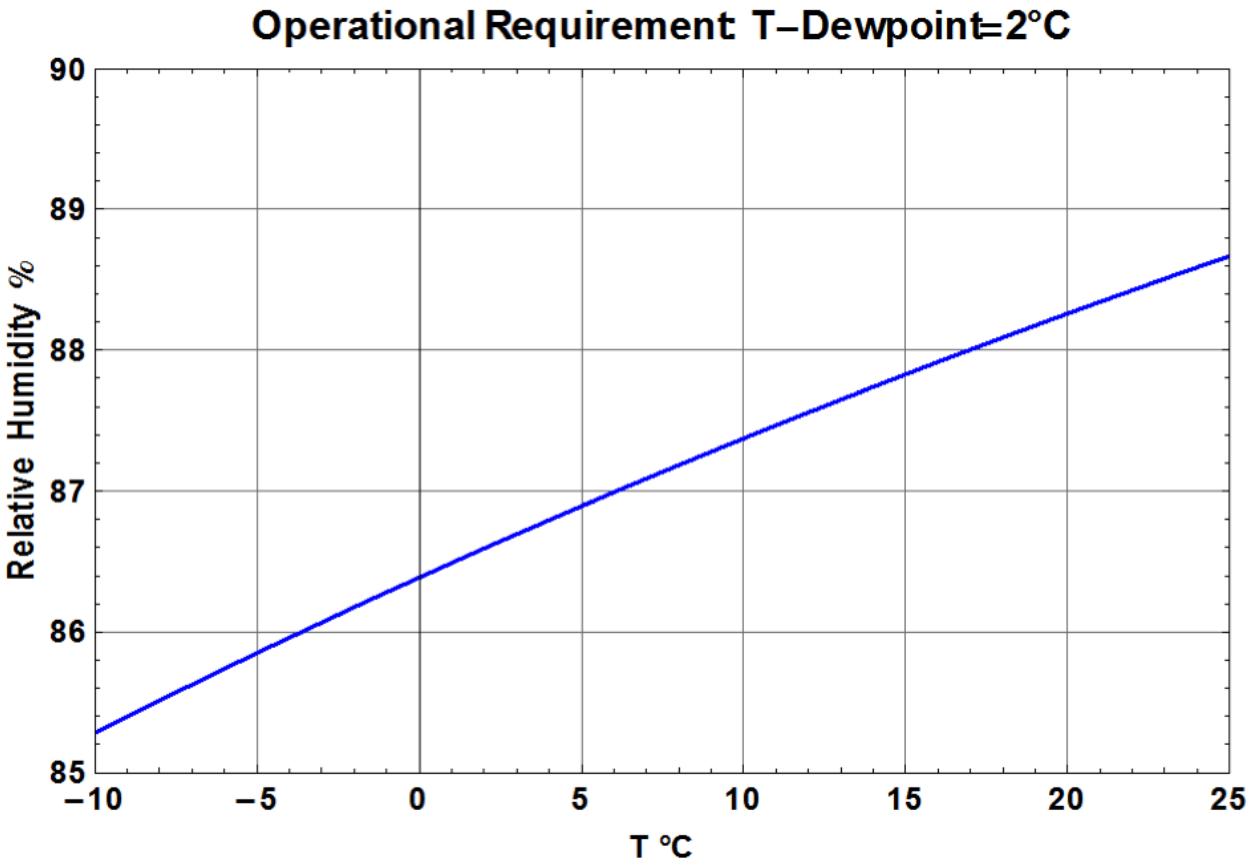

Figure 2: The requirement A-ENV-00330 as an upper limit of relative humidity as a function of ambient temperature.

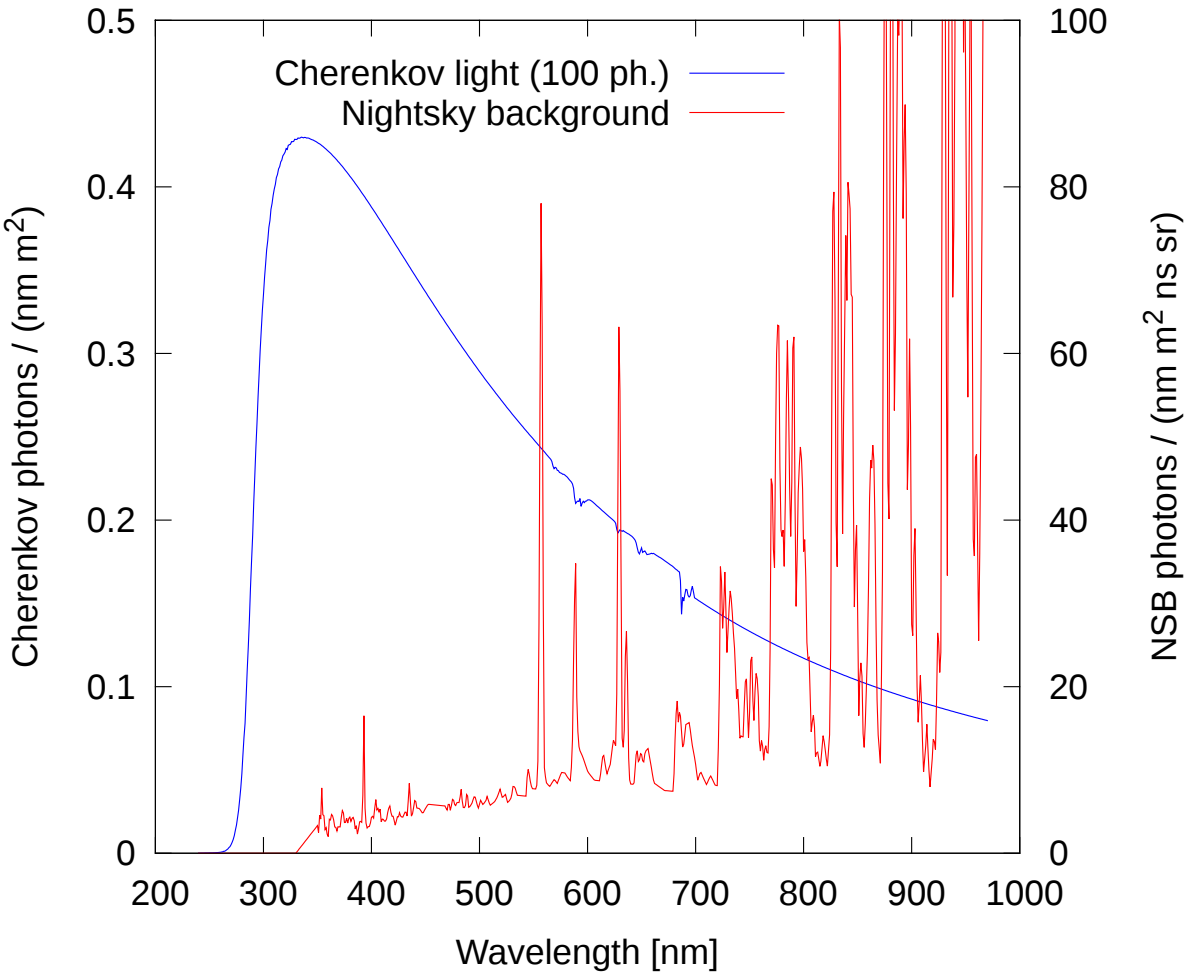

Figure 3: Reference spectra for night sky background (NSB) light and Cherenkov light from γ-ray initiated air-showers at ground-level. The Cherenkov light spectrum is shown for showers at 20° zenith angles and detected at 2000 m above sea level. The Cherenkov light is scaled to 100 photons/m^2 in the wavelength range from 300 600 nm, a value typical for gamma-ray showers of about 500 GeV at small core distances.

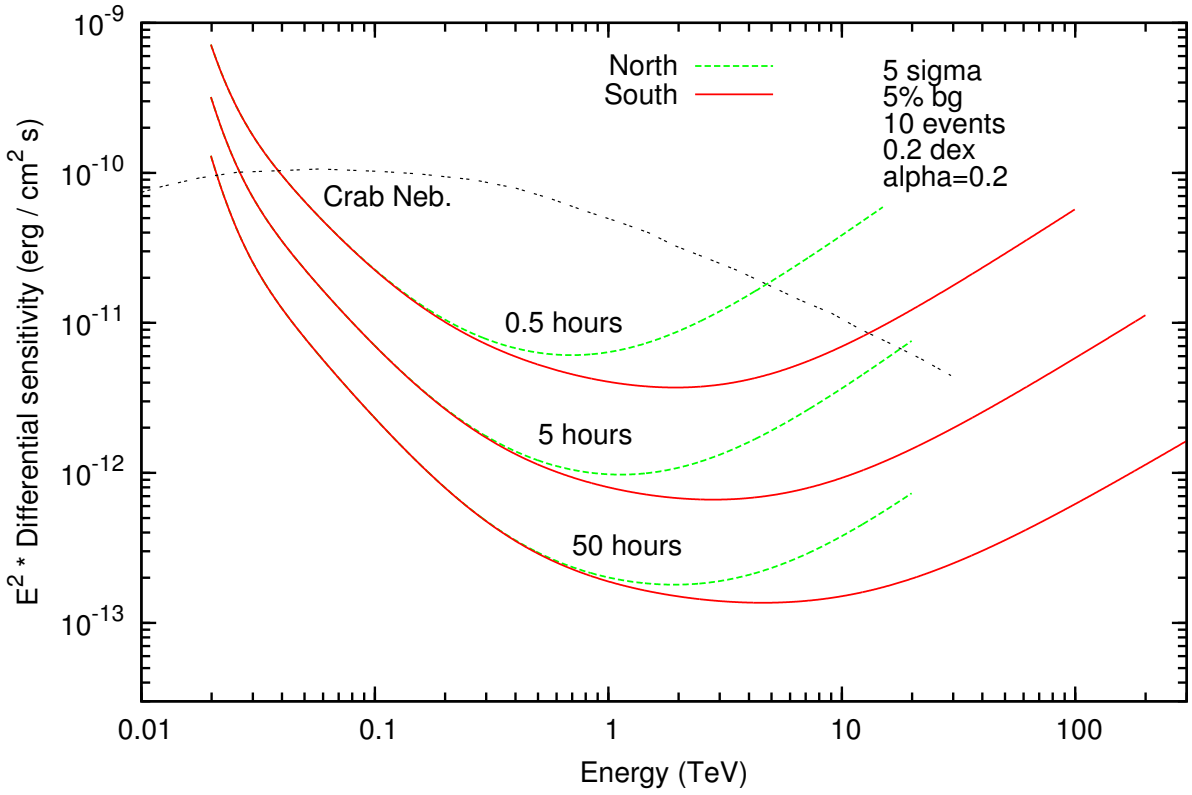

Figure 4: Required differential sensitivity for the CTA south and north arrays, calculated in five bins per decade of energy, for different observation times. The sensitivity is scaled with E^2. For comparison, the dashed black line indicates the expected flux from the Crab Nebula.

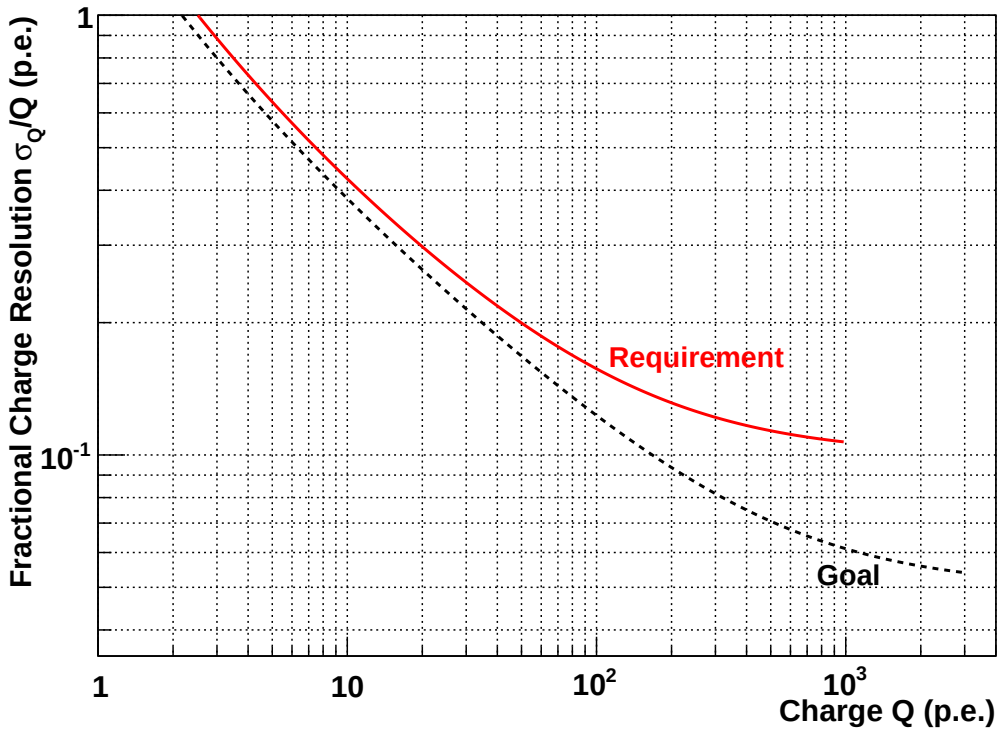

Figure 5: Fractional rms charge resolution σ_Q/Q per pixel for different Cherenkov light signal amplitudes, expressed in units of photoelectrons (p.e.). The red line describes the required performance and the dashed black line the goal performance for a specified background level of 0.125 photoelectrons/ns.

4 SUMMARY TABLE

Req. #	Title	Type	Value	Flow down
A-ENV-0010	Operating Conditions	R	Text	CTA-100+
A-ENV-0020	Transition Conditions	R	Text	CTA-100+
A-ENV-0030	Survival Conditions	R	Text	CTA-100+
A-ENV-0130	Altitude	R	1500 - 3800 m	CTA-010+
A-ENV-0210	Observation temperature	R	-10 to +25 °C	A-ENV-0010
A-ENV-0220	Survival temperature	R	-20 to +40 °C	A-ENV-0030
A-ENV-0230	Temperature gradient	R	5 °C/h	A-ENV-0010
A-ENV-0240	Temperature shocks	R	±30 °C	A-ENV-0030
A-ENV-0310	Observation humidity	R	4-95 %	A-ENV-0010
A-ENV-0320	Survival humidity	R	2-100 %	A-ENV-0030
A-ENV-0330	Mirror misting	R	Text	A-ENV-0010
A-ENV-0410	Rain in 24 hours	R	200 mm	A-ENV-0030
A-ENV-0420	Rain in 1 hour	R	70 mm	A-ENV-0030
A-ENV-0430	Rain wind speed	R	90 km/hour	A-ENV-0030
A-ENV-0440	Rain droplet size	R	0.5-4.5 mm	A-ENV-0030
A-ENV-0450	Rain during observations	R	Text	A-ENV-0010
A-ENV-0460	Rain during transition	R	0.5 mm/minute	A-ENV-0020
A-ENV-0510	Observation snow load	R	Text	A-ENV-0010
A-ENV-0520	Survival snow load	R	<50 cm	A-ENV-0030
A-ENV-0530	Hailstone damage	R	<20 mm	A-ENV-0030
A-ENV-0540	Hailstone frequency	R	<0.03 $year^{-1}$	A-ENV-0030
A-ENV-0610	Observation ice load	R	Text	A-ENV-0010
A-ENV-0620	Survival ice load	R	<20 mm	A-ENV-0030
A-ENV-0710	Observation wind speed	R	<36 km/h	A-ENV-0010
A-ENV-0720	Transition wind speed	R	<50 km/h	A-ENV-0020
A-ENV-0730	Survival wind speed	R	<120 km/h	A-ENV-0030
A-ENV-0810	Solar radiation level	R	Text	A-ENV-0030
A-ENV-0820	UV resistance	R	Text	A-ENV-0030
A-ENV-0910	Dust and sand	R	Text	A-ENV-0010
A-ENV-1010	Aggressive atmosphere	R	Text	A-ENV-0010
A-ENV-1110	Earthquake damage limitation	R	Text	CTA-100
A-ENV-1120	Earthquake collapse prevention	R	Text	CTA-110
A-ENV-1210	Lightning	R	Text	A-ENV-0030
A-ENV-1420	Operating illumination	R	0.24-1.2 ns^{-1} sr^{-1} cm^{-2}	A-ENV-0010
A-ENV-1430	Survival illumination	R	Text	CTA-100
A-RAMS-0010	RAMS Plan	R	Text	CTA-70+

Table 1: Summary of the requirements in this document (table 1 from 3). In the *type* column: R=requirement, G=goal and C=consideration.

Req. #	Title	Type	Value	Flow down
A-RAMS-0015	Quality Plan	R	Text	CTA-70+
A-RAMS-0017	Documentation	R	Text	CTA-90+
A-RAMS-0040	SST Availability	R	>97 %	SCI-120+
A-RAMS-0100	Maintenance/access Points	R		SCI-120+
A-RAMS-0102	Spare Components	R	Text	CTA-100+
A-RAMS-0110	SST Maintenance	R	<3 person-hours/week	SCI-120+
A-RAMS-0160	Telescope Parking Position	R	Text	SCI-120
A-RAMS-0170	Telescope Parking Speed	R	5 minutes	CTA-100
A-RAMS-0180	Safety Regulations	R	Text	CTA-110
A-RAMS-0190	Human Safety	R	Text	CTA-110
A-RAMS-0200	Human Errors	R	Text	CTA-110
A-RAMS-0210	Telescope Movement	R	Text	CTA-110
A-RAMS-0275	Safety Practices	R	Text	CTA-110
A-RAMS-0300	Entrance Controls	R	Text	CTA-100+
A-RAMS-0310	Safety Signaling	R	Text	CTA-110
A-RAMS-0330	Automatic Transition	R	Text	CTA-110
A-RAMS-0335	State Transitions	R	Text	CTA-110+
A-RAMS-0340	Drive Control Safety	R	Text	CTA-110
A-RAMS-0350	High Voltage Safety	R	Text	CTA-110
A-RAMS-0360	Observation Pointing Safety	R	Text	CTA-110
A-RAMS-0400	Performance Monitoring	R	Text	CTA-100
A-RAMS-0410	Logging	R	Text	CTA-100
A-RAMS-0420	Status Information	R	Text	CTA-100
A-RAMS-0430	Backups	R	Text	CTA-100
A-PERF-0610	Inter-telescope Timing	G	2 ns	A-PERF-0100
A-PERF-1210	SST sub-system sensitivity above 10 TeV	R	See Figure 4	SCI-180
A-PERF-1220	SST sub-system sensitivity above 100 TeV	R	See Figure 4	SCI-180
A-PERF-1230	SST sub-system collection area at 100 TeV	G	>7 km^2	SCI-180
A-PERF-1240	SST sub-system sensitivity above 50 TeV	R	See Figure 4	SCI-180
A-PERF-2020	Telescope/camera throughput	R	>11 %	A-PERF-0100
A-PERF-2025	Telescope/camera signal to noise	R	>0.3	A-PERF-0100
A-PERF-2050	Absolute throughput error	R	<10 %	A-PERF-0260
A-PERF-2060	Absolute throughput error	G	5 %	A-PERF-0260
A-PERF-2110	Elevation Range for Observations	R	25-91 degrees	SCI-130+
A-PERF-2120	Azimuth Range for Observations	R	540 degrees	SCI-130+
A-PERF-2130	Tracking range	R	89.2 degrees	SCI-130+

Table 2: Summary of the requirements in this document (table 2 from 3). In the *type* column: R=requirement, G=goal and C=consideration.

Req. #	Title	Type	Value	Flow down
A-PERF-2140	Tracking precision	R	<0.1 degrees	A-PERF-2010
A-PERF-2250	Camera deadtime	R	<8 %	SCI-120
A-PERF-2260	Camera maximum illumination	R	10^6 ph. $ns^{-1}sr^{-1}cm^{-2}$	A-ENV-1330
B-SST-0020	Post-calibration Pointing Precision	R	<7 arcseconds	A-PERF-0230
B-SST-0110	Mirror area	R	>5 m^2	A-PERF-2010
B-SST-0130	Optical PSF quality	R	<0.25 degrees	A-PERF-2150
B-SST-0140	Optical time dispersion	R	<1.5 ns	A-PERF-2070
B-SST-0210	Repositioning time	R	90 s	A-PERF-2040
B-SST-0220	Repositioning time	G	60 s	A-PERF-2040
B-SST-1010	Charge Resolution	R	See Figure 5	A-PERF-2220
B-SST-1020	Charge Resolution	G	See Figure 5	A-PERF-2220
B-SST-1030	Time Resolution	G	2 ns	A-PERF-2240
B-SST-1110	Focal Plane Positioning in x and y	R	<0.06 degrees	A-PERF-2030
B-SST-1120	Focal Plane Positioning in z	R	Text	A-PERF-2150
B-SST-1130	Field of view diameter	R	>8 degrees	A-PERF-0020
B-SST-1140	Field of view diameter	G	9 degrees	A-PERF-0020
B-SST-1150	Angular Pixel Size	R	<0.25 degrees	A-PERF-2210
B-SST-1160	Deadspace	R	Text	A-PERF-2020
B-SST-1170	Photon Detection Efficiency	R	13 %	A-PERF-2020
B-SST-1210	Integration Window	R	20-30 ns	A-PERF-2230
B-SST-1220	Readout Window	G	80 ns	A-PERF-2230
B-SST-1230	Minimum Image Amplitude	R	<100 pe	A-PERF-1210+
B-SST-1240	Minimum Image Amplitude	G	80 pe	A-PERF-1210+
B-SST-1250	Pixel readout	R	2 %	A-PERF-0100
B-SST-1260	Deadtime	R	<5 %	A-PERF-2250
B-SST-1270	Deadtime measurement	R	Text	A-PERF-0410
B-SST-1280	Event rate	R	>300 Hz	A-PERF-1210+
B-SST-1290	Event rate	G	600 Hz	A-PERF-1210+

Table 3: Summary of the requirements in this document (table 3 from 3). In the *type* column: R=requirement, G=goal and C=consideration.

REFERENCES

[1] Bernlöhr, K., Hermann, G. & Hinton, J.A. Level b: Cta sub-system performance requirements. MAN-TPC/120321, March 2012.

[2] CTA Consortium. CTA Basic Definitions. MAN-PO/120726, October 2012.

[3] C. R. Benn and S. L. Ellison. Brightness of the night sky over La Palma. *New Astronomy Reviews*, 42:503–507, November 1998.

[4] S. Preuss, G. Hermann, W. Hofmann, and A. Kohnle. Study of the photon flux from the night sky at La Palma and Namibia, in the wavelength region relevant for imaging atmospheric Cherenkov telescopes. *Nuclear Instruments and Methods in Physics Research A*, 481:229–240, April 2002.

[5] D. Britzger, E. Carmona, P. Majumdar, O. Blanch, J. Rico, J. Sitarek, R. Wagner, and for the MAGIC Collaboration. Studies of the Influence of Moonlight on Observations with the MAGIC Telescope. *ArXiv e-prints*, July 2009.

[6] CTA Consortium. RAMS Plan for CTA. MAN-QA/111121, November 2012.

[7] CTA Consortium. Quality Plan for CTA. MAN-QA/110405, April 2011.

[8] Ohm, S. and Hinton, J. Impact of measurement errors on charge resolution and system performance. Internal Note, SCI-MC/121113, November 2012.

B Overview of the ASTRI data analysis

The Data Analysis Chain, for both the ASTRI SST–2M prototype and the mini–Array, is composed of several different steps that are illustrated in Figure B.1.

The main analysis steps are briefly described in the following.

Data Preparation (L0). The binary raw data, coming directly from the DAQ system, are properly organized into the custom file format (the current baseline format is FITS, but considerations of storage space and data access efficiency may require this to be changed). This process will be done separately for each telescope of the mini–array.

Calibration (L1a). The information for each pixel of the camera coming from the DAQ are properly calibrated and converted into a number of photoelectrons, including the timing information for the signal. This process will be done separately for each telescope of the mini–array.

Image Cleaning and Parameterization (L1b). The aim of this analysis step is to remove, for each Cherenkov triggered event, those pixels containing light most likely not related to a Cherenkov event, and subsequently to perform the calculation of the parameters associated with the image of each event. This process will be done separately for each telescope of the mini–array.

Data Quality Check (L1c). The quality of the data coming from the Camera will be checked by means of information provided by the telescope subsystems and using the basic image parameter distributions computed in the previous analysis step. During this step, standard quality cuts related to some image parameters (and/or their combinations) can be generally applied. This process will be done separately for each telescope of the mini–array.

Merging of the information coming from the different telescopes (L2a) [Mini-Array Only]

Up to the image parameterization step, the analysis chain will run separately over the data streams of each telescope. The multi–telescope analysis will proceed:

to identify the matching images belonging to the same Cherenkov event from the N data streams.

to calculate further image parameters based on the multi–telescopes view of the same showers (stereo parameters). In particular, the primary incoming direction, the reconstructed impact point on the ground with respect to each telescope and the estimated height of the shower maximum (MaxHeight) will be derived.

At the end of this analysis step, just one data stream will be produced.

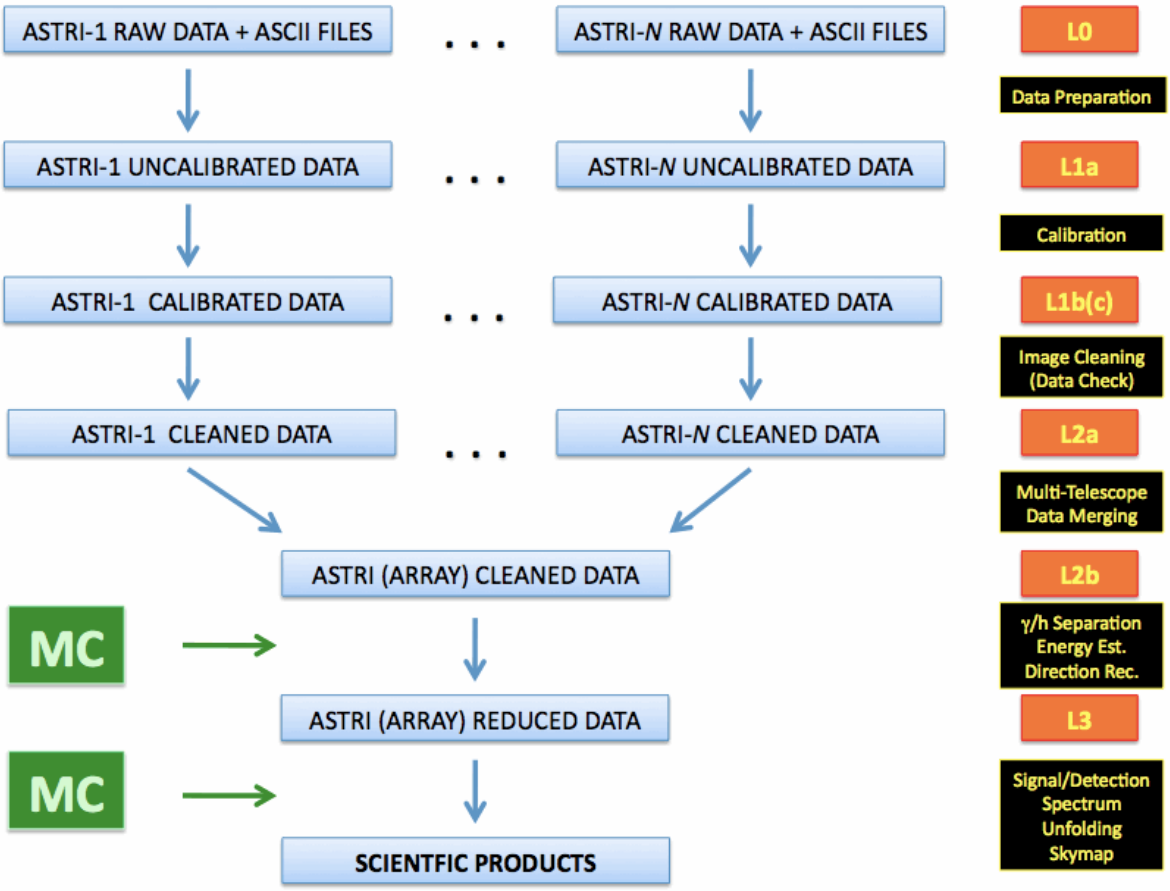

Figure B.1: ASTRI Prototype and mini–Array Data Reduction & Analysis Chain compliant with the CTA data flow

In the case of single-telescope observation this analysis step is of course not carried out and no multi-telescope image parameters will be available.

γ/hadron Separation, Energy Estimation, Direction Reconstruction (L2b). Once for each triggered event the image parameters (plus, in the multi–telescope case, the stereo parameters) are available, calibration will be applied in order to estimate the nature of the events (hadron–like or γ–like) and to reconstruct their energy and incoming direction.

Signal determination (L3a). In order to determine the significance of a given observation the so–called $\theta 2$–plot (or alternately the so-called Alpha–plot, in case of single–telescope data) will be computed, after applying proper analysis cuts to the events (such as Hadronness, reconstructed energy, single-telescope image parameter cuts, ...). Since an irreducible background is expected to survive (in all energy ranges), a background region (i.e. a region where no known γ-ray sources are present) will be necessary to estimate the significance of the observation.

Skymaps (L3b). The reconstruction of the direction of incomungγ–like events from the camera(s) reference frame to the RA/Dec system will be properly computed following specific algorithms.

Spectrum and Light Curve Calculation (L3c). Several calculations will be performed during this step of the analysis. The Effective Time of the observation is estimated from the data sample (taking into account the dead time of the detector). Through the application of proper γ/hadron separation cuts (in bins of Erec) to the data and to the test MC–γ sample, the number of excess events and the Effective Collecting Area of the observation will be extracted. The spectrum and the light curve will be then computed as a function of Erec and Time. In case the observation does not show significant γ–ray excesses, the calculation of flux upper limits will be performed. A single program will carry out all these calculations.

C GATE

C.1 Analytical size of the Tower

The principle of analytical size of the tower is briefly detailed here.

This step takes into account several loads and criteria: Compression of the tower caused by the mass of the Elevation Structure. If this load is too high, there is a buckling hazard. Bending of the tower caused by the wind First eigenfrequency of the tower

Compression stress is deduced from the ratio F to A where F is the load corresponding to the mass of the Elevation Structure and A is the area of the tower. As the tower may be considered as a beam, it is possible to apply to it the beam theory. So we can express the bending deviation, the corresponding stress and the first eigenfrequency. The buckling hazard is estimated by Euler's law. Calculated stresses are compared to the traction yield stress of the steel.

C.2 Azimuth Drive Wheel and Worm

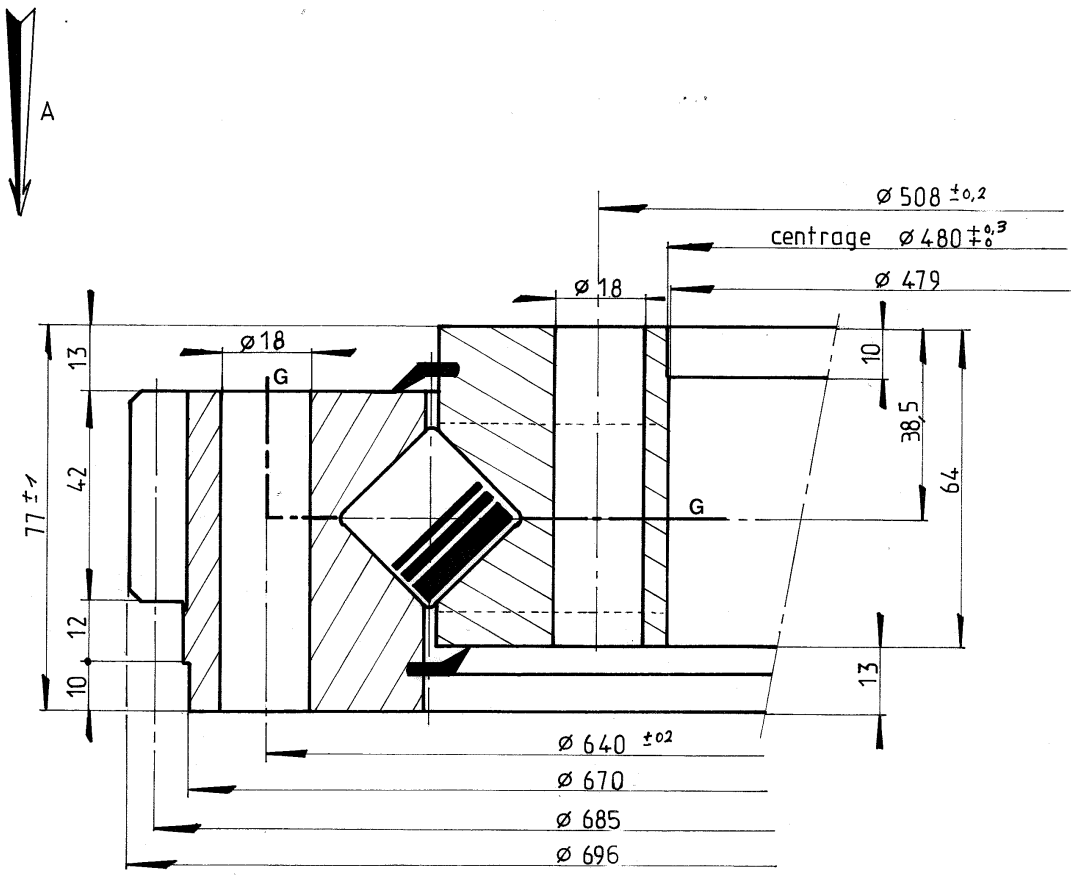

Ansicht nach A
implantation according to A
implantation suivant A

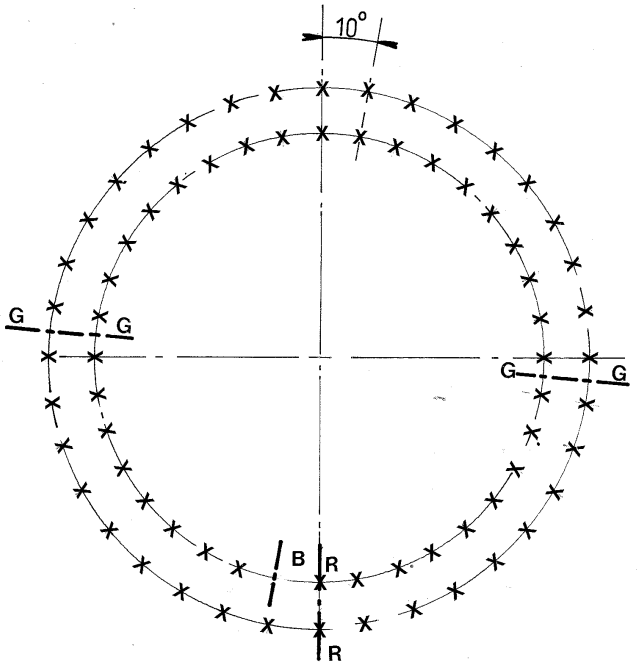

ENGRENE AVEC VIS 05-0070-00

entr'axe 377,63 jeu 0 à 0,23 mm

module apparent 6,02216
inclinaison à droite 4° 55'

moucher les angles

Denture - Gear - Verzahnung: hélicoïdale tronquée

Module - Modul: 6	Angle de pression - Pressure angle - Eingriffswinkel: 14°30
Diametral Pitch	
Nbre de dents - Nr. of teeth - Zähnezahl: 114	Troncature - Truncature - Kopfkürzung: 0,5
Diamètre primitif - Pitch diameter - Teilkreisdurchmesser: 686,526	
Correction 2δM - Correction 2δM - Korrektur 2δM: -1,52	
Cote sur 10 dents - Measurement on teeth - Zahnmesswerte bei Zähnen: 176,75 -0,13	
Faux-rond au diamètre primitif - Run out on pitch dia. - Unrundheit am Teilkreis	
Non trempée - No hardened gear - ungehärtet: 0,35	
Trempée - hardened gear - gehärtet	

Matière - Material - Werkstoff
Z → XC 45 - AISI 1045 - CK 45 (200 HB)
X → XC 45 - AISI 1045 - CK 45 (250-300 HB)
N → 42 CD 4 - AISI 4142 - 42 CrMo 4 (205-235 HB)
D → 42 CD 4 - AISI 4142 - 42 CrMo 4 (250-300 HB)

X	B.E.	36	Trous de fixation - Mouting holes - Befestigungsbohrungen	Ø 18 — équid. equis. gl. Abst.
	O.R.			
	A.R.			
	B.I.	36	Trous de fixation - Mouting holes - Befestigungsbohrungen	-1 Ø 18 — équid. equis. gl. Abst.
	I.R.			
G	B.E.	2	Trous graisseurs - Grease holes - Schmierbohrungen	10 x 100 — équid. equis. gl. Abst.
	O.R.			
	A.R.			
	B.I.	2	Trous graisseurs - Grease holes - Schmierbohrungen	10 x 100 — équid. equis. gl. Abst.
	I.R.			

BR: Position approximative bouchon et raccord de trempe
Filler plug and hardening connection of raceway
ca Stopfen - und Haerteschlupf - Position

Spécifications particulières - Particular Specifications - Sonderausführungen

Ind.	Date Datum	Nature - Change - Art	Visa Name
A	14-11-85	Ancien N° était 06-114.3-05	MC
05	02-04-73	Correction ESX: -1,52 était -2,52	JPS
04	4-12-76	Faux-rond 0,40 devient 0,35	DL
03	7-2-76	Ajouter valeur faux-rond	JPS
02	13-1-76	Perçage B.E et BI 36 trous au lieu de 18	JPS
01	15-11-75	hauteur denture 42 dégagement 13	DL

Des. Drawn Bearb. Date Datum: DL 7-11-72
Vér. Ver. Kontr. Date Datum: DL 7-11-72
Ech. Scale Maßstab: 1

Poids estimé - Gewicht ca - Estimated weight: 77 kg lbs

N° 06-0574-04

A

ROLLIX DEFONTAINE

Usine : 85530 LA BRUFFIERE
Tél. (51) 62.20.17 Télex 711378 F

C.3 Azimuth Drive Worm Gear

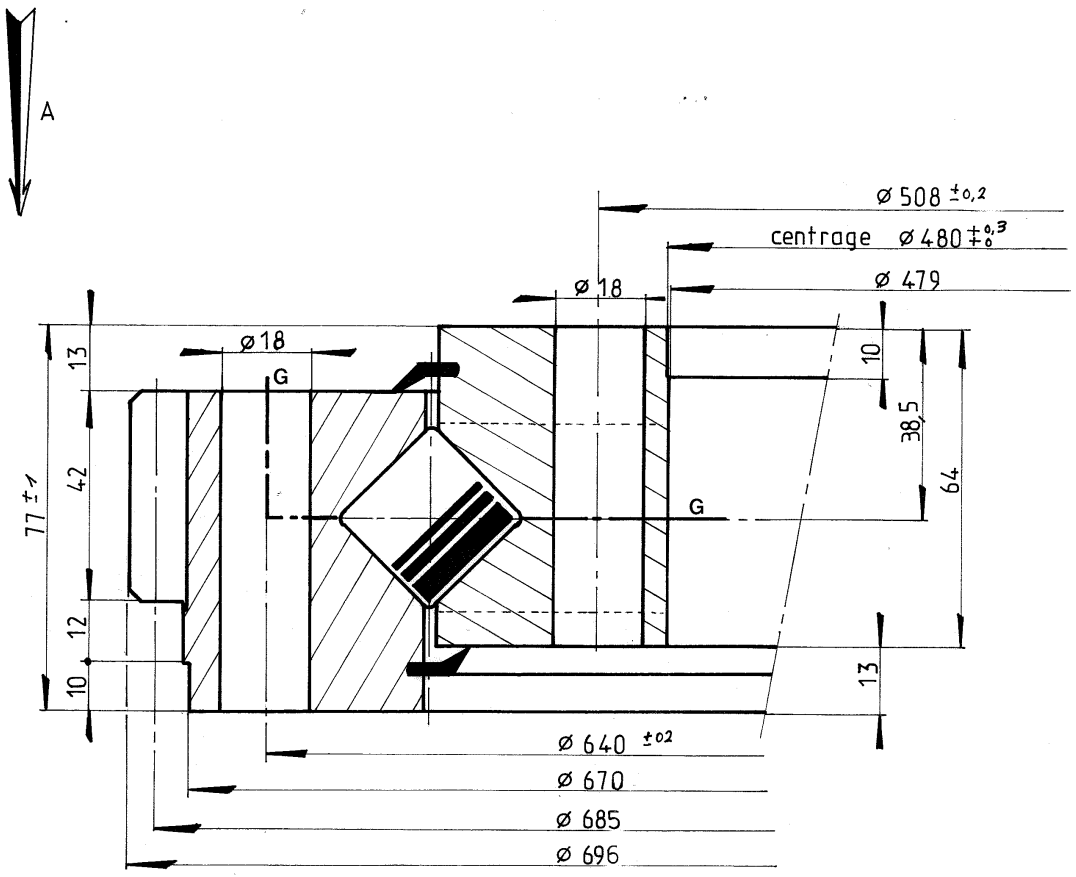

Ansicht nach A
implantation according to A
implantation suivant A

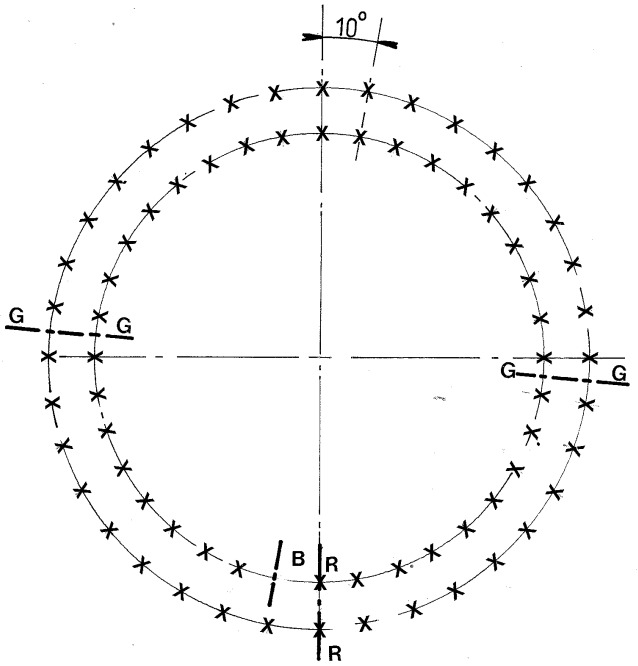

ENGRENE AVEC VIS 05-0070-00

entr'axe 377,63 jeu 0 à 0,23 mm

module apparent 6,02216
inclinaison à droite 4° 55'

moucher les angles

Denture - Gear - Verzahnung: hélicoïdale tronquée

Module - Modul: 6	Angle de pression - Pressure angle - Eingriffswinkel: 14°30
Diametral Pitch	
Nbre de dents - Nr. of teeth - Zähnezahl: 114	Troncature - Truncature - Kopfkürzung: 0,5
Diamètre primitif - Pitch diameter - Teilkreisdurchmesser: 686,526	
Correction 2δM - Correction 2δM - Korrektur 2δM: -1,52	
Cote sur 10 dents - Measurement on teeth - Zahnmesswerte bei Zähnen: 176,75 -0,13	
Faux-rond au diamètre primitif - Run out on pitch dia. - Unrundheit am Teilkreis	
Non trempée - No hardened gear - ungehärtet: 0,35	
Trempée - hardened gear - gehärtet	

Matière - Material - Werkstoff
Z → XC 45 - AISI 1045 - CK 45 (200 HB)
X → XC 45 - AISI 1045 - CK 45 (250-300 HB)
N → 42 CD 4 - AISI 4142 - 42 CrMo 4 (205-235 HB)
D → 42 CD 4 - AISI 4142 - 42 CrMo 4 (250-300 HB)

X	B.E.	36	Trous de fixation - Mouting holes - Befestigungsbohrungen	Ø 18 — équid. equis. gl. Abst.
	O.R.			
	A.R.			
	B.I.	36	Trous de fixation - Mouting holes - Befestigungsbohrungen	-1 Ø 18 — équid. equis. gl. Abst.
	I.R.			
G	B.E.	2	Trous graisseurs - Grease holes - Schmierbohrungen	10 x 100 — équid. equis. gl. Abst.
	O.R.			
	A.R.			
	B.I.	2	Trous graisseurs - Grease holes - Schmierbohrungen	10 x 100 — équid. equis. gl. Abst.
	I.R.			

BR: Position approximative bouchon et raccord de trempe
Filler plug and hardening connection of raceway
ca Stopfen - und Haerteschlupf - Position

Spécifications particulières - Particular Specifications - Sonderausführungen

Ind.	Date Datum	Nature - Change - Art	Visa Name
A	14-11-85	Ancien N° était 06-114.3-05	MC
05	02-04-73	Correction ESX: -1,52 était -2,52	JPS
04	4-12-76	Faux-rond 0,40 devient 0,35	DL
03	7-2-76	Ajouter valeur faux-rond	JPS
02	13-1-76	Perçage B.E et BI 36 trous au lieu de 18	JPS
01	15-11-75	hauteur denture 42 dégagement 13	DL

Des. Drawn Bearb. Date Datum: DL 7-11-72
Vér. Ver. Kontr. Date Datum: DL 7-11-72
Ech. Scale Maßstab: 1

Poids estimé - Gewicht ca - Estimated weight: 77 kg lbs

N° 06-0574-04

A

ROLLIX DEFONTAINE

Usine : 85530 LA BRUFFIERE
Tél. (51) 62.20.17 Télex 711378 F

C.4 Torque Motor

TORQUE MOTOR

TMB0140-150

PERFORMANCES		Winding codes	3UBS	3RBN	3UBS	3RBN
		UNIT	FREE AIR CONVECTION		WATER COOLING	
Tp	Peak torque	Nm	191		191	
Tc	Continuous torque	Nm	41.6	41.2	99	98.1
Ts	Stall torque	Nm	31.7	31.3	78.3	77.5
Kt	Torque constant	Nm/Arms	3.92	7.74	3.92	7.74
Ku	Back EMF constant (*)	Vrms/(rad/s)	2.27	4.48	2.27	4.48
Km	Motor constant	Nm/√W	2.58	2.55	2.58	2.55
R20	Electrical resistance at 20°C (*)	Ohm	1.55	6.17	1.55	6.17
L1	Electrical inductance (*)	mH	10.8	42.2	10.4	40.7
Ip	Peak current	Arms	78.1	39.5	78.1	39.5
Ic	Continuous current	Arms	10.8	5.39	27.3	13.7
Is	Stall current	Arms	8.16	4.09	20.7	10.4
Pc	Max continuous power dissipation	W	380	380	2480	2480

SPECIFICATIONS		UNIT	FREE AIR CONVECTION	WATER COOLING
Udc	Nominal input voltage	VDC	600	600
τ th	Thermal time constant	s	2100	66
Rth	Thermal resistance	K/W	0.275	0.0433
2p	Number of poles	-	22	22
J	Rotor inertia	kgm²	4.9E-003	4.9E-003
Mr	Rotor mass	kg	3.57	3.57
Ms	Stator mass	kg	14.3	14.3
Td	Max Detent torque (average to peak)	Nm	0.98	0.98
ns	Stall speed	rpm	0.027	0.83
Δθ w	Water temperature difference for Pc	K	--	5
qw	Minimum water flow for Δθw	l/min	--	7.1
Δpw	Max pressure drop at qw	bar	--	1

Notes: (*) terminal to terminal

Hypothesis and tolerances are in ETEL's Handbook

Ambient Temperature = 20° Celsius, Inlet Water Temperature = 20° Celsius
Max Coil Temperature = 130 ° Celsius
Power with stator connected to a total surface of 0.25 m² and rotor to a total surface of 0.063 m²

Caution: Any use of the motor beyond rated speed could lead to hazardous voltage and serious injuries. ETEL cannot be held responsible if the previous recommandation is not strictly applied

T = f(n) for 3UBS

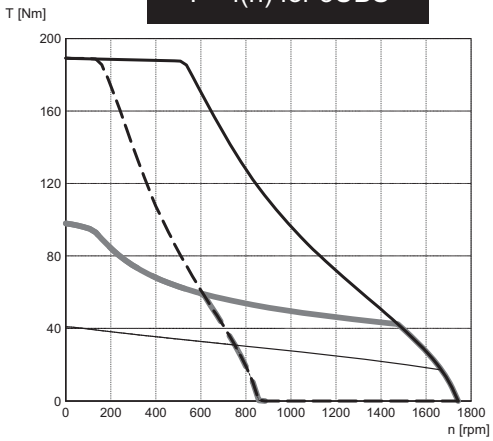

T = f(n) for 3RBN

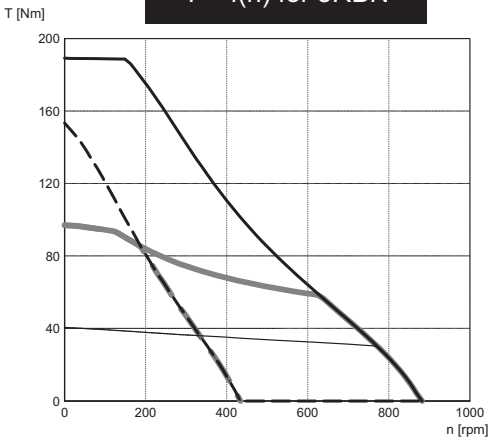

Peak Torque
Tp @ 600 VDC
Tp @ 300 VDC

Continuous Torque with water cooling :
Tc @ 600 VDC
Tc @ 300 VDC

with air convection :
Tc @ 600 VDC
Tc @ 300 VDC

ETEL SA
Zone industrielle - 2112 Môtiers - SWITZERLAND
Phone : +41 32 862 01 00
Fax : +41 32 862 01 01
E-mail : etel@etel.ch
http://www.etel.ch

D Effects of seismic activity upon the SST telescopes

D.1 Introduction

The SST telescopes are designed to withstand loads imposed by seismic ground motion (earthquake). Ground motion during an earthquake will impose horizontal and vertical ground accelerations onto the base of the telescope. The acceleration magnitudes experienced by the telescope will be dependent upon the mechanical properties of the soil, foundation and telescope structure. Since it is not possible to seismically isolate the telescopes from the ground motion it becomes necessary to design the telescopes for earthquake conditions. This is achieved by defining the seismic environment, identifying the relevant design codes, specifying structure limit state criteria and by adopting analysis methods which are the accepted best practice in industry.

D.1.1 Seismic Environment

Two seismic design conditions are specified in the CTA Environmental Requirements.

- A survival event having a horizontal peak ground acceleration 0.50G and a vertical peak ground acceleration of 0.60 G. (10% probability of exceedance in 50 years, reference return period 475 years).
- An operational event having a horizontal peak ground acceleration of 0.34 G and a vertical peak ground acceleration of 0.45 G (10% probability of exceedance in 50 years, reference return period 95 years).

Time waveforms of the horizontal and vertical ground accelerations and response spectra will be used assuming the ESO ELT site in Chile as the CTA site.

D.1.2 Design Standards and SST Structure Limit State Criteria

The seismic analysis of the CTA telescopes must be undertaken in compliance with Eurocode 8 (design of structures for earthquake resistance).

For the survival event the SST's will be designed for a no collapse requirement as defined in Eurocode 8. CTA specific limit state criteria for the CTA telescope structures are also defined in the CTA Environmental Requirements.

D.2 Analysis Methods

Three approaches to the seismic analysis of the SST structures are proposed. The first method (Equivalent Static Method) applies the peak ground acceleration (with an assumed structural amplification factor) directly to the structure. The second method (Response Spectrum Method) applies an acceleration magnitude derived from site specific response spectra to each significant participating mode identified in the modal

analysis. The third method (Direct Time Integration) applies site specific acceleration time waveforms of the seismic ground motion to the telescope base, a detailed finite element model is constructed incorporating not only the telescope structural elements but also the foundation compliance and soil-structure interaction.

D.2.1 Equivalent Static Method

Two load cases are specified for the equivalent static method analysis.

Survival event Horizontal peak ground acceleration 0.50 G
Vertical peak ground acceleration 0.60 G
Operational event Horizontal peak ground acceleration 0.34 G
Vertical peak ground acceleration 0.45 G

In order to account for structural resonance at the first mode an amplification factor is applied to scale the peak ground acceleration magnitudes. An amplification factor of 2.5 is specified in both horizontal directions and an amplification factor of 3.0 specified in the vertical direction. The actual acceleration magnitudes applied to the telescope structure therefore become:

Survival event Horizontal peak ground acceleration 1.25 G
Vertical peak ground acceleration 1.80 G
Operational event Horizontal peak ground acceleration 0.85 G
Vertical peak ground acceleration 1.35 G

D.2.2 Response Spectrum Method (Linear Dynamic Analysis)

If the equivalent static method analysis indicates that the telescope structure is likely to survive the seismic events then the dynamic response of the telescope structure to seismic loads should be evaluated. Site specific response spectra for the ESO ELT site in Chile will be used for the analysis. If these are not available then a normalised response spectrum defined in the seismic design codes (e.g. Eurocode 8) shall be used with appropriate correction for soil classification for the candidate site.

The modal analysis of the telescope structure should ensure that at least 90% of the translational and torsional structural masses are included in the analysis. Then having identified the eigenfrequencies of each significant participating mode the acceleration response may be determined from the response spectrum design curve. If significant structural masses exist that do not contribute to the structural stiffness they may be coupled to the structure using constraint equations or link elements having the appropriate stiffness and degrees of freedom. The modal responses should be combined to give an estimate of the overall structural response using the complete quadratic combination (CQC) method for summating the modal responses since this considers the signs of the modal contributions.

D.2.3 Direct Time Integration (Non Linear Dynamic Analysis)

Direct integration time history analysis is the preferred analysis method for the CTA telescopes. It provides detailed information of the dynamic and non linear local and global responses for all of the telescope system elements including structural response, foundation compliance and soil-structure interaction.

If coupled modes are not present then the output accelerations of the main structure may be used as the input motions for any subsystems (e.g. camera or mirrors). If coupled modes exist a fully coupled analysis of the main and subsystem structures (incorporating the mass and stiffnesses of the subsystem structure) must be undertaken. It may be possible to reduce the computational overhead required for the analysis by representing the telescope structure as a series of beams, plates and lumped masses in a reduced finite element model with constraint equations used to tie the lumped masses to the structure.

The compliance of the underlying soil may result in amplification or attenuation of ground motion and change the eigenfrequencies and eigenmodes of the structure. If the telescope structure is built directly on solid rock then soil-structure interaction can be ignored and the ground acceleration be applied directly to the base of the structure. If the structure is built onto soil a linear spring or spring-damper representing the soil stiffness and damping characteristics may be attached to the base of the structure. As a minimum requirement the soil characteristics should be represented by a first order linear spring-damper soil model using an isotropic linear elastic-plastic model with damping (Mohr-Coulomb).

D.2.4 Seismic Analysis Outputs

The outputs of the seismic analysis are:

- Identification of the telescope structure global response.
- Identification of areas of stress or strains exceeding the design limit.
- Identification of areas where differential displacements may cause failures (e.g. motion of displacement sensitive components such as encoder and motor air gaps, mirror edge gaps).
- Calculation of reaction forces at base/foundation (uplift & overturning moment with maximum wind load and seismic load condition).
- Calculation of interface loads and response spectra for critical subsystems such as the camera, mirrors, drive systems.

E SST Array Power Requirements

Due to the large number of SST telescopes in the CTA array it is necessary to consider not only the construction costs but also the infrastructure capital and operating costs over the lifetime of the array. Significant cost savings may be achieved by reducing the power requirements for the telescopes, particularly by minimising the peak power required for the drive systems during slewing operations.

A power system model is proposed for the SST drive systems and two energy storage solutions for reducing the peak power requirement are proposed, these being lead acid batteries and ultracapacitors.

E.1 Power System Model For The SST Drives

The power model for the SST drive systems assumes the following:

- → 1/3, 1/3, 1/3 velocity profile
- → Azimuth and elevation drives move simultaneously
- → Operating wind speed 50 km/h
- → 3 slew motions of 120 seconds each per hour.
- → 8 hours observing per night

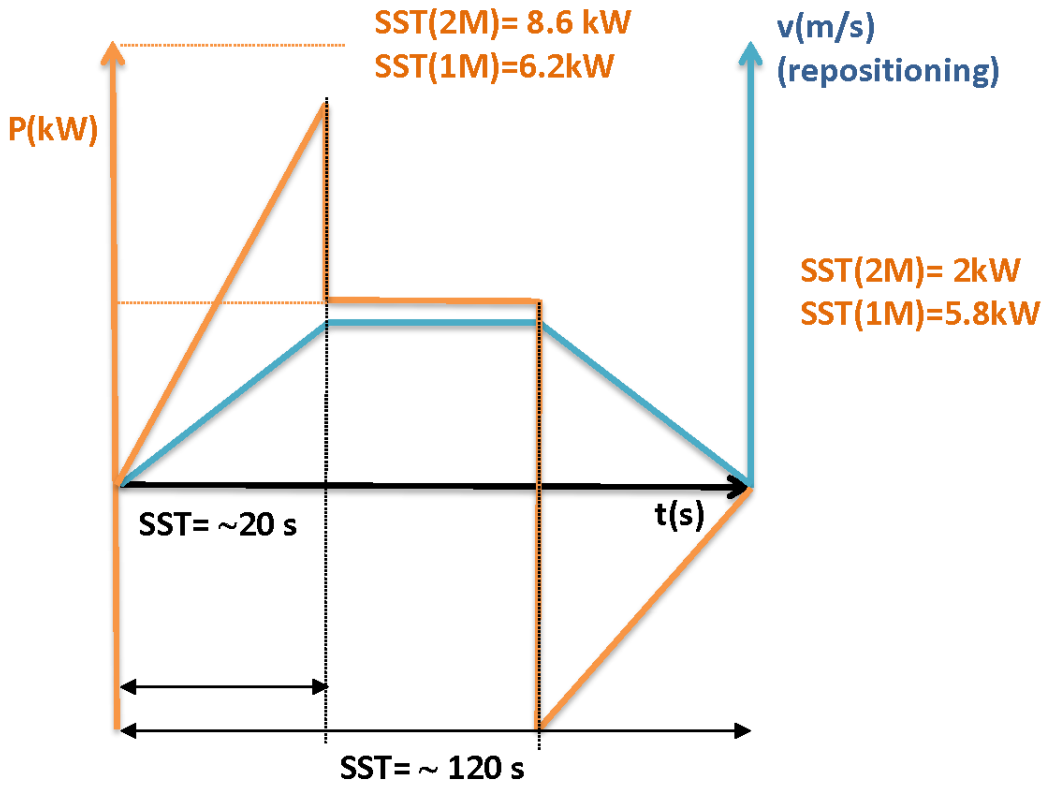

Figure E.1: Power requirements during telescope slewing

E.2 Power Requirements For The SST Telescopes.

The drive power requirements for the SST telescope are estimated by the design groups to be as follows:

- SST-SC (ASTRI) → 8.6 kW Peak, 2 kW Tracking (Camera & Auxiliary Systems)
- SST-DC (7m) → 6.2 kW Peak, 5.8 kW Tracking (Camera & Auxiliary Systems)

The peak shaving potential for the SST telescope drive systems is calculated as:

- SST-SC → 8.6 kW-2 kW = 6.6 kW
- SST-DC (7m) → 6.2 kW- 5.8 kW = 0.4 kW

E.3 Peak Power Shaving Solutions

Various energy storage technologies are available that could be used for peak power shaving for the SST telescopes. These are summarised in table 31:

Using the example of the SST-SC, two technologies appear feasible, conventional lead-acid batteries and ultracapacitors. A proposed solution for each is summarized in table 32.

Type	Pro's	Cons
Lead Acid Battery	• Mature Technology • Low Initial Cost • Total Efficiency AC-AC ∼ 75% • Cost ∼ 400 €/kW	• Limited Life Cycle (∼1000 recharge cycles) • Capacity reduces at low temperatures (∼ 50% at 20°C) • Capacity reduces at over 1000m altitude • Need to replaced over lifetime of array
Ni-Cadmium Battery	• Mature Technology • Cost ∼ 600 €/kW • Tolerant Of Low Temperature	• Limited Life Cycle (∼10,000 cycles) • "Memory Effect" reduces capacity depending on charge/discharge cycling • Toxic, disposal is a problem
Sodium Sulphur Battery	• 3x energy density of lead aci battery • Cost ∼ 800 €/kW	• Needs to be maintained at > 270°C • Thermal management required • Safety risk
Super Capacitor	• Long life (>1 million cycles) • No "Memory Effect" • Stable output from -20 to +70°C • Maintanence free, non-hazardous	• Cost ∼ 1500 €/kW

Table 31: Peak power shaving solutions

Lead Acid Battery	Super Capacitor For 3 Phase Operation
Peak Shaving Requirement = 6.6kW. Recharging between slews is not possible, therefore assuming 8 hours operation with 3 slews of 120s x 3 x 8 = 48 minutes $\simeq$ 1 hour. The required battery capacity is 6.6 kW/1 hour = 550 Amp hr battery 12 Volt	Peak Shaving Requirement = 6.6kW. Can recharge between slews, therefore require 6.6 kW for 2 minutes. Totalenergy = 6600 W $\times$ 120 $s = 7.92 \times 10^5$J Assuming V_{max} = 560V, V_{min} = 450V to allow drives to operate at 3 phase Total energy = 0.5 x Capacitance x ($V_{max}{}^2 - V_{min}^2$). Required Capacitance = 13 Farad.
Solution 6 off Yuasa NPL-100-12 100 Amp-hr lead acid batteries 500€each. Each battery dimensions = 407mm L x 172 mm W x 240 mm H. Weight = 39kg	**Solution** 10 off Maxwell BMOD0130P056 130 Farad ultra capacitor module connected in series. Each ultra capacitor dimensions = 683 mm L x 175 mm W x 177 mm H. Weight = 18kg
Maintenance Requirements Replacement required every 1000 cycles, approximately every 3 years over lifetime of array.	**Maintenance Requirements** No replacement required over lifetime of array.
Cost Initial installation cost = 3k€/SST-2M Total cost over 30 year lifetime = 30 k€/SST-2M	**Cost** Initial installation cost = 9k€/SST-2M Total cost over 30 year lifetime = 9 k€/SST-2M

Table 32: Example power solutions